Impacts of Climate Variation and Change on Hydrologic and Vegetation Dynamics

by

Yanlan Liu

Environment
Duke University

Date: _____

Approved:

_____
Mukesh Kumar, Supervisor

_____
Gabriel G. Katul

_____
Amilcare Porporato

_____
James S. Clark

Dissertation submitted in partial fulfillment of the requirements for the degree of
Doctor of Philosophy in Environment
in the Graduate School of Duke University
2019

ABSTRACT

Impacts of Climate Variation and Change on Hydrologic and Vegetation Dynamics

by

Yanlan Liu

Environment
Duke University

Date: _____
Approved:

_____
Mukesh Kumar, Supervisor

_____
Gabriel G. Katul

_____
Amilcare Porporato

_____
James S. Clark

An abstract of a dissertation submitted in partial fulfillment of the requirements for
the degree of Doctor of Philosophy in Environment
in the Graduate School of Duke University
2019

Abstract

Human-induced changes in climate and landscape characteristics are driving the coupled climate-hydrological-ecological system (CHES) into unchartered territories, with major implications on natural resource availability and sustainability at both local and global scales. Given that soil-plant-atmosphere are part of a hydrologic continuum, the variability and changes in climate may impact hydrological states and fluxes, which in turn can increase vegetation stress potentially resulting in an abrupt regime shift in the ecohydrological system. Describing and predicting the non-linear dynamics of CHES is challenging in part due to uncertainties in the parameters that describe the system and insufficient understanding of the physical mechanisms that control these responses. This dissertation strives to bridge these gaps through synergistic use of data analytics and physically-based modeling so as to characterize a spectrum of dimensionality, nonlinearity, and stochasticity of CHES across a range of spatial-temporal scales. Three overarching questions frame the direction and scope of this dissertation: Q1 – how do meteorological conditions affect groundwater dynamics in forested wetlands? Q2 – how to evaluate forest mortality risk under long-term climate change, and predict near-term forest mortality? Q3 – how does plant hydraulics regulate plant water use under hydro-climatic stress across biomes? Addressing these questions will improve the understanding of CHES dynamics and representations of hydrologic and vegetation dynamics in Earth System Models. The findings and methodologies developed here can be leveraged for

devising mitigation and adaptation strategies for water resource management and ecosystem conservation under current and future climate regimes.

Contents

List of Tables

List of Figures

Acknowledgements

This dissertation would not have been possible without enormous support from several people who inspired me with their ideas and guided me in this journey. Though I will likely fail to adequately express the extent of my gratitude to them, this is a humble attempt.

First and foremost I would like to thank my advisor and mentor, Prof. Mukesh Kumar. His guidance, constant attention, and precise remarks were invaluable in helping me explore a range of environmental science questions. His patience and encouragement greatly empowered me to make progress in a step-by-step and methodical manner, even in the most challenging days. I thank him for his openness and curiosity, and for providing me opportunities to develop independent research, explore new directions, and share my research with the best in the field.

I am excitingly grateful to Prof. Gabriel Katul for his generous guidance, support, and encouragement. His advice and remarks were always an immense source of inspiration. Few experiences, if any, have given me the chance to develop inventive ways of thinking and nurture passion for science as much as working with him. I sincerely thank Prof. Amilcare Porporato and Prof. James Clark, for their research work that spurred my interest in ecohydrology and ecology. I thank them for their insightful suggestions on my work that made the experience productive and joyful.

I would like to also thank Prof. Alexandra Konings at Stanford University for her constant support and guidance on the project described in Chapter 5. I am

1

Introduction

1.1   Background and motivation

Human-induced changes in climate and land cover are driving the coupled climate-hydrological-ecological system (CHES) into unchartered territories with existential implications on natural resource availability and sustainability at both local and global scales. The Fifth Assessment Report by the Intergovernmental Panel on Climate Change noted that rising CO_2 resulting from anthropogenic emissions has a first-order influence on ecosystem and hydrological responses (Settele et al., 2015). At the global scale, CO_2 traps infrared radiation and reduces outgoing radiation from the top of the atmosphere, resulting in warming of the atmosphere. Warming temperature alters atmospheric humidity, precipitation pattern, and frequency and duration of extreme events such as storms and droughts (IPCC, 2013), which in turn changes surface and subsurface hydrologic regimes. These impacts are manifested in rivers and wetlands, affecting their ecological functions (Solomon, 2007; Miao et al., 2013; Rodriguez-Iturbe et al., 2007). Changes in hydrologic regimes also impact vegetation dynamics and distribution. Rising CO_2 and altered hydroclimatic con-

ditions affect vegetation growth, susceptibility and resilience through modulation of stomatal kinetics and root water uptake. As the dynamics of vegetation cover and stomatal kinetics control the exchange of water vapor and CO_2 between the terrestrial biosphere and the atmosphere, response of vegetation to hydrometeorogloical change and variation provides feedbacks to the atmosphere through mediated water, carbon and energy budgets. As the physical processes controlling these interactions in the CHES remain far from being thoroughly understood (Council et al., 2012), uncertainties exist in predicting the concomitant dynamics of hydrological-ecological systems. Improved understanding and prediction of these dynamics, guided by synergistic use of diagnostic modeling and empirically based data analytics, are needed for managing natural resources and sustainability.

Among a range of CHES, freshwater wetlands are considered as one of the most vulnerable systems under changing climate (Dudgeon et al., 2006). As increasing evidence has shown, a multitude of ecological processes and functions of wetlands, including methane emission, nitrogen cycling, flood buffering and vegetation dynamics, are controlled and will be significantly altered by climate-induced changes in hydrologic regimes (Settele et al., 2015). Thus it is imperative to understand the impact of inter-annual20 variability of climate conditions on hydrological regimes in wetlands. This improved understanding will serve as a key to predicting ecological functions under future climate.

Forested ecosystems are another CHES that are threatened by changing climate. With projected warming temperature and increasing variability of precipitation pattern, climate-induced water and heat stress to trees are expected to intensify in the future. A catastrophic impact of the stresses can be tree mortality, which is being widely observed throughout the globe in recent decades (IPCC, 2013; Allen et al., 2010). Given that forest covers 30% of the globe's land surface (Bonan, 2008) and assimilates around 2.4 Pg carbon per year (Pan et al., 2011), wide-spread tree

mortality may offset the carbon sink provided by forests, impair a wide variety of ecological functions, and increase the risk of forest fires. However, prediction of wide-spread tree mortality and its corresponding impacts remains largely uncertain (Settele et al., 2015). Thus improved understanding of tree mortality in response to both long-term climate trends and near-term fluctuations of hydro-climatic stresses is required to provide critical insights into future dynamics of CHES. Furthermore, climate-induced stress on forested ecosystems also alters the biosphere-atmosphere interactions through dynamical response of stomatal kinetics. Plants remove CO_2 from the atmosphere via photosynthesis while inevitably losing water into the dry atmosphere. Such gas exchange provides feedbacks to water-carbon budgets, energy partitioning, and cloud formation that could in turn modify convective precipitation (Konings et al., 2010; Manoli et al., 2016). However, how stomatal kinetics responds to hydro-climatic variation has long been an active research field and remains as one major uncertainty source of future climate projections (IPCC, 2013). The challenge arises mainly from complex manifolds of driving forces, interactive mechanisms, and heterogeneous plant properties lacking extensive measurements. Therefore, a framework is needed to incorporate improved understanding in biophysical mechanisms and appropriate parameterization to further reduce uncertainties in estimating biosphere-atmosphere interactions under hydro-climatic stresses.

1.2 Dissertation structure

Here I present four studies concerning the prediction of the impacts of hydro-climatic variations and changes in hydrographic and ecological features. Specifically, these chapters address dynamics of hydrologic regime in wetland system, responses of forest resilience and mortality to climate, and biosphere-atmosphere gas exchange under hydro-climatic stresses. Physically-based modeling approaches across scales are combined with advanced statistical analytics to achieve the research goals. The

objectives and methodologies of each chapter are outlined as follows.

Chapter 2. Meteorological controls on wetland groundwater dynamics

Based on the work by Liu and Kumar (2016), the influence of meteorological conditions on groundwater table (GWT) dynamics at a watershed scale is investigated in this chapter. As many ecological functions of wetlands are influenced by wet-periods, i.e., the time interval when GWT near the land surface. Hence, there is a crucial need to understand the controls on interannual variations of wet-periods. Given the scarcity of long-term measurements of GWT in wetlands, understanding variations in wet-periods using a measurement approach alone is challenging. Here a physically based, fully distributed hydrologic model and hydrologic data are used to simulate long-term wet-period variations in 10 inland forested wetlands in a southeastern US watershed. A Bayesian regression and variable selection framework was then implemented to (a) evaluate the extent to which the simulated wet-periods can be estimated and predicted by precipitation and potential evapotranspiration and (b) infer the relative roles of seasonal Ppt and PET. The prediction performance for wet-period variations from publicly available meteorological data using the Bayesian framework is also examined.

Chapter 3. Effects of long-term climate trends on forest mortality risk

Climate-induced forest mortality is being increasingly observed throughout the globe. Alarmingly, it is expected to exacerbate under climate change due to shifting precipitation patterns and rising air temperature. However, the impact of concomitant changes in atmospheric humidity and CO_2 concentration through their influence on stomatal kinetics remains a subject of debate and inquiry. Based on the work by Liu et al. (2017), this chapter uses a dynamic soil-plant-atmosphere model to analyze mortality risks associated with hydraulic failure and stomatal closure for 13 temperate and tropical forest biomes across the globe. Using the climate projection for the

4

period 2050-2069 by the Coupled Model Intercomparison Project Phase 5 (CMIP5) models, the mortality risk is evaluated in response to both individual and combined changes in precipitation amounts and their seasonal distribution, mean air temperature, specific humidity, and atmospheric CO_2 concentration. Different responses of mortality risk among plant functional types (PFTs) are discussed.

Chapter 4. Detection of early warning signal of forest mortality

Apart from the long-term response of forest mortality risk to climate trends discussed in 3, predicting near-term mortality induced by climate variability remains challenging, in part due to physiological mechanisms causing mortality are not fully understood and empirical relations between climatology and mortality are subject to change. Based on the work by Liu et al. (2019), this chapter proposes to use the temporal loss of resilience, a phenomenon often detected as a system approaches a tipping point, as an early warning signal (EWS) to predict the potential for forest mortality directly from remotely sensed vegetation dynamics. The time-varying resilience is evaluated using a Bayesian Dynamic Linear (DLM) model to identify EWS. The proposed approach is applied to forests in California, USA. The fraction of area with detected EWS is compared with documented mortality maps from annual aerial surveys conducted by the US Forest Survey. The lead times of EWS with respect to both reduced greenness, as identified from remotely sensed vegetation index, and observed mortality are examined. This chapter also evaluates the capability in predicting spatial-temporal variation of forest mortality using EWS detected with a range of lead times.

Chapter 5. Influence of plant hydraulics on evapotranspiration

Vegetation-mediated evapotranspiration (ET) plays significant roles in the interactions between the biosphere and the atmosphere. Although plant physiological dynamics control water transfer through the soil-plant continuum, most land surface

models simulate ET without explicitly accounting for plant hydraulics but empirically prescribing restriction function of hydro-climatic stresses based on plant functional types. While interest in incorporating plant hydraulics in land surface models has grown, doing so is challenged in part by parameterization difficulties due to the limited measurements of hydraulic traits and the scale gap between measurements for a segment and ET for a stand. This chapter investigates the impact of plant hydraulics on ET estimation. To tackle the challenges related to parameterization, a model-data fusion approach that integrates a soil-plant continuum model and observed ET at multiple FLUXNET sites is implemented to retrieve plant and soil hydraulic traits using a Markov Chain Monte Carlo method. The identified effective hydraulic traits at a stand scale are compared with available measurements. The performance of models with and without consideration of plant hydraulics are examined. To further explore the mechanisms underlying the difference of model performance, sensitivities of stomatal kinetics to two major hydro-climatic stresses, i.e., soil moisture and vapor pressure deficit, are also investigated.

2

Meteorological controls on wetland groundwater dynamics

2.1 Introduction

Wetlands have recently drawn increased attention in ecosystem science and management because of their strong influence on carbon and nitrogen cycles, water quality, and biodiversity. It is estimated that 18 - 30 % of total global soil carbon is stored in wetlands despite them covering only 6 - 7 % of the land area (Lehner and Döll, 2004). CH_4 emissions from wetlands constitute a significant component of the global CH_4 budget, accounting for 20 - 40 % of the total CH_4 emissions (Solomon, 2007; Bousquet et al., 2006; Ciais et al., 2014). Wetlands also act as nitrogen sinks and help buffer nutrient contamination of streams (Brinson et al., 1984; Hefting et al., 2004; Vidon and Hill, 2004). One of the key controls on the aforementioned ecohydrological functions of wetlands is the groundwater table (GWT). GWT variations have been observed to influence the greenhouse gas emissions from wetlands (Moore and Roulet, 1993; Nykänen et al., 1998; Walter et al., 2001; Chimner and Cooper, 2003; Strack et al., 2004; Bohn et al., 2007; Jungkunst and Fiedler, 2007; Turetsky

et al., 2008; Zona et al., 2009; Bloom et al., 2010; Miao et al., 2013; Schäfer et al., 2014). Nitrogen cycling processes such as nitrification, denitrification and ammonification, which are triggered by the anoxic conditions in wetland soil, are also known to be strongly influenced by GWT variations (Regina et al., 1996; Hefting et al., 2004; Rodriguez-Iturbe et al., 2007; Schilling, 2007; Lohila et al., 2010; Goldberg et al., 2010). Several studies have also highlighted the role of GWT in influencing the vegetation distribution (Schilling, 2007; Todd et al., 2010), vegetation community competition (Schäfer et al., 2014) and transpiration and biomass dynamics (Patten et al., 2008) in wetlands. In this context, a GWT height of -0.3 m (negative sign indicates GWT depth below the land surface datum) is often considered as a critical threshold that influences the eco-hydrological functions of wetlands. For example, observed CH_4 emissions (Figure 2.1) compiled from multiple wetlands situated in climatically diverse settings (Moore and Knowles, 1989; Moore and Dalva, 1993; Shannon and White, 1994; MacDonald et al., 1998; Strack et al., 2004; Jungkunst and Fiedler, 2007; Turetsky et al., 2008) show that CH_4 emissions were significantly larger (p-value < 0.001) when the GWT was higher than -0.3 m. Hefting et al. (2004) indicated that ammonification and denitrification mainly occurred when GWT was higher than -0.3 m while nitrification occured when GWT was lower than -0.3 m in a riverine wetland. Average root zone depth of many wetland vegetation species is also around 0.3 m (Lieffers and Rothwell, 1987; Sjörs, 1991; Lewis, 1995), hence the threshold is likely to influence many wetland vegetation functions by controlling aerobic/anoxic conditions in the root zone. The significance of the -0.3 m threshold is also obvious from its use as one of the criteria for wetland delineation by US National Research Council (Lewis, 1995). These studies indicate that for better understanding and prediction of carbon and nitrogen cycle, and vegetation functions in wetlands, it is crucial to first evaluate wet-periods i.e. the duration for which GWT is higher than -0.3 m in wetlands.
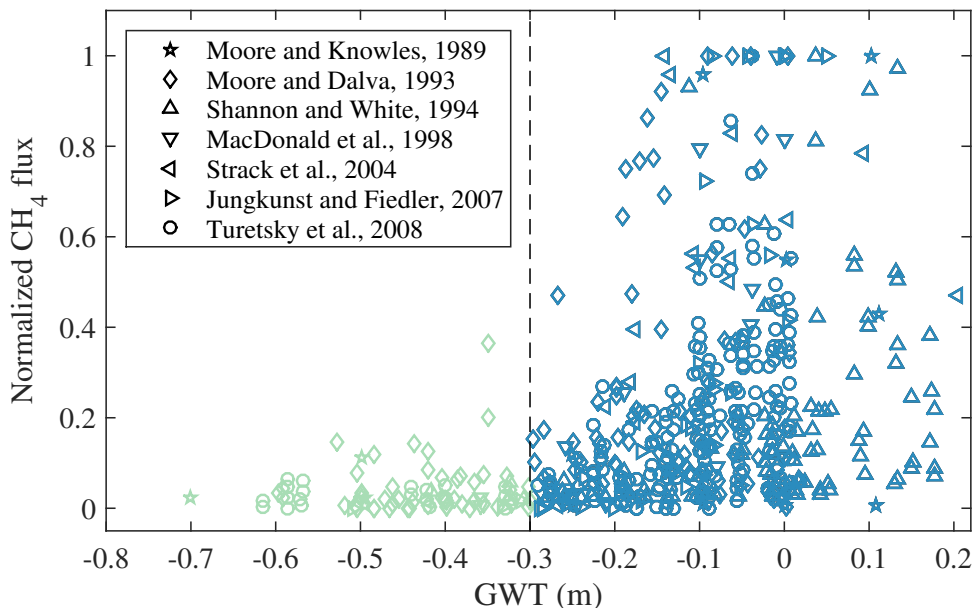
FIGURE 2.1: Relation between CH_4 fluxes and GWT in wetlands. To account for different magnitudes of CH_4 emissions from different wetlands, the data was compiled by normalizing the CH_4 flux rates within each wetland into a [0,1] interval, following Jungkunst and Fiedler (2007). Blue and green points represent the observations with GWT above and below -0.3 m respectively.

This study focuses on evaluating interannual variations in start date and duration of wet-periods in ten inland forested wetlands located in a southeastern US watershed. Although temporal variations in GWT are mediated by a number of factors including microtopography (Frei et al., 2010; Moffett et al., 2010), landscape drainage network (Todd et al., 2006), land use (Batelaan et al., 2003), soil properties (Vidon and Hill, 2004) and vegetation (Baird and Maddock, 2005; McCarthy, 2006), these variations are known to be primarily driven by meteorological conditions (Changnon et al., 1988; Reich et al., 2002; von Asmuth and Knotters, 2004; Yu et al., 2015) in inland wetlands. As such, we also explore the role of meteorological conditions on interannual variations in wet-period characteristics.

Given that observing GWT is time and effort consuming, a majority of the studies on wetland GWT dynamics have focused on measurements spanning a few months

9

or years (Devito et al., 1996; Rosenberry and Winter, 1997; Ferone and Devito, 2004; Wolski and Savenije, 2006; Todd et al., 2006; Kaplan et al., 2010; Cao et al., 2012). Clearly, the lack of long term measurements of GWT in wetlands, especially in the southeastern US, poses a challenge for studying interannual variations in wet-period characteristics using a measurement approach alone. Moreover, considering that most of the measurements were usually confined to areas within or close to a single wetland, the studied GWT dynamics may be site specific and not representative of the GWT response in other nearby wetlands. To circumvent these challenges, here we use a distributed integrated hydrologic model, in synergy with publicly available hydrologic data, to simulate long term GWT dynamics in multiple wetlands within a southeastern US watershed. The simulated GWT in wetlands are then analyzed using a Bayesian regression approach to answer four specific questions: (1) What is the range of interannual variations in wet-periods? (2) To what extent can annual and seasonal meteorological conditions explain interannual variations in wet-periods, and do antecedent conditions also impact wet-period variations? (3) What is the relative seasonal influence of meteorological conditions on wet-period variations? and (4) How well can the interannual wet-period variations be predicted using seasonal meteorological conditions?

2.2   Data and methods

2.2.1   Study site

The study was conducted in a southeastern US watershed (area = 325 km^2) that drains into Second Creek near Barber, North Carolina (35.6°N, 80.7°, USGS stream-flow gage 02120780). The watershed was selected because it contains multiple forested freshwater wetlands within its boundary. The forested wetlands are widespread across the southeastern US and account for more than 35% of the total forested wet-land area in the continental US (Bridgham et al., 2006). These wetlands are known

to provide several ecological functions including carbon sequestration and greenhouse gas emissions (Schipper and Reddy, 1994; Roden and Wetzel, 1996; Bridgham et al., 2006), nutrient cycling (Schilling and Lockaby, 2006), and biodiversity (Snodgrass et al., 2000; Gibbons, 2003). Another reason for the selection of this watershed was the availability of long term streamflow and groundwater data that could be used to validate the hydrologic model simulations. Physiography of the watershed is characterized by valleys and ridges oriented along the southwest-northeast direction. Watershed elevation ranges from 197m to 331m (Figure 2.2a). Land cover in the watershed mainly consists of hay/pasture (37.6%), deciduous forest (32.9%), developed area (6.8%) and evergreen forest (5.4%) (Figure 2.2b). The most common soil types in the watershed are loam in the riverbed and riparian regions and sandy clay loam in uplands (Figure 2.2c). The watershed falls in warm temperate climate with humid and warm summer based on the Koppen-Geiger climate classification (Kottek et al., 2006). Thirty-year average temperature in the watershed is 15.5°C and annual precipitation ranges from 703mm to 1473mm.

2.2.2 Hydrologic model

Model description

A physically-based, fully distributed hydrologic model, Penn State Integrated Hydrologic Model (PIHM) (Qu and Duffy, 2007; Kumar et al., 2009a; Kumar, 2009) was used to simulate coupled hydrologic states and processes. PIHM has been previously applied at multiple scales and in diverse hydro-climatological settings (Kumar et al., 2013; Shi et al., 2013; Yu et al., 2014; Chen et al., 2015; Kumar and Duffy, 2015; Yu et al., 2015). The model uses a semi-discrete, finite-volume approach to discretize the model domain and solve the ordinary differential equations (ODEs) of multiple states such as surface water depth, soil moisture, groundwater depth and river stage. Processes simulated in the model include evaporation, transpiration,
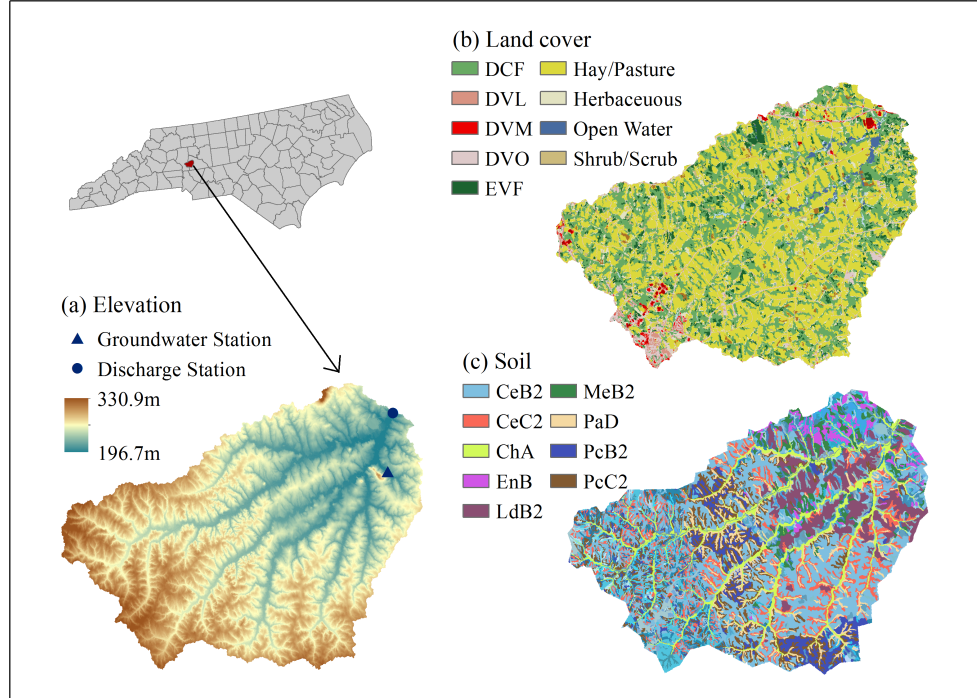
FIGURE 2.2: (a) Elevation and USGS observation stations, (b) land cover type and (c) soil type in the Second Creek watershed. Land cover in the watershed include deciduous forest (DCF), developed low intensity (DVL), developed medium intensity (DVM), developed open space (DVO) and evergreen forest (EVF). Soil cover symbols are MUKEY from SURGGO data. CeB2, CeC2, PcB2 and PcC2 indicate sandy clay loam, ChA indicates loam, EnB and PaD indicatesandy loam, LdB2 and MeB2 indicate clay loam. Refer to Soil Survey Staff (1995) for detailed information.

infiltration, recharge, overland flow, subsurface flow and stream flow. Evapotranspiration in the model is computed using the Penman-Monteith method; overland flow is modeled using diffusion wave approximation of depth-averaged 2-D St. Venant equations; subsurface flow is based on Richard's equation with moving boundary approximation; and stream channel routing is modeled with depth-averaged 1-D diffusive wave equation (Kumar, 2009). Laterally, hillslopes and rivers are discretized using triangular grids and line elements, respectively. Vertically, each triangle ele-

12

ment consists of four layers: a surface layer, a 0.25 m thick unsaturated layer, an intermediate unsaturated layer extending downward from 0.25m to the groundwater table and a groundwater layer. Soil moisture in the two unsaturated layers may vary from residual moisture to full saturation. As the average combined thickness of soil, saprolite and the transition zone of regolith has been estimated to be less than 20 meters in the region (Daniel, 1989), a uniform depth of 20 meters was considered as the lower boundary of the subsurface layer. A spatially adaptive flexible domain discretization scheme was used to generate the model grid. Given that this study concerns hydrologic dynamics in wetlands, a hydrographic feature that accounts for less than 1% of the watershed area, a nested domain discretization (Kumar et al., 2009b) with a total of 4525 elements was used (Figure 2.4). Because of computational constraints, we focused our attention on the largest ten wetlands with area ranging from 57,000 m^2 to 167,000 m^2. Elements smaller than 10,000m^2 were generated in and around these wetlands to improve the representational accuracy, while larger elements (smaller than 5000,000m^2) were used away from the wetlands to ensure computation efficiency. Number of discretization elements within the ten wetlands ranged from 18 to 74, with an average size of 5,710 m^2. At each time step, which was adaptively defined by a numerical ODE solver, ODEs of hydrologic states from all the elements were assembled and solved simultaneously.

Model parameterization, calibration and validation

To set up the model, we used the 30-meter resolution elevation data from National Elevation Dataset (NED) (U.S. Geological Survey, 1999), USDA-NRCS Soil Survey Geographic (SSURGO) soil data (Soil Survey Staff, 1995) and National Land Cover Dataset (NLCD) land cover data (Homer et al., 2015). Meteorological forcings such as precipitation, air temperature, relative humidity, wind speed, and radiation were obtained from North America Land Data Assimilation System Phase 2 (NLDAS-2)

data (Xia et al., 2012), which has a spatial and temporal resolution of $1/8°$ and an hour respectively. Ecological and hydrogeological parameters, and meteorological forcings relevant to the model simulation were automatically extracted from the raw datasets using an integrated model-GIS framework, PIHMgis (Bhatt et al., 2014).

As the goal of this study is to characterize the role of meteorological controls on interannual wet-period variations in wetlands, a long term model simulation from 1981 to 2013 was performed. Calibration of model parameters was performed using the observation data from 1993, which is a normal year with annual precipitation of 1085mm. The calibration year presented a range of meteorological conditions with large precipitation events (e.g. 57 mm on March 13th, 1993) and long dry periods with flow lower than the 30th percentile for 112 days. The diverse hydrologic conditions during the calibration period allowed tuning of model parameters such that the model could capture responses during both high and low flows. The first step in the calibration process was initialization of the PIHM model with water table at the land surface. The model was then allowed to relax with no precipitation input until the stream flow recession rate matched the observed during the low flow period in summer. The modeled stream flow magnitude was then compared with the observed value. The basis of this comparison is that streamflow during low flow period is largely due to groundwater base flow, and hence a match between observed and modeled streamflow would indicate reasonable estimation of the groundwater distribution in summer. During this process, the hydraulic conductivity of the subsurface was calibrated uniformly across the entire model domain (Refsgaard and Storm, 1996). Then starting from the derived groundwater table initial condition, the model was forced with real meteorological inputs. After a one-year warm-up period, the simulation results were compared against the observed streamflow and groundwater data at USGS guaging stations USGS 02120780 and USGS 354057080362601 respectively (Figure 1a). Manual calibration of hydrogeological parameters such as soil

14

hydraulic conductivity, macroporosity, and soil drainage parameters, was performed in this step. Both the Nash-Sutcliffe efficiency (NSE) (Nash and Sutcliffe, 1970) and the log-transformed NSE (logNSE) were used to evaluate the accuracy of simulation results, as the two metrics emphasize on high and low flows respectively (Wöhling et al., 2013). The modeled streamflow within the calibration period matched the observed data reasonably well, with NSE and logNSE of 0.84 and 0.87 respectively (Figure 2.3a). The modeled GWT also matched the observation well with NSE of 0.79.

The model simulation was validated using streamflow and GWT data from November 1989 to September 2013. For the 24-year validation period, the daily and monthly streamflow NSE was 0.42 and 0.61 respectively. The daily and monthly logNSE for the same period was 0.72 and 0.69. For GWT, the daily and monthly NSE was 0.59 and 0.62 respectively (Figure 2.3b). It should be noted that NSE for the daily streamflow time series was relatively low, in part because of the underprediction of streamflow in response to extremely large hurricane storms. This is partially attributable to NLDAS precipitation input that was used to drive the simulation, which tends to be smaller than station observations Luo et al. (2003), especially for large isolated events. If the largest 10 storm events with daily precipitation greater than 65 mm were discarded, the daily NSE would rise up to 0.58.

To further evaluate the simulation results, we compared the model identified wetlands with the National Wetland Inventory (NWI) wetlands (U.S. Fish and Wildlife Service, 1993). Model detected wetlands were locations with simulated GWT being higher than -0.3 m for at least two continuous weeks in the growing season every other year. This delineation procedure conforms with National Research Council's definition of wetlands (Lewis, 1995). The growing season used for wetland detection ranged from March 26th to November 11th in North Carolina (Tiner, 1999). The wetlands identified by the model correspond well with the overall distribution of NWI

15
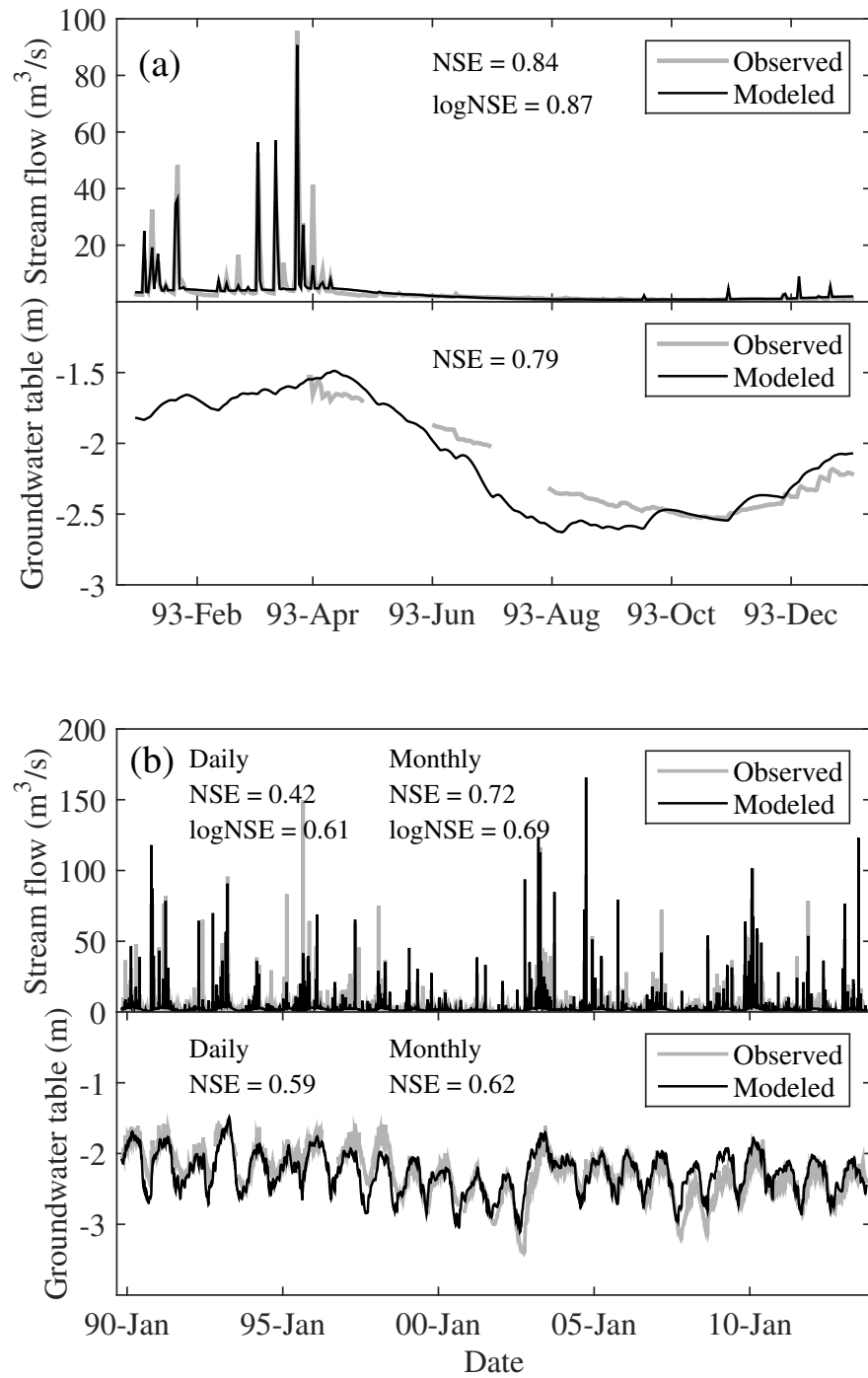
FIGURE 2.3: Comparison of modeled and observed streamflow and groundwater during (a) the calibration period (1993); and (b) the validation period (1989-2013).
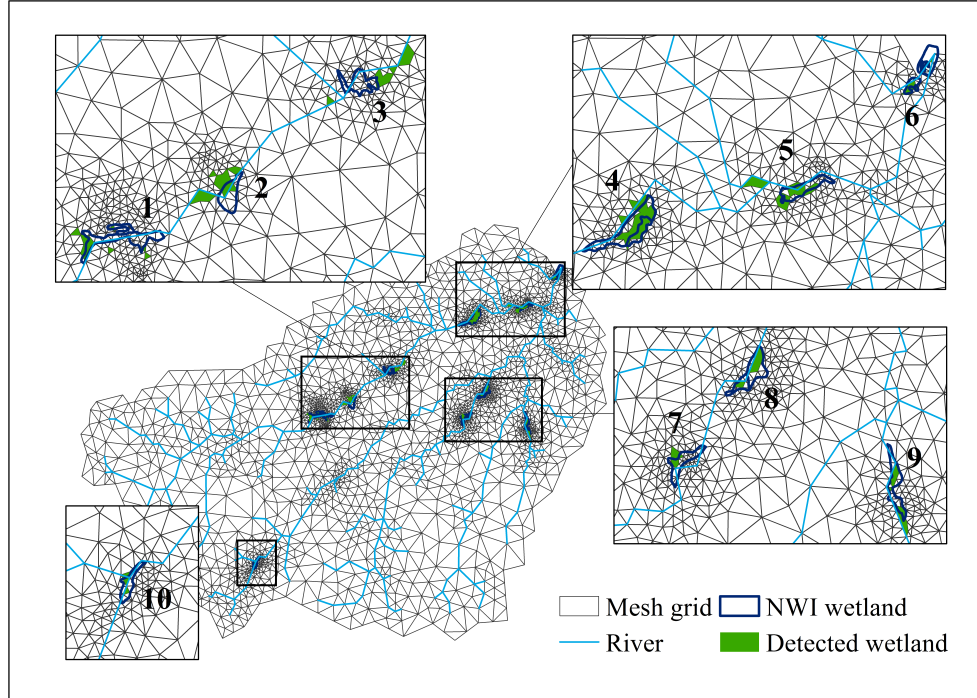
FIGURE 2.4: Spatial distribution of model detected wetlands and NWI wetlands.

wetlands (Figure 2.4). 58% of the wetland area detected by the model overlapped with the NWI wetlands. Possible reasons for the mismatch include: (1) inaccurate representation of microtopography in the model due to coarse grid resolution; (2) inherent uncertainties in the NWI wetland boundaries (Tiner, 1999; Wardrop et al., 2007); and (3) incompatibility in the definition of wetland used in NWI and this study. NWI wetlands were identified from high altitude imagery based on vegetation, visible hydrology and geography; whereas the model used groundwater dynamics to detect wetlands. Overall, the model was able to capture the spatial distribution wetlands, which is a direct function of the spatio-temporal distribution of groundwater in the watershed.

Validation of the long term streamflow and GWT series at the gauging stations,

and the spatial distribution of wetlands, established sufficient confidence in the PIHM simulation. The simulated GWT series in wetlands were then used to study variations in wet-period characteristics in response to meteorological conditions.

2.2.3 Quantifying wet-period characteristics and their dependence on meteorological controls

Defining wet-period characteristics and meteorological controls

In this study, we quantified two wet-period characteristics: wet duration and start date (Figure 2.5). Wet duration tracks the length of time for which GWT is higher than the critical threshold. This characteristic could potentially be used to estimate ecological functions of wetlands (see Section 1). Together with wet duration, start date evaluates timing of wet-period in each year. These two characteristics can then be used to define the prevailing environmental conditions during wet-periods, thus allowing more accurate quantification of ecological functions of wetlands (Christensen et al., 2003). As GWT in the Second Creek watershed generally increases in autumn and winter and decreases in spring and summer, start date and wet duration were extracted for an annual period starting from September 1st to August 31st of the next year. The annual period, referred hereafter as a "hydrologic year", ensures that the GWT time series contains a single seasonal peak with low GWT at the start and the end of year. The wetland GWT was quantified as the average across all the elements within a wetland. Start dates and wet durations were then extracted for each hydrologic year using a 10-day moving average of daily GWT time series to smooth-out transient daily fluctuations.

In line with our goals to evaluate the extent to which meteorological controls alone can be used to estimate and predict interannual wet-period variations in wetlands, here we consider Ppt and PET as the primary meteorological variables for our analysis. The two variables were selected because of their widespread availability and
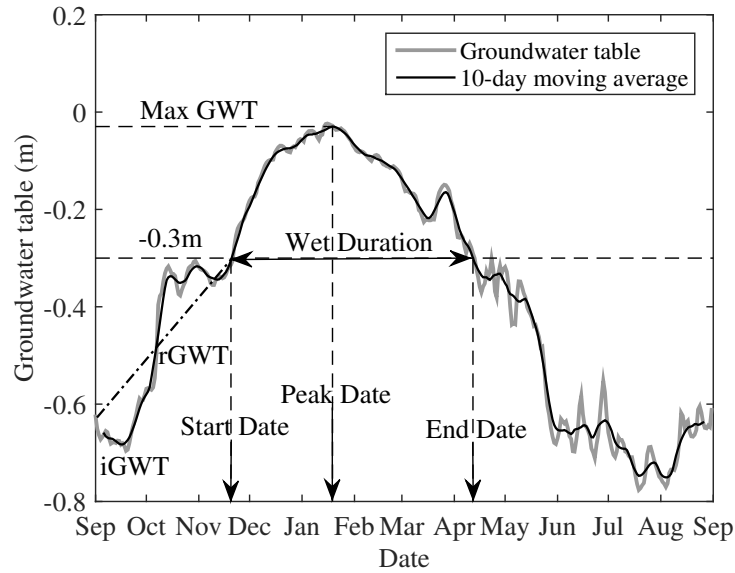
FIGURE 2.5: Typical wetland groundwater table variation within a hydrologic year.

their influence on groundwater dynamics. Ppt and PET are expected to influence the wetland GWT by modulating groundwater recharge and actual evapotranspiration (ET) from the wetland and by indirectly controlling the lateral flux exchange with the neighboring aquifer and streams. Ppt data is readily available for the entire continental US from national databases such as NCDC and NLDAS, while PET can be obtained based on Penman-Monteith equation (Penman, 1948; Monteith et al., 1965) using relevant meteorological data from NCDC and NLDAS datasets. As such, the methods presented in this paper can be used for other inland wetlands with available Ppt and PET data. Another notable advantage for choosing these two variables is that their predictions are generally available from climate models (Hartmann et al., 2013), which makes it feasible to readily apply the presented methods to understand the future impacts on wet-period variations.

A Bayesian regression framework for estimation, variable selection and prediction

In order to estimate and predict wet-period characteristics using the aforementioned meteorological controls, and to identify the relative seasonal contributions for each meteorological variable, a Bayesian linear regression and variable selection method (Mitchell and Beauchamp, 1988; Hoff, 2009) was implemented. The Bayesian regression method assumes a linear relation between a dependent variable y_i and a p-dimensional independent variable $\boldsymbol{x}_i = (x_{i,1}, x_{i,2}, \ldots, x_{i,p})$, with $i = 1, \ldots, n$. In this study, start date and wet duration are used as a dependent variables. The independent variable is either Ppt or PET or both. n = 32 corresponds to the length of simulation in years. The relation between $\boldsymbol{y} = (y_1, y_2, \ldots, y_n)^{\mathrm{T}}$ and $\boldsymbol{X} = (\boldsymbol{x}_1, \boldsymbol{x}_2, \ldots, \boldsymbol{x}_n)^{\mathrm{T}}$ is expressed as:

$$y_i = z_1 b_1 x_{i,1} + z_2 b_2 x_{i,2} + \ldots + z_p b_p x_{i,p} + \epsilon_i \tag{2.1}$$

where $i = 1, \ldots, n$; ϵ_i is independent and identically distributed normal noise with a mean and variance of 0 and σ^2 respectively; $z_j \in \{0, 1\}, j = 1, \ldots, p$, indicates whether variable $x_{i,j}$ is included in the regression; and b_j is the regression coefficient for variable $x_{i,j}$; T denotes the matrix transpose. In order to estimate $\boldsymbol{y}$ using $\boldsymbol{X}$, the parameters of $\boldsymbol{z} = (z_1, z_2, \ldots, z_p)^{\mathrm{T}}$ and $\boldsymbol{b} = (b_1, b_2, \ldots, b_p)^{\mathrm{T}}$ are to be evaluated. Based on the Bayesian regression and variable selection framework shown in Figure 2.6, posterior distributions of the parameters were derived by combining the prior distributions (Equation (A3)) and the time series of $\boldsymbol{X}$ and $\boldsymbol{y}$ using Equation (A7) (see Appendix A for details). Based on the posterior distributions, 10^4 samples of each parameter were drawn using Gibbs sampling, one of the most widely applied Markov Chain Monte Carlo (MCMC) algorithms (Bishop, 2006). The running average and trace plot of each parameter were checked to ensure convergence. The first 10^3 samples of each parameter belonging to the burn-in period were discounted. With the remaining effective samples, the Bayesian regression coefficient
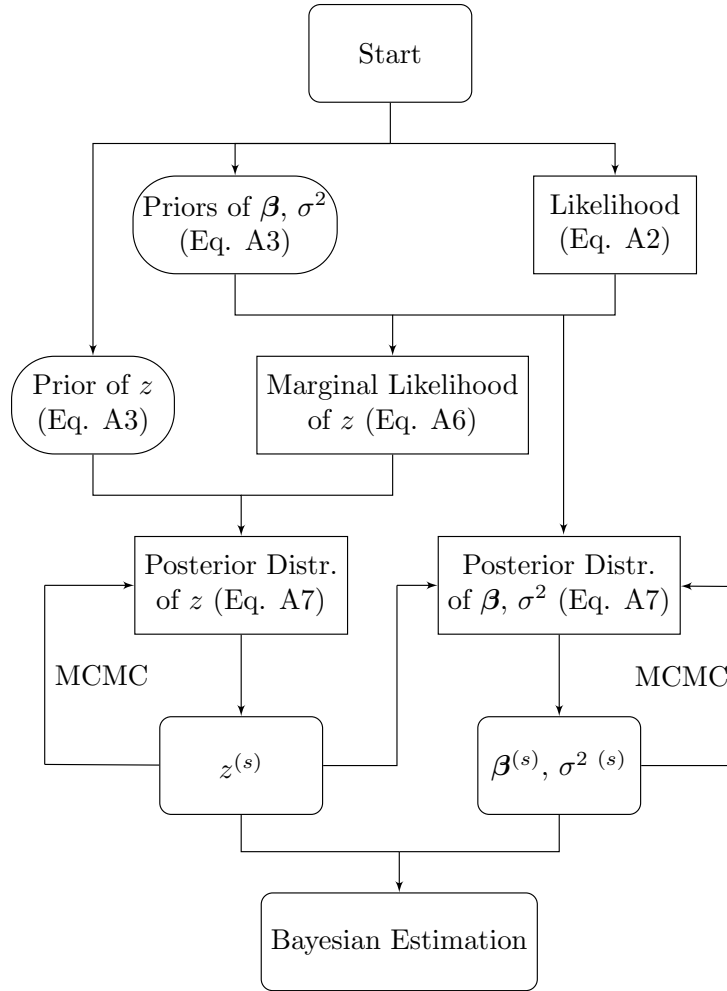
FIGURE 2.6: Framework of Bayesian regression and variable selection. s denotes the generation of samples ($s = 1, 2, \ldots, 10^4$).

of $\hat{\boldsymbol{\beta}} = (z_1 b_1, z_2 b_2, \ldots, z_p b_p)^{\mathrm{T}}$ was computed as the average over the remaining samples, which is a simple case of Bayesian Model Averaging (BMA) (Hoeting et al., 1999). The Bayesian estimated wet-period characteristics were then computed using $\hat{\boldsymbol{y}} = \boldsymbol{X} \hat{\boldsymbol{\beta}}$.

Estimating wet-period characteristics using meteorological controls

Twelve Bayesian regressions were generated for both start date and wet duration. The first three regressions used annual Ppt, PET and both Ppt and PET as independent variables, respectively. The next three regressions used the same independent variable configuration, but instead of the annual magnitudes, seasonal values of the variables in the four seasons, i.e., autumn (September to November), winter (December to February), spring (March to May) and summer (June to August), were used. Because of the inherent memory of the hydrologic system (Shook and Pomeroy, 2011; Nippgen et al., 2016), it is reasonable to expect that antecedent meteorological conditions may affect wet-period characteristics. To test this hypothesis, the following three regressions used seasonal magnitudes of Ppt and PET from the four seasons and an antecedent season from the previous hydrologic year. The antecedent season used here is the summer right before the start of a hydrologic year. The final three regressions used two antecedent seasons, i.e., the previous summer and spring in addition to the four seasons of a hydrologic year. In order to inter-compare the efficacy of different variable configurations for estimating wet-period variations, we calculated the coefficient of determination (R^2) for each Bayesian regression. The differences in R^2 obtained using only Ppt, only PET, and both of them together would indicate the relative abilities of these two variables in explaining interannual wet-period variations. Similarly, comparison of R^2 for regressions using either annual or seasonal meteorological variables would highlight the role of seasonal forcings on wet-period variations. The comparison between R^2 obtained with zero, one and two antecedent seasons would help evaluate the role of antecedent meteorological conditions on wet-period variations.

Identifying the controlling seasons that influence wet-period variations

Variable selection, i.e., identification of the relative importance of each independent variable for capturing variations in the dependent variable, was performed using the Bayesian framework. Since the framework selects the regression model that is likely to have high accuracy and small uncertainty, independent variables that contain more effective information and introduce minimal uncertainty have a greater chance to be included in the regression model. Under this mechanism, the probability for each variable to be included, which was approximated by the frequency of $z_j = 1$ (Equation (2.1)) in the posterior effective samples, represents how critical this variable is in explaining variations of the dependent variable, relative to all the other independent variables. For example, in the Bayesian regressions that use seasonal Ppt, the probability of $z_j = 1$ provides information on which seasonal Ppt is critical in capturing variations in start date or wet duration. High probability of $z_j = 1$ for a variable indicates that it is crucially needed to capture variations in the dependent variable.

Predicting wet-period characteristics using meteorological controls

The Bayesian approach has been widely applied to make predictions as it generally improves the confidence in prediction by reducing uncertainties associated with parameter estimation (Thiemann et al., 2001; Jin et al., 2010). After establishing the relation between meteorological conditions and wet-period characteristics using historical data, either from observations or a model, future response of wet-periods can be predicted using projections of meteorological conditions. Here we evaluated the accuracy of the Bayesian estimator for predicting wet-period variations. Error estimates from the method represent the uncertainty in prediction of wet-period characteristics. The 32-year time series was divided into two parts, a training and a testing set with 16 data points each. Using the training set, parameters of the

Bayesian estimator were obtained for each wetland separately. The estimator was then applied to quantify wet-period variations in the testing set. To minimize bias in the performance of the testing set due to the choice of the training set, we rotated the training set for cross validation (Kohavi, 1995). A full cross validation would involve $C_{16}^{32} \approx 6 \times 10^8$ trials. To reduce the computational expense, we randomly generated 1000 mutually exclusive training and testing sets to quantify the errors.

2.3 Results and discussions

2.3.1 Interannual variations in wet-period characteristics

Over the 32 year study period (1981 to 2013), wet-periods generally started in autumn or early winter, reached groundwater peak in late winter or early spring, and ended in spring or early summer (Figure 2.7). Of the 320 simulation years (= 32 years × 10 wetlands), 75% had wet-periods spanning from 3 to 8 months and 56% had wet-periods spanning from 4 to 7 months in a year. Median of start date and wet duration was November 13th and 164 days respectively. The simulated temporal distribution and duration ranges are mostly consistent with those observed in the forested wetlands in South Carolina and Louisiana (Megonigal et al., 1997), which lie in the same climatological classification region as North Carolina (Kottek et al., 2006)). The results also show that large temporal variations exist in wet-periods (Figure 2.7). Start date varied by several months or even seasons. For instance in wetland 1 (Figure 2.7), start date varied from September 5th (in 2003) to March 17th (in 2001), with an average variation range of 194 days and a standard deviation of 45 days. Also, the wet duration in wetland 1 ranged from 47 days to 275 days with a standard deviation of 55 days. In wetland 7, wet duration was as long as 196 days in 1992, but was zero in 2001 as the GWT was never higher than -0.3 m during the year. Since meteorological variables are the primary dynamic forcings that are expected to drive interannual variations in wet-period variations (Changnon et al.,
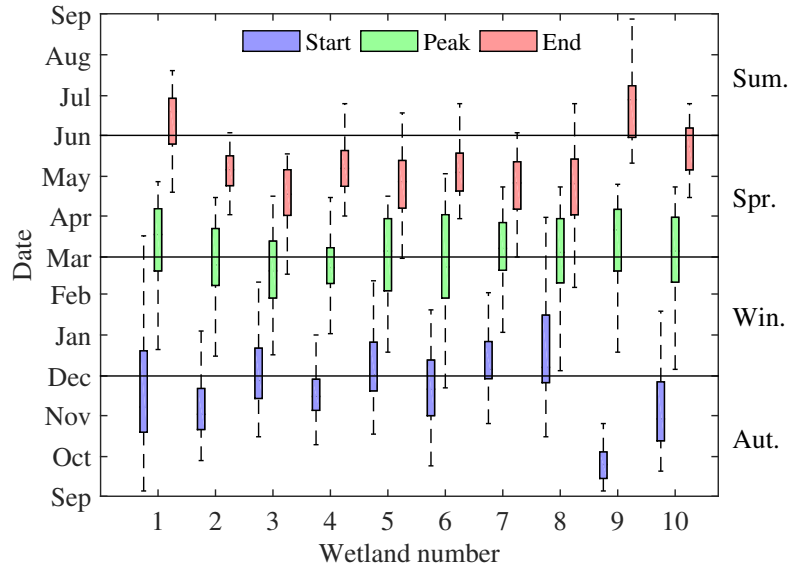
FIGURE 2.7: Box plot of start date, peak date and end date of wet-periods for the ten wetlands in Second Creek watershed. The lower and upper edges of the boxes represent the 25th and 75th percentiles respectively. The whiskers around the boxes extend to the most extreme data points except for outliers.

1988; Reich et al., 2002; von Asmuth and Knotters, 2004), next we quantify their influence on wet-period characteristics.

2.3.2 Estimation of wet-period characteristics using meteorological controls

Annual precipitation amount is expected to be inversely related with start date and positively related with wet-period duration. This is because higher annual precipitation tends to enhance the groundwater recharge, which should result in an earlier start and longer duration of wet-periods. In contrast, annual PET is expected to be positively related with start date and inversely related with wet duration, as higher atmospheric demand for moisture should enhance water losses resulting in a delayed start date and a shorter wet duration. However, Bayesian regression results using annual precipitation showed that the annual magnitudes only explained a small part of variation in start date and wet duration, with average R^2 of 0.172 and 0.437 respectively for the ten wetlands (Table **??**, column (1)). By combining annual PET with

precipitation in the regression, the average R^2 increased marginally to 0.193 and 0.478 (Table **??**, column (3)). Remarkably, the average R^2 improved significantly from 0.193 to 0.611 and 0.478 to 0.707 for start date and wet duration respectively (Table **??**, column (3) and (6)), when instead of the annual variables, seasonal Ppt and PET were used. The significant improvements in R^2 indirectly indicate that the meteorological conditions in each season do not exert uniform impact on interannual variations of wet-periods.

Combining seasonal PET with seasonal Ppt improved the estimation accuracies further, with the average R^2 increasing from 0.534 to 0.611 and 0.638 to 0.707 for start date and wet duration respectively (Table **??**, column (4) and (6)). To identify the conditions under which improvement in the estimation accuracy was large, wetland characteristics simulated by the PIHM model and those estimated using the Bayesian regressions with only seasonal Ppt and both seasonal Ppt and PET were compared (Figure 2.8). The results indicate that PET mainly improved the estimation for cases with late start date (later than the 150th day) or short wet-period duration (shorter than 4 months), which are general characteristics of dry years (years with small precipitation) (Figure 2.8b, d). For example, wet duration for wetland 3 in 2010, a dry year with annual precipitation of 874 mm, was 44 days based on the PIHM simulated GWT. If only seasonal precipitation was used in the regression, the duration was overestimated to be 83 days. After incorporating both seasonal PET and Ppt in the regression, the estimated duration reduced to 58 days (Figure 2.8c). This improvement could be attributed to the large PET of 1635mm in 2010 (much higher than the long term average of 1405 mm) that shortened the wet duration. In fact, more than 70% of all the cases showing late start date or short wet-period duration were characterized by a simultaneous occurrence of small Ppt ($<$ 40th percentile of annual Ppt) and large PET ($>$ 60th percentile of annual PET). These results indicate that by considering seasonal PET in addition to seasonal Ppt in the
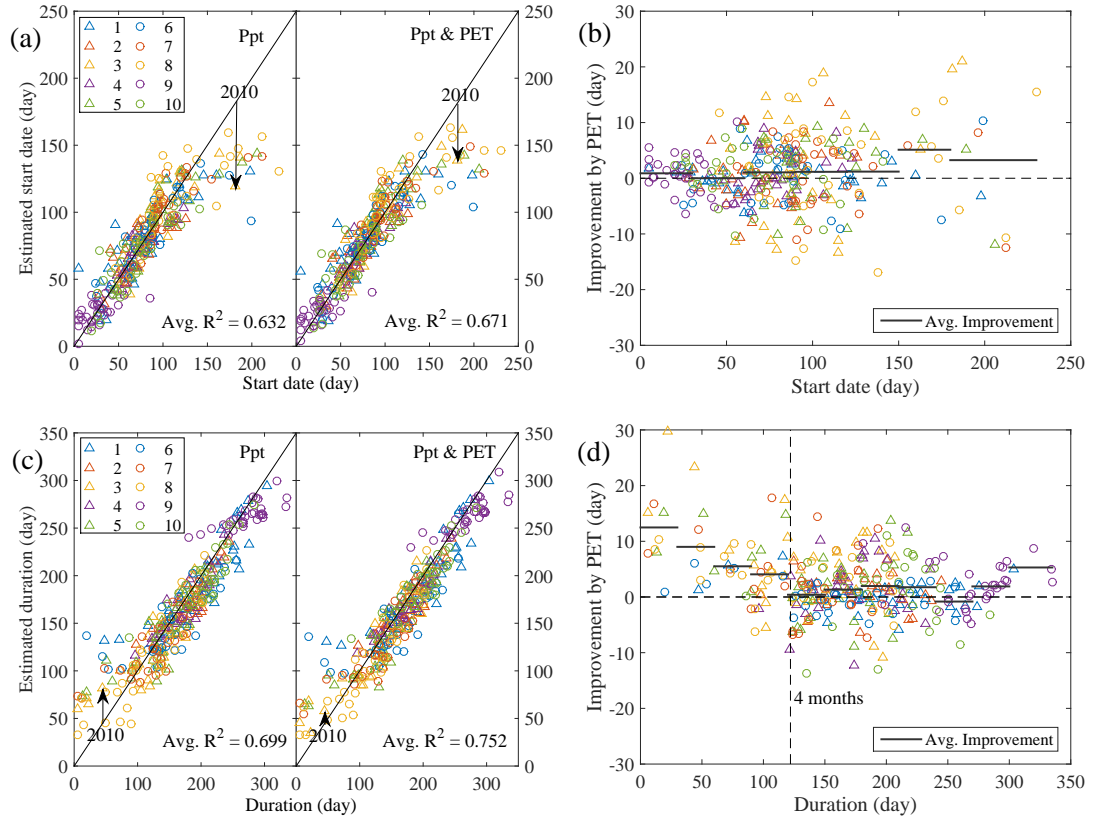
FIGURE 2.8: Performance comparison for estimating the (a) start date and (c) duration using merely seasonal Ppt, and both seasonal Ppt and seasonal PET (Ppt & PET). The improvements by PET for the (b) start date and (d) duration were calculated as $|\hat{y}_{Ppt} - y| - |\hat{y}_{Ppt\&PET} - y|$, where the $\hat{y}_{Ppt}$, $\hat{y}_{Ppt\&PET}$ and y are the estimations by Ppt, Ppt & PET using Bayesian method and the base values simulated by the hydrologic model respectively. The average improvements over an interval of 30-days were plotted using dark horizontal lines.

Bayesian regression, wet-periods with extremely late start dates and short durations can be captured more accurately. To sum up, seasonal precipitation was able to capture most of the variations in start date and wet duration on its own. Further improvement in estimation accuracy was registered, especially for years with late start or short wet-period duration, by incorporating seasonal PET in the regressions.

The estimation accuracy improved furthermore when in addition to the four seasons of a hydrologic year, one antecedent season, i.e., the previous summer, was also

27

included in the regression (SN + AT1). By considering the antecedent season, average R^2 increased from 0.611 to 0.671 and 0.707 to 0.752 for start date and wet duration respectively (Table **??**, column (6) and (9)). When one more antecedent season, i.e., the previous spring, was also considered in the regression (SN + AT2), the R^2 only increased marginally by 2.4% (from 0.671 to 0.687) and 0.4% (from 0.752 to 0.755) for start date and wet duration respectively (Table **??**, column (9) and (12)). These results indicate that although wet-periods were influenced by antecedent meteorological conditions, the influence was negligible for meteorological conditions beyond one antecedent season.

Notably, the estimation accuracies of wet duration in wetland 6 and 9 were relatively low (Table **??**, column (9)). This was partly because isolated precipitation events could raise the GWT height above the -0.3 m threshold in these two wetlands, thus masking out the effects of seasonal forcings. In wetland 6, bank overflow from a nearby stream, which inundated the wetland after large autumn and winter storms, generally raised the GWT above the threshold. In wetland 9, the GWT was well near the -0.3 m threshold at the beginning of autumn (Figure S1). As such, isolated precipitation events in autumn were able to lift the GWT above the threshold. Also, a few weeks without precipitation near the end of the hydrologic year could let the GWT drop down. These results indicate that the seasonal meteorological conditions may not capture wet-period variations when: (1) response of GWT to isolated precipitation events is larger than or comparable to its seasonal variation, or (2) GWT is close to the critical threshold throughout the year.

Table 2.1: R^2 for the twelve Bayesian regressions used to estimate start date of the wet-period in the wetlands of Second Creek watershed. The regressions used either precipitation (Ppt) or potential evapotranspiration (PET) or both Ppt and PET (Both) as independent variables. Annual magnitudes (AN) of the independent variables or their seasonal magnitudes in four seasons (SN) with an option to use one (AT1) or two (AT2) antecedent seasons were used for regression.

	Start date											
	AN			SN			SN+AT1			SN+AT2		
WetID	Ppt	PET	Both	Ppt	PET	Both	Ppt	PET	Both	Ppt	PET	Both
(0)	(1)	(2)	(3)	(4)	(5)	(6)	(7)	(8)	(9)	(10)	(11)	(12)
1	0.097	0.049	0.100	0.517	0.335	0.550	0.710	0.355	0.711	0.724	0.353	0.724
2	0.087	0.099	0.128	0.605	0.500	0.708	0.622	0.498	0.729	0.699	0.498	0.756
3	0.265	0.281	0.353	0.593	0.538	0.693	0.655	0.544	0.708	0.685	0.551	0.712
4	0.218	0.130	0.215	0.661	0.480	0.736	0.706	0.481	0.764	0.723	0.483	0.771
5	0.214	0.075	0.200	0.548	0.340	0.624	0.674	0.350	0.686	0.692	0.350	0.696
6	0.423	0.114	0.422	0.609	0.344	0.648	0.662	0.361	0.700	0.683	0.358	0.703
7	0.144	0.098	0.160	0.461	0.329	0.527	0.623	0.334	0.618	0.655	0.342	0.633
8	0.140	0.076	0.151	0.517	0.366	0.589	0.536	0.382	0.629	0.560	0.391	0.641
9	0.022	0.059	0.071	0.226	0.309	0.363	0.375	0.312	0.444	0.442	0.322	0.500
10	0.109	0.081	0.128	0.599	0.444	0.675	0.714	0.444	0.720	0.721	0.444	0.729
Avg.	0.172	0.106	0.193	0.534	0.399	0.611	0.632	0.409	0.671	0.658	0.409	0.687

Table 2.2: R^2 for the twelve Bayesian regressions used to estimate wet-period duration in the wetlands of Second Creek watershed. Refer to Table 2.1 for abriviations

	AN			SN			SN+AT1			SN+AT2		
						Duration						
WetID	Ppt	PET	Both	Ppt	PET	Both	Ppt	PET	Both	Ppt	PET	Both
(0)	(1)	(2)	(3)	(4)	(5)	(6)	(7)	(8)	(9)	(10)	(11)	(12)
1	0.455	0.246	0.457	0.590	0.378	0.609	0.732	0.432	0.749	0.734	0.437	0.751
2	0.367	0.284	0.411	0.720	0.488	0.779	0.752	0.498	0.784	0.760	0.498	0.789
3	0.473	0.513	0.611	0.733	0.682	0.833	0.771	0.688	0.841	0.773	0.701	0.844
4	0.462	0.381	0.507	0.741	0.595	0.806	0.773	0.605	0.815	0.773	0.606	0.817
5	0.440	0.295	0.458	0.677	0.559	0.743	0.715	0.561	0.788	0.715	0.563	0.789
6	0.397	0.143	0.397	0.518	0.418	0.543	0.601	0.429	0.621	0.600	0.430	0.621
7	0.378	0.337	0.412	0.605	0.563	0.673	0.670	0.564	0.752	0.672	0.573	0.758
8	0.472	0.363	0.532	0.819	0.615	0.858	0.826	0.613	0.874	0.828	0.623	0.875
9	0.523	0.345	0.564	0.351	0.319	0.485	0.402	0.353	0.525	0.414	0.354	0.532
10	0.407	0.313	0.432	0.626	0.523	0.740	0.750	0.545	0.773	0.752	0.546	0.775
Avg.	0.437	0.322	0.478	0.638	0.514	0.707	0.699	0.529	0.752	0.702	0.533	0.755

2.3.3 Relative role of seasons in controlling wet-period characteristics

As indicated in section 3.2, Ppt and PET do not exert a uniform influence throughout a hydrologic year. Using the SN + AT1 regression configuration, next we identify the controlling seasons for Ppt and PET in regard to their role in estimation of wet-period characteristics.

Identifying seasons that control start dates

Among the five seasons considered for regression, start date was found to be dominantly controlled by autumn precipitation, followed by precipitation in the previous summer. Other seasons had relatively limited influence (Figure 2.9a). As wet-periods generally started in late autumn or early winter for most wetlands (Figure 2.7), the seasons that occur before the start date, i.e. the previous summer and autumn, were naturally detected as controlling seasons. For wetlands wherein wet-periods started in mid or late winter, such as wetland 3, 5, 6, 7 and 8 (Figure 2.7), start date was also influenced by winter precipitation. Notably, even though wet-periods usually started in autumn, which means that only part of autumn precipitation (before the start date) could have affected the variation in start date, autumn still had the strongest influence in most wetlands (Figure 2.9b). Wetland 9 was an exception in the sense that the previous summer had the strongest influence in this case, as wet-periods usually started right at the beginning of autumn (Figure 2.7). Relative dominance of autumn precipitation with respect to the previous summer can be explained by first conceptualizing start date as a function of initial GWT (iGWT) at the beginning of each hydrologic year (or the end of the previous summer), and the GWT increasing rate (rGWT) from the beginning of autumn to the start date (Figure 2.5). Next, influence of iGWT and rGWT on variations in start date was evaluated. For this, standard deviation of start date was calculated by: (1) assuming that iGWT for each year was identical and equal to the long term average iGWT, while rGWT

varied across different years; (2) assuming rGWT for each year was identical but iGWT varied across different years. Average standard deviation of start date for the two cases were 83 days and 28 days respectively. Larger standard deviation in the first case i.e., with constant iGWT and variable rGWT, indicates that rGWT played a bigger role in influencing start date. A smaller contribution of iGWT, which is directly correlated with summer Ppt (correlation coefficient, $r = 0.79$), was a result of groundwater relaxation in summer which led to a diminished variance in GWT in late summer. Since rGWT had a much stronger influence on start date, and as rGWT was largely determined by autumn Ppt ($r = 0.74$), autumn was identified as the most dominant season.

Following a similar line of inquiry, relative roles of seasonal PET were evaluated. Although both autumn and the previous summer PET were expected to affect start date, only autumn was detected to have a significant influence (Figure 2.9c, d). This is because rGWT, which is the primary control on start date, is affected by autumn PET. The influence of summer PET was relatively small because: (1) its impact on rGWT was negligible; and (2) the correlation between actual ET and PET in summer was smaller ($r = 0.61$) than that between ET and PET in autumn ($r = 0.82$).

Identifying seasons that control wet durations

In regard to the seasonal influence of precipitation on wet duration, autumn precipitation was the most dominant. Notably, precipitation in the previous summer, winter and autumn also had moderate influence on variations in wet duration (Figure 2.10a). Since wet-periods generally spanned from autumn to spring (Figure 2.7), precipitation in the previous summer and autumn affected wet duration via the start date while precipitation in winter and spring affected wet duration via the end date. For start date, as discussed in Section 3.3.1, precipitation in autumn contributed
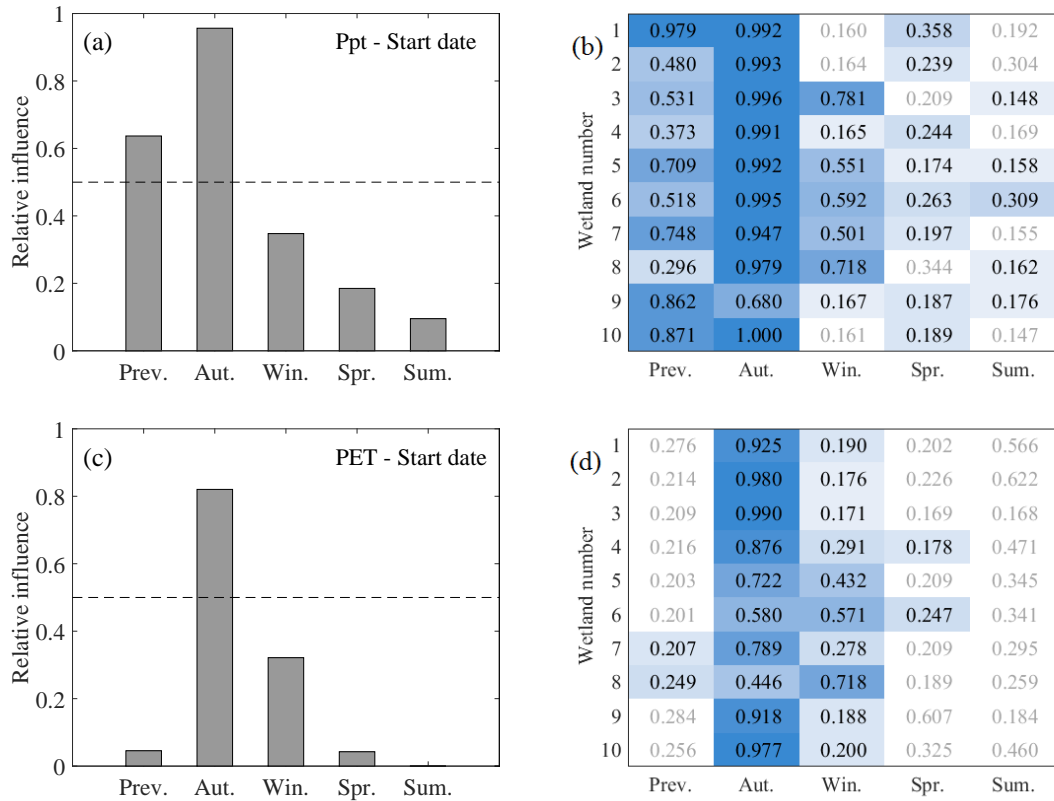
FIGURE 2.9: Relative seasonal influence on the interannual variations of start date by (a) Ppt and (c) PET, for the ten wetlands. Individual seasonal contribution for each wetland by (b) Ppt and (d) PET is presented in the colored table. Darker blue cells indicate larger contributions and vice-versa. Smaller contributions in gray in (b) and (d) indicate noisy anti-correlations of respective seasons on the dependent variables, and have been left out for calculating the average contributions in (a) and (c).

more than precipitation in the previous summer. For the end date, in wetlands with long average wet durations (155 to 270 days), such as wetland 1, 2, 4, 6 and 10 (Figure 2.7), precipitation in spring contributed more than that in winter (Figure 2.10b). In these wetlands, the GWT was generally near the ground surface during winter. Precipitation during winter promoted discharge from wetland into the river, which prevented the GWT from rising as much as it would happen when the GWT was deep to begin with (Figure S1). Therefore, wet duration was less sensitive to winter

precipitation for these wetlands. In contrast, GWT variation in spring, which was much larger (-0.43m) than in winter (+0.13m), was influenced by the spring precipitation amount. As a result, spring precipitation exerted relatively larger influence on the end date and hence the wet duration. However for wetland 9, which also showed long wet durations (Figure 2.7), wet duration variations were not captured well using seasonal meteorological variables due to the strong event-scale effects. Hence a clear seasonal influence of Ppt was not detected for this wetland. For wetlands 3, 5, 7, and 8, wherein average of wet duration was short (< 130 days) (Figure 2.7), winter precipitation contributed more than spring precipitation (Figure 2.10b). In these wetlands, due to the late start of wet-periods, the net vertical recharge and lateral incoming fluxes were not large enough to saturate the wetland. As a result, the winter precipitation affected the GWT change more effectively; that is, precipitation before the peak date influenced the maximum GWT and that after the peak date influenced the decreasing rate. Since wet-periods in these wetlands generally ended in early to mid spring, the impacts of spring precipitation was muted. To sum up, wet duration was mostly controlled by precipitation in autumn via the start date, and precipitation in winter or spring (depending on the length of wet duration) via the end date.

PET in autumn, winter and spring influenced wet duration more uniformly (Figure 2.10c, d). Given that the previous summer PET contributed little to start date (as discussed in Section 3.3.1), its influence on wet duration was also muted. Winter and spring PET affected wet duration via the end date. Larger PET in winter led to smaller maximum GWT and faster GWT recession, thus shortening the wet duration. The spring PET also contributed to wet duration via the rate of GWT recession. As start date showed a larger variation range than end date (Figure 2.7), and as autumn was the only dominant season for start date, autumn PET had a slightly larger contribution than winter and spring.
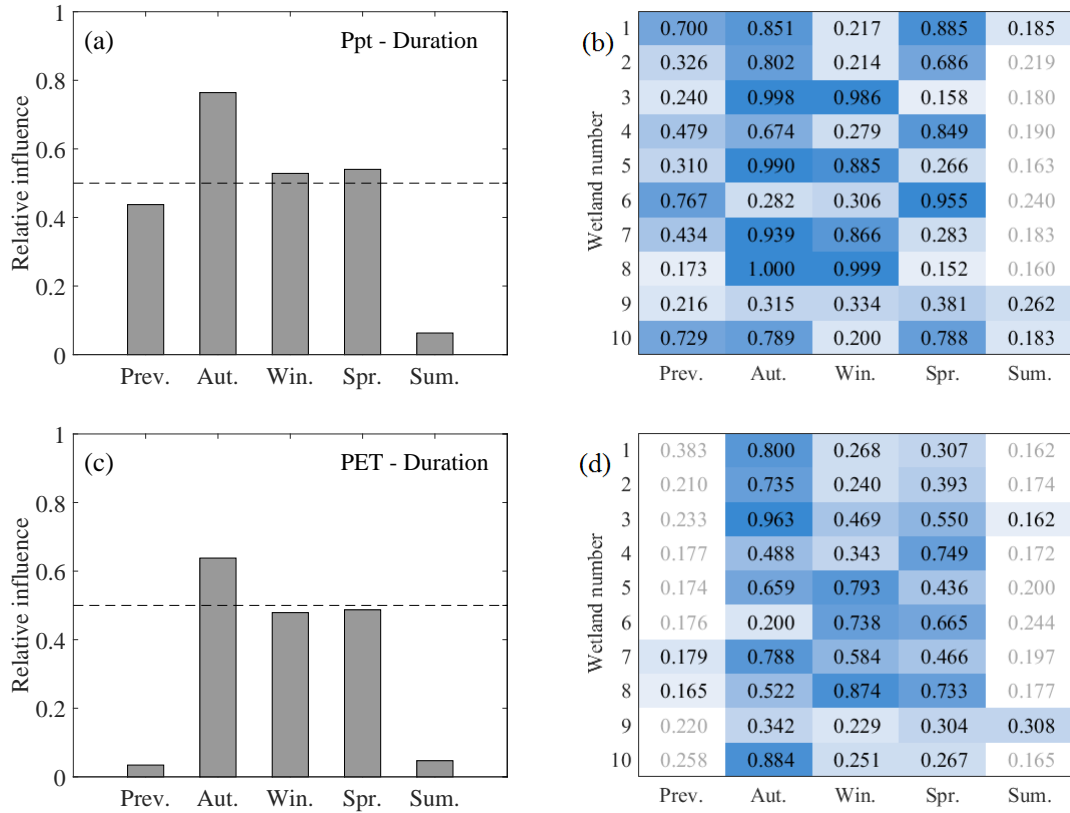
FIGURE 2.10: Relative seasonal influence on the interannual variations of wet duration by (a) Ppt and (c) PET, for the ten wetlands. Individual seasonal contribution for each wetland by (b) Ppt and (d) PET is presented in the colored table. Darker blue cells indicate larger contributions and vice-versa. Smaller contributions in gray in (b) and (d) indicate noisy anti-correlations of respective seasons on the dependent variables, and have been left out for calculating the average contributions in (a) and (c).

2.3.4 Predicting wet-period characteristics

The Bayesian estimator was able to predict start date with errors smaller than two weeks, three weeks, and one month at confidence levels of 32.8%, 73.1% and 95.1% respectively (Figure 2.11). Corresponding errors for wet duration were predicted at confidence levels of 14.3%, 58.4% and 93.6% respectively. Even though the Bayesian estimator was trained using the GWT and meteorological conditions of only 16 years,
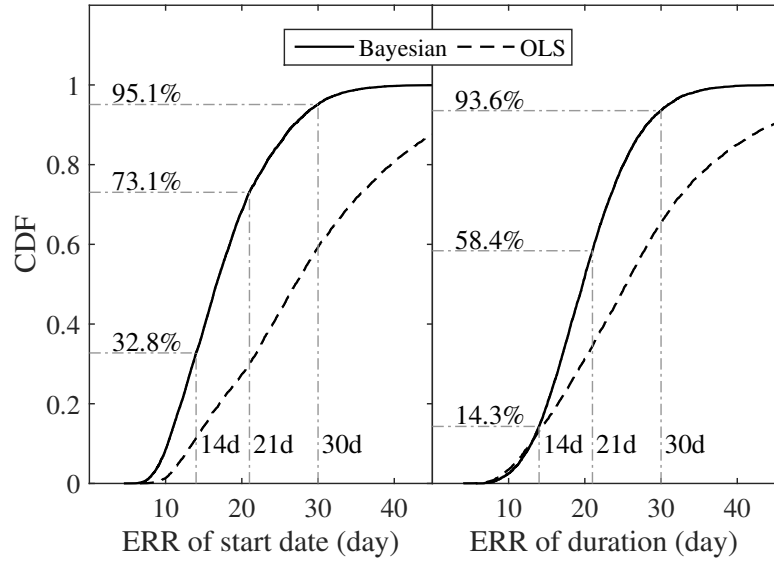
FIGURE 2.11: Cumulative density functions (CDF) of the prediction error (ERR = $|\hat{y}_{Ppt\&PET} - y|$) for start date and wet duration using Bayesian and OLS regression methods.

both start date and wet duration could be predicted with errors smaller than 1 month at a 90% confidence level. Lower prediction errors are expected for longer available time series. Considering that start date and wet duration varied by several months or even seasons among different years, these results indicate that the Bayesian estimator can serve as an effective tool for predicting start dates and wet durations. Notably, start date and wet duration can be estimated with even higher R^2 using the OLS method, as its goal is to minimize the squared error. For example, R^2 for OLS regression of start date and wet duration is 0.699 and 0.759 respectively, which is slightly higher than that of 0.671 and 0.752 obtained using the Bayesian estimator respectively (Table **??**, column (9)). However, the Bayesian estimator is preferable for the purpose of prediction, as it is able to predict with much less error than the OLS estimator (Figure 2.11). For example, at a 90% confidence level, the OLS estimator predicted start date with an error up to 67-days, while the corresponding error based on the Bayesian estimator was less than 28-days.

2.4 Conclusions

This study evaluated interannual variations in wet-period characteristics of ten inland forested wetlands in a southeastern US watershed, and quantified the extent to which these variations can be explained based on annual or seasonal meteorological conditions, specifically precipitation and potential evapotranspiration. The main conclusions and limitations of this study, and its implications for future research are as follows:

(1) Start date and duration of wet-periods in the forested wetlands of the southeastern US exhibit significant interannual variations. Among the ten studied wetlands, the start date could be as early as September or as late as March, and the wet duration could vary by more than 6 months. As multiple ecological functions of wetlands such as greenhouse gas emissions (Moore and Knowles, 1989; Moore and Dalva, 1993; MacDonald et al., 1998; Strack et al., 2004; Jungkunst and Fiedler, 2007; Turetsky et al., 2008) and nitrogen cycling (Hefting et al., 2004), are influenced by wet-periods (see Section 1 for literature review), it is expected that the ecological functions of wetlands may also vary significantly through the years. Notably, although wet-periods strongly influence wetland functions, more accurate estimation of interannual variations in the ecological functions should account for the influence of other physical controls such as wetland ecology and substrate characteristics (Ramirez et al., 2015).

(2) The annual meteorological conditions could only capture 19.3% and 47.8% of the variations in start date and wet duration respectively, indicating that a longer or shorter wet-period in a year can not be explained simply based on if the year is wet or dry. Limited ability of annual variables to explain interannual variations in wet-period characteristics can be attributed to non-uniform influence of seasonal meteorological conditions on wet-period variations. In the studied wetlands, meteo-

rological conditions in autumn were identified to be the most dominant in influencing wet-period variations. This is expected to be true for other forested wetlands in the southeastern US, as hydro-climatology in the region is characterized by autumn and winter that act as recharge periods (Anderson and Emanuel, 2008). The relative dominance of autumn indicates that between two years with identical annual precipitation, the one with a wetter autumn is more likely to experience an earlier start date and longer duration of wet-period, potentially causing larger methane emissions and denitrification rates. The results also indicate that for future predictions of wet-period characteristics and associated ecological functions, robust projections of meteorological conditions at least in the dominant seasons are paramount.

(3) 60% to 90% of the variations in wet-period characteristics could be captured by the Bayesian regression using seasonal Ppt and PET as independent variables. As the two meteorological variables are readily available within the continental US, the methods presented in this paper can easily be used for other inland wetlands. The efficacy of the framework for inland forested wetlands suggest that the method can be used for wetlands wherein temporal GWT dynamics are primarily driven by Ppt and PET in the regional watershed. However, the framework may not be as accurate for wetlands where isolated precipitation events could raise the GWT above the wet-period threshold (see details Section 3.3.1). These wetlands are generally expected to have GWT height near the wet-period threshold. The applicability of this framework is also likely to be limited for wetlands where GWT dynamics may be affected by tidal fluxes (e.g. coastal wetlands) or irrigation (e.g. agricultural wetlands). Future work should include testing the robustness and applicability of the framework in diverse climatic and hydrogeological settings.

(4) Estimation accuracy of wet-periods was higher when in addition to the four seasons within a hydrologic year, meteorological conditions in an antecedent season were also considered. However, an additional antecedent season made negligible

improvement to the estimation accuracy. This highlights that inherent hydrologic memory of the wetlands should be appropriately accounted for while estimating and predicting interannual wet-period variations. Although hydrologic memory of groundwater systems may vary with climatological forcings and watershed properties (Nippgen et al., 2016), the Bayesian framework presented here is flexible enough to incorporate varied lengths of hydrologic memory, which can be identified using the method discussed in section 2.3.3.

(5) In the studied wetlands, errors for predicting start date and wet duration were less than 1 month at a 90% confidence level, indicating that the Bayesian regression and variable selection framework provides an effective approach to predict interannual wet-period variations. By pairing it with short term observation experiments, the presented framework could potentially be applied to evaluate long term variations in wetland ecological functions. For example, the framework may be first used to predict wet-period variations using Ppt and PET projections from climate models. Concurrently, a quantitative relation between wet-period and ecological functions, such as methane emissions, may be established via short term observation experiments (e.g. Nykänen et al. (1998) and Altor and Mitsch (2006)). The derived relation can then be used with the predicted wet-periods to evaluate the impacts of climate change on methane emissions from wetlands. However, as the relation between GWT and ecological functions are often site specific and may vary a lot among wetlands (Walter and Heimann, 2000; Turner et al., 2016), it is important to first verify the applicability of GWT vs. ecological function relation at a site before the framework is applied for future predictions. In order to use the results for decision making, appropriate uncertainty characterization should also be performed.

(6) In this study, wet-periods were defined based on a GWT threshold of -0.3 m. However, depending on the ecological function of interest and the vegetation, substrate, and meteorological properties, the critical GWT threshold in some wetlands

may differ from -0.3 m. For example, methane emission rates from a Ohio riparian wetland (Altor and Mitsch, 2006) and a Michigan peatland (Shannon and White, 1994) were observed to be much higher when GWT was higher than -0.2 and -0.15 m, respectively. It is suggested that appropriate thresholds should be chosen based on the site-specific relation between GWT and the ecological function of interest. Notably, the Bayesian framework used in this study is flexible enough to incorporate different thresholds.

(7) While the presented Bayesian framework should ideally be trained using long term observed groundwater data, in the absence of observed data, a physically-based model may be used to generate long term groundwater time series in wetlands. However, accuracy of the Bayesian approach in this case is bound to be dependent on the model's ability to simulate GWT in wetlands. In this study, even though the PIHM results were extensively validated against multiple observations, uncertainty in the simulated wet-period characteristics can not be overlooked. Further confidence in the modeled results and the analyses could be established by validating against additional observations.

In spite of the aforementioned limitations, the study highlights an undeniable influence of seasonality and hydrologic memory on wet-period variations of inland forested wetlands. The presented framework provides a simple, yet effective, approach for estimating and predicting wet-period variations in inland wetlands. The approach can also be used to estimate variations in associated ecological functions in wetlands.

3

Effects of long-term climate trends on forest mortality risk

3.1 Introduction

Forest mortality can lead to irreversible change in vegetation cover, thereby affecting many processes pertinent to water, carbon, and nutrient budgets (Allen et al., 2010). Multiple studies (Allen et al., 2015; Breshears et al., 2005; Adams et al., 2009; Williams et al., 2013; McDowell et al., 2015; Anderegg et al., 2013b, 2012, 2013a; Parolari et al., 2014) have noted close association between forest mortality and water and heat stress, owing to shifting precipitation patterns and rising air temperature. However, the influence of concurrent changes in specific humidity and CO_2 concentration, which affect plant response to stress by altering stomatal kinetics (Katul et al., 2009a), have not received similar attention. Although elevated CO_2 concentration is expected to promote future forest productivity (Schimel et al., 2015), the extent to which it affects forest mortality in the context of water and heat stress remains a subject of inquiry. Short-term records (Breshears et al., 2005; Adams et al., 2009) and long-term manipulative field studies in forests such as the

Free Air CO_2 Enrichment experiments (Norby and Zak, 2011; Ainsworth and Long, 2005; Ellsworth et al., 2004) have tried to fill the knowledge gap, however they do not cover the entire manifold of projected climate conditions. The goals of this study are to evaluate the individual and combined influence of projected changes in precipitation, temperature, specific humidity and CO_2 concentration on forest mortality risk; and investigate whether the response of mortality risk differs among plant functional types (PFTs).

Tree mortality may occur through several mechanisms including hydraulic failure, carbon starvation, phloem transport limitation, and biotic attack (McDowell et al., 2008, 2011). Hydraulic failure is characterized as the malfunction of xylem water transport associated with cavitation, which is induced by low xylem water potential under limited soil water availability. Carbon starvation occurs when carbohydrate supply and storage cannot meet demand (McDowell et al., 2011), which could result from low photosynthesis due to stomatal closure in response to low plant water potential and high atmospheric vapor pressure deficit (VPD). Reduced photosynthesis and plant water potential also pose limitations for phloem to maintain turgor pressure and may further impair phloem transport (Sala et al., 2010). Intense and prolonged stresses could weaken the defenses of forests to biotic attack (Williams et al., 2013) and may alter plant adaptation, seed production, and germination (Allen et al., 2015). Despite these mechanisms being far from thoroughly understood (McDowell et al., 2011; Sala et al., 2010), they primarily result from low plant water potential and restricted photosynthesis.

3.2   Methods

3.2.1   Quantification of mortality risk

To quantify the risk of mortality induced by low plant water potential, previous studies (Choat et al., 2012; Delzon and Cochard, 2014) used the safety margin, i.e.,
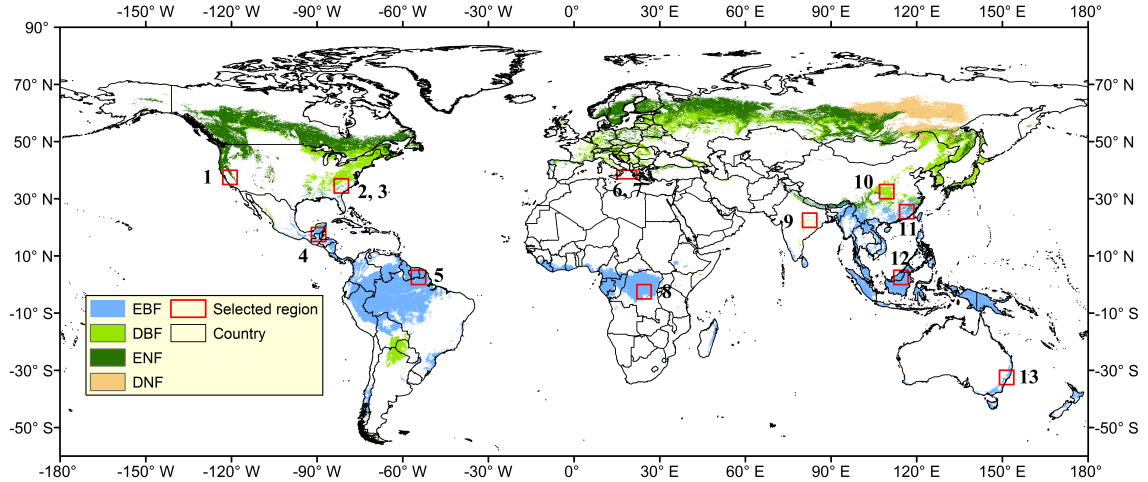
FIGURE 3.1: Distribution of plant functional type (PFT) and locations of the thirteen investigated biomes. Biomes are the areas within the selected rectangular regions that are covered by a given PFT. PFTs shown in the map include evergreen broadleaf forest (EBF), deciduous broadleaf forest (DBF), evergreen needleleaf forest (ENF) and deciduous needleleaf forest (DNF).

the difference between the minimum observed xylem water potential and the xylem water potential at 50% loss of conductivity (ψ_{50}). Plants with narrower or more negative safety margins are considered to be more susceptible to hydraulic failure. The safety margin provides a static assessment of plant susceptibility to hydraulic failure, though its representativeness may be undermined by limited field observations. It has also been suggested that instead of the minimum water potential plants reach, the duration plants operate under high percentage loss of conductivity could more likely distinguish mortality (McDowell et al., 2013; Sperry and Love, 2015). Here, a duration-based hydraulic failure risk (HFR) is introduced, which quantifies the fraction of days when the daily minimum xylem water potential ($\psi_{x,\min}$) falls below ψ_{50}. Because stomatal closure restricts photosynthesis (McDowell et al., 2015, 2011; Poyatos et al., 2013), a stomatal closure risk (SCR) can also be formulated as the fraction of days on which stomata are completely closed (Appendix B, Section 1). The aggregated mortality risk is then defined as the fraction of days with occurrence

of either hydraulic failure or stomatal closure, two physiological states contributing to dieback and eventual mortality. Alternative quantification of risk that account for stress duration and severity are also considered to test the robustness of the analysis here (Appendix B, Section 5). This quantification of modeled risk evaluated using the model described below is shown to capture the temporal variation of observed mortality in response to climate stressors at four sites, (Appendix B, Section 3).

3.2.2 SPAC model

The mortality risk is evaluated using a soil-plant-atmosphere continuum (SPAC) model, which computes hourly dynamics of xylem water potential and stomatal conductance. The model consists of three process components: a soil water balance, a plant water transport that is based on cohesion-tension theory and associated hydraulic properties, and an atmospheric boundary layer (ABL) development model that permits evapotranspiration to alter the height, temperature and specific humidity of the boundary layer (Appendix B, Section 1).

Soil water balance. Soil is characterized as a two-layer bucket. Assuming negligible lateral flux due to the effects of topography and contribution from groundwater, the vertically averaged relative soil moisture in the first layer (s_1) is recharged by throughfall $(P_T = P - I)$, and depleted by leakage (L_1) to the second layer, surface runoff (Q), soil evaporation (V) and plant root extraction (E_1). The second layer soil moisture (s_2) is recharged by L_1 and depleted through leakage to deeper soil (L_2) and root extraction (E_2). Here P is precipitation and I is interception loss. The soil water balance at an hourly scale for the two layers is expressed as

$$n_1 Z_{r1} \frac{\mathrm{d}s_1}{\mathrm{d}t} = P_T - L_1 - Q - V - E_1 \tag{3.1}$$

$$n_2 Z_{r2} \frac{\mathrm{d}s_2}{\mathrm{d}t} = L_1 - L_2 - E_2 \tag{3.2}$$

44

where n_j and Z_{rj} $(j = 1, 2)$ denote soil porosity and root zone depth of the two layers, respectively. Daily precipitation is modeled as a marked Poisson process (Rodríguez-Iturbe and Porporato, 2007), with a frequency parameter of λ_P and rainfall depth drawn from an exponential distribution with a mean of α_P. Daily precipitation is randomly assigned within an hour. Interception is quantified as $I = \max(P - I_s, 0)$, where $I_s = 10^{-4}\mathrm{LAI}$ (m) (Wigmosta et al., 1994) is the interception storage and LAI is leaf area index. According to Darcy's law for unsaturated flow, the water flux between the two soil layers is

$$L_1 = K\frac{\psi_{s,1} - \psi_{s,2}}{\rho_w g \Delta l} \tag{3.3}$$

where ρ_w is water density; g is gravitational acceleration; the soil vertical unsaturated hydraulic conductivity (K) and flow path (Δl) are taken as the harmonic mean of the two layers, i.e., $K = (Z_{r1} + Z_{r2})/(Z_{r1}/K_1 + Z_{r2}/K_2)$, $\Delta l = (Z_{r1} + Z_{r2})/2$, where K_1 and K_2 are the unsaturated hydraulic conductivities of the two layers.

Leakage from the second layer occurs only when $s_2 > s_{sfc,2}$ with a rate of K_2 (Rodríguez-Iturbe and Porporato, 2007), where $s_{fc,2}$ is the field capacity of the second layer corresponding to $\psi_{s,2} = -0.03$ MPa (Dingman, 2002). Q is generated when the first layer is fully saturated. Soil evaporation is controlled by the potential evaporation rate (V_p) and the limitation induced by top soil moisture (s_1). V_p is calculated using the adapted Penman-Monteith equation (Penman, 1948; Monteith, 1964), i.e.,

$$V_p = \frac{\Delta R_n^b + \rho_a c_p(e_s - e_a)/r_a}{\rho_w \lambda_w \left[\Delta + \gamma(1 + r_s/r_a)\right]} \tag{3.4}$$

where Δ is the saturation vapor pressure function with respect to air temperature at 2 m height T (°C); R_n^b is the below-canopy shortwave net radiation, which depends on shortwave net radiation (R_n) and an exponential decay function given by $R_n^b = R_n \exp(-b_0\mathrm{LAI})$ (Martens et al., 2000); ρ_a is air density; c_p is the constant-pressure

specific heat capacity of air; e_s and e_a are saturated and actual vapor pressure; λ_w is the latent heat of vaporization; γ is the psychrometric constant; $r_a = 50$ s m^{-1} and $r_s = \exp(8.206 - 4.255 s_{fc,1})$ s m^{-1} (Oleson et al., 2008) are the aerodynamic and soil resistance to water vapor transport, respectively. The actual soil evaporation V is calculated using the following piecewise linear function:

$$V = \begin{cases} V_p & \text{if } 1 \geqslant s_1 > s_{fc,1} \\ (s_1 - s_{h,1})/(s_{fc,1} - s_{h,1}) \times V_p & \text{if } s_{fc,1} \geqslant s_1 > s_{h,1} \\ 0 & \text{if } s_{h,1} \geqslant s_1 > 0 \end{cases} \qquad (3.5)$$

where $s_{h,1}$ is the hygroscopic point of the top layer soil, i.e., the soil moisture corresponding to ψ_s of -3 MPa (Dingman, 2002).

Plant water transport. Water transport from soil to plant and within plant is modeled as a resistance system with no capacitance. Soil water is extracted by roots in both layers, i.e.,

$$E_j = g_{sr,j}(\psi_{s,j} - \psi_r) \qquad (3.6)$$

where ψ_r is the root water potential; the soil-root conductance (g_{sr}) is computed using a cylindrical root model (Katul et al., 2003):

$$g_{sr,j} = \frac{K_j\sqrt{\text{RAI}_j}}{Z_{rj}\pi\rho_w g} \qquad (3.7)$$

in which RAI_j is root area index in each layer. Assuming negligible plant water storage, according to continuity, the total transpiration (E) is

$$E = E_1 + E_2 \qquad (3.8)$$

$$E = 2g_p\left[\psi_r - \left(\psi_x + \frac{1}{2}\rho_w g H_c\right)\right] = g_p\left[\psi_x - (\psi_l + \rho_w g H_c)\right] \qquad (3.9)$$

where ψ_x and ψ_l are xylem (located at half the canopy height (H_c)) and leaf water potential respectively; the plant conductance g_p depends on the most negative water

potential in plant, i.e., ψ_l (Manzoni et al., 2013),

$$g_p = g_{p,\text{max}} \left[1 + (\psi_l / \psi_{50})^a \right]^{-1} \tag{3.10}$$

where $g_{p,\text{max}}$ is the maximum plant conductance; ψ_{50} is the xylem pressure at 50% loss of conductivity; a is the shape parameter of plant vulnerability curve.

CO_2 and water vapor transfer between leaves and atmosphere can be described by Fickian diffusion through the stomata:

$$f_c = g_s(c_i - c_a) \tag{3.11}$$

$$f_e = a_0 g_s(e_i - e_a)/P_0 \approx a g_s D \tag{3.12}$$

where f_c and f_e are CO_2 and water vapor flux; g_s is the stomatal conductance to CO_2; $a_0 = 1.6$ is the relative diffusivity of water vapor with respect to CO_2; c_i and c_a are intercellular and ambient CO_2 concentration; e_i is intercellular water vapor pressure; D is the vapor pressure deficit normalized by atmospheric pressure P_0, i.e. $D = (e_s - e_a)/P_0$. Here, for the sake of simplicity, saturated water vapor pressure at the leaf surface is approximated as e_s, without considering the influence of leaf size and wind speed on leaf temperature.

According to the Farquhar photosynthesis model (Farquhar et al., 1980), the assimilation rate of CO_2 is described as a function of c_i (when ignoring the mesophyll conductance), R_n and T. Accounting for the limitation by RuBP (J_E), Rubisco (J_C) and sucrose synthesis (J_S), the carbon assimilation rate is computed as

$$f_c = A(c_i, R_n, T) = \phi(J_E, J_C, J_S) - R_d \tag{3.13}$$

Representations of gross assimilation $\phi(J_E, J_C, J_S)$ and the respiration from the leaf (R_d) come from the model by (Collatz et al., 1991). Based on the stomatal optimization theory (Katul et al., 2009a), the net carbon gain for the leaf is defined as

$$f(g_s) = f_c - \lambda f_e \tag{3.14}$$

47

The stomata is assumed to operate under a trade-off between maximizing f_c and minimizing f_e in order to achieve the maximum net carbon gain with the optimal g_s subject to $\mathrm{d}f(g_s)/\mathrm{d}(g_s) = 0, f(g_s) \geqslant 0$. λ is the marginal water use efficiency (mWUE), i.e., $\lambda = \mathrm{d}f_c/\mathrm{d}f_e$. To account for the responses of stomata to water stress, λ is quantified as (Manzoni et al., 2011)

$$\lambda = \lambda^*_{WW} \frac{c_a}{c_a^*} \exp(\beta_0 \bar{\psi}_l) \tag{3.15}$$

where λ^*_{WW} is the mWUE under well-watered condition at $c_a = c_a^*$; $c_a^* = 400$ ppm is the reference ambient CO_2 concentration; β_0 is the slope parameter; $\bar{\psi}_l$ is the average leaf water potential in the previous day. Increase of λ with c_a was validated in previous studies (Manzoni et al., 2011; Katul et al., 2009b).

The stomatal conductance (g_s) can be solved by combining Equations (3.11) – (3.15). The water flux at a leaf scale (f_e) can then be obtained based on Equation (3.12). By upscaling the water flux to a canopy scale based on continuity, i.e., $E = f_e\mathrm{LAI}$, and combining with Equations (3.6), (3.8), (3.9), the plant hydraulic system is closed.

ABL development. The energy and mass components in ABL development are affected by feedback of total water flux from the ground surface (de Arellano et al., 2012), including interception, soil evaporation and plant transpiration. The coupled SPAC model simulates ecohydrologic states at an hourly interval. The hourly dynamics of the soil-plant system above is coupled with the development of the ABL to obtain diurnal mean air temperature and humidity that are consistent with land-atmosphere heat and mass exchange (de Arellano et al., 2012). The ABL is represented as a well-mixed slab of air with a height h and constant potential temperature θ and specific humidity q. At the ground surface, neglecting the ground heat flux, available solar energy is partitioned into latent heat and sensible heat (H),

$$R_n = \lambda_w \rho_w ET + H \tag{3.16}$$

where $ET = E + V + I$ is the total water flux from the soil-plant system. Within ABL, temperature and humidity are governed by energy and water balance (McNaughton and Spriggs, 1986). According to the first law of thermodynamics and mass conservation, the energy and water balance are

$$\rho_a c_p h \frac{\mathrm{d}\theta}{\mathrm{d}t} = H + \rho_a c_p (\theta_f - \theta)\frac{\mathrm{d}h}{\mathrm{d}t} \tag{3.17}$$

$$\rho_a h \frac{\mathrm{d}q}{\mathrm{d}t} = \rho_w ET + \rho_a (q_f - q)\frac{\mathrm{d}h}{\mathrm{d}t} \tag{3.18}$$

where θ_f and q_f are the potential temperature and specific humidity of the free atmosphere at height h respectively. In the free atmosphere, potential temperature and specific humidity are assumed to vary linearly with height (Porporato, 2009),

$$\theta_f = \theta_{f0} + \gamma_\theta h$$

$$q_f = q_{f0} + \gamma_q h$$

where γ_θ and γ_q are the lapse rate of potential temperature and specific humidity in the free atmosphere, respectively.

θ_{f0} and q_{f0} are the intercepts of the assumed linear profiles, which can be obtained by inserting the initial conditions. Following (McNaughton and Spriggs, 1986), the simplified ABL growth rate is expressed as

$$\frac{\mathrm{d}h}{\mathrm{d}t} = \frac{H}{\rho_a c_p h \gamma_\theta} \tag{3.19}$$

The dynamics of θ, q and h are solved by Equations (3.17) – (3.19). At the beginning of each day and during precipitation events, ABL is reset to the daily initial conditions based on daily climate data (see Appendix B Section 2 for details). The diurnal development of ABL, in response to the feedback of heat and

water vapor flux from the soil-plant system, provides dynamic forcing of temperature and humidity to the soil-plant system. Code for the SPAC model is available at https://github.com/YanlanLiu/SPACModel_2017.
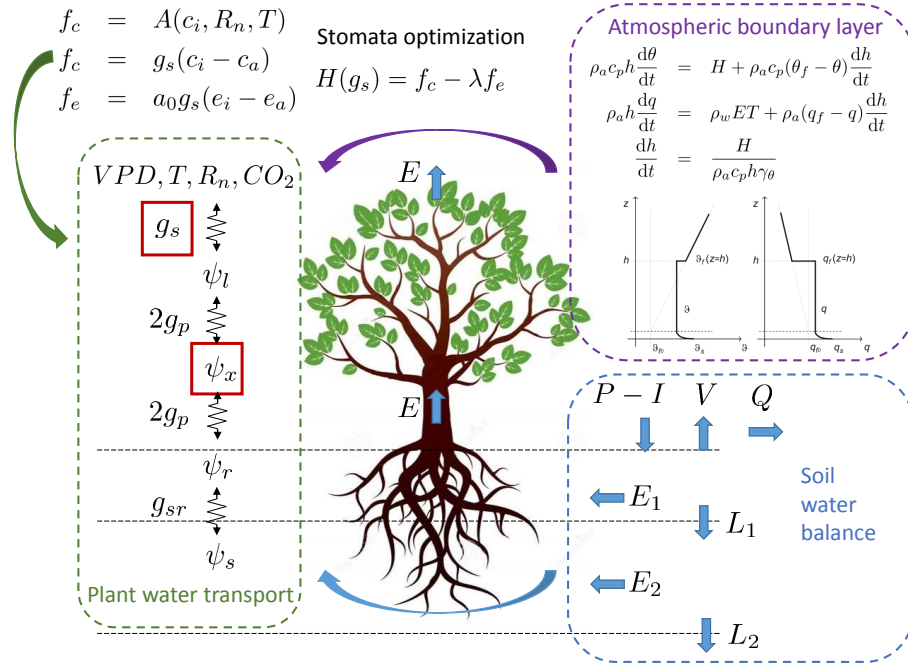
FIGURE 3.2: Processes and states in the SPAC model. See the text for notations.

Soil and vegetation properties

Based on the global land cover type from MODIS (MCD12C1) (NASA LP DACC, 2013), thirteen forest biomes were selected across the globe. The biomes cover three PFTs and a variety of climate types (Figure 3.1, Table B.11) with mean annual precipitation ranging from 500 to 3000 mm. Regions with shallow-groundwater (Fan et al., 2013) and snow-dominated climate (Kottek et al., 2006) were avoided as the influence of groundwater and snow is not considered in the model. The SPAC model in each biome was parameterized with local soil and representative plant properties. Soil texture compositions were obtained from the Harmonized World Soils Database (FAO, 2009). Soil hydraulic properties were calculated based on the generalized

50

statistical relations (Saxton et al., 1986). Annual cycle of LAI was extracted from the level-4 MODIS global Leaf Area Index (LAI) and Fraction of Photosynthetically Active Radiation (FPAR) product (MCD15A2) (NASA LP DACC, 2016). Plant hydraulic traits were obtained from a global database containing hydraulic traits of 866 species (Kattge et al., 2011). Photosynthetic parameters were derived from a cross-species study (Medlyn et al., 2002). Stomatal optimization parameters were obtained based on a meta-analysis study across PFTs and climates reported in previous study (Manzoni et al., 2011). These plant properties were obtained at a biome-level by averaging the properties of trees belonging to the same PFT and climate type (Kattge et al., 2011) as found in the given biome.

Historical and projected climates

The SPAC model in each biome is forced by local daily climate, including stochastic precipitation, net shortwave radiation, and initial and boundary conditions of potential temperature and specific humidity of ABL. At the beginning of each day, the ABL was reset with the corresponding initial and boundary conditions. The stochastic precipitation is represented as a marked Poisson process characterized by frequency and mean rainfall depth statistics (Rodríguez-Iturbe and Porporato, 2007). Daily historical climates were calculated based on the NCEP/NCAR reanalysis data (Kalnay et al., 1996) from 1986 to 2005. Projected climate changes were obtained from multi-model outputs of CMIP5 experiments under four RCP scenarios (Table B.12). For each model under each RCP scenario, changes in climate variables were quantified as the difference between the averages for 1986 – 2005 and 2050 – 2069. Future precipitation statistics and other climate forcings for the model were generated by incorporating these changes into the historical climates from NCEP/NCAR (Appendix B, Section 2) to eliminate the influence of biases in climate model outputs (Knutti et al., 2010). Historical and future atmospheric CO_2 concentrations under

the four RCP scenarios were provided in (Meinshausen et al., 2011). The response of mortality risk to changes in the following climate characteristics is analyzed: mean annual precipitation (MAP), precipitation seasonality (PS), mean annual air temperature (T), mean annual atmospheric specific humidity (SH), and atmospheric CO_2 concentration. PS is quantified as the fraction of MAP that falls within the growing season.

3.2.3 Experimental design and statistics

The mortality risk under a given climate was quantified based on plant dynamics by running the SPAC model at hourly resolution for 30 annual ensembles after a 5-year warm-up period. Influence of changes in each individual climate variable was analyzed by keeping the others the same while only changing the target climate variable. Influence of combined changes in climate variables as projected by multi-models were grouped together to evaluate the overall response of mortality risk under each RCP scenario. Each reported change in risk is the average of changes of all the biomes, unless stated otherwise. Change in each biome was calculated as the difference between the historical risk and the future risk, i.e., the average risk based on multi-model projections, in proportion to the historical risk. Biomes with historical risks lower than 0.01% were excluded from the statistics.

3.3 Results

3.3.1 Influence of individual changes in climate variables

Mortality risk is found to increase with reduced annual precipitation and a lower fraction of precipitation in the growing season. Reduced precipitation decreases plant water potential via low soil moisture, hence increasing HFR (Figure 3.3d, horizontal axis). Meanwhile, low plant water potential also restricts stomatal conductance, hence increasing SCR (Figure 3.3a, horizontal axis). Plants experience higher risk in
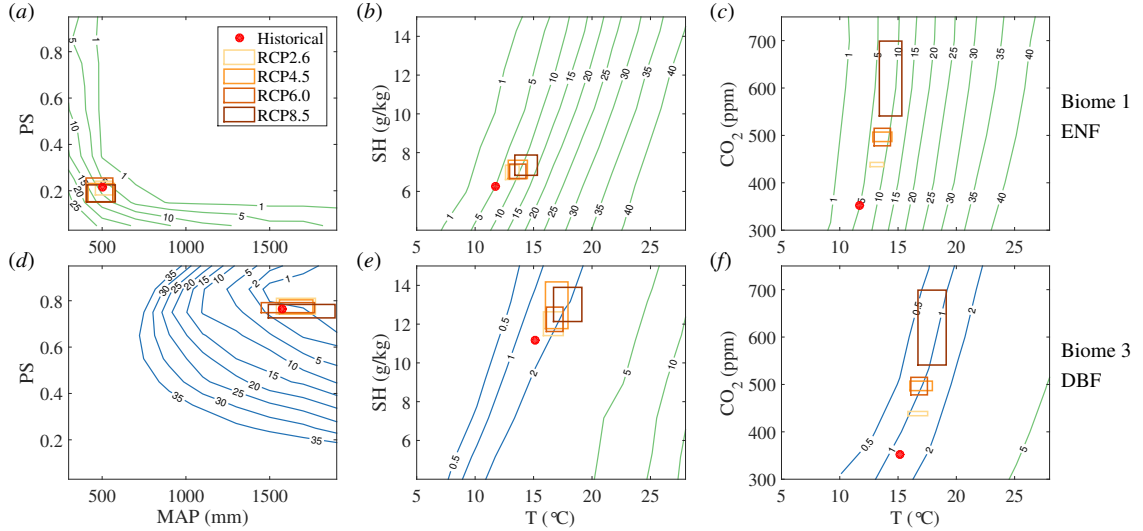
FIGURE 3.3: Responses of mortality risk to individual changes in mean annual precipitation amount (MAP), precipitation seasonality (PS), mean annual air temperature (T), specific humidity (SH) and CO_2 concentration for ENF in the western US (a, b and c) and DBF in the southeastern US (d, e and f). PS is quantified as the fraction of MAP that falls within the growing season. Changes in MAP and PS are incorporated in daily precipitation time series through their impact on the statistical distribution of stochastic precipitation; changes in T, SH and CO_2 are incorporated uniformly throughout the year, keeping the intra-annual patterns unchanged. Numbers on the contours denote risk magnitude (%). Predicted ranges by multi-models under the four RCP scenarios are illustrated by rectangles. Blue and green contours represent risks due to hydraulic failure and stomatal closure, respectively.

the growing season than in the non-growing season, due to low plant water potential and atmospheric aridity imposed by a high VPD. Given the same annual precipitation, more growing season precipitation (higher PS) generally decreases the risk (Figure 3.3a, d, vertical axis). Reduced precipitation during the non-growing season typically does not increase the risk, as the stressed conditions mostly occur in the growing season.

Sensitivity of mortality risk to precipitation amount and seasonality varies across soil, plant, and climate conditions as expected. For ENF in the western US (Figure 3.3a, biome 1 in Figure 3.1), the risk is primarily controlled by annual precipitation amount when less than 400 mm. For wetter climates (MAP > 800 mm) with low

growing season precipitation (PS < 0.2), seasonality becomes the dominant factor. Under the historical climate in this region, both precipitation amount and seasonality play significant roles in mortality risk. Although large uncertainties exist in the projected annual precipitation, CMIP5 models mostly predict lower PS in this region, which is likely to increase mortality risk. For DBF in the southeastern US (Figure 3.3d, biome 3 in Figure 3.1), both precipitation amount and seasonality affect the risk over a wide range of climatic conditions. Although the risk generally decreases with higher PS when PS < 0.7, the trend reverses for PS > 0.8. As CMIP5 projections point to increase in precipitation with little change in seasonality, mortality risk of this biome is expected to decrease under future precipitation patterns.

Modeled mortality risk increases with warming air temperature but decreases with rising specific humidity (Figure 3.3b, e) and CO_2 concentration (Figure 3.3c, f). Elevated temperature promotes water loss through higher VPD. Although stomata close in response to high VPD to prevent excessive water loss, the same action increases the risk of full stomatal closure. Increasing specific humidity, on the other hand, offsets the increase of VPD by air temperature, hence attenuating intensified risks caused by warming. Under higher atmospheric CO_2 concentration, plants can operate at lower stomatal conductance to meet their biochemical demand for CO_2. This so-called "carbon fertilization effect" allows plants to enhance water-use efficiency, hence reducing the risks of both hydraulic failure and stomatal closure simultaneously. All three climate variables exhibit significant influence on mortality risk of ENF in the western US and DBF in the southeastern US. For the projected changes in temperature and specific humidity (Figure 3.3b, e), the intensifying influence of rising air temperature overwhelms the opposing influence of rising specific humidity, leading to higher VPD and thus higher risk. Remarkably, elevated CO_2 concentrations offset the intensified risk imposed by elevated temperature (Figure 3.3c, f).

Despite the similar patterns of response to climate change, sources of risk in the two biomes (Figure 3.3) are markedly different. Under both historical and projected climates, the risk for the ENF in the western US mostly originates from stomatal closure. The risk for the DBF in the southeastern US mostly originates from hydraulic failure. However, under extremely high air temperature (annual mean > 23°C) in the DBF, high VPD induces full stomatal closure, resulting in a switch from HFR to SCR (Figure 3.3e, f). The different sources of risk for these two biomes can be attributed to their response strategies under stress, which are controlled by their hydraulic traits. ENF consists of conifers, which mostly operate with a wide safety margin ($\psi_{x,min} - \psi_{50}$) (Choat et al., 2012) and exhibit an isohydric strategy under stress (McDowell et al., 2008), i.e., restricting transpiration by reducing stomatal conductance while maintaining high water potential to prevent run-away cavitation (Figure B.12). Owing to this conservative water use strategy and the wide safety margin, isohydric conifers are more susceptible to SCR than HFR. In contrast, DBF consists of angiosperms, which operate with a narrower safety margin (Choat et al., 2012) and largely use an anisohydric strategy under stress McDowell et al. (2008), i.e., stomata remain open to sustain photosynthesis at the expense of decreased water potential (Figure B.12). With this less conservative water use strategy and a narrow safety margin, anisohydric DBFs are more susceptible to HFR than SCR. These contrasting stress responses have been widely reported (McDowell et al., 2008; Choat et al., 2012; McDowell, 2011). Previous studies also suggested hydraulic failure as the major mechanism in an aspen (angiosperm) mortality event (Anderegg et al., 2012) and near-zero stomatal conductance as the main contributor to conifer mortality events (McDowell et al., 2008; Poyatos et al., 2013). It is to be noted that large variations in hydraulic traits exist within each PFT, and the results presented here are based on the average traits of species falling within a PFT and climate type in a given biome.

3.3.2   Influence of combined changes in climate variables
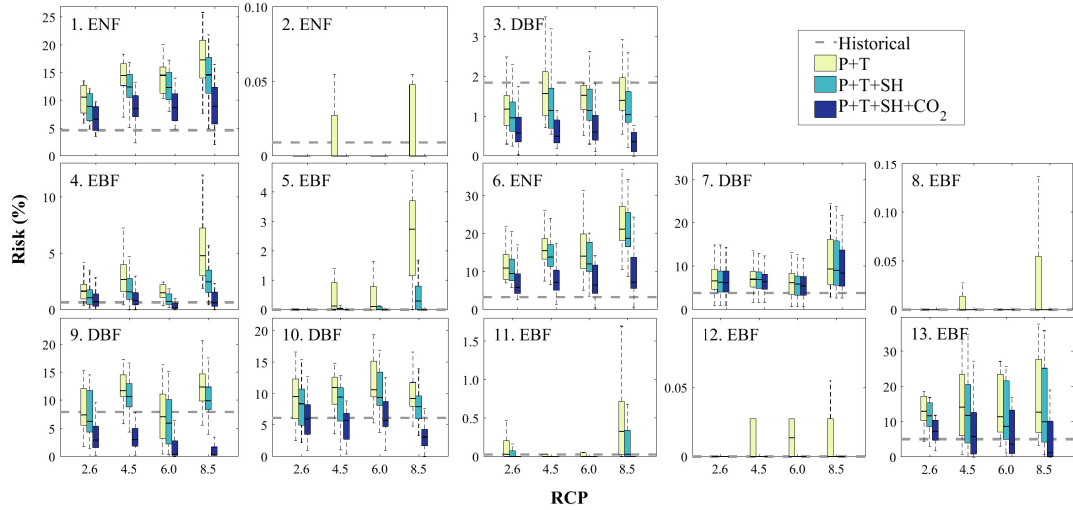
FIGURE 3.4: Response of mortality risk to combined changes in climate variables. P+T includes changes in mean annual precipitation, precipitation seasonality and air temperature; P+T+SH includes additional changes in specific humidity; P+T+SH+CO_2 includes additional changes in atmospheric CO_2 concentration. Gray dashed lines in the subplots show the risks under historical climates. Upper and lower boundaries of the boxes correspond to the 25th and 75th quantiles of the risk based on multi-model projections in each RCP scenario. Numbers in the subplots correspond to the biome locations in Figure 3.1.

Based on the CMIP5 projections of four representative concentration pathway (RCP) scenarios in all the 13 biomes (Figure B.15), the response of mortality risk to changes in three combinations of climate conditions are examined (Figure 3.4): (1) P + T; (2) P + T + SH; and (3) P + T + SH + CO_2. Here changes in P include combined changes in MAP and PS. For the 13 investigated biomes, on average, shifting precipitation patterns and rising temperature projected by RCP4.5 are found to intensify the risk by 158.8% for the period 2050 – 2069 relative to the historical risk. This increase in risk is consistent with previous studies highlighting the exacerbating effects of higher temperature (Allen et al., 2010; Breshears et al., 2005; Adams et al., 2009; Williams et al., 2013; Anderegg et al., 2013b; McDowell

et al., 2015). However, by incorporating increases in specific humidity, the risk decreases by 46.6%. More remarkably, the risk drops an additional 91.2% under the added influence of elevated CO_2 concentration. In aggregate, changes in all four climate conditions increase the risk by 21.0% on average, which is much lower than the increase of 158.8% when only the changes in precipitation and air temperature are considered. Under high emission scenarios (RCP6.0, RCP8.5), elevated humidity and CO_2 concentration might even overwhelm the effects of higher temperature, possibly resulting in a lower risk than the historical level (Figure 3.4). These alleviating effects are robust across alternative risk measures (Table B.41, Figure B.42). The alleviating effect of increasing atmospheric CO_2 concentration is in line with reported decrease in stomatal conductance and increase in water use efficiency across various climate regions and species (Allen et al., 2015; Ainsworth and Rogers, 2007; Brodribb et al., 2009; Lammertsma et al., 2011; Keenan et al., 2013; Drake et al., 2016).
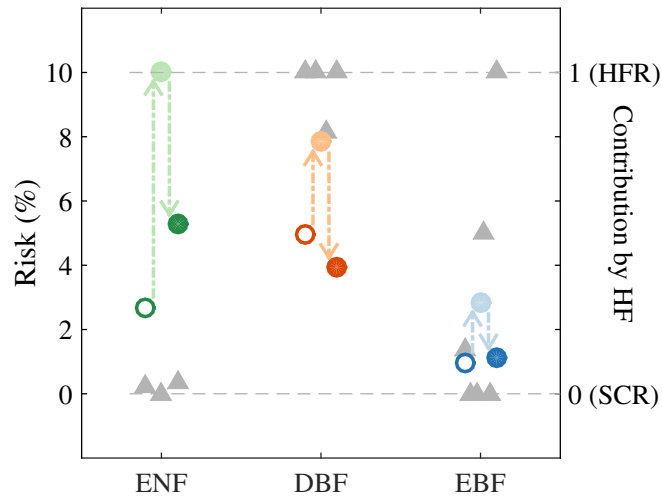
FIGURE 3.5: Average risk under historical climates (empty circles), changes in P+T (light filled circles) and changes in P+T+SH+CO_2 (dark filled circles), for each PFT based on RCP4.5. Gray filled triangles denote the relative contribution of hydraulic failure to the mortality risk, i.e., 1 denotes that all the risk is due to hydraulic failure (HF) and 0 denotes all the risk is from stomatal closure.

On average, the combined changes of P+T+SH+CO_2 in RCP4.5 are found to increase the mortality risks by 101.1%, –18.3%, and 19.6% for ENF, DBF and EBF biomes respectively (Figure 3.5). The significantly higher increase for ENF compared to the other two PFTs results from their distinct risk sources (Figure 3.5). SCR, the primary risk source for ENF, shows notably higher sensitivity to air temperature rise than HFR. Specifically, for 1 °C increase in air temperature from historical climates, HFR and SCR are estimated to increase by 23.5% and 125.1%. Remarkably, the increase in SCR is close to the previously reported 116.3% $°C^{-1}$ increase in die-off events of *Pinus edulis* (Adams et al., 2009), a conifer species likely threatened by SCR. From a mechanistic perspective, elevated temperature increases VPD and reduces stomatal conductance. This restricts carbon assimilation but promotes water loss, which results in a higher probability of full stomatal closure, i.e., higher SCR. The increase in HFR is smaller as the reduction in stomatal conductance partly alleviates the increase in water loss due to increased VPD. Under projected changes of precipitation and VPD in RCP4.5, HFR increases by 135.5% on average, while SCR increases by 305.8%. When CO_2 is also considered, the aggregate changes are –8.6% and 83.7% for HFR and SCR, respectively. These findings imply a larger increase in mortality risk of ENFs, more specifically of isohydric species, than other PFTs under changes in the considered climate conditions.

3.4   Discussion and implications

The study evaluates how projected climate change will affect mortality risks, and how the risks may be mediated by different PFTs across the globe. In this regard, the study introduces a measure of mortality risk that accounts for the duration plants operate under high percentage loss of conductivity or stomatal closure. Although large uncertainty exists in the exact physiological mechanisms that cause mortality (McDowell et al., 2011; Sala et al., 2010), the proposed mortality risk measure cap-

tures two of the fundamental causes, i.e., low water potential and severely restricted carbon assimilation, which contribute to the downstream mortality mechanisms. Notably, the quantification of mortality is made possible by synergistic coupling of multiple prior sub-models connecting plant physiological status to hydrological and meteorological conditions. This coupling allows the SPAC model to resolve hourly dynamics of xylem water potential and stomatal conductance, the variables required to evaluate mortality risk (Appendix B, Sections 1 and 5). For example, by accounting for the feedback between evapotranspiration and atmospheric boundary layer (ABL) development, the SPAC model is able to simulate a physically-consistent hourly dynamics of air temperature and specific humidity during droughts. During drought, when evapotranspiration is restricted by low soil moisture, the model partitions larger fraction of incoming energy into sensible heat thus enhancing the ABL and raising the temperature during daytime. This evapotranspiration-ABL coupling allows SPAC to consider the co-occurrence of extreme drought and heat stress, which has been pointed out as the main environmental trigger of tree mortality (Breshears et al., 2005; Adams et al., 2009; Williams et al., 2013; Anderegg et al., 2013b). The SPAC model also uses an optimization based stomatal conductance representation that accounts for the effect of plant hydraulic limitation (Appendix B, Section 1). The representation is an advantage over several widely used dynamic global vegetation models (DGVMs), where the stomatal regulation is disconnected or empirically connected with soil water stress (McDowell et al., 2013, 2015). Many of these semi-empirical models are derived from observations under ambient CO_2 concentration, and their parameter values are subject to change in an elevated CO_2 environment (Katul et al., 2009a), thus undermining their efficacy under future climate. In contrast, the optimization based stomatal regulation model used here has been demonstrated to predict stomatal response to stress under both historical and elevated CO_2 concentration (Katul et al., 2009b).

Although the modeled risk shows strong correspondence with observed mortality (Appendix B, Section 3), the estimated risk should be interpreted with care. Given the uncertainties inherent in model structure and parameters, and the complexity of forest ecosystem, it is unrealistic to accurately assess the exact magnitude of mortality risk. Large variations in plant hydraulic traits, tree height, diameter at breast height (DBH) and stand density (Rowland et al., 2015; Bottero et al., 2017) may impact the actual mortality risk. Sensitivity of mortality risk to aforementioned factors and to uncertainties in model structure are examined (Appendix B, Section 4). Results indicate that despite their influence on the magnitude of mortality risk, the alleviating effect of increasing specific humidity and CO_2 concentration is still found to be robust. Notably, actual mortality risk may also be altered by forest fire frequency and insect outbreak, rooting profile, seed production, community level competition, local acclimation to drought and adaption to long-term climate change (Clark et al., 2016; Wolf et al., 2016; Wolfe et al., 2016; Jump et al., 2017), factors whose characterization is still fraught with uncertainties (Norby et al., 2005). Their impacts in relation to the direct influence of climate conditions discussed here deserve further investigation. However, independent of these indirect influence, results reported here demonstrate a ubiquitous and robust alleviating effect of elevated atmospheric humidity and CO_2 concentration, which is comparable in magnitude to the intensifying effect of changes in precipitation patterns and air temperature. The combined influence of changes in these climate variables on mortality risk is also strongly mediated by plant hydraulic traits. These results highlight that ignoring the influence of elevated atmospheric humidity and CO_2 concentration may lead to overestimation of future forest mortality risk.

4

Detection of early warning signal of forest mortality

4.1   Introduction

Episodes of forest mortality have been widely observed in recent decades (Allen
et al., 2010; van Mantgem et al., 2009). Such abrupt transitions in land cover impact
local species composition and ecosystem services as well as the global carbon balance
(Allen et al., 2010; Settele et al., 2015). Predictive approaches to forest mortality are
now proliferating either through modeling of plant physiological dynamics (McDowell
et al., 2013; Parolari et al., 2014; Liu et al., 2017) or by drawing relations with
hydroclimatic stresses (Adams et al., 2009; Anderegg et al., 2013a, 2015). However,
given the complexity of mortality at the individual tree (McDowell, 2011; McDowell
et al., 2011) and ecosystem levels (Clark et al., 2016; Wolf et al., 2016), compounded
by uncertainties in model structure and parameterization, predicting mortality using
vegetation models alone remains challenging (Sala et al., 2010). Relations between
hydroclimatic stress and mortality provide another predictive approach, though its
efficacy can be undermined by acclimation of vegetation properties and community
competition. As these two approaches entail estimation of water and carbon budgets

within the soil-plant system subject to projected climatic variability, uncertainties in these estimations are bound to influence the accuracy and uncertainty of mortality.

Here, an alternative approach for predicting climate-induced forest mortality through direct monitoring of vegetation dynamics is proposed. As theoretical analyses and observations across a range of systems have revealed (Scheffer et al., 2009), near the tipping point where an abrupt shift in the system state occurs, the resilience or the recovery rate from a deviated state is generally reduced. A consequence of this reduced recovery rate or the critical slowing down near the tipping point is high temporal autocorrelation (Scheffer et al., 2009). This property was leveraged in a recent study (Verbesselt et al., 2016) to assess spatial patterns of static forests resilience using remotely sensed greenness, i.e, normalized difference vegetation index (NDVI). In this context, the tipping point is in the form of forest mortality that nudges the ecosystem to an alternate dynamical regime such as a different forest composition, shrub land or grassy open area (Scheffer et al., 2001). The idea of static resilience obtained for a given time period using autocorrelation can be extended to a dynamic metric to track temporal variations in resilience. This study develops such a metric and evaluates the potential of using reduced resilience as an early warning signal (EWS) for impending mortality. The following specific questions are addressed: (1) Can resilience based EWS be identified prior to observed forest mortality? (2) How much area featured EWS, and how early does the EWS appear prior to observed mortality? (3) Can the EWS be used to predict the extent of documented forest mortality?

Previous studies (Scheffer et al., 2009; Dakos et al., 2008, 2015) demonstrated the effectiveness of using an increased lag-1 temporal autocorrelation within a moving window as a EWS to abrupt changes. However, most of these studies were based on fully defined theoretical systems or control experiments and took advantage of sufficiently long time series. Application of this method in a 'real' ecosystem setup

is expected to be more challenging, in part due to the limited duration of the available time series, the presence of dominant seasonal frequencies in variations of both ecosystem response and forcing signals, variations in autocorrelation of the forcing signals, and the presence of stochastic noise. These challenges have partly contributed to the scarcity of examples detecting critical slowing down in real natural systems (Scheffer et al., 2009). For these reasons, a Bayesian dynamic linear model (DLM) (Methods, Appendix C Section 1) is proposed.

A probability distribution of autocorrelation was obtained from DLM at each time point during 1999–2015. Based on the estimated mean and uncertainty range of autocorrelation at each time point, EWS was identified as the presence of the mean autocorrelation exceeding a threshold and lasting for at least 3 months. The threshold was computed as the long-term average of the 80th percentile of estimated autocorrelation uncertainty range.

4.2   Methods

4.2.1   Bayesian dynamic linear model.

The Bayesian DLM detects time-varying autocorrelation in time series while accounting for intrinsic stochastic noise anxd seasonality inherent in both observed vegetation dynamics and climate forcings. It also accounts for the trend of vegetation and climate variability to avoid false alarms that merely arise from changes in the trend of NDVI time series or increasingly auto-correlated climate conditions (Appendix C Section 2). The DLM consists of an observation equation and a state evolution equation, i.e.,

$$y_t = \boldsymbol{F}_t^T \, \boldsymbol{\theta}_t + v_t \tag{4.1}$$

$$\boldsymbol{\theta}_t = \boldsymbol{G} \, \boldsymbol{\theta}_{t-1} + \boldsymbol{w}_t \tag{4.2}$$

where y_t is the observed variable (NDVI) at time t after subtracting the long-term mean; $\boldsymbol{F}_t$ is a p-dimensional vector of known constants or regressors at time t, including climate variables and NDVI at time $t-1$; $\boldsymbol{\theta}_t$ is a p-dimensional state vector at time t, containing coefficients representing local mean, trend, seasonality, sensitivity to climate conditions and the lag-1 autocorrelation of NDVI; v_t is the observation noise following a zero mean Gaussian distribution; $\boldsymbol{G}$ is a known $p \times p$ state evolution matrix considered as time-invariant; $\boldsymbol{w}_t$ is the state evolution noise at time t following a mean zero multivariate Gaussian distribution, and is independent of ν_t. Non-informative priors for $\boldsymbol{\theta}_0$ and noises were provided (Appendix C Section 1). At each time t, using forward filtering (27), the posterior distribution of $\boldsymbol{\theta}_t$ was estimated by combining the prior from the summary of history $(y_0, y_1, \ldots, y_{t-1})$ and the likelihood from current observation of y_t, resulting in a time-varying posterior distribution of $\boldsymbol{\theta}_t$. Of particular interest is the temporal trajectory of the entry in $\boldsymbol{\theta}_t$ quantifying the relation between y_t and y_{t-1}. This lag-1 autocorrelation was used as a time-varying measure of resilience. EWS was then identified as the presence of this autocorrelation being higher than a threshold (Figure 4.1). Theoretical details and controlled synthetic experiments demonstrating the efficacy of DLM can be referred in Appendix C Sections 1 and 2. The source code of DLM is available at `https://github.com/YanlanLiu/early-warning-signal-DLM`.

4.2.2 Vegetation and climate data.

The area of interest includes all the forested area in California (CA), USA, hereafter referred to as the study area. Mortality in the study area has been widely observed in recent years based on the annual aerial surveys conduced by the United States Forest Service (U.S. Forest Service, 2015a), with potential to reduce the gross primary productivity both locally and across North America through eco-climate teleconnections (Swann et al., 2018). The observed mortality maps from 2005 to

2015, consisting of polygons delineating the areas with aerially observed mortality, were re-projected and rasterized at 30 m resolution to match with remotely sensed NDVI data. Regions with mortality intensity greater than 1 tree per acre based on the aerial survey data were used for analysis. Landsat 7 ETM+ surface reflectance product (U.S. Geological Survey, 2017) from 1999 June to 2015 December with a spatial resolution of 30 m and a temporal interval of 16-day was used to compute NDVI in the study area. Due to a large amount of the original Landsat data, NDVI was computed and exported in tiles from Google Earth Engine. Based on the 30 m resolution map of tree cover in 2000 (Hansen et al., 2013), all the pixels in CA with non-zero canopy closure for vegetation taller than 5m were included in the study area. Mortality caused by human activities, as indicated in the aerial survey maps, were excluded from analysis. Pixels affected by fire each year were identified based on the MODIS Active Fire product (U.S. Forest Service, 2016) and removed from estimation and prediction analysis. Data on cloudy or snow cover days were removed based on the "cfmask" band, and were considered as missing data in DLM (see Appendix C Section 1 for details). Climate conditions of daily precipitation, snow water equivalent, air temperature, incident shortwave radiation and water vapor pressure were obtained from Daymet V3 (Thornton et al., 2014). These daily climate conditions at 1 km spatial resolution were downscaled and averaged over the 16 days between two satellite observations to achieve consistent spatial and temporal resolutions with NDVI. Covariates of elevation (Abatzoglou, 2013) and live basal area (LEMMA group, 2015) that quantify topography (25) and community competition (24) were also rescaled to uniform scales for spatial estimation and prediction. Vegetation species distribution derived from field surveys during 1997–2014 (U.S. Forest Service, 2004) was grouped to a genus level. Spatial distribution of dominant species covering an area greater than 1000 km^2 were used to develop species-specific relations between EWS and observed forest mortality and abnormally low NDVI (ALN).

65

Using the DLM and relevant climate data, the time-varying autocorrelation of NDVI was estimated for EWS detection for each 30 m pixel in Landsat 7 images for the study area. Temporal and spatial variations in detected EWS were compared with aerially observed mortality provided by the U.S. Forest Service each year since 2005 (U.S. Forest Service, 2015a). Mortality noted as caused by fire or human activities were excluded from the analyses. As the forest mortality map from the aerial surveys delineates geospatial polygons within which some rather than all of the trees died whereas EWS provides a pixel-based estimate at a 30 m resolution, the comparison may introduce errors due to the spatial scale mismatch. Hence, comparison of EWS was also performed against incidence map of ALN, which has the same resolution as EWS and could be associated with leaf shedding or vegetation die-off (Breshears et al., 2005; Brodrick and Asner, 2017). Hereafter, ALN represents the occurrence of NDVI lower than a threshold, lasting for at least half of the time in the following 3 months. This threshold is set equal to the lower 20th percentile of all the observed NDVI values in that month at a given pixel location. Sensitivity analyses were performed on the thresholds used to quantify both EWS and ALN. Results suggest that the main conclusions presented here are robust to the choice of thresholds (Appendix C Section 7).

4.2.3 *Spatial-temporal estimation and prediction.*

Temporally, the total fraction of area showing EWS and the average EWS duration for each species within the entire study area were used to explain and predict mortality area across years. For years of 2005–2015, all pixels in the study area except for those affected by fire within three years were aggregated to assess the coefficient of determination (R^2) of temporal estimation. For prediction, one of the eleven years was taken out each time and then predicted based on relations developed using the rest of the years. Then the accuracy was computed by comparing the predictions

with the observations. Estimation and prediction accuracies using different combinations of EWS characteristics and lead times were examined (Figure 4.5, Appendix C Figure C.51). Spatially, as the mortality area is highly zero-inflated, mortality occurrence and intensity was modeled separately using a Gaussian model and binomial model respectively. Candidate predictors include the fraction of area showing EWS, EWS duration, basal area and elevation in each pixel. Among the linear, quadratic and interaction terms of these predictors, the most informative predictors were selected based on the Bayesian Information Criterion (BIC) for each species respectively (Appendix C Table C.51). Apart from the selected predictors, a spatial Gaussian process was also incorporated to describe spatial similarity among close neighbors. The point-based Gaussian process model is expressed as follows.

$$y(\boldsymbol{s}) = \boldsymbol{x}^T \boldsymbol{\beta} + w(\boldsymbol{s}) + \sigma \tag{4.3}$$

where $y(\boldsymbol{s})$ is mortality intensity at location $\boldsymbol{s}$ in the Gaussian model and the *logit* of mortality occurrence probability in the binomial model; $\boldsymbol{x}$ is a vector containing the selected predictors at location $\boldsymbol{s}$ and $\boldsymbol{\beta}$ contains the corresponding coefficients; $w(\boldsymbol{s})$ is the spatial effect of a Gaussian process with an exponential covariance function; and σ is the residual. Due to the distinct relations between EWS and mortality area among species (Figure 4.4), this spatial model was fitted for each of the dominant species separately. For spatial estimation, the model was fitted for mortality occurrence and log-transformed intensity in each year using the functions *spGLM* and *spLM* respectively in the "spBayes" software (Finley et al., 2015) in R (R Core Team, 2017). A non-informative flat prior was used for $\boldsymbol{\beta}$; and priors for $w(\boldsymbol{s})$ were obtained from empirical variogram. Estimates were computed using posterior means of $\boldsymbol{\beta}$ and $w(\boldsymbol{s})$ from 10^4 Markov Chain Monte Carlo samples after a 2000 burn-in period. For spatial prediction, $\boldsymbol{\beta}$ was set as the coefficient of linear regression using data from all pixels and years; and the spatial structure $w(\boldsymbol{s})$ was considered as a random

walk from that of the previous year (Gelfand et al., 2005), with the mean spatial surface unchanged. In this way, the spatial distribution of mortality occurrence and intensity in a given year can be predicted using only historical data, i.e., predictors observed at given lead time and the mean spatial structure from the most recent year. Spatial accuracies for mortality occurrence in each year were assessed with the overall accuracy (ACC), i.e., the summation of true positive and true negative divided by the total number of samples, and the area under the receiver operating characteristic curve (AUC); accuracies for mortality intensity were assessed using Bayesian coefficient of determination (R^2) (Gelman et al., 2018).

4.3 Results

4.3.1 An example of EWS detection

An example application of the DLM on a pixel in the southern Sierra dominated by pines shows that the autocorrelation in NDVI time series became abnormally high, i.e., exceeded the long-term average of its 80th percentile of the uncertainty range after October 2012 (Figure 4.1b). Abnormally low NDVI (ALN) that may indicate foliage shedding was identified in September 2014 (Figure 4.1a) and eventual mortality was observed in July 2015. No mortality or fire was observed in the previous years. The presence of abnormally high autocorrelation, i.e., reduced resilience, from October 2012 onwards serves as a EWS, with lead times of 23 months and 33 months to ALN and mortality respectively in this case. Although high autocorrelation is a typical signature of critical slowing down, it does not guarantee the occurrence of critical slowing down and an impending critical transition, i.e., it is necessary but not sufficient. To further examine the representativeness of EWS for critical slowing down, an independent analysis of NDVI data within the context of a nonlinear dynamic model of vegetation dynamics with two stable states was conducted. The two stable states in the model represent an existing vegetation cover and an alternative

68

state (Scheffer et al., 2001). The analysis suggests that during the period when EWS was identified, the system slowed down and the basin of attraction shrank (Appendix C Section 3). These shifts represent reduced recovery rate and a higher likelihood of a switch to an alternative state under stochastic perturbations. The occurrence of critical slowing down in the NDVI data during the EWS period within this model provides an additional affirmation for using the empirically derived EWS to predict abrupt transitions.

4.3.2 Fraction of area showing EWS

During 2005–2015, the Palmer drought severity index (PDSI) (Dai et al., 2004a) indicated that the state of California underwent two major droughts spanning 2007 to 2009 and 2012 to 2015 (Figure 4.2a). For the entire study area, the fraction of area with observed mortality intensity greater than 1 tree per acre (U.S. Forest Service, 2015a), referred as mortality area hereafter, remained below 2% during the first drought but rapidly increased to 6.7% in 2015 (Figure 4.2a). This sharp increase in mortality area during the second drought was in contrast to the temporal variation of PDSI, which gradually increased during 2012–2014 and remained around a high value afterward. Notably, the temporal pattern of mortality follows a typical signature of critical transition under slowly varying drivers (Dakos et al., 2015). Remarkably, the fraction of area showing EWS exhibited similar temporal variation, with the areal fraction remaining around 10% during the first drought but then increasing to a high value of 16% by 2015 (Figure 4.2b). The computed EWS area was generally larger than the mortality area, indicating some trees operated under low resilience without loss of life. The extent of area with EWS and ALN (Figure 4.2c) depends on the thresholds used to identify abnormally high autocorrelation and ALN (Appendix C Section 7). However, all the considered thresholds result in temporal trajectories of area exhibiting EWS to follow a similar pattern as ALN and mortality. Such
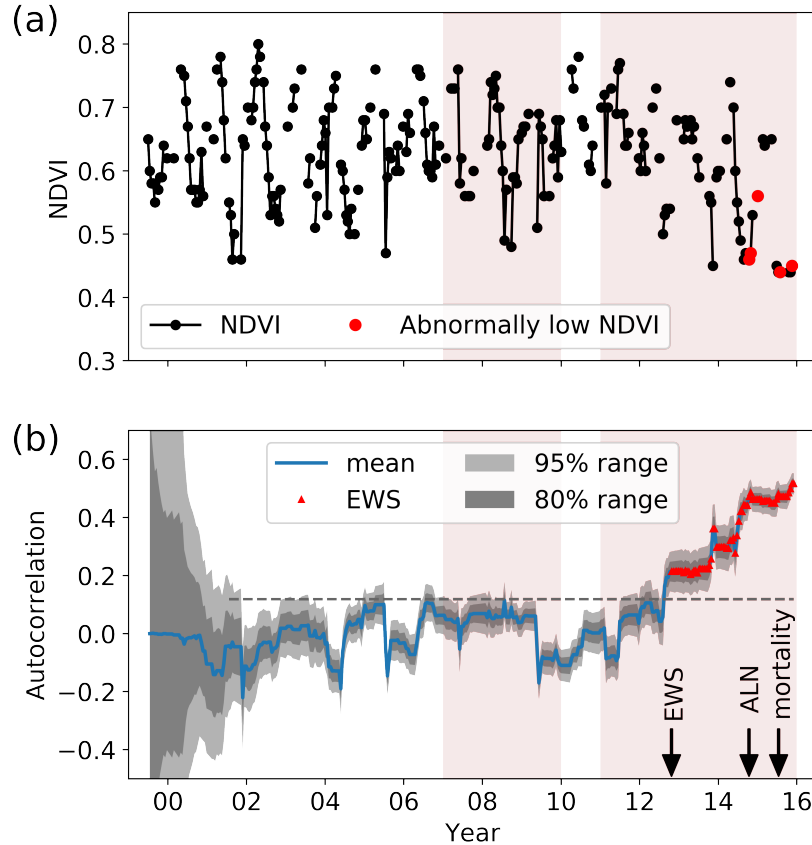
FIGURE 4.1: (a) NDVI time series of a pixel in southern Sierra, CA. Red dots represent NDVI lower than the 20th percentile after considering seasonality. (b) Mean and uncertainty range of time-varying autocorrelation estimated using DLM. Red triangles show the identified early warning signal (EWS) when the mean autocorrelation exceeds a threshold (gray dashed line), calculated as the long-term (excluding a 2-year warm-up period) average of the upper boundary of the uncertainty range. Shaded time ranges indicate the two droughts based on Palmer Drought Severity Index. "00" in the x-axis denotes January 1st, 2000.

prominent temporal correspondence highlights the potential of using low resilience as a EWS to track inter-annual variations in forest mortality.

4.3.3 Lead time of EWS

For areas where EWS was detected before the observed mortality, 75% of the cases exhibited EWS more than 6 months before mortality; 25% of the cases showed EWS more than 19 months before mortality (Figure 4.3a). When compared with detected
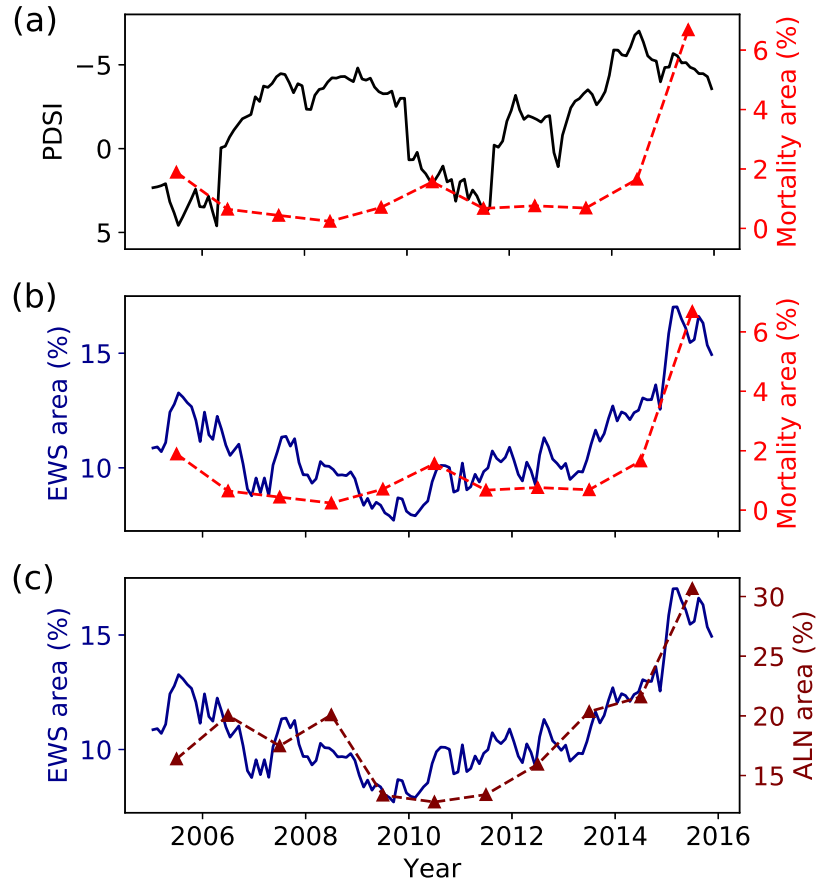
FIGURE 4.2: (a) Monthly Palmer Drought Severity Index (PDSI) (Dai et al., 2004a) for the state of California from 2005 to 2015 (black line); and fraction of area with tree mortality (red line) from annual aerial survey. (b) Fraction of areas exhibiting EWS (blue line) and with observed tree mortality (red line). (c) Fraction of area exhibiting EWS (blue line) and fraction of area with abnormally low NDVI (ALN, dark red line). "2006" in the x-axis denotes January 1st, 2006.

ALN (Figure 4.3b), EWS was identified earlier in 87% of the cases and 9 months earlier in 50% of the cases, highlighting the advantage of the resilience-based EWS over the drop in greenness to predict mortality. Among differing species, the lead time of EWS exhibited little difference with respect to mortality (Figure 4.3a) but larger difference with respect to ALN (Figure 4.3b). For example, *Juniperus* and *Quercus* experienced ALN much sooner after the first occurrence of EWS compared with *Abies* and *Pinus*, possibly due to their higher tendency to drop leaves under

stress (Limousin et al., 2012; Gaylord et al., 2013). As the mid-half of EWS can be detected between 6 and 19 months ahead of mortality, it may potentially be used to predict near-term forest mortality.
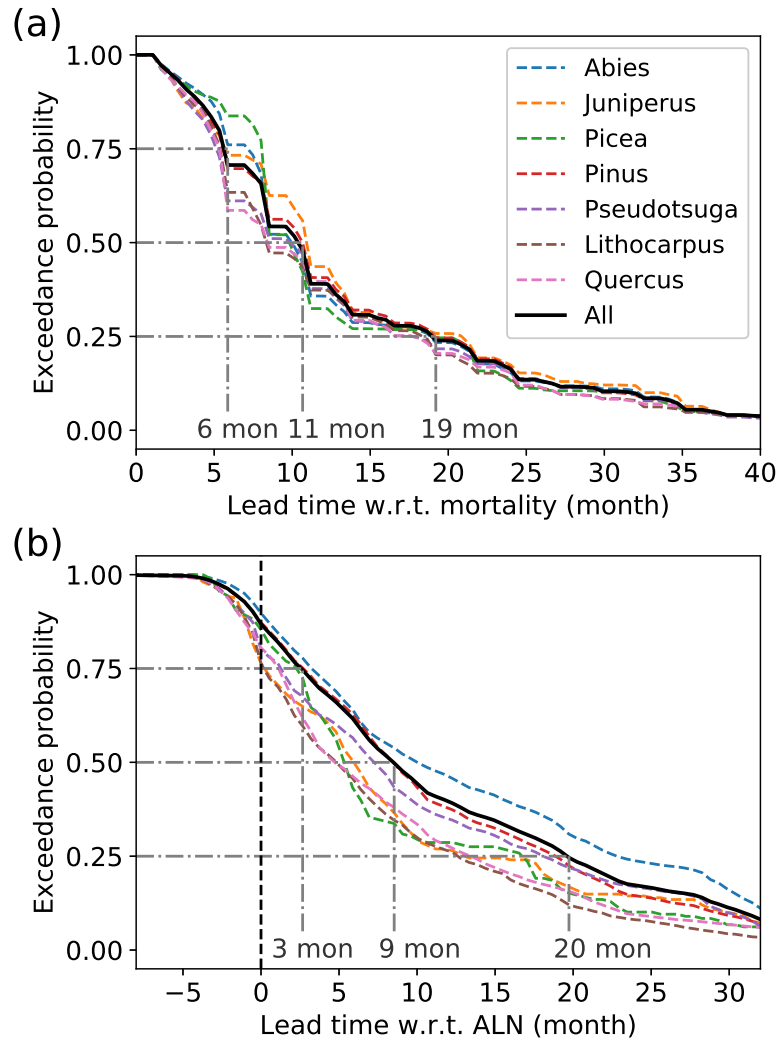
FIGURE 4.3: (a) Exceedance probability of the time difference from the first occurrence of EWS to observed mortality, when EWS is detected. For example, more than 75% of the cases had EWS 6 months earlier than the time when mortality was observed. (b) Exceedance probability of the time difference from the first occurrence of EWS to abnormally low NDVI (ALN), when EWS is detected. Black solid lines in both figures represent the entire surveyed area; colored dashed lines represent the area dominated by a major species within the surveyed area.

4.3.4 Spatial-temporal estimation and prediction

Throughout the entire study area, mortality area and ALN area in each year were positively correlated with EWS area ($p < 0.05$) (Figure 4.4a,b, black dots). However, they did not exhibit an apparent relation to the duration of EWS (Appendix C Section 4). The relation between EWS area and mortality area differed among the seven dominant species in the study area (Figure 4.4a,b, colored triangles). For example, for *Quercus* (oak), *Lithocarpus* (tanoak), *Pinus* (pine) and *Picea* (spruce), 10% of EWS area corresponded to 0.1%, 0.6%, 1.4% and 6.5% of mortality area, respectively. These differences imply that oaks are more likely to survive under low resilience than spruces and pines. The result is consistent with previous studies conducted in the western U.S., where isohydric species such as pines and spruces were found to succumb at a higher frequency during prolonged drought, possibly due to stomatal closure (Mueller et al., 2005; McDowell et al., 2008); whereas anisohydric species such as junipers and oaks experienced less mortality partly because of smaller likelihood of stomatal closure and advantages arising from adjustments of fine root density and leaf area (McDowell et al., 2008; Munné-Bosch and Alegre, 2004). Notably, the correlations between EWS area and mortality area vanished when aggregating all species together even if they were located in the same eco-climate region (Appendix C Section 4). This distinction suggests that resilience signatures are species dependent. The direct implication is that species distribution information is necessary when translating detected EWS into mortality area.

Temporally, with a zero lead time, i.e., at the same time point when mortality was observed, 96% of the interannual variation in mortality area for the entire study area was explained using species-specific quadratic functions of EWS area (Figure 4.5). For lead times of 3, 6, 9 and 12 months, i.e., using EWS area detected months earlier than observed mortality, the explanation accuracy gradually decreased to 91%, 77%,
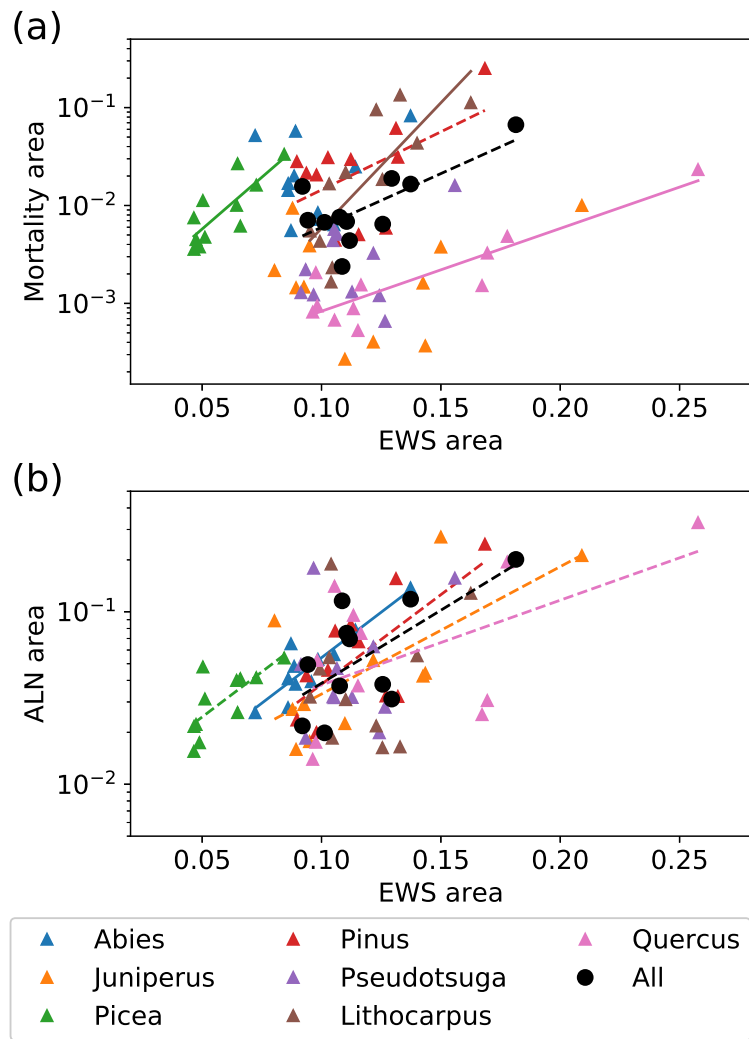
FIGURE 4.4: Species-specific relations between the fractional area showing EWS and (a) fractional areas with mortality and (b) abnormally low NDVI (ALN) across years of 2005–2015 (one dot per year). Major species covering an area greater than 1000 km^2 are plotted. Solid trend lines denote significance level of $p < 0.01$ and dashed trend lines denote significance level of $p < 0.05$. Trend lines are not plotted for species without significant relations.
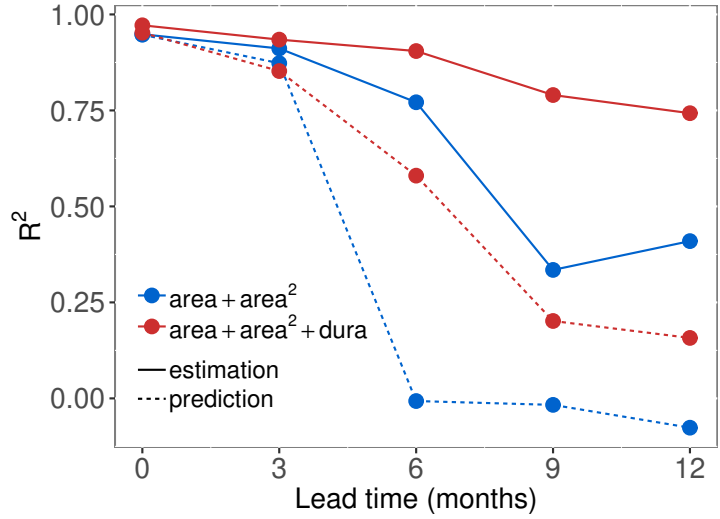
FIGURE 4.5: Temporal estimation (solid lines) and prediction (dashed lines) accuracies derived from the coefficient of determination (R^2) using EWS area only (blue), and both EWS area and duration (red) with different lead times. Estimation accuracy is computed using the regression relation obtained based on data of all years, while prediction accuracy is obtained using leave-one-out cross validation strategy.

33% and 41% respectively (Figure 4.5, blue solid line). Prediction accuracy was evaluated by excluding a year out one at a time from the regression, and evaluating mortality area for that year. Prediction accuracy was found close to the estimation accuracy for lead times smaller than or equal to 3 months, but dropped to around zero with longer lead times (Figure 4.5, blue dashed line). Additional consideration of EWS duration in the regression improved both estimation and prediction accuracies. For example, the prediction accuracy for a lead time of 6 months improved from 21% to 73%. Adding a quadratic term of EWS duration or an interaction term of EWS area and duration did not significantly improve the accuracy (Appendix C Section 5). In summary, temporal variation of mortality area can be reasonably explained and predicted by EWS area, although the accuracy decreases with longer lead times. The accuracy can be further improved by additionally considering EWS duration, especially when using lead times longer than 6 months.

Spatially, estimation accuracy of mortality was analyzed at multiple spatial reso-

lutions ranging from an eco-climate region scale to 1/2 degree, 1/8 degree and 3 km scales. As the mortality area for each pixel is highly zero-inflated, following (Young et al., 2017), mortality occurrence, i.e., whether mortality area is greater than 0.1%, and mortality intensity, i.e., the magnitude of mortality area for pixels with mortality occurrence, were modeled separately (see Methods). In addition to previously studied variables such as spatial heterogeneity in topography (Tai et al., 2017) and community competition (Young et al., 2017) that are known to influence the spatial pattern of mortality, contribution of EWS area and duration were also found to be crucial based on the Bayesian Information Criterion (BIC, Appendix C Section 5). For years from 2005 to 2015, at a spatial resolution of 1/8 degree and a 6-month lead time, the selected variables provide overall estimation accuracies of 0.89–0.93 and area under the receiver operating characteristic curve (AUC) of 0.61–0.71 for mortality occurrence, and coefficient of determination (R^2) of 0.41–0.59 for mortality intensity. The estimation performance decreases with finer spatial scale (Appendix C Section 6). For example, 69%, 57%, 53% and 47% of the spatial variation in mortality intensity can be explained at spatial scales of eco-climate region, 1/2 degree, 1/8 degree, and 3km, respectively for the median year. Such decrease could result from the larger influence of stochastic perturbation at finer scales (see Discussion), and spatial scale mismatch between polygons delineating mortality area and grids used to aggregate EWS characteristics. As the exact locations of dead trees within polygons were not identified, the difference in actual mortality occurrence and intensity among fine grids may not be seen from mortality maps. Small areas that underwent mortality may also get omitted in mortality maps (Forest Health Monitoring Program, 1999), thus undermining accuracies at fine resolutions. Notably, at a 1/8 degree resolution, compared with mortality observed in 2009 (Figure 4.6a) and 2015 (Figure 4.6d) drought years, EWS characteristics together with information on topography and community competition can capture the spatial gradient of mortal-
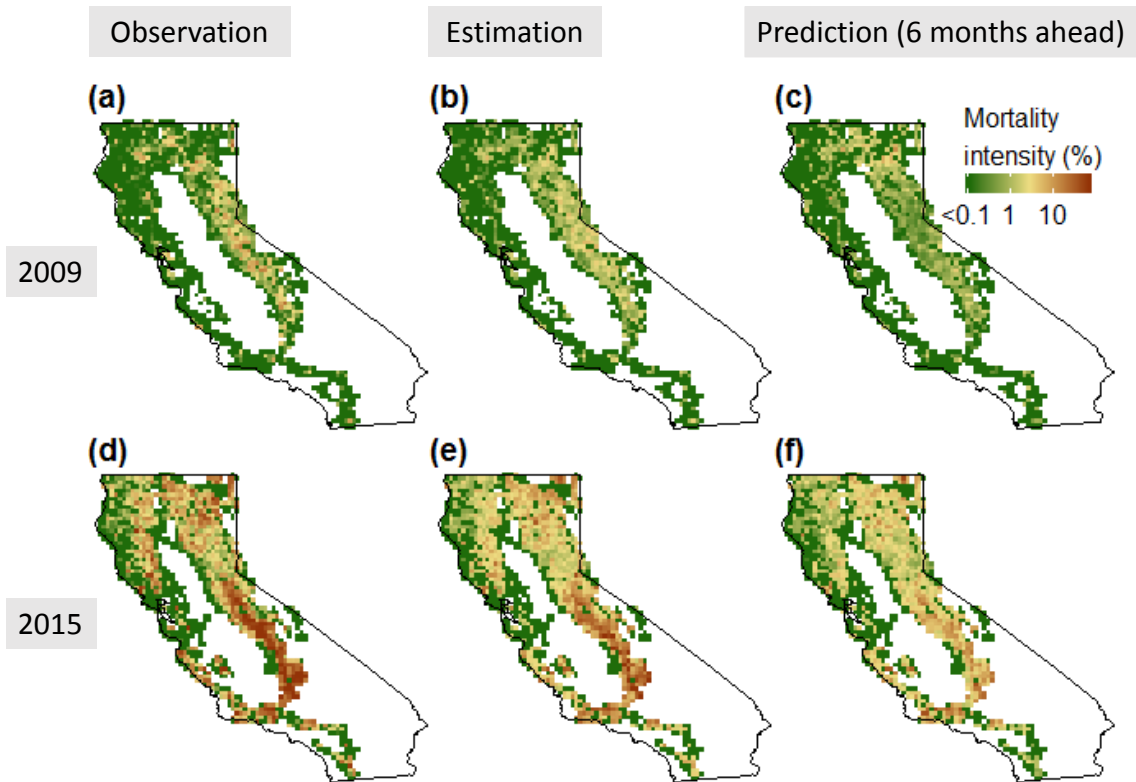
FIGURE 4.6: Observed (a, d), estimated (b, e) and predicted (c, f) mortality intensity in 2009 (a, b, c) and 2015 (d, e, f). Estimation was conducted using EWS detected with a zero lead time and prediction was conducted using EWS detected 6 months ahead. Both estimated and predicted mortality intensity was computed using a Gaussian process model considering predictors of EWS, elevation and basal area and a spatial correlation structure (see Methods).

ity within each year (Figure 4.6b, e), as well as the overall higher mortality intensity in 2015. Spatial prediction of mortality, even using EWS detected 6 months ahead of observation, showed that the overall spatial gradient and differences between the two drought years were ably captured (Figure 4.6c,f). However, mortality rates were higher than predicted in the southern Sierra and the northeast of the study area in 2015 (Figure 4.6d).

4.4   Discussion

A novel approach to detect low-resilience based EWS is proposed. The lead time of EWS and its ability to estimate and predict forest mortality are examined. Given that EWS relies on the physical phenomenon of critical slowing down near a tipping point, its detection is made possible by integrating a theoretical basis of resilience of nonlinear dynamical systems approaching a tipping point (Scheffer et al., 2009), a statistical technique for inferring time-varying autocorrelation (Prado and West, 2010), and use of ever-proliferating high spatial resolution remote sensing images of NDVI. Here the tipping point is forest mortality due to drought.

The reduction in the resilience before climate-induced mortality can also be viewed through the lens of physiological response of vegetation under stress. During drought, heat stress and water deficit deplete plant water content (Brodrick and Asner, 2017), induce malfunction of plant hydraulic system due to cavitation spread, and restrict carbon uptake and transport via stomatal closure (McDowell, 2011). These stresses could further limit the capability of plants to refill cavitated xylem and replenish carbon storage to support metabolism and growth (McDowell et al., 2011), thus handicapping the recoverability from drought. As these responses are highly diverse across time and space, in part due to nonlinear interactions between a number of physical controls such as species properties, soil and nutrient conditions, community competition and acclimation (Sala et al., 2010), significant gap exists between mortality and climate stress metrics such as climate water deficit (Anderegg et al., 2015; Young et al., 2017). In contrast, the impact of the aforementioned stressors can be expressed as a slowed recovery rate of photosynthetic capability and foliage biomass, which can be captured in NDVI dynamics (Vicente-Serrano et al., 2013). As the derived dynamic metric allows detection of low resilience directly from NDVI time series, it circumvents the uncertainties inherent in prediction of mortal-

ity based on climate stress metrics alone. Furthermore, EWS provides predictability without relying on the prediction of climate conditions given its dependence on increased autocorrelation.

While the results demonstrate the potential of EWS to capture the spatial-temporal variations in ALN and mortality over a range of parameters used to detect EWS (Appendix C Section 7) and across both snow-affected and snow-free regions (Appendix C Section 8), two major challenges are apparent. The first is the representativeness of the identified resilience signal based on autocorrelation of NDVI, which can be impaired by missing data on cloudy and snow days, and uncertainties inherent in NDVI data, such as those due to measurement error, varying atmospheric composition over time and mixed signal from understory species. The effectiveness of EWS may also be affected by autocorrelation signature in latent driving factors other than the considered climate conditions, such as local nutrient availability and biotic interactions with microbes and insects. In addition, as the relation between EWS and mortality is found to be species-specific, uncertainties in species distribution map and coexistence of multiple species may impair the accuracy in EWS. Second, and perhaps more importantly, is the influence of stochastic perturbations on vegetation stress within the lead time period and across space. While low resilience indicates a higher probability of state transition for given stochastic perturbations, mortality may still occur without reduction in resilience if climate conditions are unfavorable during the lead time and vice versa. This explains lower accuracies using EWS for longer lead times (Figure 4.5). Similarly, mortality may also intensify at locations with moderate resilience due to localized insect/pathogen attack. This in fact is noted as the major damage causal agent for 83% of forest mortality in the study area (U.S. Forest Service, 2015a). Notably such outbreaks are strongly influenced by climate-induced stresses, as limited carbon uptake and transport during drought restrict resin production, which is known to be a major defense agent against bi-

otic attack (Sala et al., 2010; McDowell, 2011; Novick et al., 2012). The increase in plant susceptibility further promotes insect/pathogen population (Gaylord et al., 2013). While these perturbations reduce the prediction accuracy of EWS for mortality, given their general dependence on climate-induced stresses, the influence is smoothed out at coarser scales, resulting in a robust relation between low resilience and mortality.

Future effort may seek to improve prediction with long lead times and fine spatial scales by combining EWS with predicted climate conditions, hydrological states, and knowledge of insect/pathogen habitation and mechanisms of infestation initiation and propagation during the lead time period. EWS based predictions can also benefit from more accurate data of species distribution, tree density and basal area. Notably, the lead time of EWS with respect to ALN and mortality mostly lies within two years (Figure 4.3), similar to the time scale of recovery from drought (Schwalm et al., 2017). Such consistency in time scales implies comparable probabilities of reaching full recovery or mortality starting from a stressed state. Further inquiry into the physiological controls on low resilience and their evolvement to eventual recovery or mortality are necessary. Investigation in this regard may involve comparison of the low resilience signal with physiological metrics observed either *in situ*, such as plant water potential and stomatal conductance, or from remote sensing, such as plant water content (Brodrick and Asner, 2017) and solar-induced chlorophyll fluorescence (Walther et al., 2016). Improved understanding of physiological controls on reduced resilience will facilitate prediction of abrupt changes in vegetation cover. Despite the aforementioned challenges, the results point toward significant opportunities ahead given the apparent spatial and temporal associations between the detected EWS and actual mortality. The lead time of EWS will allow forest managers to assess resource risks, and possibly prescribe approaches to mitigate insect and fire risks, and restore stand health through prescribed burning, variable density thinning, and altering age

structure and species composition (Churchill et al., 2013; Hessburg et al., 2016). The presented framework can potentially be used for live monitoring of forest health under drought (Trumbore et al., 2015), and near-term prediction of climate-induced mortality in most forested regions of the world.

<div align="right">

5

</div>

Influence of plant hydraulics on evapotranspiration

5.1 Introduction

The significance of plant responses to water stress is not in dispute when evaluating water, carbon and energy exchanges between the biosphere and the atmosphere (Vicente-Serrano et al., 2013; Settele et al., 2014). How to represent these responses continues to draw research attention and frames the scope of this study. Guided by plant functional types (PFTs), most current Earth System Models (ESMs) empirically restrict transpiration with reduced root-zone soil moisture based on limiting functions assigned to each PFT (Wullschleger et al., 2014). Partial support for this representation is provided by elementary physiological principles. Guard cells controlling stomatal aperture respond to leaf water potential, an 'internal' state representing the integrated outcome of soil-plant hydraulics, which in turn responds to root-zone soil moisture. Two implicit assumptions embedded in the empirical representation are: (1) variation of leaf water potential is surrogated to variation of root-zone soil moisture, and (2) a set of plant hydraulic traits (HTs) based on PFT are sufficient to capture water use strategies under stress across various biomes.

However, given the large variability in HTs (Anderegg, 2015; Franks et al., 2018) and nonlinear co-variation in the dynamics of soil moisture and leaf water potential (Sperry et al., 2002, 2016), the empirical representation commonly used to estimate evapotranspiration (ET) is expected to lead to significant biases (Franks et al., 2018; Anderegg et al., 2017; Trugman et al., 2018). These errors can be propagated into the estimation of the overall carbon sink strength of ecosystems, water resources available for groundwater and streams, and energy partitioning between sensible and latent heat fluxes that could impact the extent of heat stress during drought (Konings et al., 2010, 2011; Manoli et al., 2016). Aforementioned limitations highlight the need for improved model representation of transpiration that integrates the regulation of plant hydraulics on stomatal kinetics.

Studies investigating the roles of plant hydraulics on evapotranspiration have been scarce. This is in part due to the scarcity of HT measurements, their cross- and within-species variability (Anderegg, 2015), and the gap between the scales at which HTs are measured and used for predictions. To address these challenges, this chapter uses a model-data fusion (MDF) approach to obtain the most likely HTs that yield results consistent with observations at a stand scale. Based on the estimated HTs, a plant hydraulics model is parameterized and compared with a widely used empirical stomatal conductance model (without plant hydraulics) to evaluate its impact on evapotranspiration across land cover and climate types.

5.2   Methods

5.2.1   Soil-plant continuum model

A soil-plant continuum model adapted from (Liu et al., 2017) is used here to estimate soil evaporation and plant transpiration by solving energy balance on the soil and leaf surfaces respectively (Campbell and Norman, 1998). Two different configurations of stomatal conductance, a key for estimating transpiration, are considered. The two

configurations are an empirical model (Oren et al., 1999) and a hydraulics model (Katul et al., 2009a; Manzoni et al., 2011; Liu et al., 2017). In the empirical model,

$$g_s = g_{s,ref}(1 - m \log(D))\beta(\theta) \tag{5.1}$$

where g_s is stomatal conductance; $g_{s,ref}$ is the reference stomatal conductance under VPD = 1 kPa; m is the sensitivity of g_s to VPD (D). $\beta(\theta) \in [0,1]$ is a piecewise linear function representing soil moisture limitation that has been widely used in ESMs (Trugman et al., 2018).

$$\beta(\theta) = \frac{\theta - \theta_w}{\theta* - \theta_w}, \text{ if } \theta_w < \theta < \theta* \tag{5.2}$$

In the hydraulics model, the stomatal conductance is calculated by optimizing the net carbon gain (Katul et al., 2009a).

$$g_s = \text{argmax } f_c(g_s) - \lambda f_e(g_s) \tag{5.3}$$

where f_c and f_e are carbon gain and water loss per leaf area respectively. The marginal water use efficiency λ responds to leaf water potential (ψ_l):

$$\lambda(\psi_l) = \lambda_{WW} \exp(b_0 \psi_l) \tag{5.4}$$

where λ_{WW} is the marginal water use efficiency under a well-watered condition; and b_0 denotes the sensitivity of λ to ψ_l. ψ_l is controlled by plant water transport through the hydraulics system from root to leaf (Sperry et al., 2017).

$$Tr = \int_{\psi_r}^{\psi_l} g_p(x)dx \tag{5.5}$$

where Tr is transpiration per ground area; ψ_r is root water potential; and g_p is xylem conductance following a vulnerability curve:

$$g_p(x) = g_{p,max} \left[1 + \left(\frac{x}{\psi_{50}}\right)^a\right]^{-1} \tag{5.6}$$

where $g_{p,max}$ is the maximum xylem conductance; ψ_{50} is the plant water potential corresponding to 50% loss of percentage loss of conductivity (PLC); and a is the shape parameter of the vulnerability curve.

Next, the connection between the empirical model and the hydraulics model is elaborated. Under light-saturated condition, solution of Equation (5.3) can be linearized (Katul et al., 2009a) as below

$$g_s = \alpha \left[-1 + \left(\frac{c_a}{a_0 \lambda(\psi_l)} \right)^{1/2} D^{-1/2} \right] \tag{5.7}$$

where α contains parameters describing biochemical demand for CO_2 (Farquhar et al., 1980); c_a is atmospheric CO_2 concentration; $a_0 = 1.6$ is the relative diffusivity of water vapor with respect to CO_2. The sensitivity of g_s to VPD is reflected in the term $D^{-1/2}$, which can be expressed using a Taylor series expansion (Katul et al., 2009b):

$$D^{-1/2} = 1 - \frac{1}{2} \log(D) + O(\log^2(D)) \tag{5.8}$$

Combining Equations (5.7) and (5.8),

$$\frac{g_s}{g_s(D=1)} \approx 1 - \frac{1}{2} \frac{\Phi}{\Phi - 1} \log(D) \tag{5.9}$$

where

$$\Phi = \left(\frac{c_a}{a_0 \lambda(\psi_l)} \right)^{1/2} \tag{5.10}$$

The term $\Phi/(2(\Phi-1))$ is equivalent to the m parameter in Equation (5.1), describing the sensitivity of g_s to VPD. Note that although m is static, $\Phi/(2(\Phi-1))$ varies with ψ_l.

5.2.2 Datasets

The soil-plant continuum model is applied at Duke Forest (US-DK3) and other 24 FLUXNET sites (FLUXNET, 2016) across the globe (Table 5.1). The sites are selected based on the availability of soil moisture, ET, and meteorological data for at least two years. Furthermore, transpiration at these sites accounted for at least half of the total ET. ET observations only during the growing season and days with no precipitation and temperature higher than 0 °C are used. April to October and November to March are considered as the growing seasons for sites in the Northern Hemisphere and the Southern Hemisphere respectively. These data filtering criteria allow robust estimation of model parameters and limit uncertainty introduced by large soil evaporation, snow cover, and understory species. Data needed to parameterize the model include plant hydraulic traits, soil properties, leaf area index, canopy height, and rooting profile. Plant hydraulic traits and soil properties are retrieved using Markov Chain Monte Carlo (MCMC, Section 5.2.3). Other information is obtained as described in Appendix B. It is noted that improved datasets of canopy height (Healey et al., 2015) and maximum rooting depth (Fan et al., 2017) are used.

5.2.3 MCMC sampling

The parameters of $g_{s,ref}$, m, θ_w and θ^* for the empirical model, and the hydraulic traits of λ_{WW}, b_0, $g_{p,max}$, ψ_{50}, and a are retrieved using a Markov Chain Monte Carlo (MCMC) method. In addition, for both models, constant soil moisture is used as the boundary condition ($soil_{bc}$) of the soil column containing roots. The constant boundary soil moisture can be a result of groundwater, which has been shown to regulate the maximum rooting depth used in this study across biomes (Fan et al., 2017). This boundary condition, together with the nonlinearity parameter in soil water retention curve ($soil_b$)(Clapp and Hornberger, 1978) are also estimated using

Table 5.1: Locations and plant functional types (PFTs) of the FLUXNET sites used in this study. PFTs of the sites include evergreen broadleaf forests (EBF), mixed forests (MF), evergreen needleleaf forests (ENF), croplands (CRO), and grasslands (GRA).

Site ID	Latitude	Longitude	PFT
AU-Wac	-37.43	145.19	EBF
AU-Wom	-37.42	144.09	EBF
BE-Vie	50.31	5.99	MF
CA-SF1	54.48	-105.82	ENF
CH-Oe2	47.29	7.73	CRO
CN-Din	23.17	112.54	EBF
CN-Qia	26.74	115.06	ENF
DE-Hai	51.08	10.45	DBF
DE-Obe	50.79	13.72	ENF
DK-Sor	55.49	11.64	DBF
FI-Hyy	61.85	24.29	ENF
FR-Gri	48.84	1.95	CRO
IT-Isp	45.81	8.63	DBF
IT-PT1	45.20	9.06	DBF
IT-Ren	46.59	11.43	ENF
NL-Hor	52.24	5.07	GRA
NL-Loo	52.16	5.74	ENF
RU-Fyo	56.46	32.92	ENF
US-Blo	38.90	-120.63	ENF
US-Me2	44.45	-121.58	ENF
US-MMS	39.32	-86.41	DBF
US-NR1	40.03	-105.55	ENF
US-UMB	45.56	-84.71	DBF
US-UMd	45.56	-84.70	DBF

MCMC. MCMC allows consideration of uncertainties associated with deep-layer soil water availability and influence of macro-pores on soil conductivity and soil-root conductance.

MCMC is used to systematically retrieve probability distributions of effective HTs and soil properties at each of the target sites. Observations in a normal year and a dry year are used for retrieval as the immediate focus is on evaluate parameterizations during moisture stress periods. Here a normal year is considered to be

one when both annual soil moisture and VPD are within the 25th and 75th percentiles. A dry year is when the annual soil moisture falls below the 25th percentile and VPD is higher than the 75th percentile. For the MCMC, a flat prior distribution from possible HT ranges based on meta-analysis (Kattge et al., 2011) are provided. A uniform distribution between the wilting point and the full-saturation is used as the prior for soil boundary condition. A Gaussian prior of $soil_b$ is used, with the mean and standard deviation from (Clapp and Hornberger, 1978) for the corresponding soil texture at each site. Each observation of daily ET is treated as independent and identically distributed, following a Gaussian distribution with a modeled mean and an unknown variance that is to be estimated. Starting from a set of random guesses, MCMC chains explore the parameter space following the Adaptive Metropolized Independence Sampling (AMIS) method with parallel tempering. This method is used to tackle the two key challenges in the context of plant hydraulic response to stress, i.e., strong model nonlinearity and equifinality (Manzoni et al., 2013). The AMIS algorithm has been shown to mix efficiently under the presence of model nonlinearity (Ji and Schmidler, 2013). The parallel tempering module facilitates identification of multi-modes in the parameter space associated with equifinality. Twenty independent MCMC chains are used for each site. Within- and among-chains convergence is diagnosed by Geweke and Gelman-Rubin values (Brooks and Gelman, 1998). The converged MCMC chains provide joint estimates of HTs and soil properties. In addition, physiological constraints from meta-analysis (Anderegg et al., 2017; Martin-StPaul et al., 2017) are also incorporated in the statistical inference to avoid unrealistic combinations of HTs that nevertheless match data.

5.2.4 *Parameter identifiability and model evaluation*

Retrieved HTs representing effective traits at the stand-scale are compared with available measurements at a segment-scale. The identifiability, i.e., the extent to which the marginal posterior distribution of each parameter can be constraint (relative to its prior range) by ET observation is also analyzed. The identifiability of each parameter $(I(\eta))$ is quantified as

$$I(\eta) = 1 - \frac{p_{75}(\eta|y) - p_{25}(\eta|y)}{p_{75}(\eta) - p_{25}(\eta)} \tag{5.11}$$

where $p_{75}(\eta|y)$ and $p_{25}(\eta|y)$ are the 75th and 25th percentiles of the retrieved posterior distribution for each parameter η; and $p_{75}(\eta)$ and $p_{25}(\eta)$ are the 75th and 25th percentiles of the prior distribution, which is equivalent to half of the prior range given the uniform prior distribution. Hence $I(\eta) = 1$ corresponds to point posterior and $I(\eta) = 0$ indicates a posterior close to the uniform prior.

Samples of parameters from the retrieved posterior distribution are used to parameterize both models to estimate ET over the entire record period for the studied sites. Performances of the empirical model and the hydraulics model are compared.

To further inquire about the impact of incorporating plant hydraulics in ET estimation, two scenarios are considered: a well-water scenario where the soil is kept saturated and a reference VPD scenario where VPD is kept as a constant of 1 kPa. Note that in the second scenario, only the restriction term of VPD on g_s is kept constant, whereas the atmospheric demand varies as the observation. The difference of ET under real soil moisture and VPD stress from these two presumed scenarios (Δ ET) indicate how much ET is restricted by each of the two hydro-climatic stresses. Taking advantage of the consistency between the two models as shown by Equations (5.1) and (5.9), the sensitivity of g_s to VPD under different regimes represented by the two models are also compared.

5.3 Results

5.3.1 Identification of plant hydraulic traits

To evaluate the model efficacy in identifying HTs, the estimated ψ_{50} for a given site is compared to available measurements for the same species. Results for Duke Forest (US-DK3) (Figure 5.1) illustrates that provided with a wide prior range of ψ_{50}, the MDF approach identifies a posterior distribution that represents an integrated property of the stand and is located within the range of ψ_{50} measured for leaves, branches, trunks and roots (Johnson et al., 2016). For sites such as IT-Lav and IT-PT1, the retrieved distribution of ψ_{50} is consistent with measurements (mostly at branches) for the dominant species (Figure 5.2). For US-Me2, dual-modes of the posterior distribution is identified, consistent with the measured values for the two dominant species, *Pinus ponderosa* ($\psi_{50} = -2.65$ MPa (Anderegg et al., 2018) or -3.92 MPa (Martin-StPaul et al., 2017)) and *Calocedrus decurrens* (-7.75 MPa (Anderegg et al., 2018)). As suggested by the flat posterior distributions, ψ_{50} is less identifiable at other sites. This indicates low sensitivity of ET to ψ_{50}, in part because ET is mostly regulated by soil-root conductance and stomatal kinetics in the model. Plants at these sites operate with near-zero percentage loss of conductivity (PLC), thus leading to a minimal constraint of xylem conductivity on transpiration. In addition, co-existence of multi-species with a wide variety of HTs, such as at US-Blo, could also contribute to low identifiability of ψ_{50}.

Figure 5.3 shows the identifiability of all the parameters retrieved using MDF. Given that MDF estimates the parameters through comparison between the modeled and observed ET, high identifiability also suggests high sensitivity of ET to a given parameter. It is to be noted that the choice of the prior range of each parameter affects the magnitude of identifiability (Equation (5.11)). However, as the prior range covers all possible values of each parameter, the identifiability measures to what
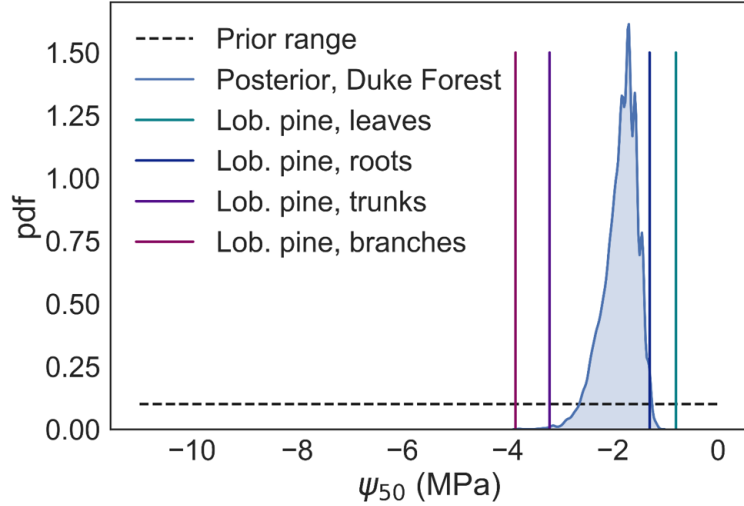
FIGURE 5.1: Estimated posterior distribution (shaded blue area) of stand-scale ψ_{50} at Duke Forest (US-DK3). The black dashed line denotes the prior range provided for parameter retrieval. Colored vertical lines denote the measured ψ_{50} at different segments for the dominant species of Loblolly Pine at the site (Johnson et al., 2016).
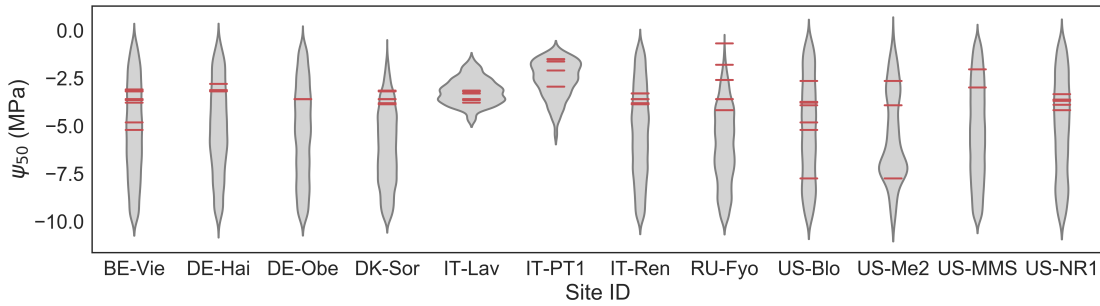
FIGURE 5.2: Estimated posterior distribution (shaded gray area) of stand-scale ψ_{50} and comparison with available measurements (red lines) for multiple species at the corresponding sites (Anderegg et al., 2018).

extent that the parameter can be narrowed down from its possible range using MDF. Although the identifiability varies across sites, the stomatal properties are generally more identifiable than the xylem properties (Figure 5.3). The marginal water use efficiency under well-watered condition (λ_{WW}) is found to be the most identifiable from observed ET, while the shape parameter of the vulnerability curve (a) is the least identifiable. This could be because that λ_{WW} always controls gas exchange,

whereas the shape of the vulnerability curve plays a role in less fraction of time mostly under stressed conditions. Notably, ET is found to be equivalently or more sensitive to the soil hydraulic properties than to the xylem properties. This highlights the need for quantifying subsurface properties and uncertainties, as misspecification could result in biased estimates of gas exchanges in spite of accurately measured plant traits.
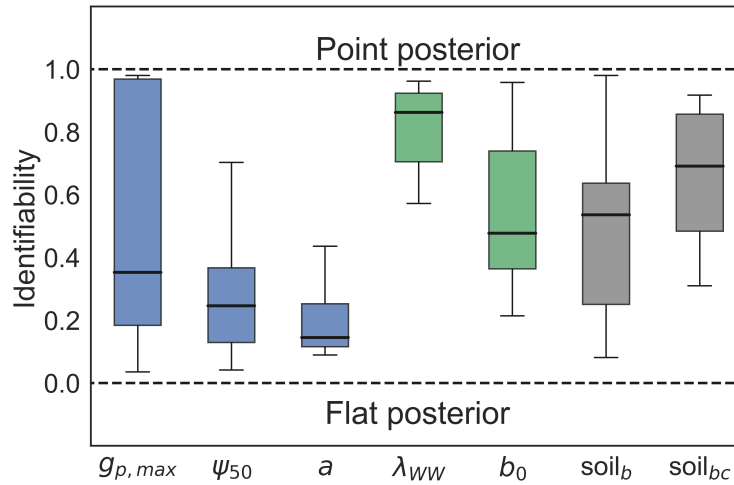
FIGURE 5.3: Identifiability of model parameters, defined as Equation (5.11). The boxes represent the variation of parameter identifiability across the studied sties. Blue, green and grey boxes denote xylem, stomatal and soil parameters, respectively.

PFT-based parameterization is widely adopted in ESMs. However, large variation of HTs exists within the same PFT, which exceeds between-PFT variation for most traits (Figure 5.4). Such variation could originate from xylem structure, phenological traits, and water use strategies of different species or the same species but acclimating to different environmental conditions. At a stand scale, maximum xylem conductance per unit ground area ($g_{p,max}$) can vary by orders of magnitude with sapwood area and stand density. In addition, the integrated HTs dictating plant water use can also be altered by site-specific interactions of competition and coordination among plants. The recognized large variation of HTs at a stand scale within each PFT

highlights uncertainties embedded in biosphere-atmosphere interactions estimated using PFT-based parameterization.
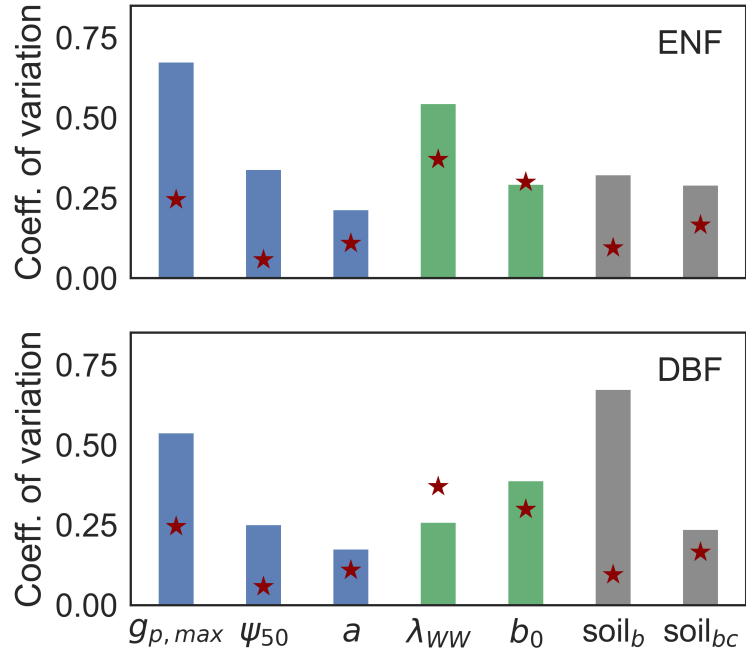
FIGURE 5.4: Coefficient of variation for plant hydraulic traits and soil parameters at sites of evergreen needleleaf forest (ENF) and deciduous broadleaf forest (DBF). Blue, green and grey bars denote xylem, stomatal and soil parameters, respectively. Red stars denote between-PFT difference of each trait, calculated as the difference between the means of each PFT normalized by the standard deviation across both PFTs.

5.3.2 Effect of plant hydraulics on ET estimation

Based on the optimally parameterized hydraulics and empirical models, daily ET across the studied sites can be captured by both models with similar R^2 ranging from 0.39–0.90 (Figure 5.5, black dots). However, when only focusing on the high-VPD periods, i.e., days with VPD greater than its 75th percentile, the empirical model does not capture ET variation as suggested by low R^2 and high RMSE values (Figure 5.5, red dots). The hydraulics model, however, shows significantly better performance for these sites during the high-VPD periods. Both models exhibit close

performance during the low-VPD periods, as suggested by low and similar RMSE values (Figure 5.5, blue dots). Such difference in model performance during the sub-periods indicates that in an empirical and a hydraulic model representation, ET responds differently to the two sources of stress, i.e., soil moisture and VPD. The impacts of these two sources of stress on stomatal conductance and ET are further analyzed in Section 5.3.3.
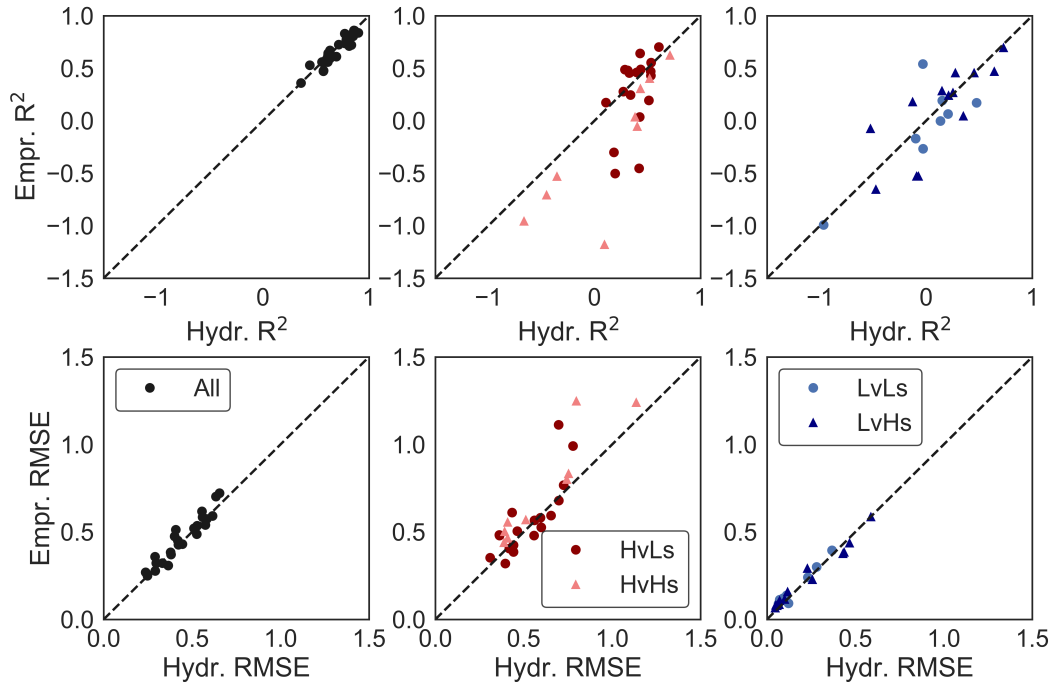
FIGURE 5.5: Coefficient of determination (R^2, first row) and root mean square error (RMSE, second row) of estimated daily ET using the empirical model (y-axis) and hydraulics model (x-axis). Model performance is evaluated over the entire growing season (black dots), high VPD low soil moisture period (HvLs), high VPD high soil moisture period (HvHs), low VPD low soil moisture period (LvLs), and low VPD high soil moisture period (LvHs). The high VPD low soil moisture period only includes days with soil moisture lower than its 25th percentile and VPD higher than its 75th percentile. Similar criteria are used for other sub-periods.

5.3.3   Restriction of hydro-climatic stresses on ET

Compared to scenarios with saturated soil and reference VPD of 1 kPa respectively, for most sites, the hydraulics model suggests less soil water limitation but greater

VPD limitation on ET than the empirical model (Figure 5.6). Although both models capture the overall ET variation, the stomatal response to the two stress sources is different. In the empirical model, the VPD sensitivity (m in Equation (5.1)) is estimated as 0.63 on the average across the studied sites (Figure 5.7), consistent with the range of 0.4–0.8 estimated in previous studies (Oren et al., 1999; Novick et al., 2016). In the hydraulics model, the equivalent sensitivity to VPD (Equation (5.9)) under medium soil moisture (between the 25th and 75th percentiles) is found to be higher, with an average value of 1.17. Note that this VPD sensitivity is considered static for each site in the empirical model. In the hydraulics model, however, it increases with decreasing leaf water potential (Equations (5.9) and (5.10)). Thus during drought when leaf water potential reduces in response to low soil moisture, stomata would close more in response to VPD. On the average of the studied sites, the equivalent VPD sensitivities across sites increase from 0.82-1.44 when soil moisture is between 25th and 75th percentiles to 0.83-2.30 when soil moisture drops below its 25th percentile, respectively. Lacking such down-regulation mechanism of plant hydraulics on VPD sensitivity, the empirical model could result in errors in ET estimation during high-VPD period especially under low leaf water potential, or equivalently, high PLC. Across the studied sites, the hydraulics model improves ET estimation during high VPD low soil moisture period most significantly at the sites with large difference in VPD sensitivities and high PLC (Figure 5.8).

5.4   Discussion

The chapter implements a model data fusion framework to estimate plant hydraulic traits at a stand scale, bridging the gap between measurements at a segment scale and a stand or larger scale relevant to land-atmosphere interactions. As large variation of traits exist within each PFT, the framework developed here could facilitate better parameterization scheme of ESMs by integrating models with cross-scale observations
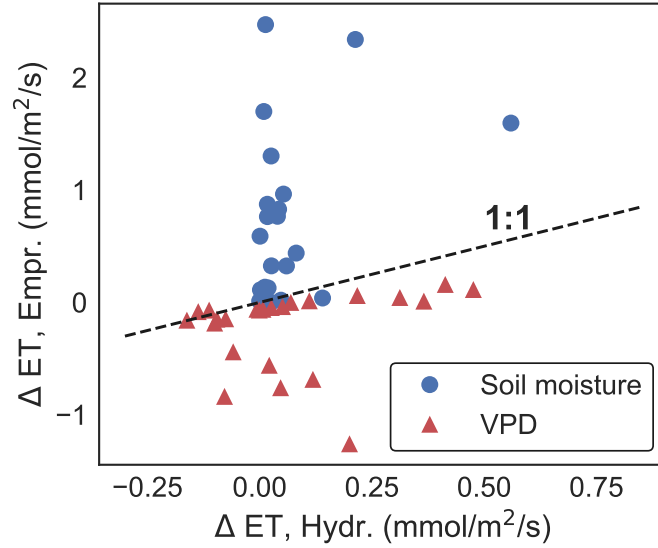
FIGURE 5.6: Average ET restricted by soil moisture (blue dots) and VPD (red triangles) as estimated by the empirical model (y-axis) and the hydraulics model (x-axis). The restricted ET is calculated as the ET under the presumed scenario minus ET under observed soil moisture and VPD. The scenarios to calculate soil moisture restriction is provided with saturated soil moisture, and that to calculate VPD restriction is provided with a constant VPD of 1 kPa for evaluation of stomatal conductance.
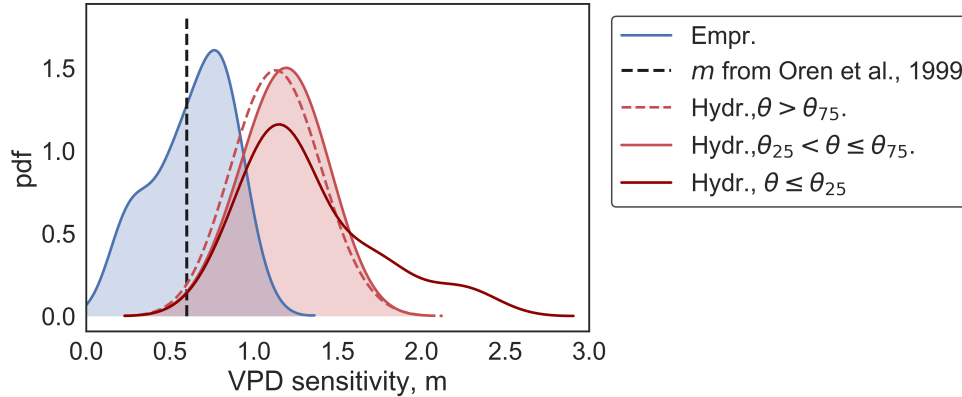
FIGURE 5.7: Distribution of VPD sensitivity from the empirical model (parameter m in Equation (5.1)) across studied sites (blue shaded area). Distribution of VPD sensitivity from the hydraulics model (Equation (5.9)) when soil moisture is above its 75th percentile ($\theta > \theta_{75}$, red dashed line), between its 25th and 75 percentiles ($\theta_{25} < \theta < \theta_{75}$, red shaded area), and below its 25th percentile ($\theta < \theta_{25}$, red solid line).
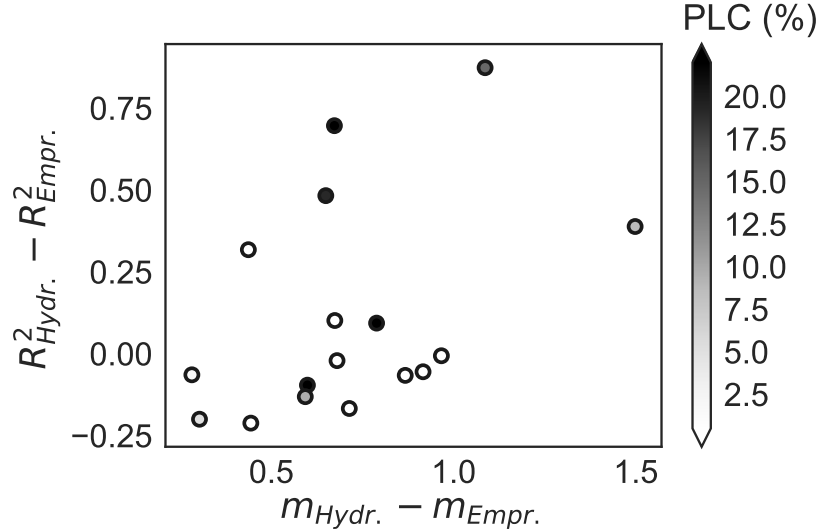
FIGURE 5.8: Relation between the improved ET estimation accuracy by the plant hydraulics model ($R^2_{Hydr.} - R^2_{Empr.}$) and the difference between the VPD sensitivities estimated the hydraulics and empirical models ($m_{Hydr.} - m_{Empr.}$) during high VPD and low soil moisture period across sites. Each dot is color-coded with the average percentage loss of conductivity (PLC) at the site.

(Konings and Gentine, 2017; Konings et al., 2017).

Although significant efforts have been made in the past to evaluate the influence of plant traits on water use, soil properties are found to play equally or more important roles in estimating ET. Through soil-root interaction and deep-layer water supply, the effect of soil hydraulics could mask out the signatures of plant traits on water use and hence ecosystem productivity, especially during droughts when soil-root interaction becomes highly nonlinear and deep-layer water provides major supply for transpiration. Hence quantification of subsurface properties and hydrologic conditions is needed to provide a refined description of ecosystem fluxes and its response under stress.

Despite that ET simulations from both optimally parameterized empirical and hydraulics models fit well to the data, they prescribe different sensitivities to hydroclimatic stresses. Overall, the hydraulics model exhibits a higher sensitivity of stom-

atal conductance to VPD, which implies that the impact of increasing temperature and thus VPD on restricting ecosystem water use and productivity can be underestimated if not considering plant hydraulics. The even stronger down-regulation mechanism of VPD under soil water stress, and the fact that leaf water potential variation cannot be fully resolved by soil moisture variation further underscores the need for accurate measurement of HTs. Aforementioned discrepancies also highlight the need to improve the mechanistic representation of plant hydraulics in ESMs to unravel and predict ecosystem responses to future climate.

It is acknowledged that limitations exist in both models. For example, deep-layer soil moisture is represented using a lumped bucket model due to lack of observations. Relevant processes and controls including lateral soil water flux, groundwater access, hydraulic redistribution, plant water storage, and vertical canopy structures are not considered in the models. In addition, rooting profile and biochemical properties are parameterized based on meta-analyses with combinations of PFT and climate type without considering site-specific variations. These uncertainties could contribute to systematic errors in ET estimates using both models. However, the parsimonious representation allows effective retrieval of stand-scale traits even under the challenge posed by strong model nonlinearity. Further studies are needed to quantify the aforementioned factors and evaluate their impacts on biosphere-atmosphere interactions.

6

Conclusions

The main results and implications of each chapter are summarized as follows. Directions for future work are also highlighted.

6.1   Summary of results

Chapter 2. Meteorological controls on wetland groundwater dynamics

The goal of this chapter was to analyze the interannual variation of wet-period in forested wetlands of the southeastern US, and how it is affected by the seasonality of meteorological conditions. The results show that,

(1) The start date and duration of wet-periods exhibit significant interannual variations. Among the ten studied wetlands, the start date could be as early as September or as late as March, and the wet duration could vary by more than 6 months. As multiple ecological functions of wetlands such as greenhouse gas emissions are influenced by wet-periods, it is expected that the ecological functions of wetlands can also vary significantly through the years.

(2) The annual meteorological conditions could only capture 20%–50% of the

variations in wet-period characteristics, which, however, can be improved to 60%–90% using seasonal precipitation and potential evapotranspiration. Limited ability of annual variables to explain interannual variations in wet-period characteristics can be attributed to nonuniform influence of seasonal meteorological conditions on wet-period variations. In the studied wetlands, meteorological conditions in autumn were identified to be the most dominant in influencing wet-period variations. This is expected to be true for other forested wetlands in the southeastern US, as hydro-climatology in the region is characterized by autumn and winter that act as recharge periods. The results also indicate that for future predictions of wet-period characteristics and associated ecological functions, robust projections of meteorological conditions at least in the dominant seasons are paramount.

(3) Estimation accuracy of wet-periods was improved when in addition to the four seasons within a hydrologic year, meteorological conditions in an antecedent season were also considered. This highlights that inherent hydrologic memory of the wetlands should be appropriately accounted for while estimating and predicting interannual wet-period variations.

(4) In the studied wetlands, errors for predicting start date and wet duration were less than 1 month at a 90% confidence level, indicating that the Bayesian regression and variable selection framework provides an effective approach to predict interannual wet-period variations. By pairing it with short-term observation experiments, the presented framework could potentially be applied to evaluate long-term variations in wetland ecological functions.

This chapter highlights an undeniable influence of seasonality and hydrologic memory on wet-period variations of inland forested wetlands. The presented framework provides a simple, yet effective, approach for estimating and predicting wet-period variations in inland wetlands. The approach can also contribute to estimating variations in associated ecological functions in wetlands.

Chapter 3. Effects of long-term climate trends on forest mortality risk

The goal of this chapter was to develop a soil-plant-atmosphere continuum model and a metric that captures dominant plant physiological dynamics related to mortality, and evaluate how mortality risk responds to long-term changes in multiple climate conditions. The main findings are as follows:

(1) The mortality risk quantified as the fraction of time when plant operates with water potential below a critical threshold or stomatal closure is able to capture the mortality probability documented at multiple sites across plant functional types and climate regimes.

(2) Based on projected climate for the mid of 21st century, warming temperature and shifting precipitation patterns, including annual amount and seasonality, could intensify the mortality risk by 159% on the average of the studied biomes. However, such increase extent can be largely alleviated to 21% by concurrent increasing atmospheric CO_2 concentration and specific humidity.

(3) As a result of disparity in hydraulic traits, the risk sources for evergreen needleleaf forests and deciduous broadleaf forests are mainly stomatal closure and hydraulic failure, respectively. As stomatal closure risk is found to be more sensitive to temperature increase, mortality risk of evergreen needle leaf forests under projected climate is expected to increase more than other plant functional types.

This chapter provides a mechanistic foundation for evaluating future responses of forest mortality risk. The results highlight that ignoring the influence of elevated atmospheric humidity and CO_2 concentration may lead to overestimation of future forest mortality risk. It is also found that the combined influence of changes in the studied climate variables on mortality risk is strongly mediated by plant hydraulic traits. These findings will facilitate decisions about intervention and management of different forest types under changing climate.

Chapter 4. Detection of early warning signal of forest mortality

The goal here was to establish a framework to assess time-varying resilience of forests from high-resolution Normalized Difference Vegetation Index (NDVI), and evaluate spatial-temporal association between early warning signal, i.e., abnormally low resilience, with observed forest mortality during 2005–2015 in the state of California, USA. The main results and implications are summarized below:

(1) Inter-annual variation of forest area that underwent mortality was not directly associated with drought severity in the study area. Instead, it exhibited a temporal pattern similar to that of the area exhibiting low resilience or EWS. The EWS area is generally larger than mortality area, indicating some trees operated under low resilience without loss of life. The prominent temporal correspondence with EWS highlights the potential of using low resilience as a EWS to track inter-annual variations in forest mortality.

(2) For most of the cases where EWS was detected before observed mortality, EWS can be detected 6 to 19 months ahead of mortality. Notably, for 87% of the cases, EWS can be detected ahead of reduced greenness as reflected by NDVI. This result highlights the advantage of EWS to predict mortality before symptoms of leaf-shedding or canopy dieback occur, thus facilitating necessary resource and risk management practices.

(3) The temporal variation of EWS area for different species exhibited distinct relations with mortality area for, suggesting that the resilience signature are highly species specific. The direct implication is that species distribution is necessary for translating detected EWS into mortality risk.

(4) Based on the species-specific relations, EWS captures the spatial-temporal variation of mortality. The prediction accuracies reduce as the lead time increases and spatial resolution refines. Such decline in performance could result from larger uncertainties in stochastic perturbations, including hydro-climatic stress and biotic

attacks, at longer lead times and finer scales.

This chapter develops a novel approach to detect low-resilience based EWS. The results above highlight EWS's potential for operational monitoring and near-term prediction of forest mortality. Further improvement is needed to quantify influences of stochastic perturbations especially for long lead times and fine spatial scales. Investigation along the line can also benefit from inquiry into mechanisms contributing to low resilience.

Chapter 5. Influence of plant hydraulics on evapotranspiration

The goal of this chapter was to retrieve plant hydraulic traits at a stand scale using ET observations and evaluate how plant hydraulics affect stomatal conductance and ET under hydro-climatic stress. This is achieved by comparing with an empirical ET model that does not account for plant hydraulics. The main findings and implications are as follows.

(1) The model-data fusion (MDF) framework identifies plant hydraulic traits, and they are found to be comparable to segment scale measurements. Stomatal traits are generally more identifiable than xylem traits from ET observation. Large variation of plant hydraulic traits is identified across sites, even when they belong to the same plant functional type (PFT). Such variation indicates uncertainties inherent in PFT-based parameterization that is commonly used in ESMs. ET across the studied sites is found to be equally or more sensitive to soil hydraulics compared to plant hydraulics, highlighting the need for improved measurements and representation of soil hydraulics.

(2) Both the empirical model and the plant hydraulics model are able to capture the overall ET variation. However, incorporating plant hydraulics improves ET estimation under dry conditions with low soil moisture and high VPD i.e., under conditions where plant hydraulic limitation or high percentage loss of plant conductivity

103

occurred.

(3) The improvement of the hydraulics model under dry conditions benefits from the down-regulation mechanism of leaf water potential on stomatal conductance that integrates the response to both soil moisture and VPD. This down-regulation mechanism is significant as leaf water potential drops during drought.

(4) The plant hydraulics model indicates a higher sensitivity of stomatal conductance to VPD than the empirical model. Such sensitivity can be intensified under compounded heat and water stress. This finding suggests that the restriction of ecosystem water use and productivity during drought can be underestimated without considering plant hydraulics.

This chapter highlights the potential of the developed MDF framework to improve the widely used PFT-based vegetation parameterization in ESMs. The stronger restriction of VPD on stomatal conductance induced by plant hydraulics, especially under co-existence of water and heat stresses, underlines the critical role of plant hydraulics on ecosystem responses to both climate trends and extreme conditions.

6.2   Future work

An outline for future work is presented below.

Effects of wetland water table height on biogeochemical processes
Wetlands act as hot spots of biogeochemical processes including methane emission, ammonification, and nitrification. These processes are closely connected to climate variability through water table dynamics in wetlands. Based on the work in Chapter 2 that describes water table dynamics using a fully-distributed hydrologic model, future study could evaluate the impact of wetland hydrologic conditions on methane emission and nitrogen processes by combining with field observations and lab experiments.

Plant susceptibility to compounded stress

Vegetation susceptibility under future climate continues to draw significant research attention in climate, hydrological, ecological, and physiological sciences. Chapter 3 focused on the response of mortality risk to changing climate. The isolated role of compounded stress periods such as warmer-droughts whose occurrence is projected to increase in future (Mazdiyasni and AghaKouchak, 2015; Zscheischler et al., 2018; Chiang et al., 2018), remains unknown. The impacts of such compounded stress need to be assessed to further reduce uncertainties in climate and ecological predictions. The model developed in Chapter 3 can allow further exploration into this aspect.

Preferred Plant Traits against climate induced stress

Acclimation and adaptation of plants properties is another pivotal aspect of predicting vegetation dynamics. In this regard, perturbation analysis of plant properties can be used to generate hypotheses about the most efficient acclimation strategies for different tree species and traits. Such investigations will provide base-line knowledge into the potential changes of forest composition and cover in response to changes in climate, and thus also shedding light on the sustainability of forest management practices and ecological restoration.

Mechanism and spatial interactions governing forest resilience

The mechanisms governing forest resilience and mortality under extreme climate conditions remain an uncharted research territory. Based on the work described in Chapter 4, the detected EWS can be compared with multi-scale physiological metrics such as in-situ plant water potential and stomatal conductance, and remotely sensed plant water content and solar-induced chlorophyll fluorescence. Such comparison will provide clues on physiological mechanisms contributing to resilience. As discussed in Chapter 4, forest mortality still exhibited clear spatial correlation structure across the state of California even after accounting for spatially heterogeneous

properties such as topography, soil, vegetation, and climate. This implies that dynamics of forests are not spatially independent. Instead, interconnections possibly exist across large scales due to hydrologic connectivity, community competition, insect and pathogen initiation and propagation. Such spatial dependence structure can be empirically quantify using spatial statistics. Process based models, especially distributed hydrologic model as used in Chapter 2, can be combined to investigate the roles of spatially connected soil moisture and groundwater flow in forest resilience and mortality.

Plant hydraulics control on carbon assimilation and atmospheric feedbacks

How to represent plant responses to water stress responses in Earth System Models (ESMs) has been an active research topic. Chapter 5 addresses the impacts of incorporating plant hydraulics on ET estimation. The model data fusion developed here, which bridges the gap between segment-scale measurements and stand-scale traits, may be used to further explore the influence of plant hydraulics on ecosystem productivity under stress, and the feedbacks to the atmosphere. The atmospheric boundary layer model developed in Chapter 3 can be integrated here to further explore under what hydro-climatic conditions and hydraulic traits are heat stress more likely to co-occur with water stress. The investigation will also examine whether there exists some passive self-regulation exerted by plants to alleviate water stress via atmospheric feedbacks.

Impacts of vegetation dynamics on water resources and quality

The tools developed and implemented in this dissertation can be integrated to obtain integrated estimates of water, vegetation and nutrient dynamics by coupling distributed hydrologic models (DHMs) such as PIHM with vegetation and biogeochemical models. As the water use strategies of different plant species, especially during droughts, are often not well captured by a lumped models, the plant hy-

draulics model developed in Chapter 3 can be coupled with a DHM to study this. In the long-term, the sensitivity of vegetation to climate variations may change over time, for example due to acclimation of plant properties, alteration of species composition, and depletion/increment of mineralized soil nutrients, thus resulting in errors in long-term hydrologic predictions. Eco-climate regions with higher sensitivity to climatological variations and change can be identified using the Bayesian time series analysis method established in Chapter 4. This will facilitate discovery of locations where DHM coupling with dynamic vegetation models is needed for improved water resources prediction and risk assessment.

Appendix A

Supporting information for chapter 2

A.1 Derivation of the posterior distributions for Bayesian regression and variable selection

Let $\boldsymbol{X}$ be the $n \times p$ matrix of $(\boldsymbol{x}_1, \boldsymbol{x}_2, \ldots, \boldsymbol{x}_n)^{\mathrm{T}}$, where $\boldsymbol{x}_j = (x_{j,1}, x_{j,2}, \ldots, x_{j,p}), (j = 1, \ldots, n)$. Let $\boldsymbol{\beta} = (z_1 b_1, \ldots, z_p b_p)^{\mathrm{T}}$, then based on Equation (2.1)

$$\{\boldsymbol{y}|\boldsymbol{X}, \boldsymbol{\beta}, \sigma^2\} \sim \text{Multivariate normal}(\boldsymbol{X}\boldsymbol{\beta}, \sigma^2 \boldsymbol{I}) \tag{A1}$$

Hence the likelihood of the time series $\boldsymbol{y}$ is

$$p(\boldsymbol{y}|\boldsymbol{X}, \boldsymbol{\beta}, \sigma^2) \propto \exp\left\{-\frac{1}{2\sigma^2}\left[\boldsymbol{y}^{\mathrm{T}}\boldsymbol{y} - 2\boldsymbol{\beta}\boldsymbol{X}^{\mathrm{T}}\boldsymbol{y} + \boldsymbol{\beta}^{\mathrm{T}}\boldsymbol{X}^{\mathrm{T}}\boldsymbol{X}\boldsymbol{\beta}\right]\right\} \tag{A2}$$

Considering that our goal is to estimate and predict $\boldsymbol{y}$ using $\boldsymbol{X}$, one needs to estimate the parameters $\boldsymbol{\beta}$ and σ^2.

The prior distributions for $\boldsymbol{z} = (z_1, \ldots, z_p)^{\mathrm{T}}, \boldsymbol{\beta} = (\beta_1, \ldots, \beta_z)^{\mathrm{T}}$ and σ^2 are obtained as follows. For each z_j, a non-informative Bernoulli prior of $\Pr(z_j = 0) = \Pr(z_j = 1) = 1/2$ is used. For $\boldsymbol{\beta}$ and σ^2, Zellner's g-prior (Zellner, 1986) and inverse-

gamma prior is applied respectively (Equation (A3)).

$$z_j \sim \text{Bernoulli}(1/2)$$

$$\boldsymbol{\beta_z} \sim \text{Multivariate normal}(\mathbf{0}, g\sigma^2(\boldsymbol{X_z^{\mathrm{T}}X_z})^{-1}) \tag{A3}$$

$$\sigma^2 \sim \text{Inverse-gamma}(\nu_0/2, \nu_0\sigma_0^2/2)$$

where for any given $\boldsymbol{z}$ with p_z being the non-zero entries, $\boldsymbol{\beta_z}$ is a $p_z \times 1$ vector consisting of all non-zero entries in $\boldsymbol{z}$; and $\boldsymbol{X_z}$ is a $n \times p_z$ matrix corresponding to non-zero entries of $\boldsymbol{z}$. The Zellner's g-prior is a widely used prior distribution for regression parameters, which provides a closed-form representation of marginal likelihoods and hence is computationally efficient (Liang et al., 2008). Specifically, unit information prior (Kass and Wasserman, 1995), a type of weakly informative prior, is provided for $\boldsymbol{\beta_z}$ and σ^2 by choosing prior parameters of $g = n, \nu_0 = 1, \sigma_0^2 = \hat{\sigma}_{ols}^2$, where $\hat{\sigma}_{ols}^2 = (\boldsymbol{y} - \boldsymbol{X\beta})^{\mathrm{T}}(\boldsymbol{y} - \boldsymbol{X\beta})/(n - p)$ is the ordinary least squares (OLS) estimate of σ^2. The multivariate normal prior for $\boldsymbol{\beta_z}$ and the inverse-gamma prior for σ^2 are semi-conjugate for the multivariate normal model (Equation (A1)), which enables the posteriors to be derived analytically.

Next, the posterior distributions for $\boldsymbol{z}, \boldsymbol{\beta}$ and σ^2 are derived. According to the Bayes theory, the posterior of $\boldsymbol{z}$ can be computed using:

$$p(\boldsymbol{z}|\boldsymbol{y}, \boldsymbol{X}) = \frac{p(\boldsymbol{z})p(\boldsymbol{y}|\boldsymbol{X}, \boldsymbol{z})}{\Sigma_{\tilde{z}}p(\tilde{\boldsymbol{z}})p(\boldsymbol{y}|\boldsymbol{X}, \tilde{\boldsymbol{z}})} \tag{A4}$$

where $\tilde{\boldsymbol{z}}$ denotes all the possible values of $\boldsymbol{z}$, i.e., 0 and 1. For each z_j, in order to calculate the posterior probability for $z_j = 1$, let $\boldsymbol{z_a} = (z_1, \ldots, z_j = 1, \ldots, z_p)^{\mathrm{T}}$ and $\boldsymbol{z_b} = (z_1, \ldots, z_j = 0, \ldots, z_p)^{\mathrm{T}}$. Then based on Equation (A4), the posterior odds of $\boldsymbol{z_a}$ and $\boldsymbol{z_b}$ are calculated using:

$$o_j = \frac{p(\boldsymbol{z_a}|\boldsymbol{y}, \boldsymbol{X})}{p(\boldsymbol{z_b}|\boldsymbol{y}, \boldsymbol{X})} = \frac{p(\boldsymbol{z_a})}{p(\boldsymbol{z_b})}\frac{p(\boldsymbol{y}|\boldsymbol{X}, \boldsymbol{z_a})}{p(\boldsymbol{y}|\boldsymbol{X}, \boldsymbol{z_b})} \tag{A5}$$

where the marginal likelihood of $\boldsymbol{z}$ is:

$$p(\boldsymbol{y}|\boldsymbol{X}, \boldsymbol{z}) = \int\int p(\boldsymbol{y}, \boldsymbol{b}, \sigma^2|\boldsymbol{X}, \boldsymbol{z})\mathrm{d}\boldsymbol{b}\mathrm{d}\sigma^2$$

$$= \int\int p(\boldsymbol{y}|\boldsymbol{b}, \boldsymbol{X})p(\boldsymbol{b}|\boldsymbol{X}, \boldsymbol{z}, \sigma^2)p(\sigma^2)\mathrm{d}\boldsymbol{b}\mathrm{d}\sigma^2 \tag{A6}$$

Equation (A6) can be integrated analytically by plugging in the priors (Equation (A3)) and the likelihood (Equation (A2)) (see Hoff (2009) for details). With the posterior odds computed (Equation (A5)), each z_j can be evaluated using a Bernoulli distribution (Equation (A7)). Then for a given $\boldsymbol{z}$, by combining the likelihood (Equation (A2)) and the semi-conjugate priors (Equation (A3)), the posteriors of $\boldsymbol{\beta_z}$ and σ^2 can be obtained as follows:

$$\Pr(z_j = 1|\boldsymbol{y}, \boldsymbol{X}, \boldsymbol{z}_{\sim j}) = \mathrm{Bernoulli}(o_j/(o_j + 1))$$

$$p(\boldsymbol{\beta_z}|\boldsymbol{y}, \boldsymbol{X_z}, \sigma^2)\propto p(\boldsymbol{y}|\boldsymbol{X_z}, \boldsymbol{\beta_z}, \sigma^2) \times p(\boldsymbol{\beta_z})\propto\text{multivariate normal}(\boldsymbol{\mu_n}, \boldsymbol{\Sigma_n}) \tag{A7}$$

$$p(\sigma^2|\boldsymbol{y}, \boldsymbol{X_z})\propto p(\boldsymbol{y}|\boldsymbol{X_z}, \sigma^2) \times p(\sigma^2)\propto\text{inverse-gamma}(\nu_n, \Gamma_n)$$

where $\boldsymbol{z}_{\sim j}$ represents all the entries in $\boldsymbol{z}$ except for z_j; $\boldsymbol{\mu_n} = g/(g+1)(\boldsymbol{X}_{\boldsymbol{z}}^{\mathrm{T}}\boldsymbol{X}_{\boldsymbol{z}})^{-1}\boldsymbol{X}_{\boldsymbol{z}}^{\mathrm{T}}\boldsymbol{y}$; $\boldsymbol{\Sigma_n} = g/(g + 1)\sigma^2(\boldsymbol{X}_{\boldsymbol{z}}^{\mathrm{T}}\boldsymbol{X}_{\boldsymbol{z}})^{-1}$; $\nu_n = (\nu_0 + n)/2$; $\Gamma_n = (\nu_0\sigma_{0z}^2 + \mathrm{SSR}_{gz})/2$; $\sigma_{0z}^2 = (\boldsymbol{y} - \boldsymbol{X_z}\boldsymbol{\beta_z})^{\mathrm{T}}(\boldsymbol{y} - \boldsymbol{X_z}\boldsymbol{\beta_z})/(n - p_z)$; $\mathrm{SSR}_{gz} = \boldsymbol{y}^{\mathrm{T}}(\boldsymbol{I} - g/(g + 1)\boldsymbol{X_z}(\boldsymbol{X}_{\boldsymbol{z}}^{\mathrm{T}}\boldsymbol{X}_{\boldsymbol{z}})^{-1}\boldsymbol{X}_{\boldsymbol{z}}^{\mathrm{T}})\boldsymbol{y}$.

Appendix B

Supporting information for chapter 3

B.1   Details on data processing

Soil and plant properties. The global distribution of plant functional type (PFT) was obtained from MODIS (MCD12C1) (NASA LP DACC, 2013) with a spatial resolution of $0.05° \times 0.05°$. Multiple regions covered by forests were selected across the globe, with a variety of climate types (Table B.11). Each biome corresponds to the areas covered by a given PFT within a selected region. Soil texture compositions were obtained from the Harmonized World Soils Database (FAO, 2009). Based on the major soil texture in each biome, the soil hydraulic properties, i.e., saturated and unsaturated conductivity, soil water potential, pore-size distribution index and porosity, were calculated using the generalized statistical relations (Saxton et al., 1986).

Leaf Area Index (LAI) was extracted from the level-4 MODIS global Leaf Area Index and Fraction of Photosynthetically Active Radiation (FPAR) product (MCD15A2) (NASA LP DACC, 2016), with a spatial and temporal resolution of 1 km $\times$ 1 km and 8-day respectively. In the SPAC model, LAI is a seasonally varying parameter.

After re-sampling LAI to $0.05° \times 0.05°$ grids and linearly interpolating to a daily scale, the intra-annual variation of LAI was represented by the average of pixels within each biome over the period of 2003 to 2015. Root zone depth for the first and second layer were taken as 0.3 m and 1.0 m for all the biomes (Rodríguez-Iturbe and Porporato, 2007; Manzoni et al., 2013; Rodell et al., 2004). For each biome, RAI in the first layer was obtained from the biome-level average reported in (Manzoni et al., 2013) (Table B.11). Because of lack of data, RAI in the second layer was taken as 1. Plant properties controlling internal water transfer, including leaf-specific conductivity $(k_{p,\text{leaf}})$, ψ_{50}, and a, were obtained from a global database containing hydraulic traits of 866 species (Kattge et al., 2011). These plant hydraulic traits were classified into categories based on combinations of PFT and climate type (Kottek et al., 2006). Each biome in this study was then assigned with the mean value of the category that has the same PFT and climate type. $g_{p,\text{max}}$ in Equation (3.10) was estimated according to $g_{p,\text{max}} = k_{p,\text{leaf}}\overline{\text{LAI}}/(H_c\rho_w)$ (Manzoni et al., 2013), in which $\overline{\text{LAI}}$ is the long term average LAI; H_c is the 90th percentile canopy height extracted from a global map (Lefsky, 2010) and averaged across the biome. Large tree height, i.e., 90th percentile instead of 50th percentile, was used since tall trees are associated with low plant conductance, and hence are likely to be the main target during mortality events (McDowell and Allen, 2015). The parameters in the biochemical model (Equation (3.13)) and their temperature corrections came from the cross-species study by (Medlyn et al., 2002). Parameters for all species were grouped by PFTs and the means for each PFT were used to parameterize the model. The response of leaf gas exchange to water availability (Equation (3.15)) was parameterized according to a recent study based on cross-biome meta-analysis (Manzoni et al., 2011). Due to large range of these parameters, starting from the biome-average values reported in (Manzoni et al., 2011), λ_{WW}^* and β_0 were calibrated to match the modeled monthly potential evapotranspiration (PET) and ET against the PET and

ET dataset derived from MODIS (Mu et al., 2011) respectively (Figure B.11), making sure that the magnitudes among PFTs and climate types are in the same order as reported in (Manzoni et al., 2011). λ_{WW}^* was first calibrated with the goal to match PET. Modeled PET equals the ET under presumptive conditions of $s_1 = s_2 = 1$ and $\lambda = \lambda_{WW}^* c_a/c_a^*$, where c_a is equal to the historical ambient CO_2 concentration. Then β_0 was calibrated according to annual actual ET, where soil moisture and mWUE were allowed to vary under actual climate conditions. It should be noted that in PET calculation, the model was decoupled with ABL and the climate forcings came from ABL development in the ET calculation, which represents the actual climate conditions. In this way, the soil-plant system in each biome is physiologically and hydrologically reasonable in representing the overall properties at a biome scale. The biome-specific soil and plant properties are listed in Table B.11.

Given the soil and plant properties in each biome, we analyzed the responses of stomatal conductance and plant water potential during dry down processes. Starting from a soil moisture at field capacity, the soil was allowed to consecutively dry down with zero precipitation. As shown in Figure B.12, ENF biomes generally operate with wider safety margins than DBF and EBF biomes. Most ENF biomes adopt an isohydric leaning strategy under stress, i.e. they decrease g_s while keeping a relatively wide safety margin even when g_s gets close to zero. In contrast, most DBF biomes adopt an anisohydric leaning strategy under stress, i.e., they tend to decrease water potential while keeping stomata open even when the safety margin drops near zero or negative. The response of EBF biomes could be either one or a hybrid of these two strategies. The exact response of each biome depends on their hydraulic traits. The typically wider safety margin and isohydric strategies for ENF compared to the other two PFTs are consistent with observations (Choat et al., 2012; McDowell et al., 2008), which indicates representativeness of the plant parameterizations and enables inter-comparison among PFTs.
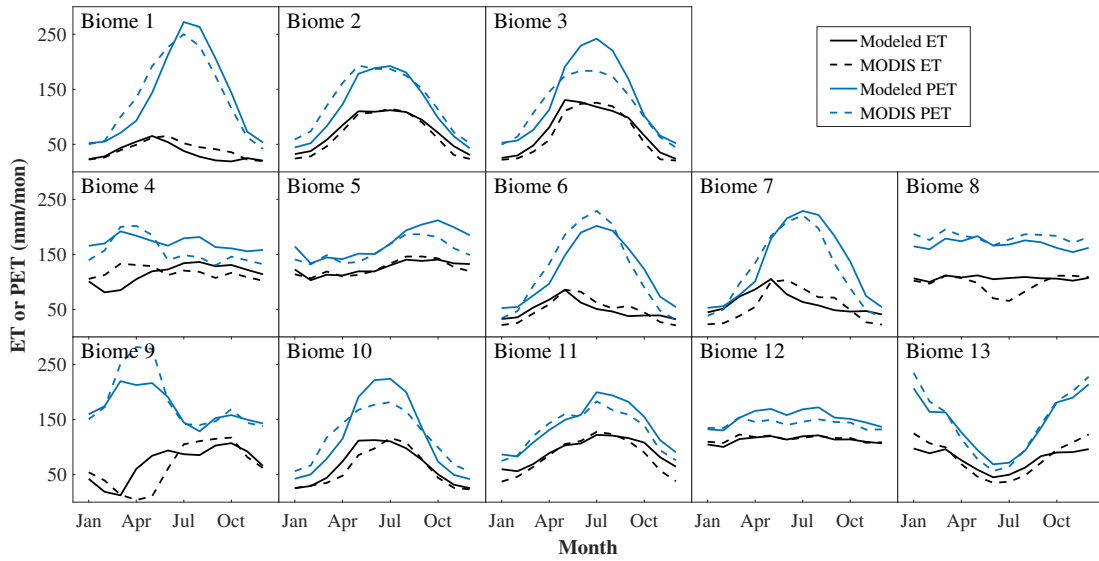
FIGURE B.11: Comparison between modeled and MODIS based monthly ET and PET. Modeled monthly ET and PET are the average of 30 annual ensembles after a 5-year warming up period. MODIS ET and PET are the average across the available time range of 2000–2014.
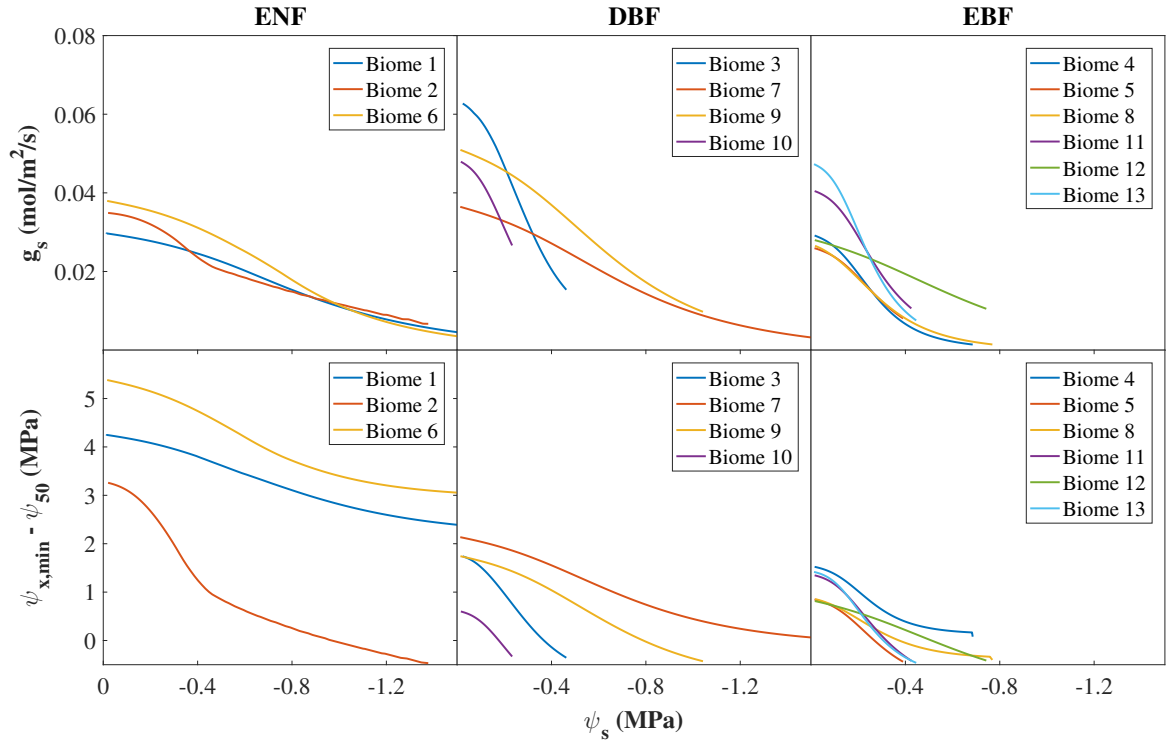
FIGURE B.12: Variation of stomatal conductance g_s and safety margin $(\psi_{x,min} - \psi_{50})$ during dry down processes for ENF, DBF and EBF biomes. ψ_s denotes soil water potential. These dry down processes were plotted for a constant air temperature of 20 °C, VPD of 1.5 kPa, and daily maximum net shortwave radiation of 700 W/m².

Table B.11: Location, soil texture, climate conditions and vegetation parameters for the investigated biomes.

ID	Latitude range	Longitude range	Major soil texture	Climate type	PFT	RAI_1	$\overline{LAI}$	H_c (m)	$k_{p,leaf}$ (kg/m/s/MPa)	ψ_{50} (MPa)	a	$\lambda_{WW}*$ mmol/mol	β_0
1	[35, 40]	[−123, −118]	Loamy sand	Mediterranean	ENF	11.6	1.2	14.2	3.25×10^{-4}	−5.62	4.36	1.0	−1.5
2	[32, 37]	[−84, −79]	Loamy sand	Temperate wet	ENF	11.0	2.3	11.8	2.14×10^{-4}	−3.26	8.04	4.5	−0.5
3	[32, 37]	[−84, −79]	Loamy sand	Temperate wet	DBF	9.8	2.4	14.0	1.45×10^{-4}	−2.03	4.8	1.5	−1.5
4	[15, 20]	[−92, −87]	Silt loam	Tropical dry	EBF	6.3	5.0	18.0	4.85×10^{-4}	−2.03	3.35	4.5	−1.5
5	[0, 5]	[−57, −52]	Loam	Tropical wet	EBF	7.4	4.9	22.1	3.09×10^{-4}	−1.05	1.55	5.5	−1.0
6	[37, 40]	[15, 22]	Loam	Mediterranean	ENF	11.6	2.2	6.8	3.25×10^{-4}	−5.62	4.36	4.0	−1.0
7	[37, 40]	[15, 22]	Loam	Mediterranean	DBF	11.6	2.4	11.3	1.40×10^{-4}	−2.49	2.75	3.2	−1.2
8	[−5, 0]	[22, 27]	Sandy clay loam	Tropical wet	EBF	7.4	4.9	16.1	3.09×10^{-4}	−1.05	1.55	5.0	−1.5
9	[20, 25]	[80, 85]	Silt loam	Tropical dry	DBF	9.8	1.5	9.0	5.85×10^{-4}	−2.23	1.88	2.5	−1.3
10	[30, 35]	[107, 112]	Loam	Temperate winter dry	DBF	9.8	1.8	16.5	4.91×10^{-4}	−1.12	2.47	2.5	−1.5
11	[23, 28]	[114, 119]	Loam	Temperate wet	EBF	9.8	2.5	16.4	4.00×10^{-4}	−1.65	2.63	3.0	−1.2
12	[0, 5]	[112, 117]	Loam	Tropical wet	EBF	7.4	4.4	15.6	3.09×10^{-4}	−1.05	1.55	5.0	−1.0
13	[−35, −30]	[149, 154]	Silt loam	Temperate wet	EBF	9.8	1.9	16.9	4.00×10^{-4}	−1.65	2.63	2.5	−1.5

Historical climate forcing. Historical climate forcings for the SPAC model, including stochastic precipitation, net shortwave radiation, and initial and boundary conditions of ABL, were obtained from the NCEP/NCAR reanalysis data ($2.5° \times 2.5°$) (Kalnay et al., 1996) for 1986 to 2005. The two statistics for stochastic precipitation, i.e., precipitation frequency (λ_P) and mean precipitation depth (α_P) were computed from the 20-year daily precipitation. To account for precipitation seasonality, λ_P and α_P were computed for two periods separately, i.e., April to October and November to March, which correspond to the growing season and non-growing season for biomes in the northern hemisphere and the opposite for those in the southern hemisphere. Stochastic precipitation in the two seasons was then generated separately for the two seasons using the corresponding statistics (Rodríguez-Iturbe and Porporato, 2007). Daily net shortwave radiation, which varies with day of year (DOY), was calculated as the average over the 20 years. Radiation for days with and without precipitation were calculated separately to account for cloud coverage on rainy days. Daily net shortwave radiation was distributed into an hourly diurnal cycle using a sine function consistent with local sunrise and sunset time, calculated from DOY and local latitude. Initial conditions of ABL include initial ABL height (h_0), potential temperature (θ_0) and specific humidity (q_0). h_0 was set as 100 m (Stull, 1988). θ_0 and q_0, which also vary with DOY, were obtained from the 4-time daily data of 2 m air temperature and near surface specific humidity, linearly interpolated to the sunrise time of each day and averaged over the 20 years. Similar to radiation, humidity for days with and without precipitation were evaluated separately as humidity is generally higher on rainy days. Boundary conditions of ABL, i.e., the lapse rates of potential temperature (γ_θ) and specific humidity γ_q, which reflect the stability of ABL, were extracted from the daily pressure level data within the troposphere. Daily mean values and the lapse rates are mostly linearly correlated (Konings et al., 2010) (Figure B.13). Though some tropical biomes (biome 4, 5, 8, 12) showed low R^2 values, their lapse rates

had small variation range, as such using these linear relations do not impair their representativeness as much. The fitted linear relations were used to represent lapse rates under given temperature and humidity. These representations of climate forcing enable the model to readily incorporate projected changes in climate conditions.

Climate projections. We calculated projected climate changes for multi-models of CMIP5 experiments under four RCP scenarios (Table B.12). Under each RCP scenario, changes projected by each model were quantified as the difference (percentage for MAP and magnitude for others (IPCC, 2013)) of the ensemble means for 2050 – 2069 relative to those for 1986 – 2005. These changes were incorporated in the historical climates from NCEP/NCAR reanalysis data to generate future climate forcings for the model. Changes in daily initial conditions of potential temperature and specific humidity were assumed to be identical to the changes in their annual means. Future boundary conditions were obtained based on the linear relationships in Figure B.13. Future precipitation amount in the growing and non-growing seasons were obtained by incorporating changes in MAP and PS. For the two seasons, precipitation amount was separated into mean precipitation depth (α_P) and precipitation frequency (λ_P) by keeping $\alpha_P \lambda_P$ equal to the future daily mean precipitation, and the ratio α_P / λ_P to be constant (Viola et al., 2008). As these statistics change in the projected climate, the occurrence frequency and duration of drought with a given severity will change accordingly. However, possible changes in the spectrum characteristics of long-term climate oscillations, such as change in El Niño Southern Oscillation which is still under debate (Wittenberg, 2009), is not included in the model.

It is to be noted that the risk was found to be dominated by precipitation amount with little sensitivity to the separation approach (Figure B.14). Hence, the results are not affected by using a different combination of α_P and λ_P. Future initial conditions of ABL were obtained by adding changes in annual mean air temperature and
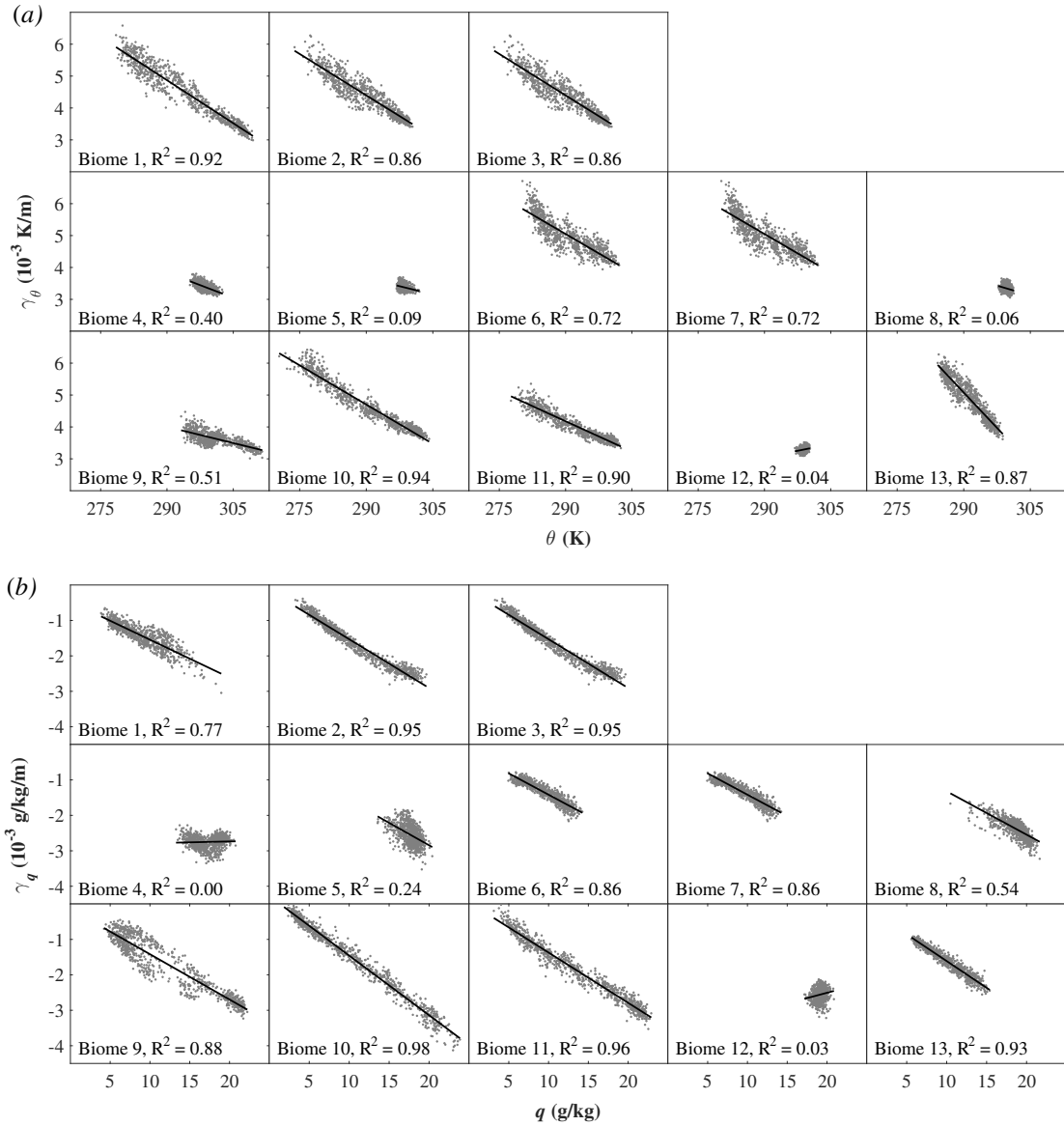
FIGURE B.13: (*a*) Relation between daily mean surface potential temperature (θ) and the lapse rate of potential temperature in the free atmosphere (γ_θ); and (*b*) relation between daily mean surface specific humidity (q) and the lapse rate of specific humidity in the free atmosphere (γ_q) based on daily NCEP data from 1986 to 2005.

Table B.12: List of CMIP5 model outputs included in this study. The used RCP scenarios of each model are denoted with "x".

Model name	RCP2.6	RCP4.5	RCP6.0	RCP8.5
CMCC-CESM				x
CMCC-CM		x		x
CMCC-CMS		x		x
CNRM-CM5	x	x		x
FGOALS-g2	x	x		x
FGOALS-s2				x
GFDL-CM3	x	x	x	x
GFDL-ESM2G	x	x	x	x
GFDL-ESM2M	x	x	x	x
HadGEM2-AO	x	x	x	x
HadGEM2-CC		x		x
HadGEM2-ES	x	x	x	x
IPSL-CM5A-LR	x	x	x	x
IPSL-CM5A-MR	x	x	x	x
IPSL-CM5B-LR		x		x
MIROC-ESM	x	x	x	x
MIROC-ESM-CHEM	x	x	x	x
MIROC5	x	x	x	x
MPI-ESM-LR	x	x		x
MPI-ESM-MR	x	x		x
MRI-CGCM3	x	x	x	x
MRI-ESM1				x
inmcm4		x		x

specific humidity uniformly throughout the year, assuming intra-annual and diurnal variation patterns remain unchanged. Future boundary conditions of ABL were changed accordingly based on the fitted linear relations with θ and q respectively (Figure B.13). Figure B.15 shows the historical climates and ranges of multi-model projections for each biome, including mean annual precipitation amount, precipitation seasonality, mean annual air temperature and mean annual specific humidity. Identical future atmospheric CO_2 concentration under each RCP scenario was used for all the biomes. The ranges shown in Figure $2c, f$ correspond to the values from

2050 to 2069, which were obtained by linear interpolation of the values reported in (Meinshausen et al., 2011).
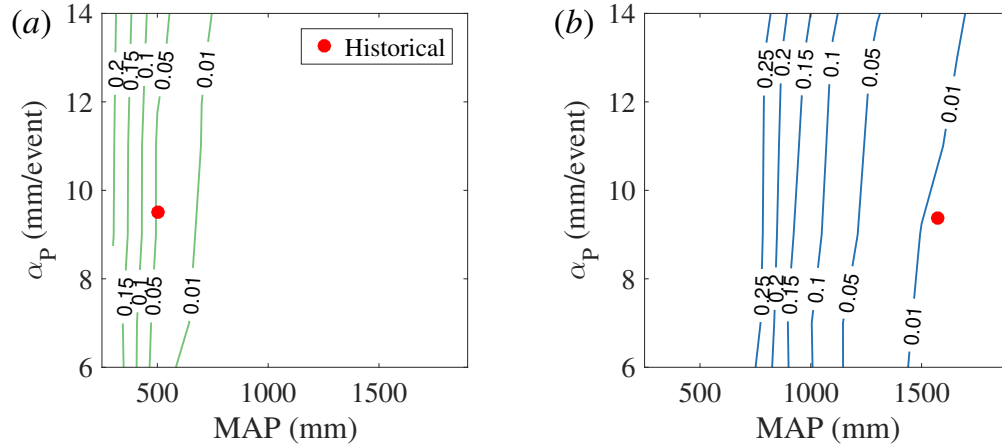
FIGURE B.14: Responses of mortality risk to individual changes in mean annual precipitation (MAP) and mean precipitation depth (α_P) for (a) ENF in the western US and (b) DBF in the southeastern US. Numbers on the contours denote risk magnitude. Blue and green contours represent risks due to hydraulic failure and stomatal closure, respectively.

B.2 Model validation

Multiple components of the SPAC model have been previously examined and validated. For example, the soil water balance under stochastic precipitation was demonstrated to be able to capture observed probablistic characteristics of soil moisture dynamics (Rodríguez-Iturbe and Porporato, 2007). An ecohydrological model forced by stochastic precipitation in the previous study (Parolari et al., 2014) was shown to capture the frequency of canopy loss across a precipitation gradient. The resistance based plant water transport model has been widely examined and applied (Katul et al., 2003; Manzoni et al., 2013). The optimization based stomatal function was shown to be able to predict the observed stomatal response in both ambient and CO_2 enriched atmosphere (Katul et al., 2009a,b). The constraint of water availability on
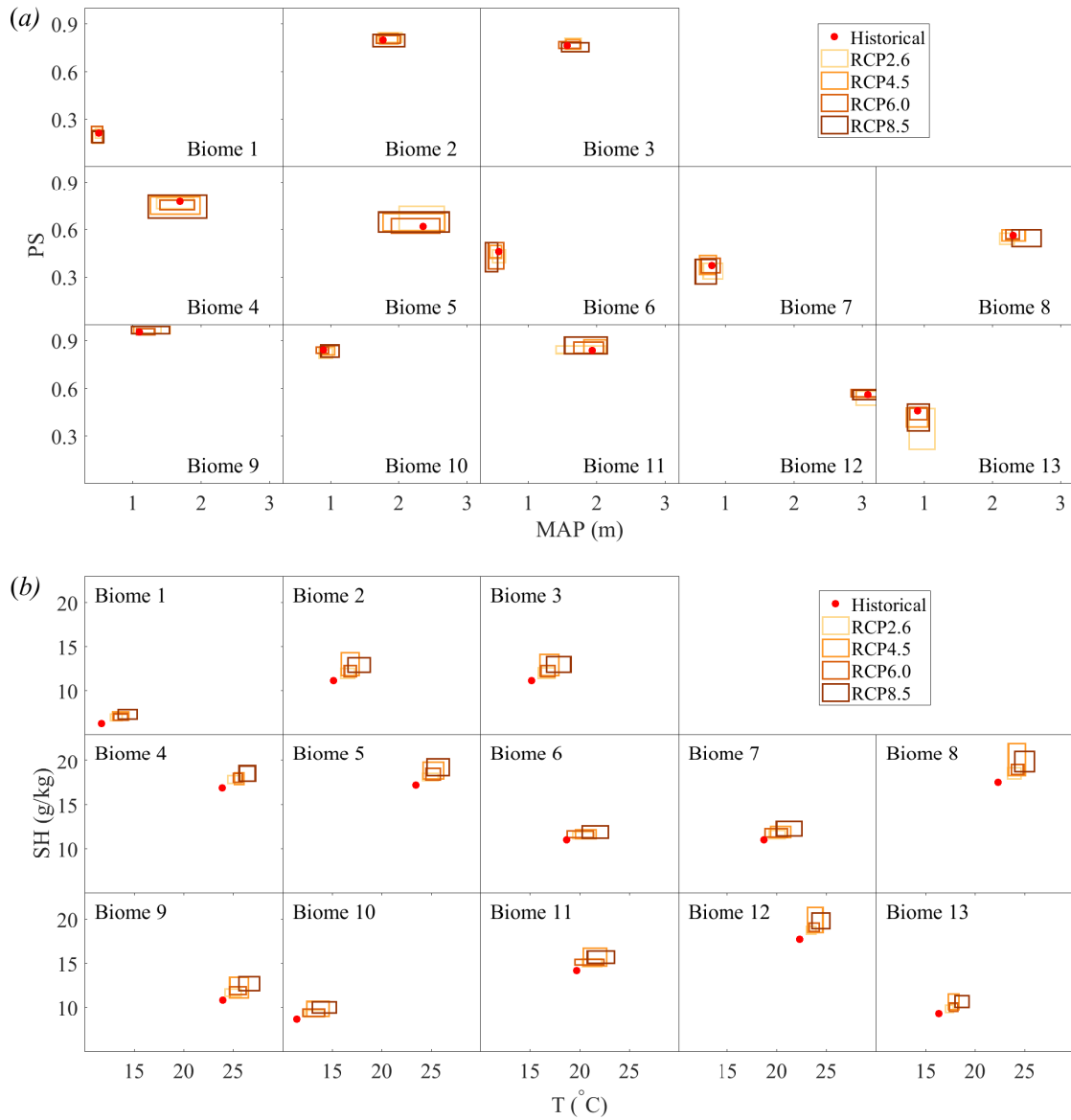
FIGURE B.15: Historical and future climate conditions of (*a*) mean annual precipitation (MAP), precipitation seasonality (PS), (*b*) annual mean air temperature (T) and annual mean specific humidity (SH) in the 13 biomes as projected by the CMIP5 models. Ranges of multi-model predictions under each RCP scenario are illustrated by rectangles.
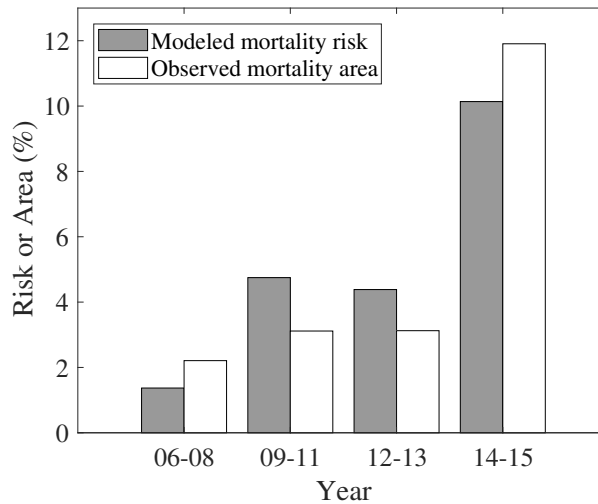
FIGURE B.21: Comparison between modeled mortality risk of evergreen needleleaf forest and observed mortality area in southern Sierra, CA.

leaf gas exchange was examined in (Manzoni et al., 2011). Feedbacks between vegetation and ABL dynamics were compared with observed data in (de Arellano et al., 2012).

To examine the efficacy of the modeled mortality risk, observed mortality in two temperate and two tropical forests were compared to modeled mortality risk.

(1) Needleleaf forest in southern Sierra, California, USA

The United States Forest Service Pacific Southwest Region Aerial Detection and Monitoring Program (ADMP) conducts annual aerial survey over the forested areas in California (U.S. Forest Service, 2015b). Areas with new mortality since last survey were delineated as polygons. The surveyed area in southern Sierra (119.28° W – 118.20° W, 35.41° N – 37.57° N), which belongs to biome 1 in this study (Figure 3.1, Table B.11), was considered for comparison as it underwent massive mortality in 2014 and 2015. The aerial survey data from 2006 to 2015 were first converted to raster data with grid resolution of 3 km and then used to calculate the area that underwent mortality in a given year. The model was parameterized with local soil properties

123
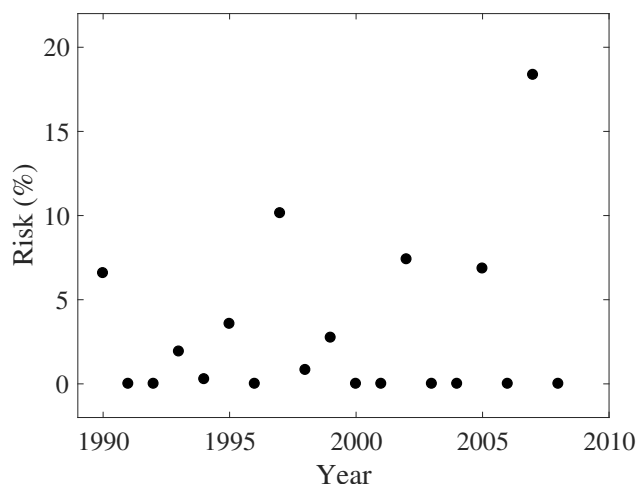
FIGURE B.22: Modeled annual mortality risk in deciduous broadleaf forest in Bond Park, NC from 1990 to 2008.

and plant hydraulic traits, as described in Section S2, and forced with climate time series of the concerned period (Saha et al., 2011). Figure B.21 compares the temporal variation of modeled mortality risk and the observed area with mortality. The temporal variation in the area with mortality can be interpreted as the temporal variation in the probability of mortality of a tree within the selected area. Result shows that the temporal variation of modeled mortality risk ably captures the variations in areal cover that underwent mortality. Notably, the modeled risk captures the increase in mortality area from 2006–2008 to 2009–2011, a non-increase in mortality area from 2009–2011 to 2012–2013, and a significant increase in mortality area from 2012–2013 to 2014–2015. It is to be noted that reasonable correspondence between modeled and observed data is captured despite using an average representative soil, vegetation and climate properties for modeling the mortality risk.

(2) Deciduous forest in Bond Park, North Carolina, USA

A recent study (Hoffmann et al., 2011) reported mortality of deciduous broadleaf forest in Bond Park, NC. The area belongs to biome 3 in this study (Figure 3.1, Table B.11). Within the surveyed area, 14% of *Acer rubrum* had died in 2007 while no
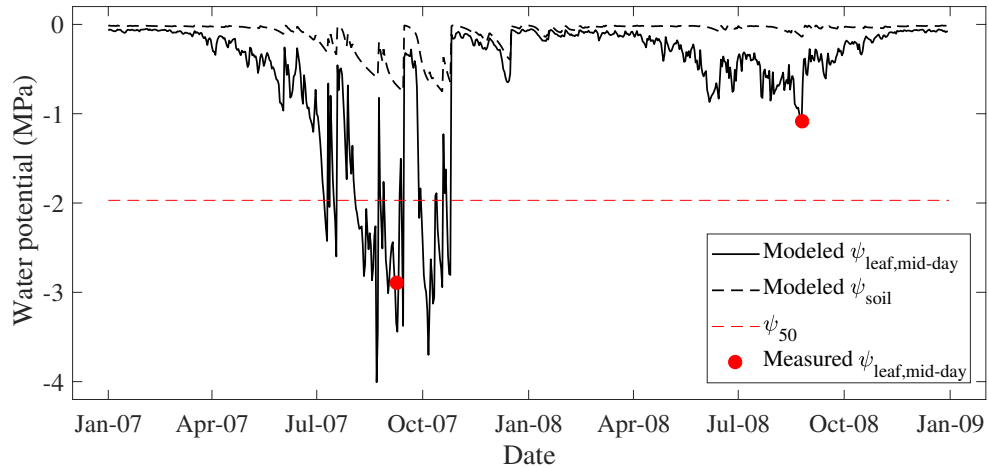
FIGURE B.23: Comparison between modeled and measured plant water potential of *Acer rubrum* in Bond Park, NC, reported in Hoffmann et al. (2011).

mortality was observed in 2008. We examine if the difference in mortality between these two years can be captured by the modeled mortality risk. The model was again parameterized with local soil properties, and plant hydraulic traits specifically for *Acer rubrum* from the TRY database (Kattge et al., 2011). Using the daily historical climate (Saha et al., 2011) for the site, the model evaluates the risk for each year from 1990 to 2008 (Figure B.22). It can be seen that the risk in 2007 is abnormally high (18.4%), and is largest between 1990 to 2008. The modeled risk in 2008 is zero, which agrees with the observation that there was no observed mortality in 2008. Figure B.23 further shows that the model was able to capture the plant water potential during 2007 and 2008 (Hoffmann et al., 2011). Notably, during the intense drought period in 2007, plant water potential fell below ψ_{50} suggesting that the observed mortality would likely have been induced by hydraulic failure, which is consistent with the conclusion in (Hoffmann et al., 2011). These results highlight the effectiveness of model in capturing both the temporal variations in mortality risk and its mechanistic control.

(3) Evergreen broadleaf forest on Barro Colorado Island, Panama
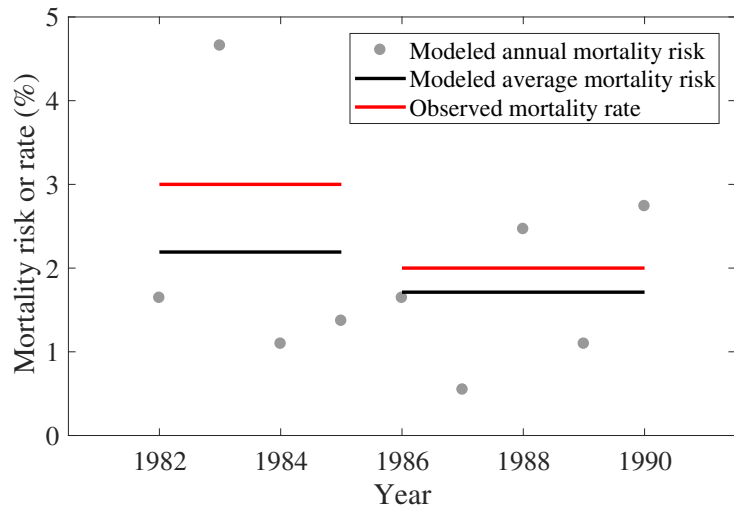
FIGURE B.24: Comparison between modeled mortality risk and observed mortality rate (Condit et al., 1995) in tropical evergreen forest at BCI, Panama.

Mortality rates in tropical forest of Barro Colorado Island (BCI) were measured for two census periods viz. 1982–1985 and 1985–1990 in a previous study (Condit et al., 1995). Based on survey of 205 species, the average forest–wide mortality rate was observed to be 3% yr^{-1} and 2% yr^{-1} during the two census periods, respectively. The higher mortality rate during the first period was attributed to low precipitation and high temperature (Condit et al., 1995) during the unusually severe dry season of 1983. To examine if the modeled mortality risk in this study is able to distinguish observed mortality during these two periods, the SPAC model was parameterized with local soil properties and average plant hydraulic traits for species found on BCI from the TRY database (Kattge et al., 2011). Forced with deterministic climate conditions (Saha et al., 2011), the model shows a higher mortality risk of 2.2% during the first period, compared to 1.7% during the second period (Figure B.24). The higher risk during 1982–1985 is primarily due to the notably high risk in 1983 (Figure B.24), which is consistent with the finding in the previous study (Condit et al., 1995).
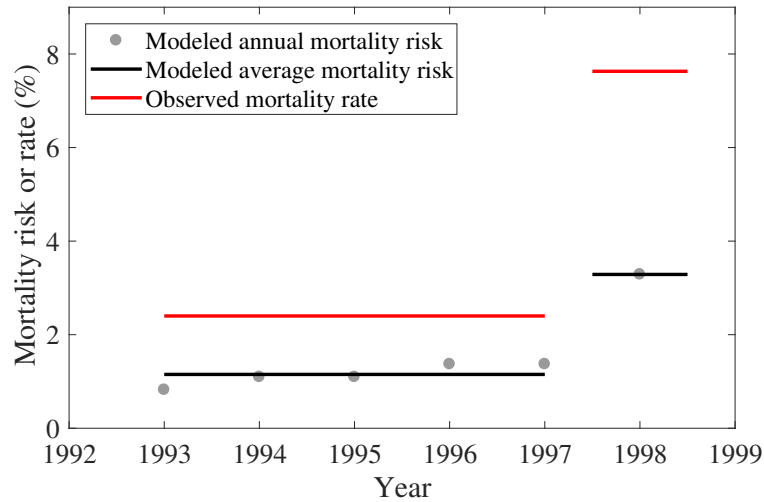
FIGURE B.25: Comparison between modeled mortality risk and observed mortality rate (Potts, 2003) in tropical evergreen forest in Malaysia.

(4) Evergreen broadleaf forest in Lambir Hills National Park, Malaysia

The tropical evergreen forest in Lambir Hills National Park, Malaysia, experienced a severe drought in 1998, which resulted in the observed forest–wide mortality rate to increase to 7.63% yr^{-1} from a mere 2.40% yr^{-1} (Potts, 2003) during pre-drought (1993–1997) years. This area belongs to biome 12 in this study (Figure 3.1, Table B.11). Annual mortality risk during 1993–1998 was estimated using the SPAC model to examine its ability to capture the response to drought. Soil properties provided in (Potts, 2003) were used to parameterize the model. As complete set of plant hydraulic traits of only two species from the region are included in the TRY database (Kattge et al., 2011), the average plant properties over all the evergreen species in tropical wet climate were used for simulation. In agreement with the observation, the model shows higher mortality risk of 3.3% in 1998, compared to the pre-drought average risk of 1.1% (Figure B.25).

The aforementioned comparisons between modeled mortality risk and observed mortality in the field indicate the effectiveness of the model in capturing the temporal

127

variation of mortality in response to climate for different PFTs under a range of climate settings.

B.3   Sensitivity analyses

Sensitivity to plant hydraulic traits. Given that plant hydraulic traits may vary significantly within each biome (Manzoni et al., 2013; Xu et al., 2016) (Figure B.31), sensitivity analyses of risks to magnitude of plant hydraulic traits are performed to test the robustness of the main conclusions of this study. In this regard, the historical mortality risks and relative change in them in response to projected climate was evaluated for 25%, 50% and 75% quantiles of the plant hydraulic traits for each biome. Table B.31 shows the estimated historical risk, the relative changes in risk under projected changes of precipitation and temperature only, and then with additional consideration of changes in specific humidity and CO_2 concentration. Higher leaf specific conductance ($k_{p,leaf}$) promotes water loss, hence increasing the magnitude of historical risk. Variations in the absolute value of ψ_{50} and a also alter the historical risk by influencing the shape of vulnerability curve (Equation (3.10)). Notably, for all considered magnitudes of the three hydraulic traits, relative change in risk significantly reduces when the effects of projected changes in specific humidity and CO_2 concentration are considered (Table B.31).

   Sensitivity to tree sizes. In addition to the plant hydraulic traits, sensitivity analysis was also performed for variations in tree height, diameter at breast height (DBH) and stand density. These variables influence the plant conductance according to $g_{p,max} = k_{sap}\text{SAI}/(H_c\rho_w)$, where k_{sap} is the sap wood conductivity; SAI is the sapwood area index; H_c is the canopy height; and ρ_w is the water density. Higher canopy height reduces the plant conductance, whereas larger DBH and higher stand density increase the plant conductance via larger SAI. Table B.32 lists the sensitivity of risks to plant conductance. 20% increase in plant conductance can result from
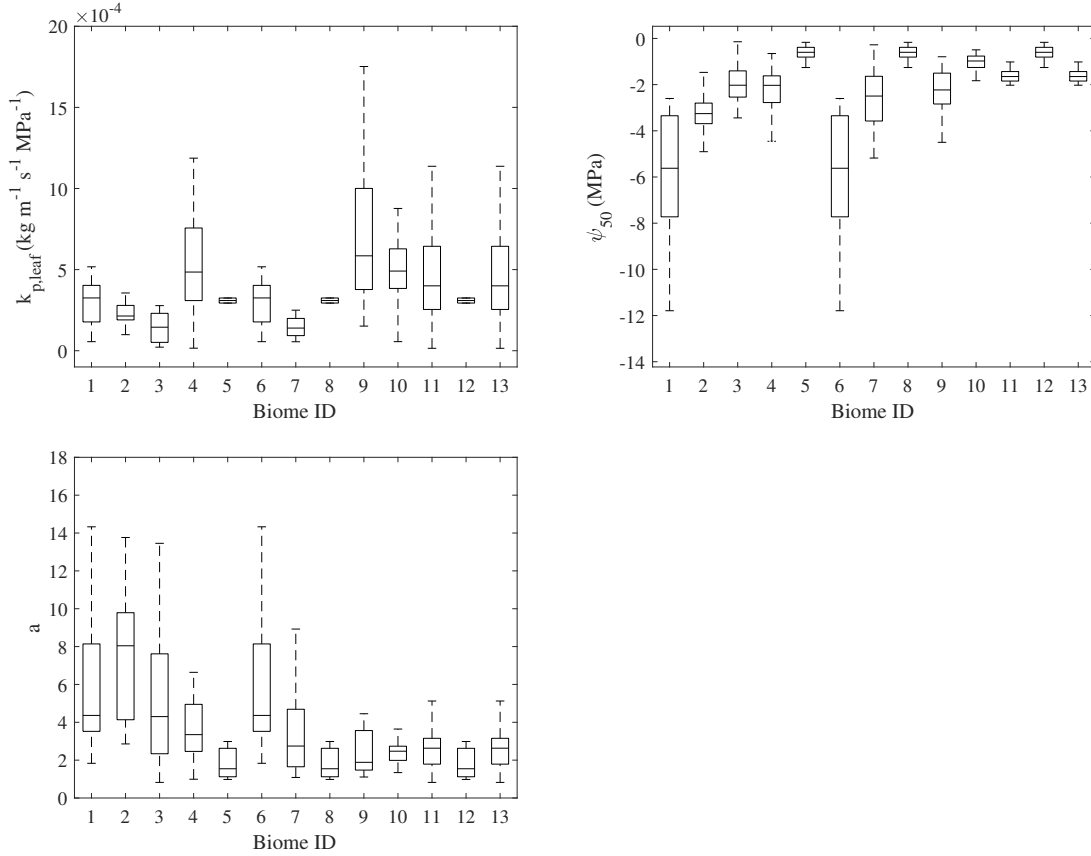
FIGURE B.31: Range of plant hydraulic traits for each biome. The range is obtained by mapping hydraulic traits of all species that belong to the same PFT and climate type as the given biome, using the TRY database (Kattge et al., 2011). The horizontal line in each box denotes the median, and the upper and lower boundaries of each box denote the 25% and 75% quantiles respectively.

20% decrease in canopy height or 20% increase in SAI due to either larger DBH or higher wood density. For all the biomes, on an average, 20% increase in the plant conductance raises the historical risk from 2.4% to 3.8%, suggesting that trees with larger DBH and higher wood density have higher mortality risk, all else being equal. This trend is consistent with previous studies suggesting tight correspondence of observed mortality with large DBH (Rowland et al., 2015) and high wood density (Bottero et al., 2017). Though the magnitude of risk could differ due to variations in tree sizes and wood density within each biome, the increasing extent of mortality risk

Table B.31: Sensitivity of historical risk and relative changes (difference between historical and future risk divided by historical risk) under projected climate to plant hydraulic traits. "HR" denotes historical risk; "P+T" denotes relative change of risk under projected changes in precipitation and temperature; "All" denotes relative change of risk under projected changes in precipitation, temperature, specific humidity and CO_2 concentration. Values are the average over all the biomes (%). Biomes with historical risk less than 0.01% were excluded from calculating the average relative change.

	25%			50%			75%		
Parameter	HR	P+T	All	HR	P+T	All	HR	P+T	All
$k_{p,leaf}$	1.2	224.4	31.0	2.4	158.8	21.0	4.6	86.0	-1.9
ψ_{50}	7.0	115.9	12.2	2.4	158.8	21.0	3.2	111.9	25.3
a	3.5	123.2	11.0	2.4	158.8	21.0	2.3	173.8	28.3

under projected climate is still found to be robustly alleviated by increasing specific humidity and CO_2 concentration (Table B.32).

Table B.32: Sensitivity of historical risk and the alleviating effect of specific humidity and CO_2 concentration to maximum plant conductance (%). Refer to Table B.31 for abbreviations.

	-20%			0%			+20%		
Parameter	HR	P+T	All	HR	P+T	All	HR	P+T	All
$g_{p,max}$	1.8	189.0	64.3	2.4	158.8	21.0	3.8	96.1	29.3

Sensitivity to model structure uncertainties. Although multiple components of the SPAC model have been previously examined and validated, given that a model is just an approximate representation of the complex reality, latent structural uncertainties (apart from parameter uncertainties) still exist. For example, the model in this study adopts a big-leaf representation, which could result in different canopy water and carbon flux compared with a two-big-leaf model or a multilayer model that explicitly considers shading effects on flux exchanges (Dai et al., 2004b; Teske and Thistle, 2004). Notably, computing gas exchange using a multilayer model at canopy scale still remains challenging because of the difficulty associated with accurately resolving the within canopy turbulence (Katul et al., 1998; Juang et al., 2008), which

generally requires large eddy simulation. Accurate estimation of the influence of leaf texture, size and inclination angle (Teske and Thistle, 2004) on incident direct and diffused radiation is challenging as well. To evaluate how sensitive the main results in this study are to the structural uncertainty inherent in the model, the modeled mortality risks for all the biomes under both historical and future climate scenarios were re-evaluated for $\pm 20\%$ uncertainty in the stomatal conductance. As stomatal conductance is influenced by leaf temperature, photosynthetically active radiation (PAR) at each leaf, humidity, air temperature, mesophyll conductance and turbulent flow right outside the stomata, $\pm 20\%$ uncertainty could be due to any of these controls. Table B.33 indicates that although lower stomatal conductance would lead to a lower mortality risk, it is still significantly intensified by changes in precipitation and warming temperature. Also, this increase in risk can again be largely alleviated by rising specific humidity and CO_2 concentration.

Table B.33: Sensitivity of historical risk and the alleviating effect of specific humidity and CO_2 concentration to uncertainties in stomatal conductance, on the average of all investigated biomes. -20% denotes the case where the 'actual' canopy level stomatal conductance should be 20% lower than the model estimates, and vice versa. Values are in %. Refer to Table B.31 for abbreviations.

-20%			0%			+20%		
HR	P+T	All	HR	P+T	All	HR	P+T	All
0.5	283.1	44.9	2.4	158.8	21.0	7.7	84.2	14.6

Therefore, although the exact magnitude of risk is difficult to estimate accurately due to uncertainties in parameters and model structure, the sensitivity analyses suggest that trend of response of mortality risk to projected climate are still robust.

B.4 Analyses based on alternative quantifications of risk

Considering that stress thresholds leading to actual mortality vary among sites and species, here we consider the following alternative metrics that employ different

thresholds of stress intensity and/or duration to evaluate the proneness to mortality. (1) *Mortality risk* is quantified as the probability of occurrence of either hydraulic failure ($\psi_{x,\min} < \psi_{50}$) or full stomatal closure. This is the risk analyzed in the main text. (2) *Cavitation risk* is the probability of $\psi_{x,\min} < \psi_{12}$. ψ_{12} is the plant water potential at 12% loss of conductivity when conduit cavitation starts to occur and may not be easy to be fully repaired (Sala et al., 2010; Delzon and Cochard, 2014). (3) *Hydraulic failure risk* is the probability of $\psi_{x,\min} < \psi_{50}$. (4) *Long-duration cavitation risk* is the probability of $\psi_{x,\min} < \psi_{12}$ existing for more than two weeks. The time threshold of two weeks was selected based on the distribution of duration for $\psi_{x,\min} < \psi_{12}$ (Figure B.41), indicating that most duration are within two weeks. (5) *Cavitation risk considering intensity* is quantified as $\int_0^T \min(\psi_{x,\min} - \psi_{12}, 0)\mathrm{dt}/T/\psi_{12}$, i.e., the integrated difference between $\psi_{x,\min}$ and ψ_{12} (only when $\psi_{x,\min} < \psi_{12}$) over time normalized by total time length and ψ_{12}. (6) *Stomatal closure risk* is the probability of full stomatal closure. (7) *Long-duration stomatal closure risk* is the probability of full stomatal closure that lasts for more than two weeks.

Figure B.42 illustrates the combined impacts of climate change on the alternative risks for the thirteen biomes, indicating a robust alleviating effect by increasing specific humidity and CO_2 concentration. Note that EBF biomes in tropical wet climate (biome 5, 8 and 12) show $\psi_{x,\min} < \psi_{12}$ almost all the time (Figure B.42a) owing to their high ψ_{12}, which can be seen from the high ψ_{50} of EBF in tropical climates, as listed in Table B.11. Table B.41 summarizes the cross-biome averaged response of each risk. Results based on different risk quantifications confirm a profound intensifying effect of changes in precipitation and temperature, which however can be significantly alleviated by rising humidity and CO_2 concentration. It is also found that combined change in climate variables tends to increase the risks associated with stomatal closure relative to that associated with low water potential. Agreement in

results based on alternative quantifications of risk indicate remarkable robustness of the findings in the main text.

Table B.41: Changes in risk using alternative quantifications, under the influence of changes in precipitation pattern and air temperature (P+T), additional changes in specific humidity (SH), additional changes in atmospheric carbon dioxide concentration (CO_2) and combined changes in all the considered climate variables (P+T+SH+CO_2) based on RCP4.5. Changes are quantified as the difference between historical and future risk divided by historical risk, and averaged across all the biomes with historical risks higher than 0.01%.

Risk type	P+T	SH	CO_2	P+T+SH+CO_2
Mortality risk	158.8 %	–46.6%	–91.2%	21.0%
Cavitation risk	174.2%	-98.8%	–87.1%	–11.7%
Hydraulic failure risk	163.4%	–27.9%	–144.1%	–8.6%
Long-duration cavitation risk	43.6%	–9.9%	–33.6%	0.1%
Cavitation risk considering intensity	54.6%	–8.3%	–47.6%	–1.3%
Stomatal closure risk	445.7%	–139.9%	–222.1%	83.7%
Long-duration stomatal closure risk	794.0%	–313.4%	–390.0%	90.6%
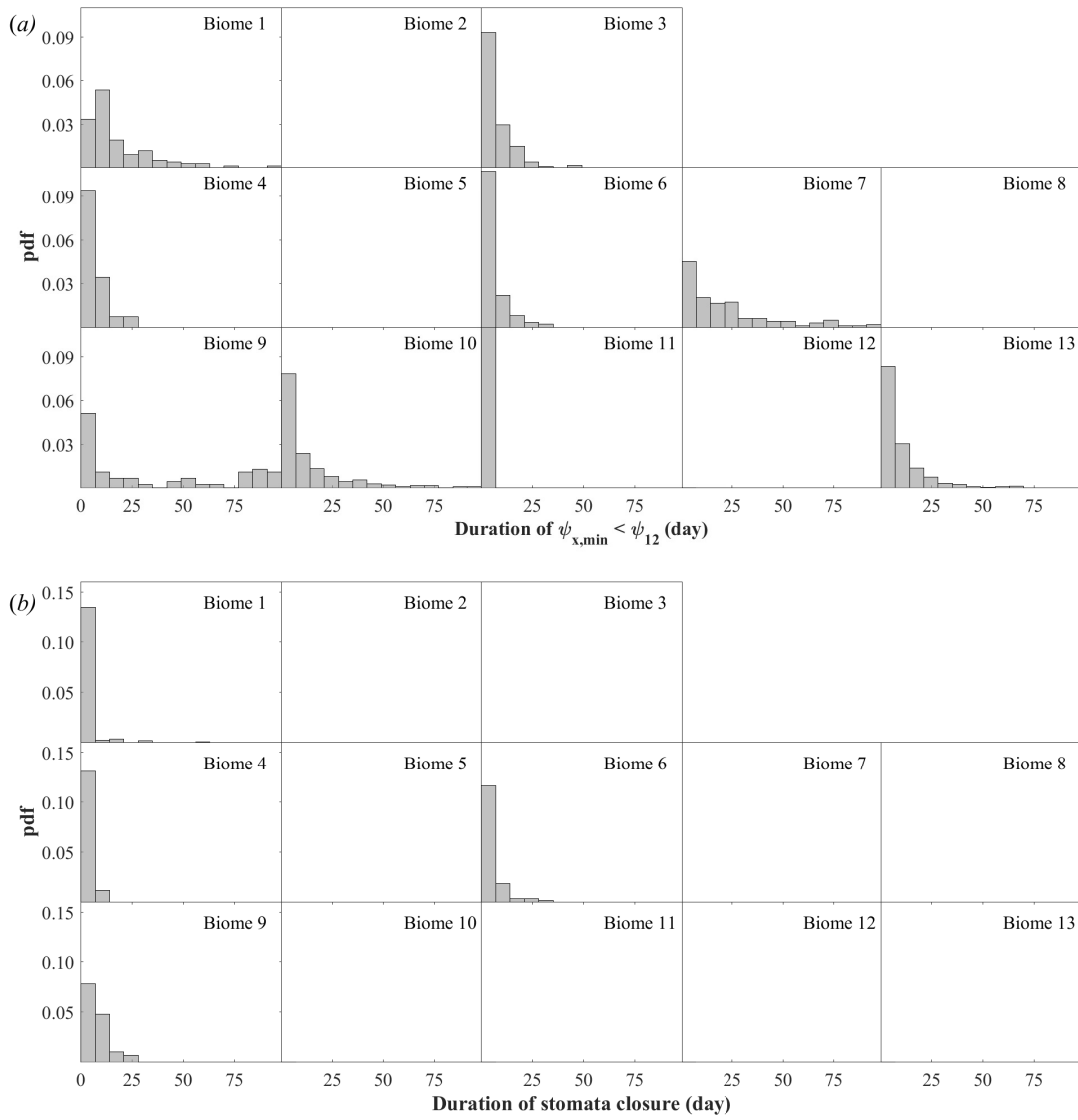
FIGURE B.41: Probability density of the duration of (a) $\psi_{x,\min} < \psi_{12}$ and (b) full stomatal closure. Bin width in the bar plots is one week.

(c)

(d)
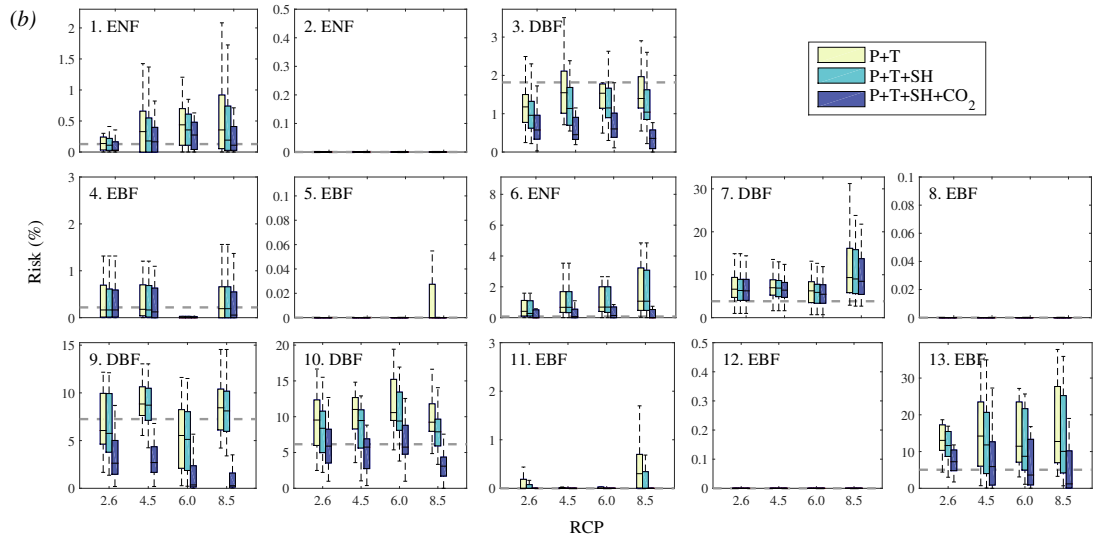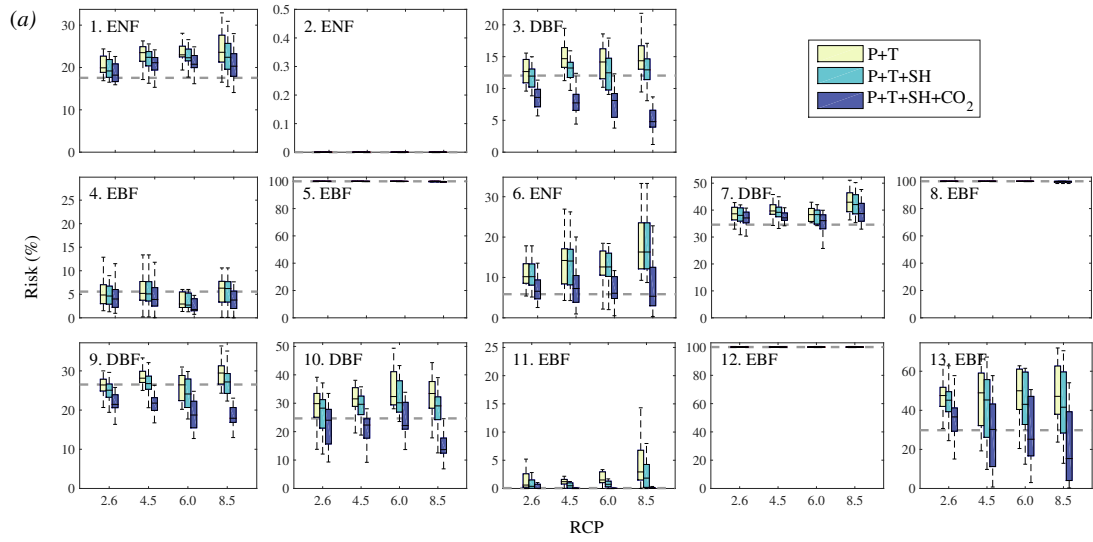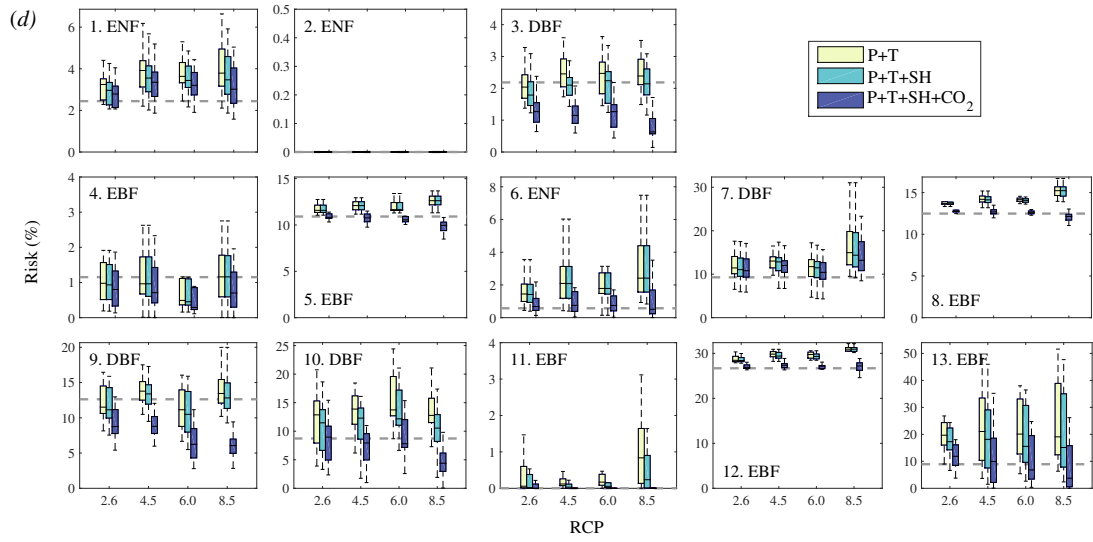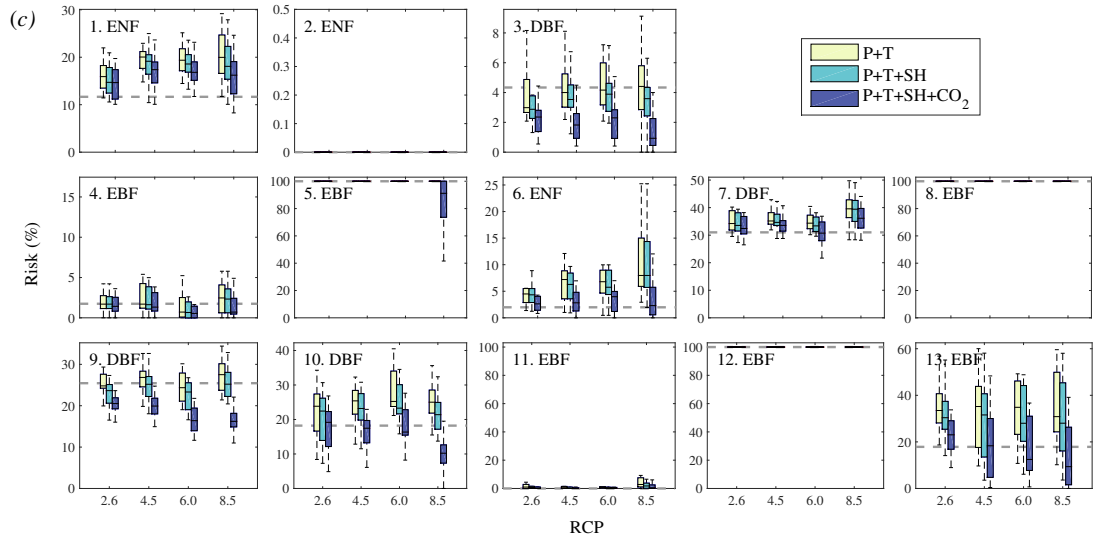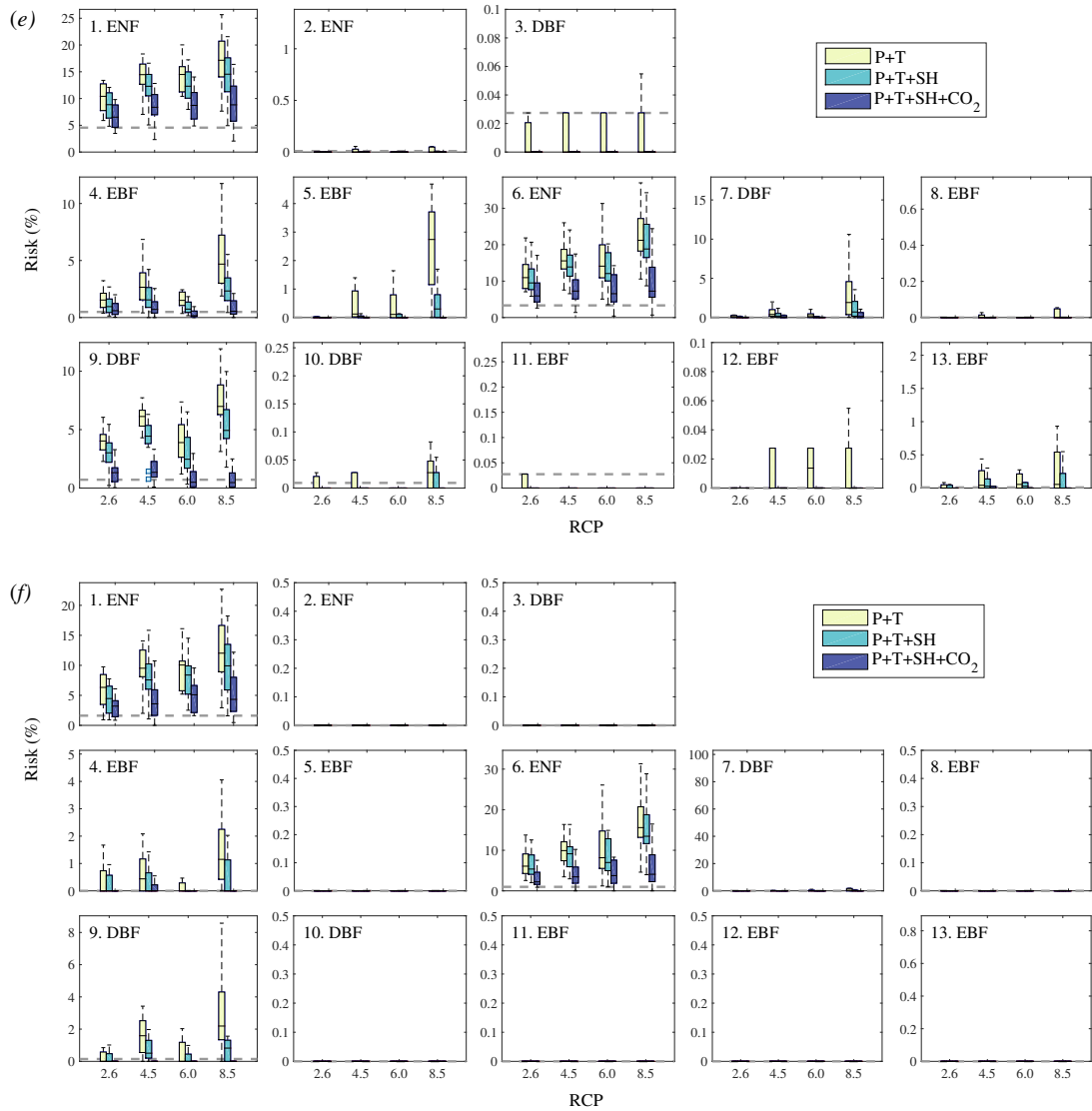
FIGURE B.42: Combined climate impacts of changes in climate on the (*a*) cavitation risk, (*b*) hydraulic failure risk, (*c*) long-duration cavitation risk, (*d*) cavitation risk considering intensity, (*e*) stomatal closure risk and (*f*) long-duration stomatal closure risk in the 13 biomes. Gray dashed lines show the risks under historical climate. Upper and lower boundaries of the boxes correspond to the 25th and 75th quantiles of the risk based on multi-model projections in each RCP scenario.

Appendix C

Supporting information for chapter 4

C.1   Bayesian dynamic linear model derivation

Model setup. The dynamic linear model (DLM) is adapted from (Prado and West, 2010; West and Harrison, 1997). Explanation of the notations are listed in Table C.11.

$$y_t = \boldsymbol{F}_t^T \boldsymbol{\theta}_t + v_t \tag{C.1}$$

$$\boldsymbol{\theta}_t = \boldsymbol{G} \boldsymbol{\theta}_{t-1} + \boldsymbol{w}_t \tag{C.2}$$

The model contains three modules, i.e., local mean and trend, seasonality and regression, which are denoted with subscripts of l,s and r respectively in the following discussions.

   The local mean and trend module describes the local mean and change between two time steps. The dimension of this module is $p_l = 2$. The corresponding regression vector ($\boldsymbol{F}_l$) and state evolution matrix ($\boldsymbol{G}_l$) are

$$\boldsymbol{F}_l = \begin{bmatrix} 1 \\ 0 \end{bmatrix}, \ \boldsymbol{G}_l = \begin{bmatrix} 1 & 1 \\ 0 & 1 \end{bmatrix}$$

Hence Equation (C.1) and (C.2) for this module can be written as

$$y_{l,t} = \theta_{l1,t} + v_{l,t}$$

$$\boldsymbol{\theta}_{l,t} = \begin{bmatrix} \theta_{l1,t} \\ \theta_{l2,t} \end{bmatrix} = \begin{bmatrix} 1 & 1 \\ 0 & 1 \end{bmatrix} \begin{bmatrix} \theta_{l1,t-1} \\ \theta_{l2,t-1} \end{bmatrix} + \boldsymbol{w}_{l,t} = \begin{bmatrix} \theta_{l1,t-1} + \theta_{l2,t-1} \\ \theta_{l2,t-1} \end{bmatrix} + \boldsymbol{w}_{l,t}$$

where $\theta_{l1,t}$ and $\theta_{l2,t}$ represent the mean and trend at time t respectively.

A Fourier form representation of seasonality (West and Harrison, 1997) is used here, with a single harmonic component represented by

$$\boldsymbol{F}_{s1} = \begin{bmatrix} 1 \\ 0 \end{bmatrix}, \quad \boldsymbol{G}_{s1} = \begin{bmatrix} \cos\omega_1 & \sin\omega_1 \\ -\sin\omega_1 & \cos\omega_1 \end{bmatrix}$$

where ω_1 is the frequency. This representation is equivalent to a Fourier component, as the expectation of the seasonal component at time $t + k$ given all the historical data till time t is

$$\mathbb{E}[y_{s,t+k}|y_{s,1},\ldots,y_{s,t}] = \boldsymbol{F}_{s1}^T \boldsymbol{\theta}_{s,t+k} = \boldsymbol{F}_{s1}^T \boldsymbol{G}_{s1}^k \boldsymbol{\theta}_{s,t}$$

$$= \begin{bmatrix} 1 & 0 \end{bmatrix} \begin{bmatrix} \cos\omega_1 k & \sin\omega_1 k \\ -\sin\omega_1 k & \cos\omega_1 k \end{bmatrix} \begin{bmatrix} \theta_{s1,t} \\ \theta_{s2,t} \end{bmatrix} = A_t \cos(\omega_1 k + \phi_t)$$

where A_t and ϕ_t are the amplitude and phase of the harmonic component that are functions of $\boldsymbol{\theta}_{s,t}$. When using q harmonic components to describe seasonality, the dimension of this module is $p_s = 2q$. Combining all harmonic components together,

$$\boldsymbol{F}_s = \begin{bmatrix} \boldsymbol{F}_{s1} \\ \vdots \\ \boldsymbol{F}_{sq} \end{bmatrix}, \quad \boldsymbol{G}_s = \begin{bmatrix} \boldsymbol{G}_{s1} & \ldots & \boldsymbol{0} \\ \vdots & \ddots & \vdots \\ \boldsymbol{0} & \ldots & \boldsymbol{G}_{sq} \end{bmatrix}$$

where $\boldsymbol{F}_{sj} = \boldsymbol{F}_{s1}$ and $\boldsymbol{G}_{sj}$ is the evolution matrix with a frequency of ω_j, for ($j = 1,\ldots,q$). In this study, one or two harmonic components with periods of one year and half year were used. The seasonality representation that gives the maximum model likelihood was selected for each pixel.

The regression module incorporates the influence of independent variables $(x_1, \ldots, x_{p_r})$ on y_t using

$$\boldsymbol{F}_{r,t} = [x_{1,t}, \ldots, x_{p_r,t}], \ \boldsymbol{G}_r = \boldsymbol{I}_{p_r}$$

The corresponding $\boldsymbol{\theta}_{r,t}$ contains the coefficients representing the influence of each independent variable on the observable at time t. In this study, independent variables include the observation at the previous time step, i.e, y_{t-1}, and one of the following candidate climate conditions from Daymet V3 (Thornton et al., 2014): air temperature, net shortwave radiation, vapor pressure deficit and available water amount. The available water amount is calculated as rainfall plus snow melt as part of the study area are located in a snow setting. These climate conditions were aggregated to 16-day average between two observations of NDVI. The anomaly for each variable was obtained by subtracting the long-term average within that 16-day interval, thus removing seasonality in climate variables. Then the anomaly for each variable was rescaled by dividing its standard deviation for computational efficiency and stability of the covariance matrices. The rescaled climate anomaly and lag-1 NDVI observation were included as independent variables in $\boldsymbol{F}_{r,t}$. Only one climate variable was used to keep the model dimension and computation load low. Models using each one of the climate variables were implemented and the one with the highest model likelihood was chosen for further analyses. The item in $\boldsymbol{\theta}_{r,t}$ corresponding to y_{t-1} is the autocorrelation used to identify EWS.

Combining these three modules together, the full DLM has a dimension of $p = p_l + p_s + p_r$ and

$$\boldsymbol{F}_t = \begin{bmatrix} \boldsymbol{F}_l \\ \boldsymbol{F}_s \\ \boldsymbol{F}_{r,t} \end{bmatrix}, \ \boldsymbol{G} = \begin{bmatrix} \boldsymbol{G}_l & \boldsymbol{0} & \boldsymbol{0} \\ \boldsymbol{0} & \boldsymbol{G}_s & \boldsymbol{0} \\ \boldsymbol{0} & \boldsymbol{0} & \boldsymbol{G}_r \end{bmatrix}, \ \boldsymbol{\theta}_t = \begin{bmatrix} \boldsymbol{\theta}_{l,t} \\ \boldsymbol{\theta}_{s,t} \\ \boldsymbol{\theta}_{r,t} \end{bmatrix}$$

Forward filtering. First assume that the variance of noise ν and $\boldsymbol{W}_t$ are known. At time $t - 1$, given all the observed data $D_{t-1} = \{y_1, \ldots, y_{t-1}\}$, $\boldsymbol{\theta}_t$ is assumed to

follow a multivariate normal distribution, i.e.,

$$\boldsymbol{\theta}_{t-1}|D_{t-1} \sim N(\boldsymbol{m}_{t-1}, \boldsymbol{C}_{t-1}) \tag{C.3}$$

Plugging in Equation (C.2), the prior distribution of $\boldsymbol{\theta_t}$ is

$$\boldsymbol{\theta}_t|D_{t-1} \sim N(\boldsymbol{a}_t, \boldsymbol{R}_t) \tag{C.4}$$

where $\boldsymbol{a}_t = \boldsymbol{G}\,\boldsymbol{m}_{t-1}$, $\boldsymbol{R}_t = \boldsymbol{G}\,\boldsymbol{C}_{t-1}\,\boldsymbol{G}^T + \boldsymbol{W}_t$. Plugging in Equation (C.1), the predictive distribution at time t is

$$y_t|D_{t-1} \sim N(f_t, q_t) \tag{C.5}$$

where $f_t = \boldsymbol{F}_t^T\,\boldsymbol{a}_t$, $q_t = \boldsymbol{F}_t^T\,\boldsymbol{R}_t\,\boldsymbol{F}_t + \nu$. Coming to time t, the posterior estimation of $\boldsymbol{\theta}_t$ given all the observation till t is given by the Bayes rule:

$$p(\boldsymbol{\theta}_t|D_t) = p(\boldsymbol{\theta}_t|y_t, D_{t-1}) \propto p(\boldsymbol{\theta}_t|D_{t-1})\,p(y_t|\boldsymbol{\theta}_t, D_{t-1}) = N(\boldsymbol{m}_t, \boldsymbol{C}_t) \tag{C.6}$$

where $\boldsymbol{m}_t = \boldsymbol{a}_t + \boldsymbol{A}_t\,e_t$, $e_t = y_t - f_t$, $\boldsymbol{A}_t = \boldsymbol{R}_t\,\boldsymbol{F}_t/q_t$, $\boldsymbol{C}_t = \boldsymbol{R}_t - q_t\,\boldsymbol{A}_t\,\boldsymbol{A}_t^T$. When y_t is missing such as on cloudy or snow affected days in this case, the prior from historical data $p(\boldsymbol{\theta}_t|D_{t-1})$ (Equation (C.4)) is used for the estimation of $\boldsymbol{\theta}_t$ (Prado and West, 2010).

However, $p(\boldsymbol{\theta}_t|D_t)$ is not completely solved yet as the variance of noise, ν and $\boldsymbol{W}_t$, are unknown in this study. Hence the following revision is incorporated for variance learning.

Without loss of generality, let $v_t \sim N(0, \nu)$ and $\boldsymbol{w}_t \sim N(0, \nu\,\boldsymbol{W}_t^*)$, where ν and $\boldsymbol{W}_t^*$ are unknown. $\boldsymbol{W}_t^*$ is a rescaled $\boldsymbol{W}_t$. Conditional on ν, the derivations of Equation (C.3)–(C.6) remain the same except the covariance matrices are rescaled,

$$\boldsymbol{\theta}_{t_1}|D_{t-1}, \nu \sim N(\boldsymbol{m}_{t-1}, \nu\,\boldsymbol{C}_{t-1}^*) \tag{C.7}$$

$$\boldsymbol{\theta}_t|D_{t-1}, \nu \sim N(\boldsymbol{a}_t, \nu\,\boldsymbol{R}_t^*) \tag{C.8}$$

$$y_t|D_{t-1}, \nu \sim N(f_t, \nu\,q_t^*) \tag{C.9}$$

$$\boldsymbol{\theta}_t|D_t, \nu \sim N(\boldsymbol{m}_t, \nu\,\boldsymbol{C}_t^*) \tag{C.10}$$

Assuming the variation of observational error follows an inverse-gamma (IG) distribution,

$$\nu|D_{t-1} \sim IG(n_{t-1}/2, d_{t-1}/2) \tag{C.11}$$

$$\nu|D_t \sim IG(n_t/2, d_t/2) \tag{C.12}$$

where $n_t = n_{t-1} + 1$ is the degree of freedom and $d_t = d_{t-1} + e_t^2/q_t^*$. After integrating (7)–(12) and marginalizing out ν, the distributions unconditional on ν become t distributions.

$$\boldsymbol{\theta}_{t_1}|D_{t-1} \sim T(\boldsymbol{m}_{t-1}, \boldsymbol{C}_{t-1}^{**}) \tag{C.13}$$

$$\boldsymbol{\theta}_t|D_{t-1} \sim T(\boldsymbol{a}_t, \boldsymbol{R}_t^{**}) \tag{C.14}$$

$$y_t|D_{t-1} \sim T(f_t, q_t^{**}) \tag{C.15}$$

$$\boldsymbol{\theta}_t|D_t \sim T(\boldsymbol{m}_t, \boldsymbol{C}_t^{**}) \tag{C.16}$$

where $\boldsymbol{C}_{t-1}^{**} = s_{t-1}\boldsymbol{C}_{t-1}^*$, $\boldsymbol{R}_t^{**} = s_{t-1}\boldsymbol{R}_t^*$, $q_t^{**} = s_{t-1}q_t^*$ and $\boldsymbol{C}_t^{**} = s_t\boldsymbol{C}_t^*$, with $s_{t-1} = d_{t-1}/n_t$ and $s_t = d_t/n_t$.

$\boldsymbol{W}_t$ is obtained using the method of discounting (Prado and West, 2010). Recall the prior variance of the state vector $\boldsymbol{\theta}_t$ (Equation (C.4)) is $\mathrm{Var}(\boldsymbol{\theta_t}|D_{t-1}) = \boldsymbol{R}_t = \boldsymbol{G}\boldsymbol{C}_{t-1}\boldsymbol{G}^T + \boldsymbol{W}_t = \boldsymbol{P}_t + \boldsymbol{W}_t$, where $\boldsymbol{P}_t$ is the variance without stochastic noise in state evolution, i.e., when $\boldsymbol{W}_t = \boldsymbol{0}$. When $\boldsymbol{W}_t \neq \boldsymbol{0}$, it can be assumed that $\boldsymbol{R}_t = \boldsymbol{P}_t/\delta$ with the parameter $\delta \in (0, 1]$. That is, due to stochastic noise, the variance of the state vector at $t-1$ gets inflated by $1/\delta - 1$ for the next time step. This is equivalent to increasing the variance of each entry of the state vector independently by $1/\delta - 1$, or discounting the degree of freedom from n_t to $\delta\, n_t$ (Prado and West, 2010). Smaller δ results in more rapid change whereas larger δ represents slower change in $\boldsymbol{\theta}_t$. In this study, an identical $\delta = 0.98$ was used for all the three modules (Prado and West, 2010; West and Harrison, 1997), which ensures that the model allows the same extent of freedom for local mean and trend, seasonality and regression

coefficients to vary through time. Under this condition, the extent of change for each module can be estimated based on the likelihood of observations following the forward filtering procedure. At time 0, non-informative priors of $\boldsymbol{m_0} = \boldsymbol{0}$, $\boldsymbol{C_0^*} = \boldsymbol{I}$, $n_0 = p$, $d_0 = 0.2^2 \, n_0$ were provided, allowing a wide range of variation for $\boldsymbol{\theta}_t$ in the beginning and let the variance gradually converge as more data points are included (Figure 4.1b). Then the posterior distribution of the state-vector at each time point given historical observations can be obtained from Equation (C.16).

Table C.11: Names and dimensions of notations in DLM.

Symbol	Dimension	Name
y_t	scalar	observation
$\boldsymbol{\theta_t}$	$p \times 1$	state vector
$\boldsymbol{F}_t$	$p \times 1$	regression vector
v_t	scalar	observation noise
ν	scalar	observation noise variance
$\boldsymbol{G}$	$p \times p$	state evolution matrix
$\boldsymbol{w}_t$	$p \times 1$	state evolution noise
$\boldsymbol{W}_t$	$p \times p$	state evolution noise covariance matrix

C.2 Synthetic experiments of DLM and comparison with alternative EWS metrics

This section examines the efficacy of EWS derived from DLM in detecting the change in system resilience and compares EWS with alternative metrics used in previous studies. Empirical metrics used as EWS in previous studies (Scheffer et al., 2009; Dakos et al., 2012, 2015), such as autocorrelation and variance that are obtained using a moving-window approach, were also computed for comparison. Note that only autocorrelation was tracked using the DLM. Variance was not tracked, as in an autoregressive model such as the DLM, variance is intrinsically dependent on autocorrelation, and its temporal variation can be contaminated by non-stationary stochastic perturbation. This can be demonstrated based on the following simplified

first-order autoregressive process (AR(1)) with a zero mean,

$$y_{t+1} = \alpha_t \, y_t + \sigma_t$$

where y_t is the deviation from the equilibrium state at time t; α_t is the lag-1 auto-correlation at time t; and $\sigma_t \sim N(0, \varepsilon_t^2)$ is the noise due to stochastic perturbations. Both α_t and σ_t are considered as independent from y_t. The variance is

$$\mathrm{Var}(y_{t+1}) = \alpha_t^2 \, \mathrm{Var}(y_t) + \varepsilon_t^2$$

When the time interval between observations is sufficiently small, $\mathrm{Var}(y_{t+1}) \approx \mathrm{Var}(y_t)$, hence

$$\mathrm{Var}(y_t) = \frac{\varepsilon_t^2}{1 - \alpha_t^2}$$

Under the assumption that the stochastic perturbation is stationary, i.e., $\varepsilon_t^2 = \varepsilon^2$, variance would increase as the autocorrelation increases. Such dependence makes it redundant to consider variance as an extra metric. In addition, under non-stationary stochastic perturbation, changes of stochastic perturbation could mask out the influence of autocorrelation. This could be the case for NDVI time series especially during drought, when forests may be exposed to chronic unfavorable climate conditions with little variation, or largely varying stress due to extreme heat wave events. For these reasons, this study focuses on DLM inferred autocorrelation which allows evaluation of resilience under both stationary and non-stationary stochastic perturbations, rather than variance.

Another metric describing resilience can be obtained from the drift term of one-dimensional Langevin equation (Racca and Porporato, 2005), which is represented by

$$\frac{\mathrm{d}x}{\mathrm{d}t} = A(x) + \sqrt{B(x)}\xi(t) \tag{C.17}$$

where $A(x)$ and $B(x)$ are the drift term and diffusion term respectively; $\xi(t)$ is zero-mean white Gaussian noise or Langevin force. The slope of $A(x)$ versus x around the stable point represents the ease with which the system may recover back to the stable point after perturbation. Larger (less negative) slope indicates slower recovery hence lower resilience. This metric, together with the non-parametric autocorrelation and variance, was also computed using a moving window and compared with the autocorrelation derived from DLM.

To evaluate the efficacy of DLM and compare the model inferred autocorrelation with the other metrics, six synthetic experiments on a simple dynamical system (Equation (C.18)) from (Scheffer et al., 2009) were implemented.

$$f(x) = \frac{\mathrm{d}x}{\mathrm{d}t} = \gamma \left(x - a\right)\left(x - b\right) + \varepsilon_t \tag{C.18}$$

This system has one stable fixed point $x_1 = a$ and one unstable fixed point $x_2 = b$ ($\gamma > 0, b > a$). It can be derived that near the stable fixed point, the recovery rate is $\lambda = \mathrm{d}f/\mathrm{d}x = -\gamma\left(b - a\right)$, and the lag-1 autocorrelation is $e^{\lambda \Delta t}$ if the noise ε_t is i.i.d. and independent of x. With fixed γ and a, smaller b leads to slower (less negative) recovery rate, i.e., lower resilience, and raises the autocorrelation around the stable fixed point. By changing the parameters and noise configuration, the performance the aforementioned metrics in detecting change in autocorrelation under different scenarios was examined.

Experiment 1. A time series, with resilience and white noise parameters as specified in Figure C.21a, was generated using Equation (C.18). Near the stable fixed point of 0.5, the parameters specify an autocorrelation of 0.50 before time step 600, which was raised to 0.74 afterwards. The magnitude of actual autocorrelation computed from the time series after adding white noise is expected to be lower than the specified values. This time series was fed to DLM to test its ability in capturing the change in autocorrelation. It can be clearly seen that after time step 600, the

146

estimated autocorrelation increased to a new level, close to but slightly lower than the specified value of 0.74 (Figure C.21b). Although some intermittency exists due to noisy fluctuations, high autocorrelation was identified for the majority of time after time step 600. Empirical autocorrelation and the drift slope follow the same pattern (Figure C.21c), with high values identified after time step 600. Standard deviation also increased slightly from an average of 0.05 to 0.06, though fluctuating around its 80th percentile due to noise.

Experiment 2. Figure C.22 illustrates an experiment similar to experiment 1 except that ε_t includes both known forcing (randomly generated using a Gaussian distribution) and unknown white noise. The known forcing was incorporated into the regression module of the DLM. With this consideration of forcing, DLM robustly identifies increased autocorrelation after time step 600 (Figure C.22b). Empirical autocorrelation and the drift slope generally exhibit a similar pattern (Figure C.22c), which, however, are more sensitive to fluctuation in data partly due to the inability to discriminate the influence of forcing.

Experiment 3. In this experiment also, ε_t includes both known forcing and unknown white noise. Unlike experiment 2 where the autocorrelation was increased by reducing system resilience, the time series here was generated with fixed resilience parameters, but the autocorrelation in forcing increased after time step 600. It can be seen that DLM effectively shows little change in autocorrelation over time, except for a few intermittent periods exceeding the threshold (Figure C.23b). The empirical metrics, however, again exhibit high yet fluctuating values after time step 600 (Figure C.23c), which is a false signal for system resilience as the increased empirical autocorrelation and drift slope are not results of reduced resilience but more auto-correlated forcing. Comparison of results from experiments 2 and 3 demonstrate the ability of DLM to clearly distinguish reduced resilience from changes in autocorrelation due to auto-correlated forcing (Figure C.22b, C.23b).
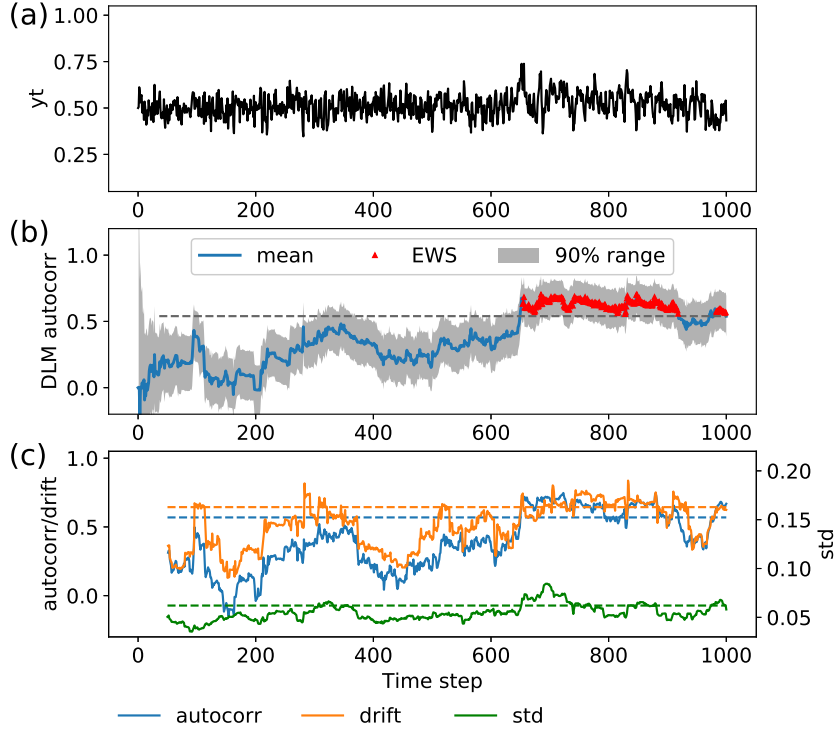
FIGURE C.21: (a) Time series generated using Equation (C.18) with $\gamma = 0.2$, $a = 0.5$, $b = 4\,(t < 600)$, $b = 2\,(t \geqslant 600)$, $\varepsilon_t \overset{\text{i.i.d.}}{\sim} N(0, 0.05^2)$. (b) Mean (blue line) and uncertainty range (grey area) of the autocorrelation in (a) identified using DLM. Abnormally high autocorrelation with mean exceeding the longterm mean of the upper boundary of the uncertainty range are identified as EWS (red triangles). (c) Empirical metrics including empirical lag-1 autocorrelation (blue line), standard deviation (green line) and the drift slope $(\mathrm{d}A(x)/\mathrm{d}x + 1$ from Equation (C.17). Evaluation was performed using a moving window with a width of 50 time steps. 1 was added to the drift slope to obtain a magnitude comparable to autocorrelation, to facilitate visual comparison. All aforementioned metrics are expected to be large under low resilience. Dashed lines denote the 80th percentile of metrics in the same color, for identification of abnormally high values.

Experiment 4. In this experiment, apart from known forcing and unknown white noise, ε_t also contains unknown seasonal cycles generated using two harmonic components. The system resilience was again reduced after time step 600, while forcing and seasonal cycles remained the same. In this case, when the time series is blended with seasonal cycles, DLM can still identify reduced resilience (Figure C.24b). The magnitudes of empirical metrics become higher than those in previous

148
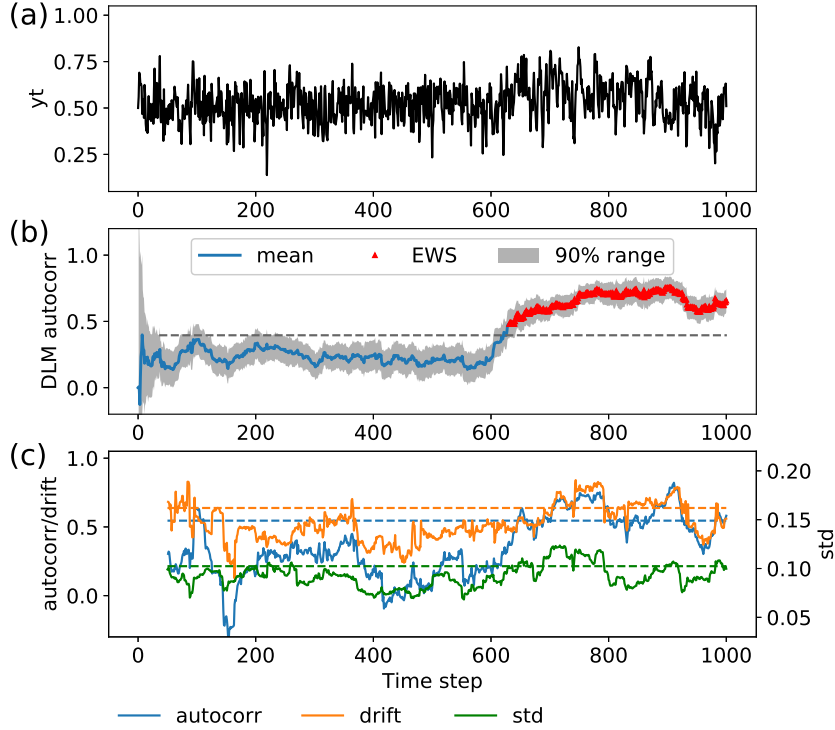
FIGURE C.22: (a) Time series generated using Equation (C.18) with $\gamma = 0.2$, $a = 0.5$, $b = 4\,(t < 600)$, $b = 2\,(t \geqslant 600)$, $\varepsilon_t = \varepsilon_{f,t} + \varepsilon_{n,t}$, where $\varepsilon_{f,t} \overset{\text{i.i.d.}}{\sim} N(0, 0.07^2)$ denotes forcing and $\varepsilon_{n,t} \overset{\text{i.i.d.}}{\sim} N(0, 0.05^2)$ denotes noise. For details on (b) and (c), refer to Figure C.21.

experiments, due to autocorrelation and higher variance embedded in the seasonal cycles (Figure C.24c). The influence of seasonal cycles and noise make the change in resilience hard to identify using empirical metrics.

Experiment 5. This experiment examines the influence of a step-wise drop in the time series on autocorrelation. After time step 600, the magnitude of the stable state dropped by 0.25 (Figure C.25a) whereas the resilience remained the same. It can be seen that such change was picked up by the term of local mean in DLM (Figure C.25b) without raising autocorrelation (Figure C.26c). This result suggests that a sudden drop in NDVI possibly due to canopy die-back would not induce false alarm of high autocorrelation if resilience remained unchanged.
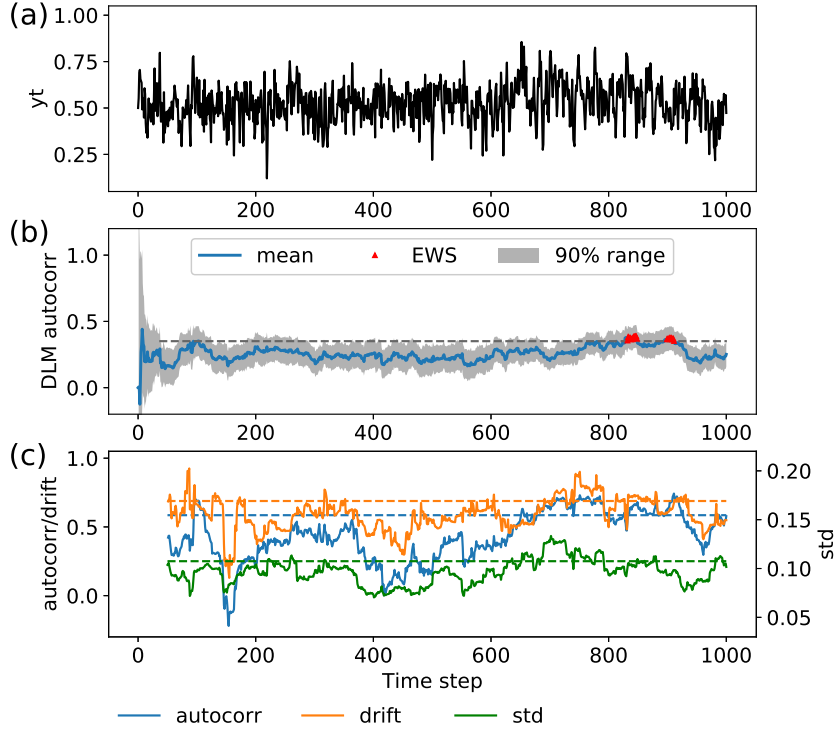
FIGURE C.23: (a) Time series generated using Equation (C.18) with $\gamma = 0.2$, $a = 0.5$, $b = 4$, $\varepsilon_t = \varepsilon_{f,t} + \varepsilon_{n,t}$, where $\varepsilon_{n,t} \overset{\text{i.i.d.}}{\sim} N(0, 0.05^2)$ is noise and the forcing $\varepsilon_{f,t} = \sigma_{f,t} + \alpha_f \varepsilon_{f,t-1}$, in which $\sigma_{f,t} \overset{\text{i.i.d.}}{\sim} N(0, 0.07^2)$ and the autocorrelation of forcing $\alpha_f = 0.2 \,(t < 600)$, $\alpha_f = 0.6 \,(t \geqslant 600)$; $\sigma_{f,t}$ is independent of $\varepsilon_{f,t-1}$. For details on (b) and (c), refer to Figure C.21.

Experiment 6. This experiment examines the influence of a trend in the time series on autocorrelation. After time step 600, instead of a step-wise change in Experiment 5, the time series gradually reduced (Figure C.26a), representing to the case where NDVI exhibits a downward trend during prolonged drought. The resilience was prescribed as the same. Again the decreasing trend can be identified by the local mean (Figure C.26b) and the autocorrelation did not increase (Figure C.26c).

Overall, these theoretical experiments suggest that empirical metrics can reasonably capture the change in system resilience under settings with a controlled level of noise and little influence of forcing and seasonality. When the observed time series is
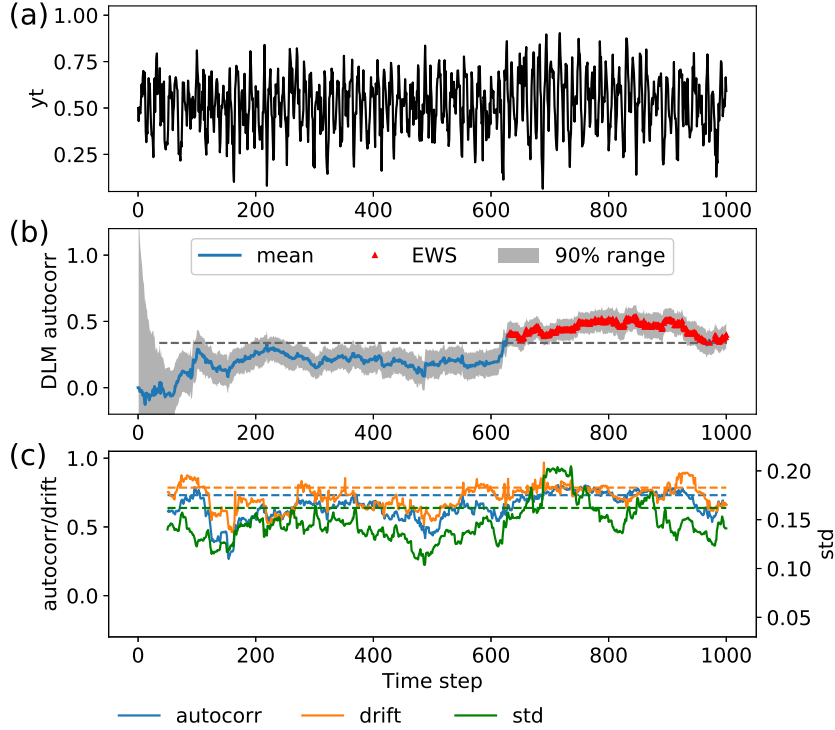
FIGURE C.24: (a) Time series generated using Equation (C.18) with $\gamma = 0.2$, $a = 0.5$, $b = 4$ $(t < 600)$, $b = 3$ $(t \geqslant 600)$, $\varepsilon_t = \varepsilon_{f,t} + \varepsilon_{s,t} + \varepsilon_{n,t}$ where $\varepsilon_{f,t} \overset{\text{i.i.d.}}{\sim} N(0, 0.07^2)$ is forcing $\varepsilon_{n,t} \overset{\text{i.i.d.}}{\sim} N(0, 0.05^2)$ is noise; and the seasonal cycle $\varepsilon_{s,t} = 0.05 \sin(\omega_1 (t - 6)) + 0.1 \sin(\omega_2 (t - 4))$, in which $\omega_1 = 2\pi/(365.25/16)$ and $\omega_2 = 2\omega_1$. For details on (b) and (c), refer to Figure C.21.

blended with forcing, seasonality and noise, empirical metrics may fail to identify the change or provide false signals. However, DLM performs more robustly by learning the influence of forcing, seasonal cycles and noise level from data, and estimating the autocorrelation conditional on these influences. Notably, such influences are ubiquitous in time series of vegetation dynamics such as NDVI, thus underscoring the need for a robust resilience estimation methodology for analyses. In addition, a step-wise or gradual decrease in the time series would not induce false alarms using DLM. Figure C.27 illustrates the fraction of area showing abnormally high empirical autocorrelation, variance and drift slope during 2005–2015, in comparison with observed mortality. Unlike the clear association between mortality and abnormally

151
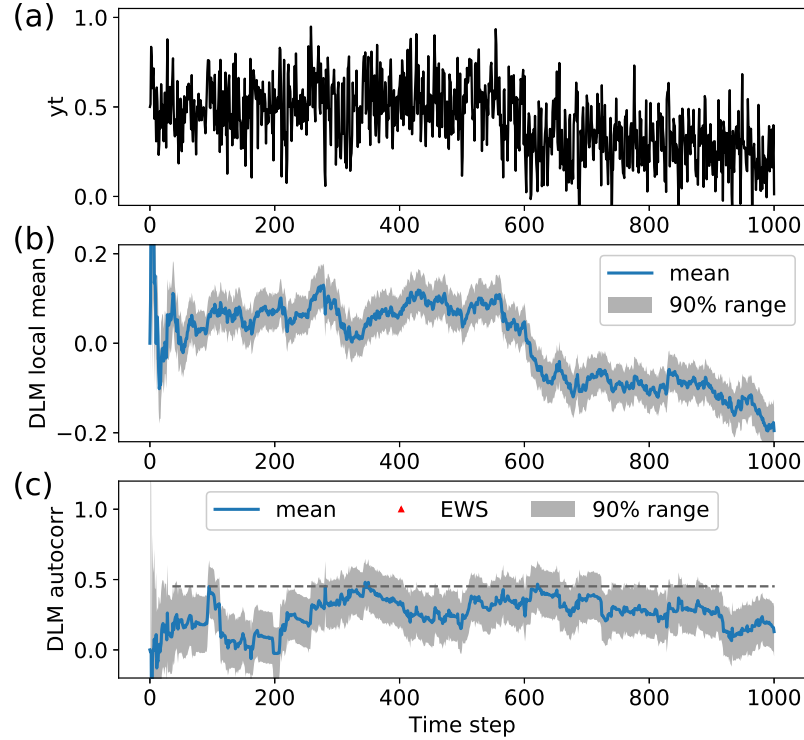
FIGURE C.25: (a) Time series generated using Equation (C.18) with $\gamma = 0.2$, $a = 0.5\,(t < 600)$, $a = 0.5 - \delta\,(t \geqslant 600)$, $b = 4\,(t < 600)$, $b = 4 - \delta\,(t \geqslant 600)$, where $\delta = 0.25$ is the magnitude of a step-wise drop in y_t; $\varepsilon_t = \varepsilon_{n,t}$ where $\varepsilon_{n,t} \overset{\text{i.i.d.}}{\sim} N(0, 0.15^2)$ is the noise; (b) Mean (blue line) and uncertainty range (grey area) of the local mean in (a) identified using DLM; (c) Mean (blue line) and uncertainty range (grey area) of the autocorrelation in (a) identified using DLM.

high autocorrelation identified using DLM (Figure 4.2, main text), the interannual variation of forest mortality was poorly captured by these metrics.

Code for theoretical experiments is available at `https://github.com/YanlanLiu/early-warning-signal-DLM`.

C.3 Critical slowing down during EWS period

To examine the connection between EWS, critical slowing-down, and loss of system resilience, a prototypical deterministic nonlinear dynamical model (Strogatz, 2014)
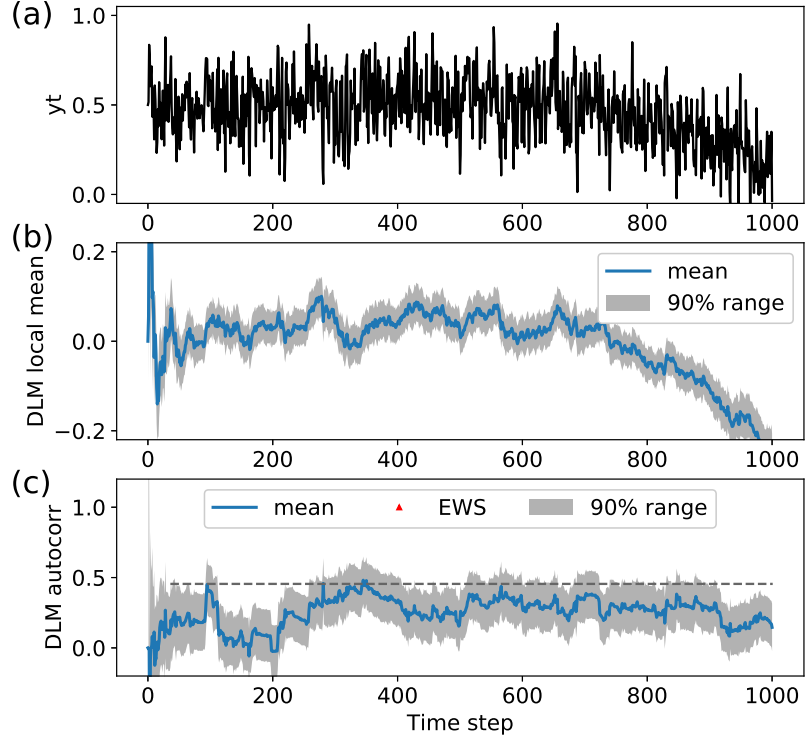
FIGURE C.26: (a) Time series generated using Equation (C.18) with $\gamma = 0.2$, $a = 0.5\,(t < 600)$, $a = 0.5 - \delta(t - 600)\,(t \geqslant 600)$, $b = 4\,(t < 600)$, $b = 4 - \delta(t - 600)\,(t \geqslant 600)$, where $\delta = 0.3/400$ is the slope of the decreasing trend in y_t; $\varepsilon_t = \varepsilon_{n,t}$ where $\varepsilon_{n,t} \overset{\text{i.i.d.}}{\sim} N(0, 0.15^2)$ is the noise; For details on (b) and (c), refer to Figure C.25.

as shown below is used.

$$f(x) = \frac{\mathrm{d}x}{\mathrm{d}t} = \tau\left(r\,x - x^3\right), \tag{C.19}$$

where r is the control parameter and τ is a time scale parameter. This model describes self-limiting growth and includes a linear term and a cubical reduction, instead of a quadratic reduction encountered in logistic models. The increased non-linearity is presumably due to intensification of competition among individuals due to climate stress. The corresponding potential $V(x)$ is

$$V(x) = -\int f(x)\,\mathrm{d}x = -\tau\left(\frac{r}{2}x^2 - \frac{1}{4}x^4\right) + C_0. \tag{C.20}$$

153
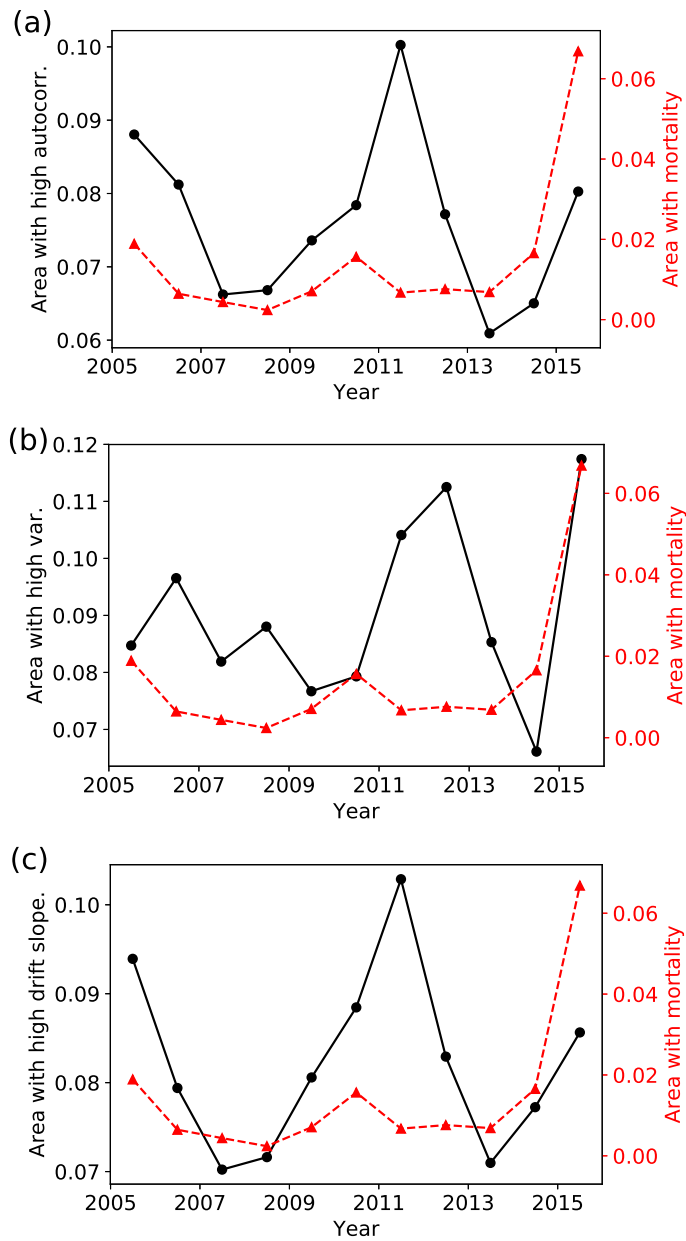
FIGURE C.27: The fraction of area showing abnormally high empirical autocorrelation (a), variance (b) and drift slope (c) during 2005–2015 in comparison to observed mortality. These empirical metrics were computed using a moving window with a width of 50 time steps (2.2 years) for each pixel in the entire study area. Abnormally high values were identified as those exceeding the 80th percentile of the metric during 2000–2015.

Without loss of generality, it may be assumed that $C_0 = 0$. When $r > 0$, this system has two stable-fixed points of $x^* = \pm\sqrt{r}$, at which $\mathrm{d}x/\mathrm{d}t = 0$ and $V = V_{\min}$. The width of each attraction basin, i.e., the range within which the system can recover without switching to another stable state, is $\sqrt{r}$. As r decreases, the attraction basin shrinks resulting in loss of resilience. In this prototypical system, bifurcation occurs at $r = 0$, and is associated with the critical slowing down (Figure C.31a). As τ decreases, the size of attraction basin does not change whereas the potential surface becomes flatter (Figure C.31b), thus contributing to a higher likelihood of switching under stochastic perturbations (i.e. loss of resilience). Change in τ and r can be captured by change in the recovery rate around the stable point, i.e.,

$$\lambda = \left.\frac{\partial f}{\partial x}\right|_{x=x*} = -2\,\tau\,r \tag{C.21}$$

which can be measured using the lag-1 autocorrelation of $e^{\lambda \Delta t}$ (Scheffer et al., 2009).

Using the NDVI time series in Figure 4.1 (main text), the model (Equation (C.19)) was fitted to data from two time periods with and without detected EWS respectively for illustration. As no abrupt shift occurred before the end, the observations are considered as samples from the attraction basin of one of the stable states. The state of the system (x) is taken here as the deseasonalized NDVI with its minimal value anchored to zero, i.e., the separation point between the two attraction basins, for both normal and EWS periods. Compared to the normal period, r is reduced from 0.022 to 0.012 during the EWS period (Figure C.32a), a signature of upcoming bifurcation and hence critical slowing down. The τ also decreased from 11.19 to 7.19. The reduction in both r and τ contributed to a flatter potential surface (Figure C.32b) and decreased recovery rate, i.e., lower resilience, and increased probability of abrupt transition under stochastic forcings. These findings suggest that critical slowing down occurred during the time when EWS was identified, supporting the

connection between empirically derived EWS, abrupt phase transitions, and loss of resilience.
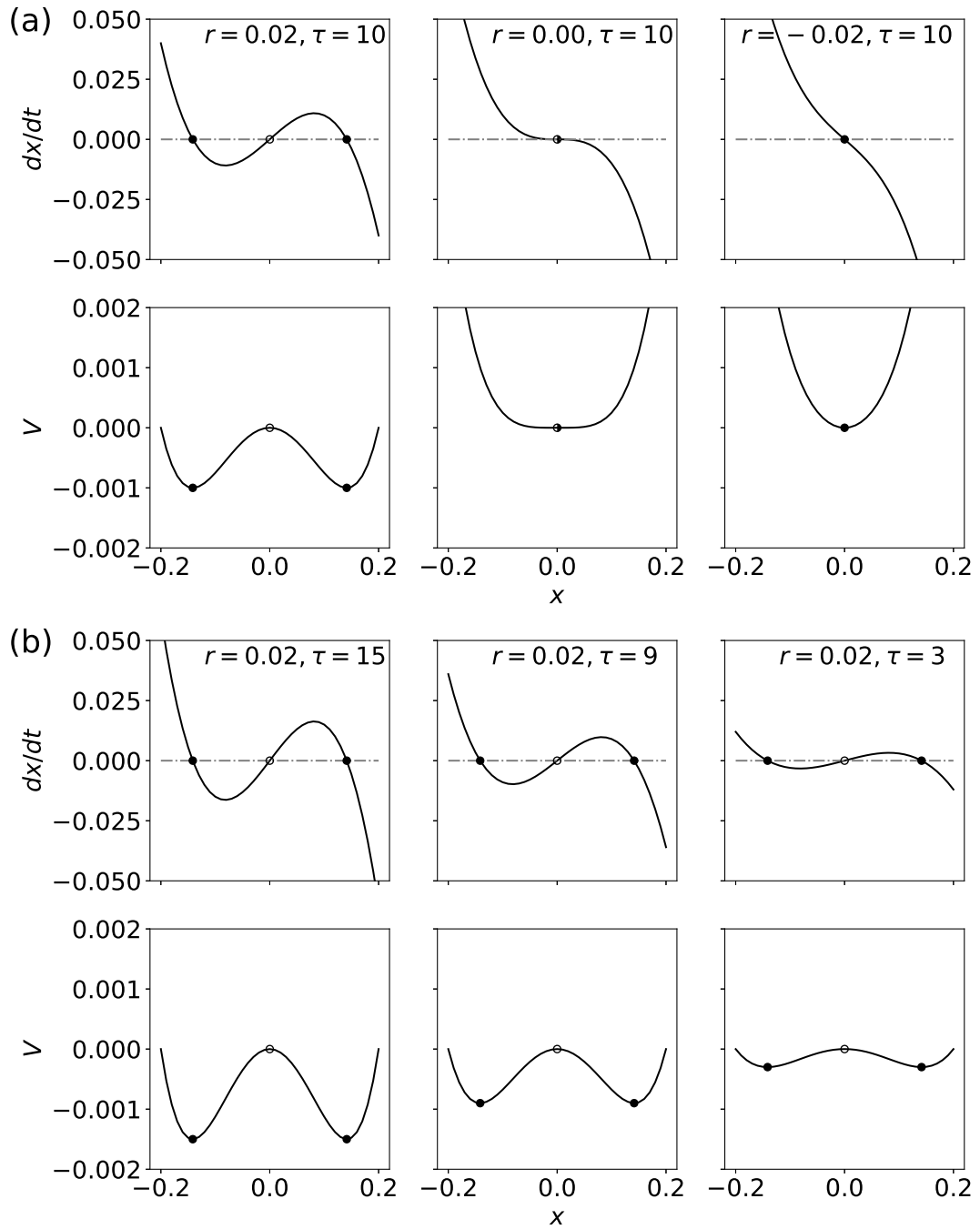
FIGURE C.31: Phase plots and potential surfaces of the dynamic system of Equation (C.19) under different values of (a) r and (b) τ.
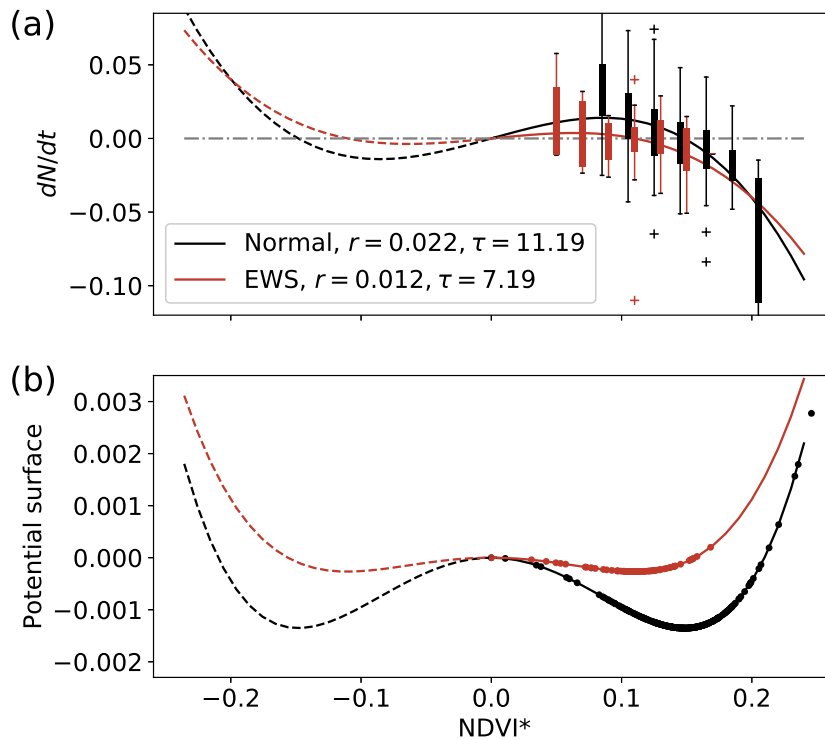
FIGURE C.32: (a) Phase plots and (b) potential surfaces of the dynamic system of Equation (C.19) fitted using NDVI during normal (without EWS, black) and EWS (red) periods (Figure 4.1, main text). NDVI* is the deseasonalized NDVI minus its minimal value (see SI Section S3 text). Box plots in (a) illustrate the range of data. Solid and dashed lines are fitted velocities and potential surfaces, representing the sampled and unsampled basins of attraction, respectively.

C.4   Relations between EWS characteristics and mortality probability across species and eco-climate regions

Relations between mortality area and the two EWS characteristics, i.e., the fraction of area showing EWS and EWS duration, were examined individually. As shown in Figure 4.4 in the main text, interannual variation in the probabilities of mortality and ALN is positively correlated with the fraction of area showing EWS. However, Figure C.41 here suggests that neither species-specific nor the integrated average of EWS duration by its own could explain the temporal variation in mortality probability. This indicates that EWS area is more effective in capturing the interannual variation of mortality probability than EWS duration.

As illustrated in Figure 4.4 in the main text, such relation between EWS area and mortality probability clearly differs among species. However, when combining all the species located within the same eco-climate region according to the classification from (U.S. Forest Service, 2004), such relation disappears for most ecoregions (Figure C.42), possibly due to co-existence of multiple species that exhibit distinct relations between their EWS area and mortality. Two exceptions are the regions of southern Sierra and the middle north coast where the species composition is relatively uniform, with 68% and 71% of the area dominated by *Pinus* respectively. As forests within each eco-climate region roughly share a similar climate type, these results imply that the translation from EWS to mortality probability strongly depends on species type rather than climate region.

C.5   Spatial-temporal model selection

Estimation and prediction accuracies were evaluated using different combinations of EWS characteristics (Figure C.51). With a zero lead time, EWS area explains 70% of interannual variation of mortality probability (Figure C.51a). However, this accuracy
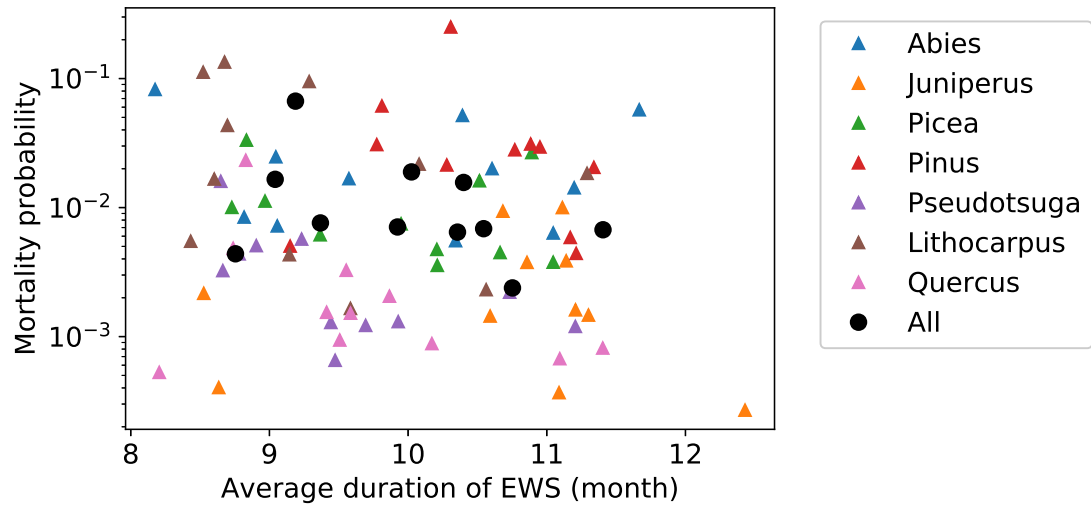
FIGURE C.41: Relations between EWS duration and interannual variation of mortality probability during 2005–2015. Average EWS duration is computed for all pixels showing EWS for each species (colored triangles) and the entire study area (black dots). No significant ($p < 0.05$) relation exists for any species.
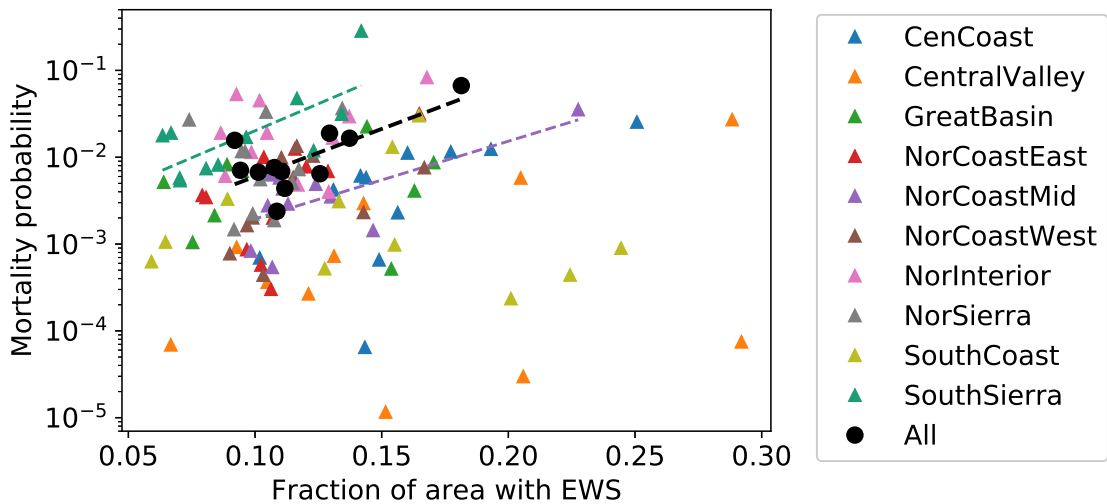
FIGURE C.42: Relations between the fraction of area showing EWS and mortality probability during 2005–2015 for all the forests in each eco-climate region according to the classification from (U.S. Forest Service, 2004). Dashed lines denote significant relations with a significance level of $p < 0.05$.

decreases to 30% when using a 12-month lead time. Adding a quadratic term of EWS area improves the estimation accuracy to 96% and 41% with lead times of 0 and 12 months respectively. These two accuracies can be further improved to 97% and 74% respectively by additionally incorporating EWS duration. Such improvement is also apparent in the prediction scenario (Figure C.51b), thus highlighting the contribution of EWS duration in the estimation and prediction of mortality, especially at long lead times. Adding a quadratic term of EWS duration or an interaction term of EWS duration and area, only marginally improved estimation accuracy. However, the prediction accuracy for lead times longer than 6 months reduced, implying less robust information contained in these additional terms.

Considering EWS characteristics with static spatial variables such as elevation and live basal area that have been shown to influence the spatial pattern of forest mortality (Tai et al., 2017; Young et al., 2017), the most informative predictors for the spatial-temporal variation of mortality were examined. The linear, quadratic and interaction terms of basal area, elevation, EWS area and EWS duration were considered as candidate predictors. For each species, linear model selection was performed using data from all the grids at a given spatial scale and all years in 2005–2015. The Bayesian Information Criterion (BIC) was computed for each possible combination with up to five predictors. The combination yielding the lowest BIC, i.e., high model likelihood and small number of parameters, is listed in Table C.51 for each species. EWS characteristics were selected for estimating both mortality occurrence and intensity for all of the seven dominant species. The results highlight that in addition to the previously studied influence of topography and community competition, the resilience signal is also crucial for capturing the spatial pattern of mortality.
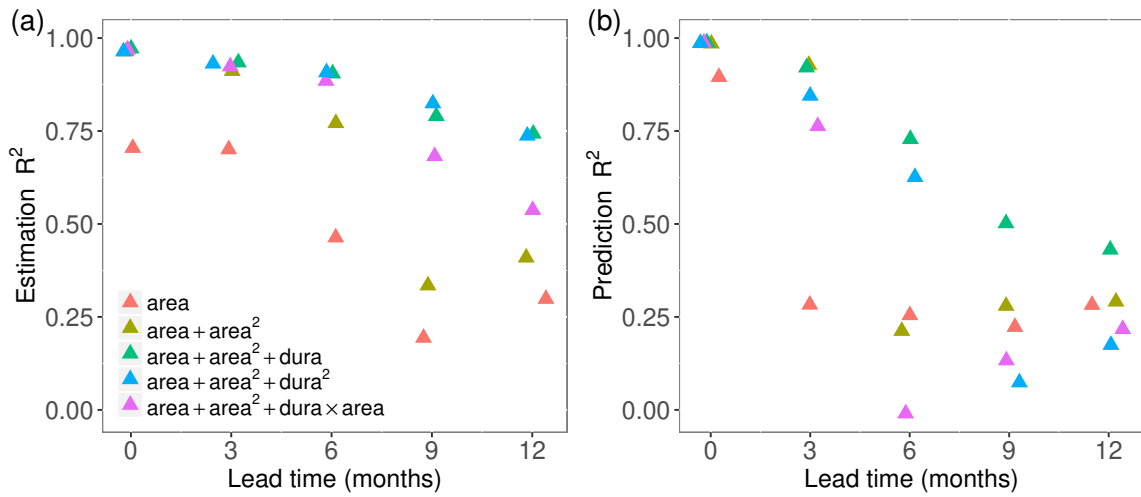
FIGURE C.51: Temporal estimation (a) and prediction (b) accuracy of mortality probability using different combinations of EWS area (area) and mean duration (dura) detected with lead times ranging from 0 to 12 months.

Table C.51: Selected predictors for capturing the spatial pattern of mortality occurrence and intensity at a 1/8 degree scale based on Bayesian Information Criterion (BIC). Candidate predictors include the linear, quadratic and interaction terms of live basal area (ba), elevation (dem), EWS area ($area$) and EWS duration ($dura$).

Genus	Mortality occurrence	Mortality intensity
Abies	$ba + dem + dura + dem^2 + dura \times area$	$ba + dura + ba^2 + dem \times dura + dura^2$
Juniperus	$ba + dura + ba^2 + dem^2 + dura \times area$	$dura + ba \times dura + dem^2$
Picea	$dura + area^2 + ba \times dem + dem^2 + dura \times area$	$ba + dem + dura + dura^2$
Pinus	$area + ba + dura + ba^2 + dura^2$	$ba + dura + ba \times dem + ba \times dura + dura^2$
Pseudotsuga	$area + dura + ba \times dem + ba \times dura + dura^2$	$dura + ba \times dura + dem^2 + dura^2$
Lithocarpus	$ba + dem + dura + ba \times area + ba \times dem$	$ba + dem + dura + ba \times area + dura^2$
Quercus	$ba + dura + ba^2 + dem \times area + dura^2$	$ba + dura + dura \times area + dura^2$

C.6 Estimation and prediction accuracies across spatial scales and lead times

Figure C.61 illustrates the estimation and prediction accuracies at spatial scales of eco-climate region, 1/2 degree, 1/8 degree and 3 km grid using EWS detected with lead times of 0, 3, 6, 9 and 12 months. The median of the overall estimation accuracy (ACC) for mortality occurrence, i.e., the summation of true positive and true negative divided by the total number of samples, is within 0.89–0.98 for all spatial scales and lead times (Figure C.61a); whereas the area under the receiver operating characteristic curve (AUC) for mortality occurrence (Figure C.61c) and R^2 for mortality intensity (Figure C.61e) decrease with finer spatial scale. For spatial scales of eco-climate region, 1/2 degree, and 1/8 degree, the median of estimated AUC lies between 0.61–0.94 for the range of considered lead times, which however drops to 0.37–0.43 at a spatial scale of 3 km. The median of R^2 ranges within 0.66–0.78, 0.57–0.70, 0.50–0.57 and 0.45–0.49 across different lead times at eco-climate region, 1/2 degree, 1/8 degree and 3 km scales, respectively. For some spatial scales, the spatial accuracies decrease slightly when using longer lead times, though the difference is less compared to that among different spatial scales. Prediction accuracies follow a similar pattern as estimation accuracies, yet have lower magnitudes as expected (Figure C.61b, d, f).

One possible reason for the reduction in performance at finer spatial scales is stochastic perturbation in space. Low resilience indicates a higher probability of mortality occurrence under the condition that the stochastic perturbation is statistically the same. However, strong perturbations at a high-resilience location can still push the system over the tipping point and result in mortality. An example of such strong perturbation could be local insect or pathogen attack. Hence spatial stochastic perturbations impair the accuracy in estimating mortality using the deter-

ministic resilience-based EWS. The influence of stochastic perturbations is expected to be larger at a finer spatial scale as it can be averaged out at a coarser scale. In addition, scale mismatch between aerial survey maps and grids used in the spatial analysis may also undermine the accuracy, especially at fine resolutions. As some but not all trees died within the polygons, it is possible that mortality rarely occurred in fine grids even when overlapping with mortality polygons. On the other hand, small area that actually underwent mortality may also get omitted in mortality maps (Forest Health Monitoring Program, 1999). In addition, stand density was also not considered in the evaluation of mortality probability, which is quantified as the fraction of mortality area rather than the fraction of dead trees, due to lack of such data with acceptable accuracy and compatible coverage. These caveats could obscure the relation between low resilience signal and mortality, thus reducing spatial estimation accuracies. Nonetheless, at larger spatial scales of eco-climate region, 1/2 degree and 1/8 degree, EWS characteristics together with metrics of topography and live basal area reasonably are shown to be able to partially capture the spatial distribution of mortality.

C.7   Sensitivity analysis

C.7.1   Thresholds for EWS and abnormally low NDVI identification

The EWS was identified as the presence of an autocorrelation being higher than a threshold and lasting for at least 3 months. The threshold was taken as the longterm average of the 80th percentile in the estimated distribution of autocorrelation (Figure 4.1, main text). Abnormally low NDVI (ALN) was quantified as the presence of NDVI being lower than a threshold, i.e., the 20th percentile of all the observed NDVI values in that month. Here instead of 80th/20th percentiles, we use a looser 70th/30th percentiles and a more stringent 90th/10th percentiles threshold and repeat the analyses to evaluate the sensitivity of the main results to these thresholds.
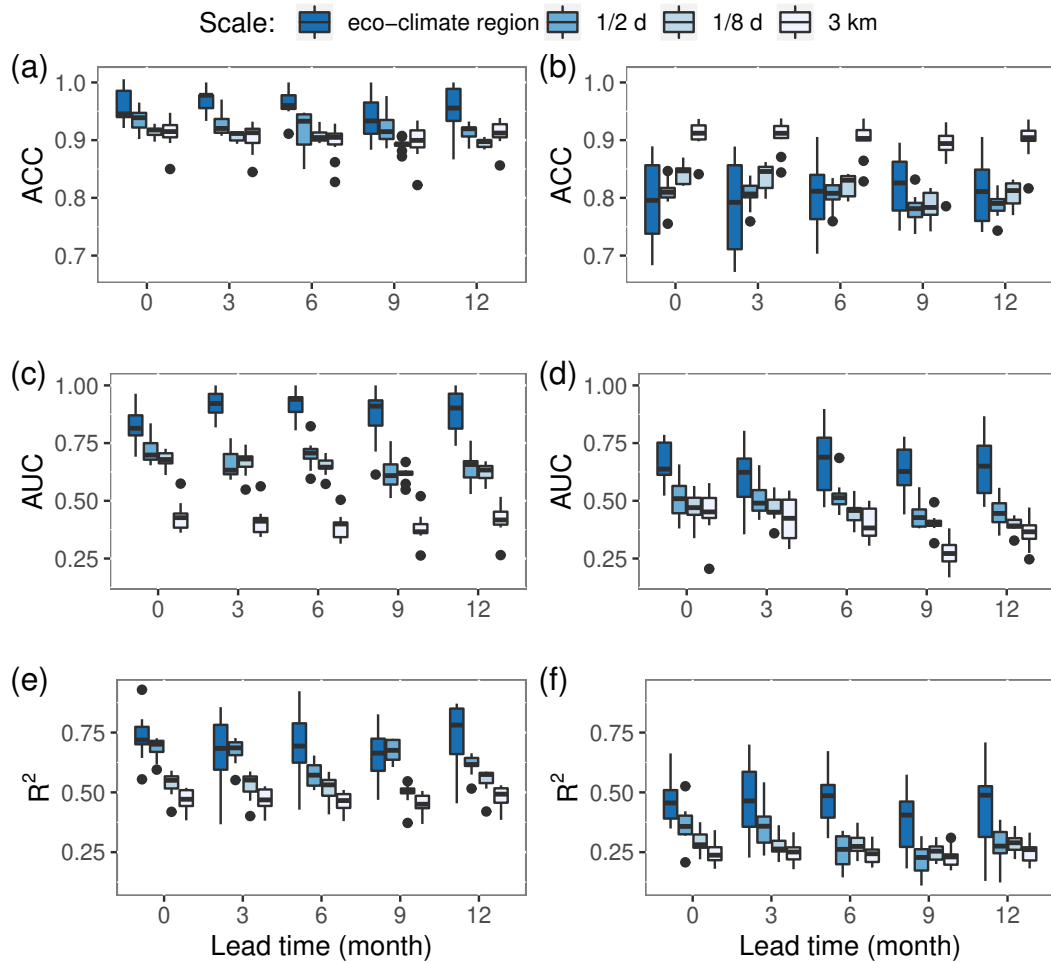
FIGURE C.61: Spatial model performance in estimating (a, c, e) and predicting (b, d, f) mortality at spatial scales of eco-climate region, 1/2 degree, 1/8 degree and 3 km grids using EWS detected with different lead times. The overall accuracy (ACC, a, b) and the area under the receiver operating characteristic curve (AUC, c, d) were computed for mortality occurrence, i.e., whether more than 0.1% of the 30 m pixels in a grid/eco-climate region underwent mortality. R^2 (e,f) was computed for mortality intensity, i.e., the fraction of 30 m pixels within a grid/eco-climate region that underwent mortality, for all grids/eco-climate regions with mortality occurrence. Spatial models were fitted for each genus separately. The accuracy in each year was assessed by combining all the estimation/prediction for different genus together. Each bar indicates the range of the accuracy across 2005–2015.

The magnitude of area with EWS and ALN shrinks as the threshold becomes more stringent, i.e. from 70th/30th percentiles (Figure C.71a) to 90th/10th percentiles (Figure C.71c). However, even while using these alternative thresholds, EWS area still captures the interannual variation in the probabilities of ALN (Figure C.71). As suggested by the exceedance probability of the lead time of EWS (Figure C.72), lead time reduces as the threshold becomes more stringent. For example, when using thresholds of 70th, 80th and 90th percentile to identify EWS, the mid-half of the cases had lead times of 7–23 months, 6–19 months and 6–13 months w.r.t. mortality occurrence, respectively. The majority of EWS still occurs earlier than ALN even when using the most stringent threshold, as suggested by the exceedance probability of a 0 lead time w.r.t. canopy ALN. The relations between EWS area and probabilities of mortality and ALN robustly exhibit strong genus dependency, and are significant for most genus when using different thresholds (Figure C.73). Notably, the significant relations for *Pinus* (w.r.t. mortality) and *Quercus* w.r.t. ALN disappear when using the most stringent thresholds of 90th/10th percentiles.

Temporally, EWS identified using the three thresholds explains more than 92% of the interannual variation in mortality probability (Table C.71). For take-one-out prediction, EWS identified using the 70th and 80th percentile predict around 94% of the variation in mortality probability, whereas EWS identified using the 90th percentile merely predicts 54% of the variation. Spatially, the median of the overall estimation accuracy (ACC, Figure C.74a) and AUC (Figure C.74b) for mortality occurrence are within 0.85–0.98 using different thresholds; the median estimation R^2 is within 0.45–0.60. Although the estimation accuracies (ACC, AUC and R^2) are the lowest when using a threshold of the 80th percentile, the difference between estimation and prediction accuracies are the least, suggesting a more robust relation between mortality and the EWS detected using the 80th percentile. AUC and R^2 in a prediction scenario are the lowest when using the 90th percentile.

166

The 3-month period is used to diminish the influence of autocorrelation spikes due to noise in NDVI data. As shown in Fig C.75, with a 1 month threshold, false alarms arose in 2006 and 2008 (Figure C.75a) due to spikes in autocorrelation. Longer thresholds of 3 months and 5 months reduce such false positives (Figure C.75b, c). But a longer duration threshold may lead to more false negatives by missing reduced resilience in a short term. In addition, a longer duration threshold results in a shorter lead time as expected. In this case, the lead times using 1 month, 3 months and 5 months thresholds are 35 months, 33 months and 31 months respectively.

These results highlight the robustness of the results in this study with respect to different thresholds used to identify EWS. It is also suggested that using a highly stringent threshold to detect EWS might leave out informative low resilience signals that could have contributed to estimation and prediction of mortality. The sensitivity analysis conducted here for the forests in California indicates that the 80th and 70th percentiles have better performance than the 90th percentile in capturing the spatial-temporal variation of mortality. The 3 months threshold was also found to provide EWS that is able to capture the spatial-temporal variations of mortality in the study area. These thresholds, however, are expected to be location specific. Similar sensitivity analyses should be performed when applying this framework to other forests.

C.7.2   Threshold of mortality occurrence

For spatial estimation and prediction, mortality occurrence is defined by mortality probability greater than 0.1%. When using a more stringent (0.01%) and a more relaxed threshold (0.5%) to classify mortality occurrence, the overall estimation accuracy and AUC for mortality occurrence reduces (Figure C.76 a, b), while the accuracy for mortality intensity showed little change (Figure C.76 c). The reduced accuracies for mortality occurrence is because a 0.5% threshold missed 45.4% of

pixels with mortality probability greater than zero (Figure C.77), thus leading to more false positives; and a 0.01% threshold includes almost all (99.6%) pixels with mortality, most of which had tiny mortality probability, thus resulting in more false negatives. In this regard, a moderate threshold of 0.1% was used to classify mortality occurrence, which was found to provide good accuracies for both mortality occurrence and intensity.

C.7.3 Discounting factor

The discounting factor δ (see methods) controls the magnitude of stochastic variation in the state vector $\boldsymbol{\theta}_t$. $\delta = 1$ corresponds to no stochastic variation. A smaller δ allows greater stochastic variation, leading to a more fluctuating time series of autocorrelation and a wider uncertainty range (Figure C.78a). This will influence the occurrence of EWS and its timing. It is to be expected that a more stable estimate of autocorrelation using a larger δ would result in less false positives and a shorter lead time, as the estimated autocorrelation responds to the data more slowly. However, using the time series in Figure 4.1 (in the main text) as an example, the lead time of EWS actually increases from 29 to 33 and 40 months with increasing δ from 0.96 to 0.98 and 0.995 (Figure C.78). In addition, for $\delta = 0.995$, EWS was also identified in September 2008, which was not followed by mortality (false positive). The reason for such counterintuitive result is that under a large δ, even though it might need more time steps to identify the change in autocorrelation, the narrower uncertainty range results in a lower threshold for EWS identification, which offsets the influence of the slow updating rate of autocorrelation. The influence of δ on the occurrence and timing of EWS gets attenuated by these two counter effects, of which the relative magnitudes depend on each specific time series. $\delta = 0.98$ was adopted in this study as it provides an effective EWS for mortality. Despite the extent of fluctuation and uncertainty range in autocorrelation estimates, all the three different

168

δ values result in similar temporal patterns, suggesting the association between EWS and mortality still holds.
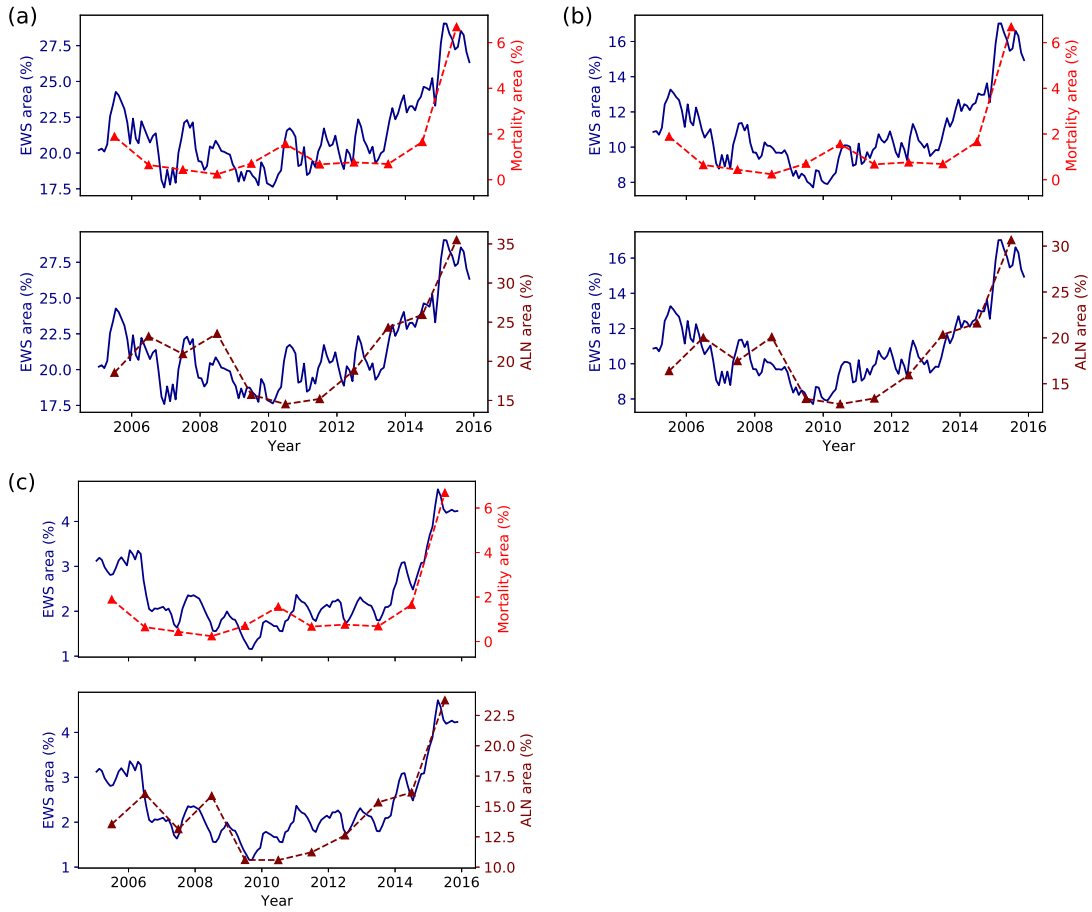
FIGURE C.71: Interannual variation of EWS area (blue lines) in comparison with observed mortality area (red lines) and abnormally low NDVI (ALN) (brown lines) identified using thresholds of (a) 70th/30th, (b) 80th/20th and (c) 90th/10th percentiles of autocorrelation and NDVI respectively.

Table C.71: Temporal estimation and prediction accuracies of mortality probability within the entire study area using a quadratic combination of EWS area ($area + area^2$) detected with a zero lead time and different thresholds.

Percentile	70th	80th	90th
Estimation	0.972	0.948	0.925
Prediction	0.937	0.947	0.541
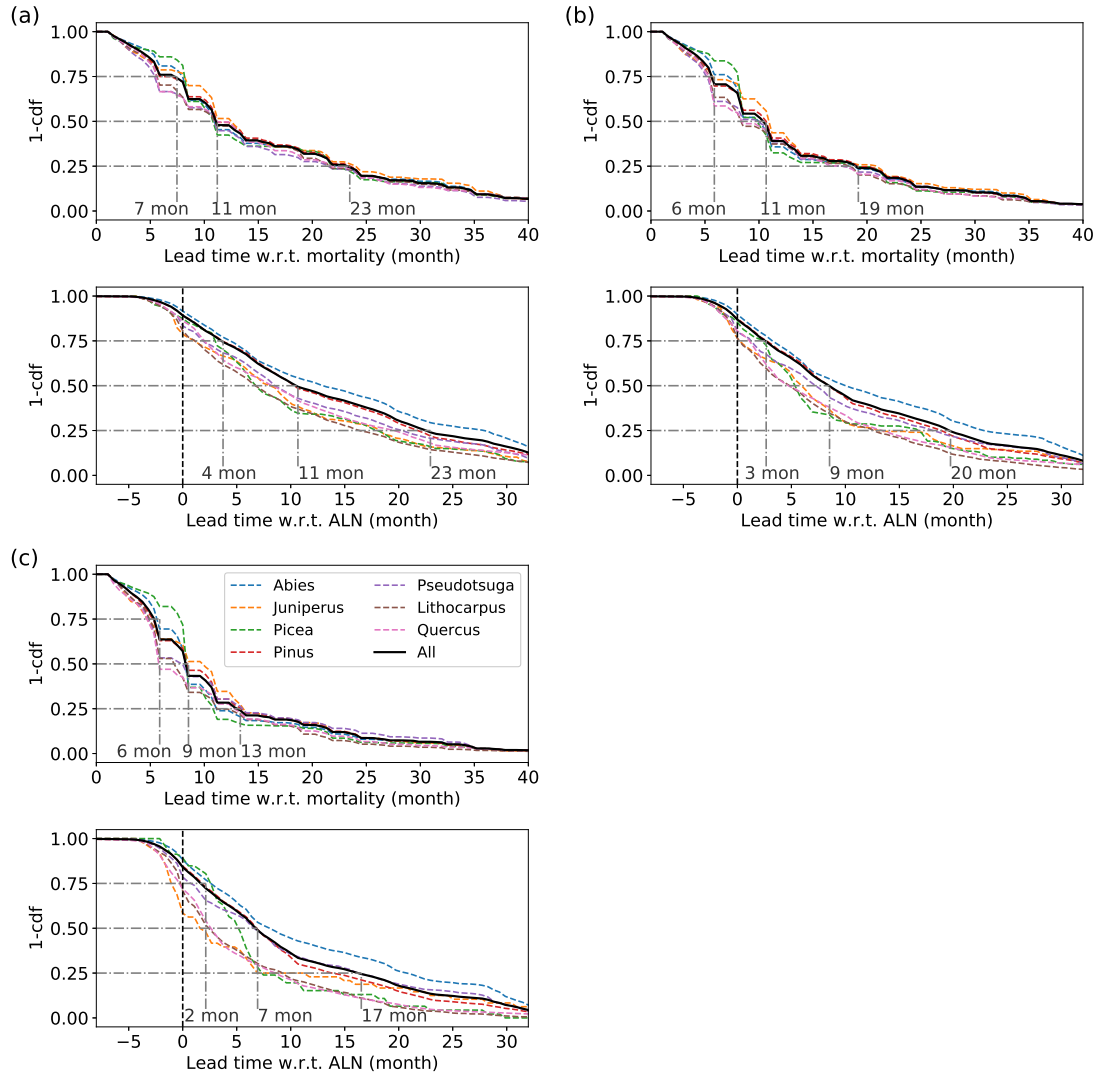
FIGURE C.72: Exceedance probability of EWS lead time w.r.t. mortality and abnormally low NDVI (ALN). EWS and ALN are identified using thresholds of (a) 70th/30th, (b) 80th/20th and (c) 90th/10th percentiles. Black solid lines in both figures represent all the surveyed area; colored dashed lines represent the area dominated by major species within the surveyed area, respectively.

C.8 EWS in snow-free and snow-affected regions

As snow affected data has been removed and treated as missing data, the presence of snow is not expected to introduce an artifact in autocorrelation pattern across years via mixed signal contribution to NDVI. To further confirm this using the data in this
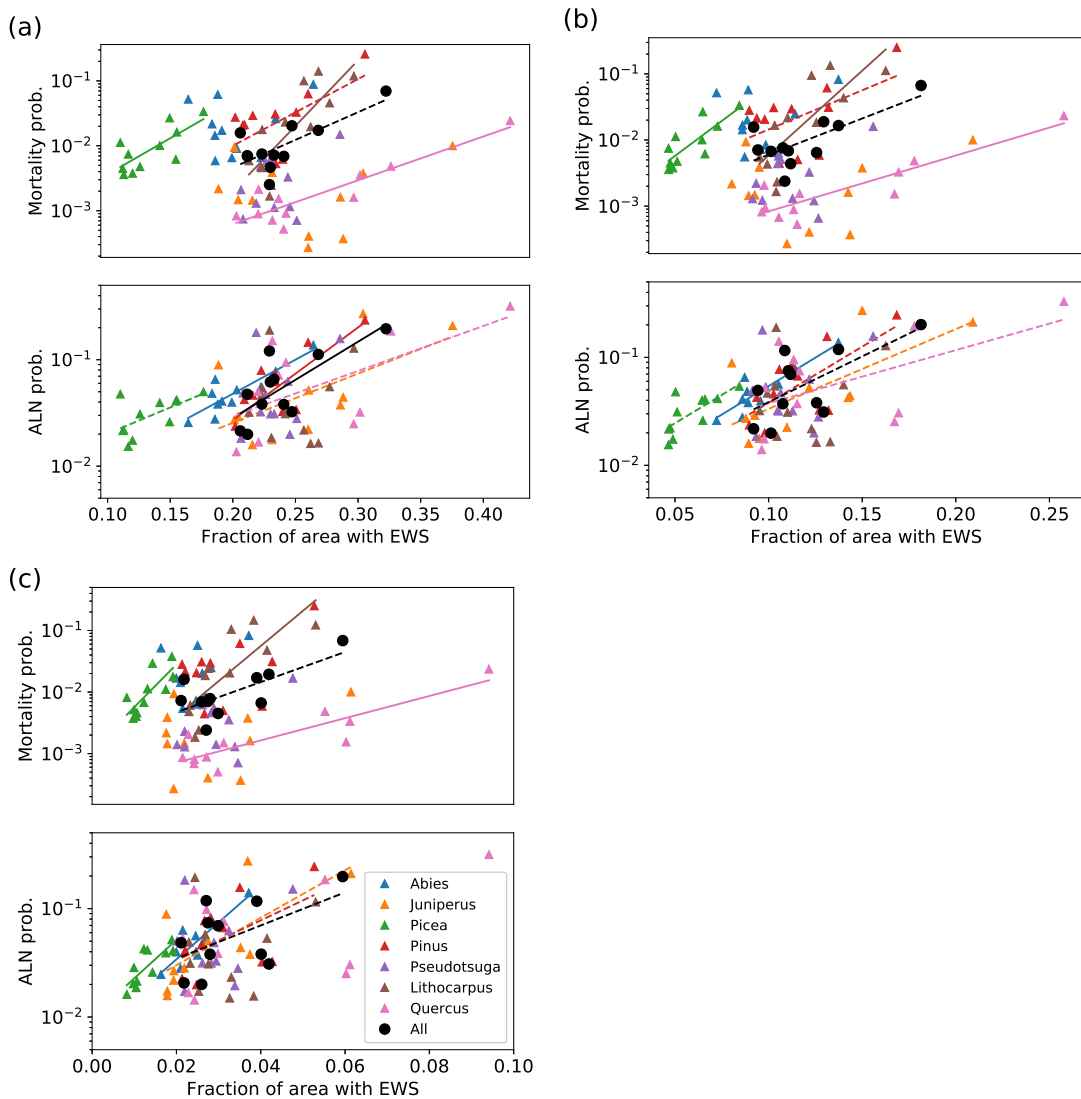
FIGURE C.73: Species specific relations between the fraction of area showing EWS and probabilities of mortality and abnormally low NDVI (ALN) during 2005–2015. EWS and ALN were identified using thresholds of (a) 70th/30th, (b) 80th/20th and (c) 90th/10th percentiles. Solid trend lines denote significance level of $p < 0.01$ and dashed trend lines denote significance level of $p < 0.05$. Trend lines are not plotted for genus with no significant relations.
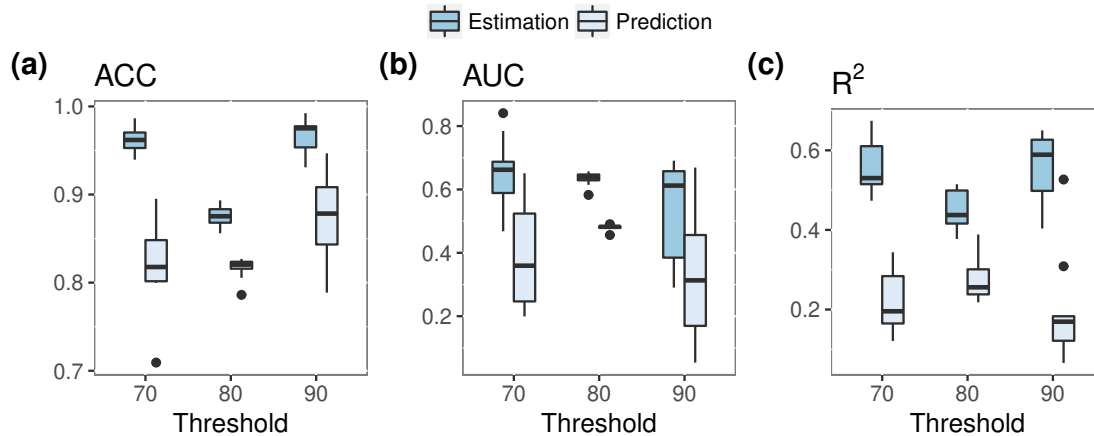
FIGURE C.74: Spatial estimation and prediction accuracies of mortality at a 1/8 degree scale using EWS characteristics detected with zero lead time and thresholds of (a) 70th, (b) 80th and (c) 90th percentiles. The overall accuracy (ACC) and AUC are for mortality occurrence and R^2 is for mortality intensity.

study, the temporal trajectories of EWS area for snow affected and snow free settings are analyzed (Figure C.81) separately. To identify regions that are little affected by snow but also with adequate samples of mortality (more than 0.5% on average), the snow free regions are marked as 1/8 degree grids in which more than 99.9% of the area had maximum SWE less than 1 mm during 2000-2015. The rest of the study area is considered as snow affected regions. As shown in Figure C.82, EWS area of both snow free and snow affected regions exhibited similar patterns with observed mortality area, suggesting that the identified high autocorrelation is not an artifact due to snow cover.
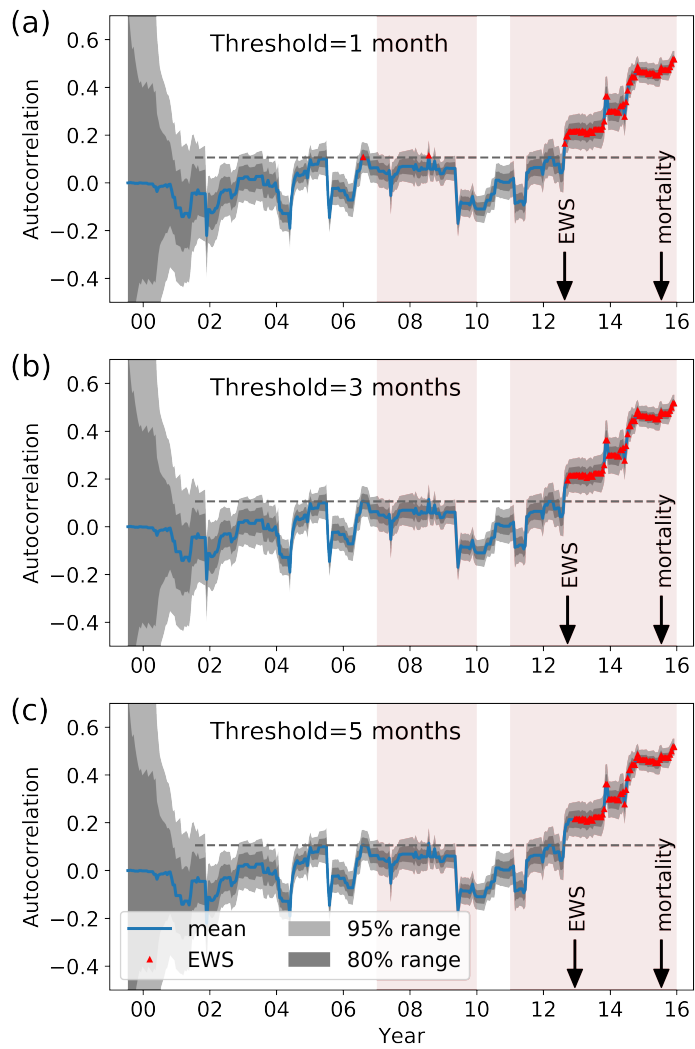
FIGURE C.75: Time-varying autocorrelation estimated using DLM and the detected EWS using different duration thresholds.
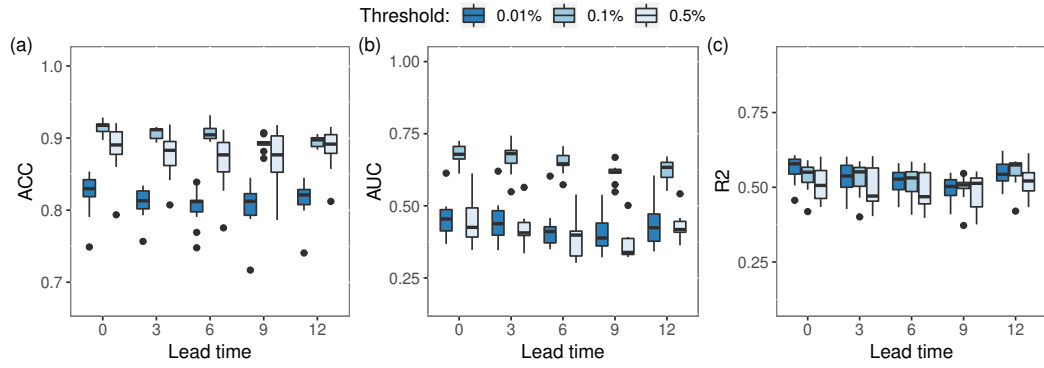
FIGURE C.76: Overall estimation accuracies (a) and area under the receiver operating characteristic curve (AUC) for mortality occurrence (b), and R^2 for mortality intensity (c) at a spatial scale of 1/8 degree. Three thresholds of 0.01%, 0.1% and 0.5% of mortality probability were used classify mortality occurrence
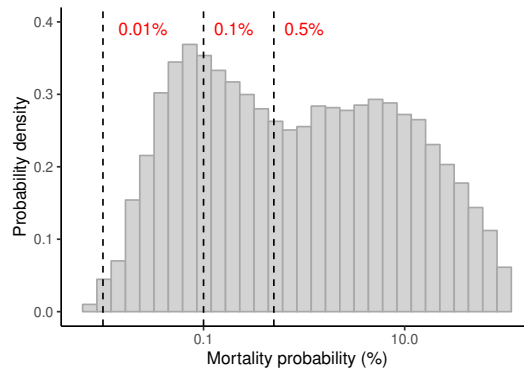
FIGURE C.77: Probability distribution of positive mortality probability, in comparison with the three thresholds used for sensitivity analysis.
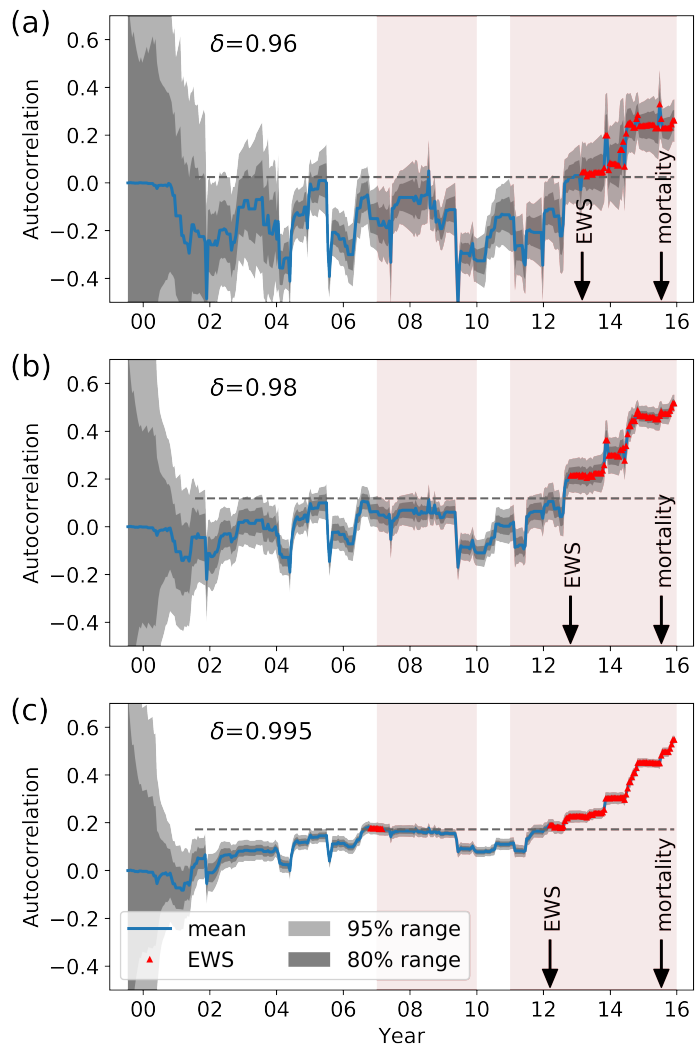
FIGURE C.78: Time varying autocorrelation estimated by DLM using different discounting factors (δ, see methods).
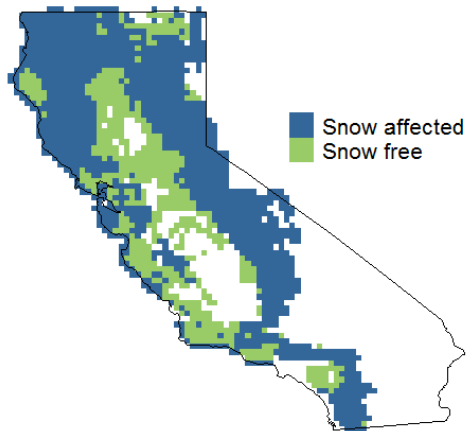
FIGURE C.81: Distribution of snow affected and snow free region based on snow water equivalent data from Daymet V3.
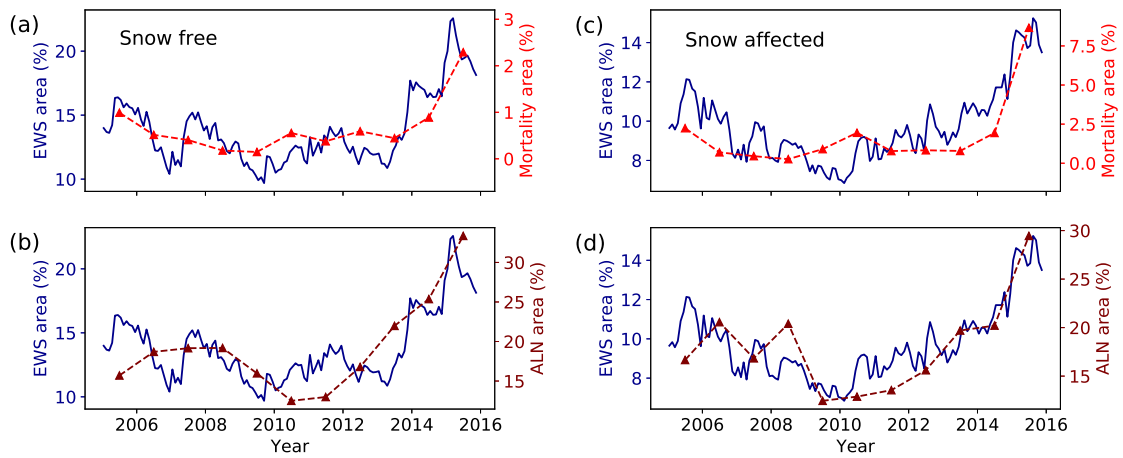
FIGURE C.82: Temporal trajectories of mortality area (red lines), EWS area (blue lines) and abnormally low NDVI (ALN) area (dark red lines) for snow free (a, b) and snow affected areas (c, d).

Bibliography

Abatzoglou, J. T. (2013), "Development of gridded surface meteorological data for ecological applications and modelling," *International Journal of Climatology*, 33, 121–131.

Adams, H. D., Guardiola-Claramonte, M., Barron-Gafford, G. A., Villegas, J. C., Breshears, D. D., Zou, C. B., Troch, P. A., and Huxman, T. E. (2009), "Temperature sensitivity of drought-induced tree mortality portends increased regional die–off under global–change–type drought," *Proceedings of the National Scademy of Sciences*, 106, 7063–7066.

Ainsworth, E. A. and Long, S. P. (2005), "What have we learned from 15 years of free–air CO_2 enrichment (FACE)? A meta–analytic review of the responses of photosynthesis, canopy properties and plant production to rising CO_2," *New Phytologist*, 165, 351–372.

Ainsworth, E. A. and Rogers, A. (2007), "The response of photosynthesis and stomatal conductance to rising CO_2: mechanisms and environmental interactions," *Plant, cell & environment*, 30, 258–270.

Allen, C. D., Macalady, A. K., Chenchouni, H., Bachelet, D., McDowell, N., Vennetier, M., Kitzberger, T., Rigling, A., Breshears, D. D., Hogg, E. T., et al. (2010), "A global overview of drought and heat-induced tree mortality reveals emerging climate change risks for forests," *Forest Ecology and Management*, 259, 660–684.

Allen, C. D., Breshears, D. D., and McDowell, N. G. (2015), "On underestimation of global vulnerability to tree mortality and forest die–off from hotter drought in the Anthropocene," *Ecosphere*, 6, 1–55.

Altor, A. E. and Mitsch, W. J. (2006), "Methane flux from created riparian marshes: relationship to intermittent versus continuous inundation and emergent macrophytes," *Ecological Engineering*, 28, 224–234.

Anderegg, L. D. L., Anderegg, W. R. L., Abatzoglou, J., Hausladen, A. M., and Berry, J. A. (2013a), "Drought characteristics' role in widespread aspen forest mortality across Colorado, USA," *Global Change Biology*, 19, 1526–1537.

Anderegg, W. R. (2015), "Spatial and temporal variation in plant hydraulic traits and their relevance for climate change impacts on vegetation," *New Phytologist*, 205, 1008–1014.

Anderegg, W. R., Flint, A., Huang, C.-y., Flint, L., Berry, J. A., Davis, F. W., Sperry, J. S., and Field, C. B. (2015), "Tree mortality predicted from drought-induced vascular damage," *Nature Geoscience*, 8, 367.

Anderegg, W. R., Wolf, A., Arango-Velez, A., Choat, B., Chmura, D. J., Jansen, S., Kolb, T., Li, S., Meinzer, F., Pita, P., et al. (2017), "Plant water potential improves prediction of empirical stomatal models," *PloS one*, 12, e0185481.

Anderegg, W. R., Konings, A. G., Trugman, A. T., Yu, K., Bowling, D. R., Gabbitas, R., Karp, D. S., Pacala, S., Sperry, J. S., Sulman, B. N., et al. (2018), "Hydraulic diversity of forests regulates ecosystem resilience during drought," *Nature*, 561, 538.

Anderegg, W. R. L., Berry, J. A., Smith, D. D., Sperry, J. S., Anderegg, L. D., and Field, C. B. (2012), "The roles of hydraulic and carbon stress in a widespread climate-induced forest die–off," *Proceedings of the National Academy of Sciences*, 109, 233–237.

Anderegg, W. R. L., Kane, J. M., and Anderegg, L. D. L. (2013b), "Consequences of widespread tree mortality triggered by drought and temperature stress," *Nature Climate Change*, 3, 30–36.

Anderson, W. P. and Emanuel, R. E. (2008), "Effect of interannual and interdecadal climate oscillations on groundwater in North Carolina," *Geophysical Research Letters*, 35.

Baird, K. J. and Maddock, T. (2005), "Simulating riparian evapotranspiration: a new methodology and application for groundwater models," *Journal of Hydrology*, 312, 176–190.

Batelaan, O., De Smedt, F., and Triest, L. (2003), "Regional groundwater discharge: phreatophyte mapping, groundwater modelling and impact analysis of land-use change," *Journal of Hydrology*, 275, 86–108.

Bhatt, G., Kumar, M., and Duffy, C. J. (2014), "A tightly coupled GIS and distributed hydrologic modeling framework," *Environmental Modelling & Software*, 62, 70–84.

Bishop, C. M. (2006), *Pattern recognition and machine learning*, Springer, New York.

Bloom, A. A., Palmer, P. I., Fraser, A., Reay, D. S., and Frankenberg, C. (2010), "Large-scale controls of methanogenesis inferred from methane and gravity spaceborne data," *Science*, 327, 322–325.

Bohn, T., Lettenmaier, D., Sathulur, K., Bowling, L., Podest, E., McDonald, K., and Friborg, T. (2007), "Methane emissions from western Siberian wetlands: heterogeneity and sensitivity to climate change," *Environmental Research Letters*, 2, 045015.

Bonan, G. B. (2008), "Forests and climate change: forcings, feedbacks, and the climate benefits of forests," *science*, 320, 1444–1449.

Bottero, A., D'Amato, A. W., Palik, B. J., Bradford, J. B., Fraver, S., Battaglia, M. A., and Asherin, L. A. (2017), "Density–dependent vulnerability of forest ecosystems to drought," *Journal of Applied Ecology*.

Bousquet, P., Ciais, P., Miller, J., Dlugokencky, E., Hauglustaine, D., Prigent, C., Van der Werf, G., Peylin, P., Brunke, E.-G., Carouge, C., et al. (2006), "Contribution of anthropogenic and natural sources to atmospheric methane variability," *Nature*, 443, 439–443.

Breshears, D. D., Cobb, N. S., Rich, P. M., Price, K. P., Allen, C. D., Balice, R. G., Romme, W. H., Kastens, J. H., Floyd, M. L., Belnap, J., et al. (2005), "Regional vegetation die–off in response to global–change–type drought," *Proceedings of the National Academy of Sciences*, 102, 15144–15148.

Bridgham, S. D., Megonigal, J. P., Keller, J. K., Bliss, N. B., and Trettin, C. (2006), "The carbon balance of North American wetlands," *Wetlands*, 26, 889–916.

Brinson, M. M., Bradshaw, H. D., and Kane, E. S. (1984), "Nutrient assimilative capacity of an alluvial floodplain swamp," *Journal of Applied Ecology*, pp. 1041–1057.

Brodribb, T. J., McAdam, S. A. M., Jordan, G. J., and Feild, T. S. (2009), "Evolution of stomatal responsiveness to CO_2 and optimization of water–use efficiency among land plants," *New Phytologist*, 183, 839–847.

Brodrick, P. and Asner, G. (2017), "Remotely sensed predictors of conifer tree mortality during severe drought," *Environmental Research Letters*, 12, 115013.

Brooks, S. P. and Gelman, A. (1998), "General methods for monitoring convergence of iterative simulations," *Journal of computational and graphical statistics*, 7, 434–455.

Campbell, G. S. and Norman, J. M. (1998), *An introduction to environmental biophysics*, Springer-Verlag, New York.

Cao, M., Xin, P., Jin, G., and Li, L. (2012), "A field study on groundwater dynamics in a salt marsh — Chongming Dongtan wetland," *Ecological Engineering*, 40, 61–69.

Changnon, S. A., Huff, F. A., and Hsu, C.-F. (1988), "Relations between precipitation and shallow groundwater in Illinois," *Journal of Climate*, 1, 1239–1250.

Chen, X., Kumar, M., and McGlynn, B. L. (2015), "Variations in streamflow response to large hurricane-season storms in a Southeastern US watershed," *Journal of Hydrometeorology*, 16, 55–69.

Chiang, F., Mazdiyasni, O., and AghaKouchak, A. (2018), "Amplified warming of droughts in southern United States in observations and model simulations," *Science advances*, 4, eaat2380.

Chimner, R. A. and Cooper, D. J. (2003), "Influence of water table levels on CO_2 emissions in a Colorado subalpine fen: an in situ microcosm study," *Soil Biology and Biochemistry*, 35, 345–351.

Choat, B., Jansen, S., Brodribb, T. J., Cochard, H., Delzon, S., Bhaskar, R., Bucci, S. J., Feild, T. S., Gleason, S. M., Hacke, U. G., et al. (2012), "Global convergence in the vulnerability of forests to drought," *Nature*, 491, 752–755.

Christensen, T. R., Ekberg, A., Ström, L., Mastepanov, M., Panikov, N., Öquist, M., Svensson, B. H., Nykänen, H., Martikainen, P. J., and Oskarsson, H. (2003), "Factors controlling large scale variations in methane emissions from wetlands," *Geophysical Research Letters*, 30.

Churchill, D. J., Larson, A. J., Dahlgreen, M. C., Franklin, J. F., Hessburg, P. F., and Lutz, J. A. (2013), "Restoring forest resilience: from reference spatial patterns to silvicultural prescriptions and monitoring," *Forest Ecology and Management*, 291, 442–457.

Ciais, P., Sabine, C., Bala, G., Bopp, L., Brovkin, V., Canadell, J., Chhabra, A., DeFries, R., Galloway, J., Heimann, M., et al. (2014), "Carbon and other biogeochemical cycles," in *Climate Change 2013: The Physical Science Basis. Contribution of Working Group I to the Fifth Assessment Report of the Intergovernmental Panel on Climate Change*, pp. 465–570, Cambridge University Press.

Clapp, R. B. and Hornberger, G. M. (1978), "Empirical equations for some soil hydraulic properties," *Water resources research*, 14, 601–604.

Clark, J. S., Iverson, L., Woodall, C. W., Allen, C. D., Bell, D. M., Bragg, D. C., D'amato, A. W., Davis, F. W., Hersh, M. H., Ibanez, I., et al. (2016), "The impacts of increasing drought on forest dynamics, structure, and biodiversity in the United States," *Global change biology*.

Collatz, G. J., Ball, J. T., Grivet, C., and Berry, J. A. (1991), "Physiological and environmental regulation of stomatal conductance, photosynthesis and transpiration: a model that includes a laminar boundary layer," *Agricultural and Forest Meteorology*, 54, 107–136.

Condit, R., Hubbell, S. P., and Foster, R. B. (1995), "Mortality rates of 205 neotropical tree and shrub species and the impact of a severe drought," *Ecological monographs*, 65, 419–439.

Council, N. R. et al. (2012), *Challenges and opportunities in the hydrologic sciences*, National Academies Press.

Dai, A., Trenberth, K. E., and Qian, T. (2004a), "A global dataset of Palmer Drought Severity Index for 1870–2002: relationship with soil moisture and effects of surface warming," *Journal of Hydrometeorology*, 5, 1117–1130.

Dai, Y., Dickinson, R. E., and Wang, Y.-P. (2004b), "A two–big–leaf model for canopy temperature, photosynthesis, and stomatal conductance," *Journal of Climate*, 17, 2281–2299.

Dakos, V., Scheffer, M., van Nes, E. H., Brovkin, V., Petoukhov, V., and Held, H. (2008), "Slowing down as an early warning signal for abrupt climate change," *Proceedings of the National Academy of Sciences*, 105, 14308–14312.

Dakos, V., Van Nes, E. H., D'Odorico, P., and Scheffer, M. (2012), "Robustness of variance and autocorrelation as indicators of critical slowing down," *Ecology*, 93, 264–271.

Dakos, V., Carpenter, S. R., van Nes, E. H., and Scheffer, M. (2015), "Resilience indicators: prospects and limitations for early warnings of regime shifts," *Philosophical Transactions of the Royal Society B: Biological Sciences*, 370, 20130263.

Daniel, C. C. (1989), "Statistical analysis relating well yield to construction practices and siting of wells in the Piedmont and Blue Ridge Provinces of North Carolina," Tech. rep., USGPO; US Geological Survey.

de Arellano, J. V.-G., van Heerwaarden, C. C., and Lelieveld, J. (2012), "Modelled suppression of boundary–layer clouds by plants in a CO_2–rich atmosphere," *Nature geoscience*, 5, 701–704.

Delzon, S. and Cochard, H. (2014), "Recent advances in tree hydraulics highlight the ecological significance of the hydraulic safety margin," *New Phytologist*, 203, 355–358.

Devito, K. J., Hill, A., and Roulet, N. (1996), "Groundwater–surface water interactions in headwater forested wetlands of the Canadian Shield," *Journal of Hydrology*, 181, 127–147.

Dingman, S. L. (2002), *Physical hydrology*, Prentice Hall, Upper Saddle River, New Jersey, USA.

Drake, B. L., Hanson, D. T., Lowrey, T. K., and Sharp, Z. D. (2016), "The carbon fertilization effect over a century of anthropogenic CO_2 emissions: higher intracellular CO_2 and more drought resistance among invasive and native grass species contrasts with increased water use efficiency for woody plants in the US Southwest," *Global Change Biology*.

Dudgeon, D., Arthington, A. H., Gessner, M. O., Kawabata, Z.-I., Knowler, D. J., Lévêque, C., Naiman, R. J., Prieur-Richard, A.-H., Soto, D., Stiassny, M. L., et al. (2006), "Freshwater biodiversity: importance, threats, status and conservation challenges," *Biological reviews*, 81, 163–182.

Ellsworth, D. S., Reich, P. B., Naumburg, E. S., Koch, G. W., Kubiske, M. E., and Smith, S. D. (2004), "Photosynthesis, carboxylation and leaf nitrogen responses of 16 species to elevated pCO_2 across four free–air CO_2 enrichment experiments in forest, grassland and desert," *Global Change Biology*, 10, 2121–2138.

Fan, Y., Li, H., and Miguez-Macho, G. (2013), "Global patterns of groundwater table depth," *Science*, 339, 940–943.

Fan, Y., Miguez-Macho, G., Jobbágy, E. G., Jackson, R. B., and Otero-Casal, C. (2017), "Hydrologic regulation of plant rooting depth," *Proceedings of the National Academy of Sciences*, 114, 10572–10577.

FAO (2009), "Harmonized World Soil Database Version 1.2," accessed June 22, 2016, at `http://www.fao.org/soils-portal`.

Farquhar, G. D., Caemmerer, S. v., and Berry, J. A. (1980), "A biochemical model of photosynthetic CO_2 assimilation in leaves of C3 species," *Planta*, 149, 78–90.

Ferone, J. and Devito, K. (2004), "Shallow groundwater–surface water interactions in pond–peatland complexes along a Boreal Plains topographic gradient," *Journal of Hydrology*, 292, 75–95.

Finley, A., Banerjee, S., and Gelfand, A. (2015), "spBayes for large univariate and multivariate point–referenced spatio-temporal data models," *Journal of Statistical Software, Articles*, 63, 1–28.

FLUXNET (2016), "FLUXNET 2015 tier 1 dataset," Available at `http://fluxnet.fluxdata.org/data/fluxnet2015-dataset/`. Accessed July 25, 2018.

Forest Health Monitoring Program (1999), *Aerial Survey Standards*, U.S. Forest Service.

Franks, P. J., Bonan, G. B., Berry, J. A., Lombardozzi, D. L., Holbrook, N. M., Herold, N., and Oleson, K. W. (2018), "Comparing optimal and empirical stomatal conductance models for application in Earth system models," *Global change biology*, 24, 5708–5723.

Frei, S., Lischeid, G., and Fleckenstein, J. (2010), "Effects of micro-topography on surface–subsurface exchange and runoff generation in a virtual riparian wetland — A modeling study," *Advances in Water Resources*, 33, 1388–1401.

Gaylord, M. L., Kolb, T. E., Pockman, W. T., Plaut, J. A., Yepez, E. A., Macalady, A. K., Pangle, R. E., and McDowell, N. G. (2013), "Drought predisposes piñon-juniper woodlands to insect attacks and mortality," *New Phytologist*, 198, 567–578.

Gelfand, A. E., Banerjee, S., and Gamerman, D. (2005), "Spatial process modelling for univariate and multivariate dynamic spatial data," *Environmetrics*, 16, 465–479.

Gelman, A., Goodrich, B., Gabry, J., and Vehtari, A. (2018), "R-squared for Bayesian regression models," *The American Statistician*, pp. 1–6.

Gibbons, J. W. (2003), "Terrestrial habitat: a vital component for herpetofauna of isolated wetlands," *Wetlands*, 23, 630–635.

Goldberg, S. D., Knorr, K.-H., Blodau, C., Lischeid, G., and Gebauer, G. (2010), "Impact of altering the water table height of an acidic fen on N_2O and NO fluxes and soil concentrations," *Global Change Biology*, 16, 220–233.

Hansen, M. C., Potapov, P. V., Moore, R., Hancher, M., Turubanova, S., Tyukavina, A., Thau, D., Stehman, S., Goetz, S., Loveland, T., et al. (2013), "High-resolution global maps of 21st-century forest cover change," *science*, 342, 850–853.

Hartmann, D. L., Klein Tank, A. M. G., Rusticucci, M., Alexander, L. V., Brönnimann, S., Charabi, Y., Dentener, F. J., Dlugokencky, E. J., Easterling, D. R., Kaplan, A., Soden, B. J., Thorne, P. W., Wild, M., and Zhai, P. (2013), *Observations: Atmosphere and Surface. In: Climate Change 2013: The Physical Science Basis. Contribution of Working Group I to the Fifth Assessment Report of the Intergovernmental Panel on Climate Change*, Cambridge University Press.

Healey, S., HERNANDEZ, M., EDWARDS, D., LEFSKY, M., FREEMAN, J., PATTERSON, P., LINDQUIST, E., and LISTER, A. (2015), "CMS: GLAS LiDAR-derived Global Estimates of Forest Canopy Height, 2004-2008." Available at `https://doi.org/10.3334/ORNLDAAC/1271`.

Hefting, M., Clement, J., Dowrick, D., Cosandey, A., Bernal, S., Cimpian, C., Tatur, A., Burt, T., and Pinay, G. (2004), "Water table elevation controls on soil nitrogen cycling in riparian wetlands along a European climatic gradient," *Biogeochemistry*, 67, 113–134.

Hessburg, P. F., Spies, T. A., Perry, D. A., Skinner, C. N., Taylor, A. H., Brown, P. M., Stephens, S. L., Larson, A. J., Churchill, D. J., Povak, N. A., et al. (2016), "Tamm review: management of mixed-severity fire regime forests in Oregon, Washington, and Northern California," *Forest Ecology and Management*, 366, 221–250.

Hoeting, J. A., Madigan, D., Raftery, A. E., and Volinsky, C. T. (1999), "Bayesian model averaging: a tutorial," *Statistical science*, pp. 382–401.

Hoff, P. D. (2009), *A first course in Bayesian statistical methods*, Springer Science & Business Media, New York.

Hoffmann, W. A., Marchin, R. M., Abit, P., and Lau, O. L. (2011), "Hydraulic failure and tree dieback are associated with high wood density in a temperate forest under extreme drought," *Global Change Biology*, 17, 2731–2742.

Homer, C., Dewitz, J., Yang, L., Jin, S., Danielson, P., Xian, G., Coulston, J., Herold, N., Wickham, J., and Megown, K. (2015), "Completion of the 2011 national land cover database for the conterminous United States — representing a decade of land cover change information," *Photogrammetric Engineering and Remote Sensing*, 81, 345–354.

IPCC (2013), *Climate change 2013: the physical science basis: working group I contribution to the fifth assessment report of the Intergovernmental Panel on Climate Change*, Cambridge University Press, Cambridge, United Kingdom and New York, NY, USA.

Ji, C. and Schmidler, S. C. (2013), "Adaptive markov chain Monte Carlo for Bayesian variable selection," *Journal of Computational and Graphical Statistics*, 22, 708–728.

Jin, X., Xu, C.-Y., Zhang, Q., and Singh, V. (2010), "Parameter and modeling uncertainty simulated by GLUE and a formal Bayesian method for a conceptual hydrological model," *Journal of Hydrology*, 383, 147–155.

Johnson, D. M., Wortemann, R., McCulloh, K. A., Jordan-Meille, L., Ward, E., Warren, J. M., Palmroth, S., and Domec, J.-C. (2016), "A test of the hydraulic vulnerability segmentation hypothesis in angiosperm and conifer tree species," *Tree physiology*, 36, 983–993.

Juang, J.-Y., Katul, G. G., Siqueira, M. B., Stoy, P. C., and McCarthy, H. R. (2008), "Investigating a hierarchy of Eulerian closure models for scalar transfer inside forested canopies," *Boundary-layer meteorology*, 128, 1–32.

Jump, A. S., Ruiz-Benito, P., Greenwood, S., Allen, C. D., Kitzberger, T., Fensham, R., Martínez-Vilalta, J., and Lloret, F. (2017), "Structural overshoot of tree growth with climate variability and the global spectrum of drought–induced forest dieback," *Global Change Biology*.

Jungkunst, H. F. and Fiedler, S. (2007), "Latitudinal differentiated water table control of carbon dioxide, methane and nitrous oxide fluxes from hydromorphic soils: feedbacks to climate change," *Global Change Biology*, 13, 2668–2683.

Kalnay, E., Kanamitsu, M., Kistler, R., Collins, W., Deaven, D., Gandin, L., Iredell, M., Saha, S., White, G., Woollen, J., et al. (1996), "The NCEP/NCAR 40-year reanalysis project," *Bulletin of the American meteorological Society*, 77, 437–471.

Kaplan, D., Muñoz-Carpena, R., and Ritter, A. (2010), "Untangling complex shallow groundwater dynamics in the floodplain wetlands of a southeastern US coastal river," *Water Resources Research*, 46.

Kass, R. E. and Wasserman, L. (1995), "A reference Bayesian test for nested hypotheses and its relationship to the Schwarz criterion," *Journal of the american statistical association*, 90, 928–934.

Kattge, J., Diaz, S., Lavorel, S., Prentice, I. C., Leadley, P., Bönisch, G., Garnier, E., Westoby, M., Reich, P. B., Wright, I. J., et al. (2011), "TRY–a global database of plant traits," *Global change biology*, 17, 2905–2935.

Katul, G., Leuning, R., and Oren, R. (2003), "Relationship between plant hydraulic and biochemical properties derived from a steady–state coupled water and carbon transport model," *Plant, Cell & Environment*, 26, 339–350.

Katul, G., Manzoni, S., Palmroth, S., and Oren, R. (2009a), "A stomatal optimization theory to describe the effects of atmospheric CO_2 on leaf photosynthesis and transpiration," *Annals of Botany*, p. mcp292.

Katul, G. G., Schieldge, J., Hsieh, C.-I., and Vidakovic, B. (1998), "Skin temperature perturbations induced by surface layer turbulence above a grass surface," *Water Resources Research*, 34, 1265–1274.

Katul, G. G., Palmroth, S., and Oren, R. (2009b), "Leaf stomatal responses to vapour pressure deficit under current and CO_2–enriched atmosphere explained by the economics of gas exchange," *Plant, cell & environment*, 32, 968–979.

Keenan, T. F., Hollinger, D. Y., Bohrer, G., Dragoni, D., Munger, J. W., Schmid, H. P., and Richardson, A. D. (2013), "Increase in forest water–use efficiency as atmospheric carbon dioxide concentrations rise," *Nature*, 499, 324–327.

Knutti, R., Furrer, R., Tebaldi, C., Cermak, J., and Meehl, G. A. (2010), "Challenges in combining projections from multiple climate models," *Journal of Climate*, 23, 2739–2758.

Kohavi, R. (1995), "A study of cross-validation and bootstrap for accuracy estimation and model selection," in *International joint conference on artificial intelligence*, vol. 14, pp. 1137–1145.

Konings, A., Williams, A., and Gentine, P. (2017), "Sensitivity of grassland productivity to aridity controlled by stomatal and xylem regulation," *Nature Geoscience*, 10, 284.

Konings, A. G. and Gentine, P. (2017), "Global variations in ecosystem-scale isohydricity," *Global change biology*, 23, 891–905.

Konings, A. G., Katul, G. G., and Porporato, A. (2010), "The rainfall-no rainfall transition in a coupled land-convective atmosphere system," *Geophysical Research Letters*, 37.

Konings, A. G., Dekker, S. C., Rietkerk, M., and Katul, G. G. (2011), "Drought sensitivity of patterned vegetation determined by rainfall-land surface feedbacks," *Journal of Geophysical Research: Biogeosciences*, 116.

Kottek, M., Grieser, J., Beck, C., Rudolf, B., and Rubel, F. (2006), "World map of the Köppen-Geiger climate classification updated," *Meteorologische Zeitschrift*, 15, 259–263.

Kumar, M. (2009), "Toward a hydrologic modeling system," Ph.D. thesis, The Pennsylvania State University, `https://etda.libraries.psu.edu/paper/9870/5576`.

Kumar, M. and Duffy, C. J. (2015), "Exploring the Role of Domain Partitioning on Efficiency of Parallel Distributed Hydrologic Model Simulations," *Journal of Hydrogeology and Hydrologic Engineering*, 12, 2.

Kumar, M., Duffy, C. J., and Salvage, K. M. (2009a), "A second-order accurate, finite volume–based, integrated hydrologic modeling (FiHM) framework for simulation of surface and subsurface flow," *Vadose Zone Journal*, 8, 873–890.

Kumar, M., Bhatt, G., and Duffy, C. J. (2009b), "An efficient domain decomposition framework for accurate representation of geodata in distributed hydrologic models," *International Journal of Geographical Information Science*, 23, 1569–1596.

Kumar, M., Marks, D., Dozier, J., Reba, M., and Winstral, A. (2013), "Evaluation of distributed hydrologic impacts of temperature-index and energy-based snow models," *Advances in Water Resources*, 56, 77–89.

Lammertsma, E. I., de Boer, H. J., Dekker, S. C., Dilcher, D. L., Lotter, A. F., and Wagner-Cremer, F. (2011), "Global CO_2 rise leads to reduced maximum stomatal conductance in Florida vegetation," *Proceedings of the National Academy of Sciences*, 108, 4035–4040.

Lefsky, M. A. (2010), "A global forest canopy height map from the Moderate Resolution Imaging Spectroradiometer and the Geoscience Laser Altimeter System," *Geophysical Research Letters*, 37.

Lehner, B. and Döll, P. (2004), "Development and validation of a global database of lakes, reservoirs and wetlands," *Journal of Hydrology*, 296, 1–22.

LEMMA group (2015), "GNN structure (species-size) maps," Available at `http://lemma.forestry.oregonstate.edu/data/structure-maps`. Accessed December 4, 2017.

Lewis, W. M. (1995), *Wetlands: characteristics and boundaries*, National Research Council (U.S.) Committee on Characterization of Wetlands. National Academy Prress, Washington, D.C.

Liang, F., Paulo, R., Molina, G., Clyde, M. A., and Berger, J. O. (2008), "Mixtures of g priors for Bayesian variable selection," *Journal of the American Statistical Association*, 103.

Lieffers, V. and Rothwell, R. (1987), "Effects of drainage on substrate temperature and phenology of some trees and shrubs in an Alberta peatland," *Canadian Journal of Forest Research*, 17, 97–104.

Limousin, J.-M., Rambal, S., Ourcival, J.-M., Rodríguez-Calcerrada, J., Pérez-Ramos, I. M., Rodríguez-Cortina, R., Misson, L., and Joffre, R. (2012), "Morphological and phenological shoot plasticity in a Mediterranean evergreen oak facing long-term increased drought," *Oecologia*, 169, 565–577.

Liu, Y. and Kumar, M. (2016), "Role of meteorological controls on interannual variations in wet-period characteristics of wetlands," *Water Resources Research*, 52, 5056–5074.

Liu, Y., Parolari, A. J., Kumar, M., Huang, C.-W., Katul, G. G., and Porporato, A. (2017), "Increasing atmospheric humidity and CO_2 concentration alleviate forest mortality risk," *Proceedings of the National Academy of Sciences*, 114, 9918–9923.

Liu, Y., Kumar, M., Katul, G. G., and Porporato, A. (2019), "Reduced resilience as an early warning signal of forest mortality," *Nature Climate Change, (in review)*, 114.

Lohila, A., Aurela, M., Hatakka, J., Pihlatie, M., Minkkinen, K., Penttilä, T., and Laurila, T. (2010), "Responses of N_2O fluxes to temperature, water table and N deposition in a northern boreal fen," *European journal of soil science*, 61, 651–661.

Luo, L., Robock, A., Mitchell, K. E., Houser, P. R., Wood, E. F., Schaake, J. C., Lohmann, D., Cosgrove, B., Wen, F., Sheffield, J., et al. (2003), "Validation of the North American land data assimilation system (NLDAS) retrospective forcing over the southern Great Plains," *Journal of Geophysical Research: Atmospheres (1984–2012)*, 108.

MacDonald, J., Fowler, D., Hargreaves, K., Skiba, U., Leith, I., and Murray, M. (1998), "Methane emission rates from a northern wetland; response to temperature, water table and transport," *Atmospheric Environment*, 32, 3219–3227.

Manoli, G., Domec, J.-C., Novick, K., Oishi, A. C., Noormets, A., Marani, M., and Katul, G. (2016), "Soil–plant–atmosphere conditions regulating convective cloud formation above southeastern US pine plantations," *Global change biology*, 22, 2238–2254.

Manzoni, S., Vico, G., Katul, G., Fay, P. A., Polley, W., Palmroth, S., and Porporato, A. (2011), "Optimizing stomatal conductance for maximum carbon gain under water stress: a meta–analysis across plant functional types and climates," *Functional Ecology*, 25, 456–467.

Manzoni, S., Vico, G., Porporato, A., and Katul, G. (2013), "Biological constraints on water transport in the soil–plant–atmosphere system," *Advances in Water Resources*, 51, 292–304.

Martens, S. N., Breshears, D. D., and Meyer, C. W. (2000), "Spatial distributions of understory light along the grassland/forest continuum: effects of cover, height, and spatial pattern of tree canopies," *Ecological Modelling*, 126, 79–93.

Martin-StPaul, N., Delzon, S., and Cochard, H. (2017), "Plant resistance to drought depends on timely stomatal closure," *Ecology letters*, 20, 1437–1447.

Mazdiyasni, O. and AghaKouchak, A. (2015), "Substantial increase in concurrent droughts and heatwaves in the United States," *Proceedings of the National Academy of Sciences*, 112, 11484–11489.

McCarthy, T. (2006), "Groundwater in the wetlands of the Okavango Delta, Botswana, and its contribution to the structure and function of the ecosystem," *Journal of Hydrology*, 320, 264–282.

McDowell, N., Pockman, W. T., Allen, C. D., Breshears, D. D., Cobb, N., Kolb, T., Plaut, J., Sperry, J., West, A., Williams, D. G., et al. (2008), "Mechanisms of plant survival and mortality during drought: why do some plants survive while others succumb to drought?" *New Phytologist*, 178, 719–739.

McDowell, N. G. (2011), "Mechanisms linking drought, hydraulics, carbon metabolism, and vegetation mortality," *Plant physiology*, 155, 1051–1059.

McDowell, N. G. and Allen, C. D. (2015), "Darcy's law predicts widespread forest mortality under climate warming," *Nature Climate Change*, 5, 669–672.

McDowell, N. G., Beerling, D. J., Breshears, D. D., Fisher, R. A., Raffa, K. F., and Stitt, M. (2011), "The interdependence of mechanisms underlying climate–driven vegetation mortality," *Trends in Ecology & Evolution*, 26, 523–532.

McDowell, N. G., Fisher, R. A., Xu, C., Domec, J., Hölttä, T., Mackay, D. S., Sperry, J. S., Boutz, A., Dickman, L., Gehres, N., et al. (2013), "Evaluating

theories of drought–induced vegetation mortality using a multimodel–experiment framework," *New Phytologist*, 200, 304–321.

McDowell, N. G., Williams, A. P., Xu, C., Pockman, W. T., Dickman, L. T., Sevanto, S., Pangle, R., Limousin, J., Plaut, J., Mackay, D., et al. (2015), "Multi–scale predictions of massive conifer mortality due to chronic temperature rise," *Nature Climate Change*, 6, 295–300.

McNaughton, K. G. and Spriggs, T. W. (1986), "A mixed–layer model for regional evaporation," *Boundary-Layer Meteorology*, 34, 243–262.

Medlyn, B. E., Dreyer, E., Ellsworth, D., Forstreuter, M., Harley, P. C., Kirschbaum, M. U. F., Le Roux, X., Montpied, P., Strassemeyer, J., Walcroft, A., et al. (2002), "Temperature response of parameters of a biochemically based model of photosynthesis. II. A review of experimental data," *Plant, Cell & Environment*, 25, 1167–1179.

Megonigal, J. P., Conner, W. H., Kroeger, S., and Sharitz, R. R. (1997), "Aboveground production in southeastern floodplain forests: a test of the subsidy-stress hypothesis," *Ecology*, 78, 370–384.

Meinshausen, M., Smith, S. J., Calvin, K., Daniel, J. S., Kainuma, M. L. T., Lamarque, J. F., Matsumoto, K., Montzka, S. A., Raper, S. C. B., Riahi, K., et al. (2011), "The RCP greenhouse gas concentrations and their extensions from 1765 to 2300," *Climatic change*, 109, 213–241.

Miao, G., Noormets, A., Domec, J.-C., Trettin, C. C., McNulty, S. G., Sun, G., and King, J. S. (2013), "The effect of water table fluctuation on soil respiration in a lower coastal plain forested wetland in the southeastern US," *Journal of Geophysical Research: Biogeosciences*, 118, 1748–1762.

Mitchell, T. J. and Beauchamp, J. J. (1988), "Bayesian variable selection in linear regression," *Journal of the American Statistical Association*, 83, 1023–1032.

Moffett, K. B., Robinson, D. A., and Gorelick, S. M. (2010), "Relationship of salt marsh vegetation zonation to spatial patterns in soil moisture, salinity, and topography," *Ecosystems*, 13, 1287–1302.

Monteith, J. (1964), "Evaporation and environment." in *Symposia of the society for experimental biology*, vol. 19, pp. 205–234.

Monteith, J. et al. (1965), "Evaporation and environment," in *Symposia of the Society for Experimental Biology*, vol. 19, p. 4.

Moore, T. and Dalva, M. (1993), "The influence of temperature and water table position on carbon dioxide and methane emissions from laboratory columns of peatland soils," *Journal of Soil Science*, 44, 651–664.

Moore, T. and Knowles, R. (1989), "The influence of water table levels on methane and carbon dioxide emissions from peatland soils," *Canadian Journal of Soil Science*, 69, 33–38.

Moore, T. and Roulet, N. (1993), "Methane flux: water table relations in northern wetlands," *Geophysical Research Letters*, 20, 587–590.

Mu, Q., Zhao, M., and Running, S. W. (2011), "Improvements to a MODIS global terrestrial evapotranspiration algorithm," *Remote Sensing of Environment*, 115, 1781–1800.

Mueller, R. C., Scudder, C. M., Porter, M. E., Talbot Trotter III, R., Gehring, C. A., and Whitham, T. G. (2005), "Differential tree mortality in response to severe drought: evidence for long-term vegetation shifts," *Journal of Ecology*, 93, 1085–1093.

Munné-Bosch, S. and Alegre, L. (2004), "Die and let live: leaf senescence contributes to plant survival under drought stress," *Functional Plant Biology*, 31, 203–216.

NASA LP DACC (2013), "Land Cover Type Yearly L3 Global 0.05Deg Climate Modeling Grid. Version 051," NASA EOSDIS Land Processes DAAC, USGS Earth Resources Observation and Science (EROS) Center, Sioux Falls, South Dakota (`https://lpdaac.usgs.gov`), accessed June 21, 2016, at `https://lpdaac.usgs.gov/dataset_discovery/modis/modis_products_table/mcd12c1`.

NASA LP DACC (2016), "Leaf Area Index – Fraction of Photosynthetically Active Radiation 8-Day L4 Global 1km. Version 005," NASA EOSDIS Land Processes DAAC, USGS Earth Resources Observation and Science (EROS) Center, Sioux Falls, South Dakota (`https://lpdaac.usgs.gov`), accessed June 23, 2016, at `https://lpdaac.usgs.gov/dataset_discovery/modis/modis_products_table/mcd15a2`.

Nash, J. and Sutcliffe, J. V. (1970), "River flow forecasting through conceptual models part I — A discussion of principles," *Journal of hydrology*, 10, 282–290.

Nippgen, F., McGlynn, B. L., Emanuel, R. E., and Vose, J. M. (2016), "Watershed memory at the Coweeta Hydrologic Laboratory: The effect of past precipitation and storage on hydrologic response," *Water Resources Research*.

Norby, R. J. and Zak, D. R. (2011), "Ecological lessons from free-air CO_2 enrichment (FACE) experiments," *Annual review of ecology, evolution, and systematics*, 42, 181.

Norby, R. J., DeLucia, E. H., Gielen, B., Calfapietra, C., Giardina, C. P., King, J. S., Ledford, J., McCarthy, H. R., Moore, D. J., Ceulemans, R., et al. (2005), "Forest response to elevated CO2 is conserved across a broad range of productivity,"

Proceedings of the National Academy of Sciences of the United States of America, 102, 18052–18056.

Novick, K., Katul, G., McCarthy, H., and Oren, R. (2012), "Increased resin flow in mature pine trees growing under elevated CO_2 and moderate soil fertility," *Tree physiology*, 32, 752–763.

Novick, K. A., Ficklin, D. L., Stoy, P. C., Williams, C. A., Bohrer, G., Oishi, A. C., Papuga, S. A., Blanken, P. D., Noormets, A., Sulman, B. N., et al. (2016), "The increasing importance of atmospheric demand for ecosystem water and carbon fluxes," *Nature Climate Change*.

Nykänen, H., Alm, J., Silvola, J., Tolonen, K., and Martikainen, P. J. (1998), "Methane fluxes on boreal peatlands of different fertility and the effect of long-term experimental lowering of the water table on flux rates," *Global Biogeochemical Cycles*, 12, 53–69.

Oleson, K. W., Niu, G.-Y., Yang, Z.-L., Lawrence, D. M., Thornton, P. E., Lawrence, P. J., Stöckli, R., Dickinson, R. E., Bonan, G. B., Levis, S., et al. (2008), "Improvements to the Community Land Model and their impact on the hydrological cycle," *Journal of Geophysical Research: Biogeosciences*, 113.

Oren, R., Sperry, J., Katul, G., Pataki, D., Ewers, B., Phillips, N., and Schäfer, K. (1999), "Survey and synthesis of intra-and interspecific variation in stomatal sensitivity to vapour pressure deficit," *Plant, Cell & Environment*, 22, 1515–1526.

Pan, Y., Birdsey, R. A., Fang, J., Houghton, R., Kauppi, P. E., Kurz, W. A., Phillips, O. L., Shvidenko, A., Lewis, S. L., Canadell, J. G., et al. (2011), "A large and persistent carbon sink in the world's forests," *Science*, 333, 988–993.

Parolari, A. J., Katul, G. G., and Porporato, A. (2014), "An ecohydrological perspective on drought–induced forest mortality," *Journal of Geophysical Research: Biogeosciences*, 119, 965–981.

Patten, D. T., Rouse, L., and Stromberg, J. C. (2008), "Isolated spring wetlands in the Great Basin and Mojave Deserts, USA: potential response of vegetation to groundwater withdrawal," *Environmental Management*, 41, 398–413.

Penman, H. L. (1948), "Natural evaporation from open water, bare soil and grass," in *Proceedings of the Royal Society of London A: Mathematical, Physical and Engineering Sciences*, vol. 193, pp. 120–145, The Royal Society.

Porporato, A. (2009), "Atmospheric boundary–layer dynamics with constant Bowen ratio," *Boundary-layer meteorology*, 132, 227–240.

Potts, M. D. (2003), "Drought in a Bornean everwet rain forest," *Journal of Ecology*, 91, 467–474.

Poyatos, R., Aguadé, D., Galiano, L., Mencuccini, M., and Martínez-Vilalta, J. (2013), "Drought–induced defoliation and long periods of near-zero gas exchange play a key role in accentuating metabolic decline of Scots pine," *New Phytologist*, 200, 388–401.

Prado, R. and West, M. (2010), *Time series: modeling, computation, and inference*, CRC Press, Boca Raton, FL, USA.

Qu, Y. and Duffy, C. J. (2007), "A semidiscrete finite volume formulation for multi-process watershed simulation," *Water Resources Research*, 43.

R Core Team (2017), *R Version 3.4.3. A Language and Environment for Statistical Computing*, R Foundation for Statistical Computing, Vienna, Austria.

Racca, E. and Porporato, A. (2005), "Langevin equations from time series," *Physical Review E*, 71, 027101.

Ramirez, J. A., Baird, A. J., Coulthard, T. J., and Waddington, J. M. (2015), "Ebullition of methane from peatlands: Does peat act as a signal shredder?" *Geophysical Research Letters*, 42, 3371–3379.

Refsgaard, J. C. and Storm, B. (1996), "Construction, calibration and validation of hydrological models," in *Distributed hydrological modelling*, pp. 41–54, Springer.

Regina, K., Nykänen, H., Silvola, J., and Martikainen, P. J. (1996), "Fluxes of nitrous oxide from boreal peatlands as affected by peatland type, water table level and nitrification capacity," *Biogeochemistry*, 35, 401–418.

Reich, C. D., Shinn, E. A., Hickey, T. D., and Tihansky, A. B. (2002), *25 Tidal and Meteorological Influences on Shallow Marine Groundwater Flow in the Upper Florida Keys. In: The Everglades, Florida Bay, and Coral Reefs of the Florida Keys.*

Rodell, M., Houser, P., Jambor, U., Gottschalck, J., Mitchell, K., Meng, C., Arsenault, K., Cosgrove, B., Radakovich, J., Bosilovich, M., et al. (2004), "The global land data assimilation system," *Bulletin of the American Meteorological Society*, 85, 381–394.

Roden, E. E. and Wetzel, R. G. (1996), "Organic carbon oxidation and suppression of methane production by microbial Fe (III) oxide reduction in vegetated and unvegetated freshwater wetland sediments," *Limnology and Oceanography*, 41, 1733–1748.

Rodríguez-Iturbe, I. and Porporato, A. (2007), *Ecohydrology of water–controlled ecosystems: soil moisture and plant dynamics*, Cambridge University Press, Cambridge, United Kingdom.

Rodriguez-Iturbe, I., D'Odorico, P., Laio, F., Ridolfi, L., and Tamea, S. (2007), "Challenges in humid land ecohydrology: Interactions of water table and unsaturated zone with climate, soil, and vegetation," *Water Resources Research*, 43.

Rosenberry, D. O. and Winter, T. C. (1997), "Dynamics of water-table fluctuations in an upland between two prairie-pothole wetlands in North Dakota," *Journal of Hydrology*, 191, 266–289.

Rowland, L., da Costa, A. C. L., Galbraith, D. R., Oliveira, R., Binks, O. J., Oliveira, A., Pullen, A., Doughty, C., Metcalfe, D., Vasconcelos, S., et al. (2015), "Death from drought in tropical forests is triggered by hydraulics not carbon starvation," *Nature*, 528, 119–122.

Saha, S., Moorthi, S., Wu, X., Wang, J., Nadiga, S., Tripp, P., Behringer, D., Hou, Y.-T., ya Chuang, H., Iredell, M., Ek, M., Meng, J., Yang, R., Mendez, M. P., van den Dool, H., Zhang, Q., Wang, W., Chen, M., and Becker, E. (2011), "NCEP Climate Forecast System Version 2 (CFSv2) 6-hourly Products," .

Sala, A., Piper, F., and Hoch, G. (2010), "Physiological mechanisms of drought–induced tree mortality are far from being resolved," *New Phytologist*, 186, 274–281.

Saxton, K. E., Rawls, W. J., Romberger, J. S., and Papendick, R. I. (1986), "Estimating generalized soil–water characteristics from texture," *Soil Science Society of America Journal*, 50, 1031–1036.

Schäfer, K., Tripathee, R., Artigas, F., Morin, T., and Bohrer, G. (2014), "Carbon dioxide fluxes of an urban tidal marsh in the Hudson-Raritan estuary," *Journal of Geophysical Research: Biogeosciences*, 119, 2065–2081.

Scheffer, M., Carpenter, S., Foley, J. A., Folke, C., and Walker, B. (2001), "Catastrophic shifts in ecosystems," *Nature*, 413, 591–596.

Scheffer, M., Bascompte, J., Brock, W. A., Brovkin, V., Carpenter, S. R., Dakos, V., Held, H., Van Nes, E. H., Rietkerk, M., and Sugihara, G. (2009), "Early-warning signals for critical transitions," *Nature*, 461, 53–59.

Schilling, E. B. and Lockaby, B. G. (2006), "Relationships between productivity and nutrient circulation within two contrasting southeastern US floodplain forests," *Wetlands*, 26, 181–192.

Schilling, K. E. (2007), "Water table fluctuations under three riparian land covers, Iowa (USA)," *Hydrological Processes*, 21, 2415–2424.

Schimel, D., Stephens, B. B., and Fisher, J. B. (2015), "Effect of increasing CO_2 on the terrestrial carbon cycle," *Proceedings of the National Academy of Sciences*, 112, 436–441.

Schipper, L. A. and Reddy, K. (1994), "Methane production and emissions from four reclaimed and pristine wetlands of southeastern United States," *Soil Science Society of America Journal*, 58, 1270–1275.

Schwalm, C. R., Anderegg, W. R., Michalak, A. M., Fisher, J. B., Biondi, F., Koch, G., Litvak, M., Ogle, K., Shaw, J. D., Wolf, A., et al. (2017), "Global patterns of drought recovery," *Nature*, 548, 202.

Settele, J., Scholes, R. J., Betts, R. A., Bunn, S., Leadley, P., Nepstad, D., Overpeck, J. T., and Toboada, M. A. (2014), "Chapter 4 - Terrestrial and inland water systems," *Climate Change 2014: Impacts, Adaptation, and Vulnerability. Part A: Global and Sectoral Aspects. Contribution of Working Group II to the Fifth Assessment Report of the Intergovernmental Panel on Climate Change*, pp. 271–359.

Settele, J., Scholes, R., Betts, R. A., Bunn, S., Leadley, P., Nepstad, D., Overpeck, J., Taboada, M. A., Fischlin, A., Moreno, J. M., et al. (2015), "Terrestrial and inland water systems," in *Climate Change 2014 Impacts, Adaptation and Vulnerability: Part A: Global and Sectoral Aspects*, pp. 271–360, Cambridge University Press.

Shannon, R. D. and White, J. R. (1994), "A three-year study of controls on methane emissions from two Michigan peatlands," *Biogeochemistry*, 27, 35–60.

Shi, Y., Davis, K. J., Duffy, C. J., and Yu, X. (2013), "Development of a coupled land surface hydrologic model and evaluation at a critical zone observatory," *Journal of Hydrometeorology*, 14, 1401–1420.

Shook, K. R. and Pomeroy, J. W. (2011), "Memory effects of depressional storage in Northern Prairie hydrology," *Hydrological Processes*, 25, 3890–3898.

Sjörs, H. (1991), "Phyto-and necromass above and below ground in a fen," *Ecography*, 14, 208–218.

Snodgrass, J. W., Komoroski, M. J., Bryan, A. L., and Burger, J. (2000), "Relationships among isolated wetland size, hydroperiod, and amphibian species richness: implications for wetland regulations," *Conservation biology*, 14, 414–419.

Soil Survey Staff (1995), "Natural Resources Conservation Service, United States Department of Agriculture. Web Soil Survey," Available online at `http://websoilsurvey.nrcs.usda.gov/`, Accessed: 2014-10-04.

Solomon, S. (2007), *The physical science basis: Contribution of Working Group I to the fourth assessment report of the Intergovernmental Panel on Climate Change*.

Sperry, J., Hacke, U., Oren, R., and Comstock, J. (2002), "Water deficits and hydraulic limits to leaf water supply," *Plant, cell & environment*, 25, 251–263.

Sperry, J. S. and Love, D. M. (2015), "What plant hydraulics can tell us about responses to climate–change droughts," *New Phytologist*, 207, 14–27.

Sperry, J. S., Wang, Y., Wolfe, B. T., Mackay, D. S., Anderegg, W. R., McDowell, N. G., and Pockman, W. T. (2016), "Pragmatic hydraulic theory predicts stomatal responses to climatic water deficits," *New Phytologist*, 212, 577–589.

Sperry, J. S., Venturas, M. D., Anderegg, W. R., Mencuccini, M., Mackay, D. S., Wang, Y., and Love, D. M. (2017), "Predicting stomatal responses to the environment from the optimization of photosynthetic gain and hydraulic cost," *Plant, cell & environment*, 40, 816–830.

Strack, M., Waddington, J., and Tuittila, E.-S. (2004), "Effect of water table drawdown on northern peatland methane dynamics: Implications for climate change," *Global Biogeochemical Cycles*, 18.

Strogatz, S. H. (2014), *Nonlinear dynamics and chaos: with applications to physics, biology, chemistry, and engineering*, CRC Press, Boca Raton.

Stull, R. B. (1988), *An introduction to boundary layer meteorology*, Springer Netherlands.

Swann, A. L., Laguë, M. M., Garcia, E. S., Field, J. P., Breshears, D. D., Moore, D. J., Saleska, S. R., Stark, S. C., Villegas, J. C., Law, D. J., et al. (2018), "Continental-scale consequences of tree die-offs in North America: identifying where forest loss matters most," *Environmental Research Letters*, 13, 055014.

Tai, X., Mackay, D. S., Anderegg, W. R., Sperry, J. S., and Brooks, P. D. (2017), "Plant hydraulics improves and topography mediates prediction of aspen mortality in southwestern USA," *New Phytologist*, 213, 113–127.

Teske, M. E. and Thistle, H. W. (2004), "A library of forest canopy structure for use in interception modeling," *Forest Ecology and Management*, 198, 341–350.

Thiemann, M., Trosset, M., Gupta, H., and Sorooshian, S. (2001), "Bayesian recursive parameter estimation for hydrologic models," *Water Resources Research*, 37, 2521–2535.

Thornton, P., Thornton, M., Mayer, B., Wei, Y., Devarakonda, R., Vose, R., and Cook, R. (2014), "Daymet: Daily Surface Weather Data on a 1-km Grid for North America, Version 3," Available at `https://doi.org/10.3334/ORNLDAAC/1328`. Accessed September 15, 2017.

Tiner, R. W. (1999), *Wetland indicators: A guide to wetland identification, delineation, classification, and mapping*, CRC Press, Boca Raton, FL, USA.

Todd, A., Buttle, J., and Taylor, C. (2006), "Hydrologic dynamics and linkages in a wetland-dominated basin," *Journal of Hydrology*, 319, 15–35.

Todd, M. J., Muneepeerakul, R., Pumo, D., Azaele, S., Miralles-Wilhelm, F., Rinaldo, A., and Rodriguez-Iturbe, I. (2010), "Hydrological drivers of wetland vegetation community distribution within Everglades National Park, Florida," *Advances in Water Resources*, 33, 1279–1289.

Trugman, A., Medvigy, D., Mankin, J., and Anderegg, W. (2018), "Soil moisture stress as a major driver of carbon cycle uncertainty," *Geophysical Research Letters*.

Trumbore, S., Brando, P., and Hartmann, H. (2015), "Forest health and global change," *Science*, 349, 814–818.

Turetsky, M., Treat, C., Waldrop, M., Waddington, J., Harden, J., and McGuire, A. (2008), "Short-term response of methane fluxes and methanogen activity to water table and soil warming manipulations in an Alaskan peatland," *Journal of Geophysical Research: Biogeosciences (2005–2012)*, 113.

Turner, T. E., Billett, M. F., Baird, A. J., Chapman, P. J., Dinsmore, K. J., and Holden, J. (2016), "Regional variation in the biogeochemical and physical characteristics of natural peatland pools," *Science of the Total Environment*, 545, 84–94.

U.S. Fish and Wildlife Service (1993), "National Wetlands Inventory website. U.S. Department of the Interior, Fish and Wildlife Service, Washington, D.C." Available online at `http://www.fws.gov/wetlands/`, Accessed: 2014-09-24.

U.S. Forest Service (2004), "Existing Vegetation–CALVEG," Available at `https://www.fs.usda.gov/main/r5/landmanagement/gis`. Accessed October 7, 2017.

U.S. Forest Service (2015a), "U.S. Forest Service Pacific Southwest Region Forest Health Protection Aerial Detection Survey," Available at `https://www.fs.usda.gov/detail/r5/forest-grasslandhealth`. Accessed September 25, 2017.

U.S. Forest Service (2015b), "U.S. Forest Service Pacific Southwest Region Forest Health Protection Aerial Detection Survey," .

U.S. Forest Service (2016), "MODIS Active Fire Detections for the CONUS (2002–2015)," Available at `https://fsapps.nwcg.gov/afm/gisdata.php`. Accessed September 13, 2017.

U.S. Geological Survey (1999), "National Elevation Dataset," Available online at `http://ned.usgs.gov/`, Accessed: 2014-10-01.

U.S. Geological Survey (2017), "Landsat 7 ETM+ Surface Reflectance product courtesy of the U.S. Geological Survey Earth Resources Observation and Science Center," Available at `https://landsat.usgs.gov/landsat-surface-reflectance-data-products`. Accessed July 21, 2017.

van Mantgem, P. J., Stephenson, N. L., Byrne, J. C., Daniels, L. D., Franklin, J. F., Fulé, P. Z., Harmon, M. E., Larson, A. J., Smith, J. M., Taylor, A. H., et al. (2009), "Widespread increase of tree mortality rates in the western United States," *Science*, 323, 521–524.

Verbesselt, J., Umlauf, N., Hirota, M., Holmgren, M., Van Nes, E. H., Herold, M., Zeileis, A., and Scheffer, M. (2016), "Remotely sensed resilience of tropical forests," *Nature Climate Change*, 6, 1028.

Vicente-Serrano, S. M., Gouveia, C., Camarero, J. J., Beguería, S., Trigo, R., López-Moreno, J. I., Azorín-Molina, C., Pasho, E., Lorenzo-Lacruz, J., Revuelto, J., et al. (2013), "Response of vegetation to drought time-scales across global land biomes," *Proceedings of the National Academy of Sciences*, 110, 52–57.

Vidon, P. G. and Hill, A. R. (2004), "Landscape controls on the hydrology of stream riparian zones," *Journal of Hydrology*, 292, 210–228.

Viola, F., Daly, E., Vico, G., Cannarozzo, M., and Porporato, A. (2008), "Transient soil–moisture dynamics and climate change in Mediterranean ecosystems," *Water Resources Research*, 44.

von Asmuth, J. R. and Knotters, M. (2004), "Characterising groundwater dynamics based on a system identification approach," *Journal of Hydrology*, 296, 118–134.

Walter, B. P. and Heimann, M. (2000), "A process-based, climate-sensitive model to derive methane emissions from natural wetlands: Application to five wetland sites, sensitivity to model parameters, and climate," *Global Biogeochemical Cycles*, 14, 745–765.

Walter, B. P., Heimann, M., and Matthews, E. (2001), "Modeling modern methane emissions from natural wetlands: 1. Model description and results," *Journal of Geophysical Research: Atmospheres*, 106, 34189–34206.

Walther, S., Voigt, M., Thum, T., Gonsamo, A., Zhang, Y., Köhler, P., Jung, M., Varlagin, A., and Guanter, L. (2016), "Satellite chlorophyll fluorescence measurements reveal large-scale decoupling of photosynthesis and greenness dynamics in boreal evergreen forests," *Global change biology*, 22, 2979–2996.

Wardrop, D. H., Kentula, M. E., Jensen, S. F., Stevens, D. L., Hychka, K. C., and Brooks, R. P. (2007), "Assessment of wetlands in the Upper Juniata watershed in Pennsylvania, USA using the hydrogeomorphic approach," *Wetlands*, 27, 432–445.

West, M. and Harrison, J. (1997), *Bayesian forecasting and dynamic models*, Springer, New York, NY, USA.

Wigmosta, M. S., Vail, L. W., and Lettenmaier, D. P. (1994), "A distributed hydrology–vegetation model for complex terrain," *Water resources research*, 30, 1665–1679.

Williams, A. P., Allen, C. D., Macalady, A. K., Griffin, D., Woodhouse, C. A., Meko, D. M., Swetnam, T. W., Rauscher, S. A., Seager, R., Grissino-Mayer, H. D., et al. (2013), "Temperature as a potent driver of regional forest drought stress and tree mortality," *Nature Climate Change*, 3, 292–297.

Wittenberg, A. T. (2009), "Are historical records sufficient to constrain ENSO simulations?" *Geophysical Research Letters*, 36.

Wöhling, T., Samaniego, L., and Kumar, R. (2013), "Evaluating multiple performance criteria to calibrate the distributed hydrological model of the upper Neckar catchment," *Environmental earth sciences*, 69, 453–468.

Wolf, A., Anderegg, W. R., and Pacala, S. W. (2016), "Optimal stomatal behavior with competition for water and risk of hydraulic impairment," *Proceedings of the National Academy of Sciences*, 113, E7222–E7230.

Wolfe, B. T., Sperry, J. S., and Kursar, T. A. (2016), "Does leaf shedding protect stems from cavitation during seasonal droughts? A test of the hydraulic fuse hypothesis," *New Phytologist*, 212, 1007–1018.

Wolski, P. and Savenije, H. (2006), "Dynamics of floodplain-island groundwater flow in the Okavango Delta, Botswana," *Journal of hydrology*, 320, 283–301.

Wullschleger, S. D., Epstein, H. E., Box, E. O., Euskirchen, E. S., Goswami, S., Iversen, C. M., Kattge, J., Norby, R. J., van Bodegom, P. M., and Xu, X. (2014), "Plant functional types in Earth system models: past experiences and future directions for application of dynamic vegetation models in high-latitude ecosystems," *Annals of Botany*, 114, 1–16.

Xia, Y., Mitchell, K., Ek, M., Sheffield, J., Cosgrove, B., Wood, E., Luo, L., Alonge, C., Wei, H., Meng, J., et al. (2012), "Continental-scale water and energy flux analysis and validation for the North American Land Data Assimilation System project phase 2 (NLDAS-2): 1. Intercomparison and application of model products," *Journal of Geophysical Research: Atmospheres (1984–2012)*, 117.

Xu, X., Medvigy, D., Powers, J. S., Becknell, J. M., and Guan, K. (2016), "Diversity in plant hydraulic traits explains seasonal and inter–annual variations of vegetation dynamics in seasonally dry tropical forests," *New Phytologist*, 212, 80–95.

Young, D. J., Stevens, J. T., Earles, J. M., Moore, J., Ellis, A., Jirka, A. L., and Latimer, A. M. (2017), "Long-term climate and competition explain forest mortality patterns under extreme drought," *Ecology letters*, 20, 78–86.

Yu, X., Duffy, C. J., Baldwin, D. C., and Lin, H. (2014), "The role of macropores and multi–resolution soil survey datasets for distributed surface–subsurface flow modeling," *Journal of Hydrology*, 516, 97–106.

Yu, X., Bhatt, G., Duffy, C. J., Wardrop, D. H., Najjar, R. G., Ross, A. C., and Rydzik, M. (2015), "A coupled surface–subsurface modeling framework to assess the impact of climate change on freshwater wetlands," *Climate Research*, 66, 211–228.

Zellner, A. (1986), "On assessing prior distributions and Bayesian regression analysis with g-prior distributions," *Bayesian inference and decision techniques: Essays in Honor of Bruno De Finetti*, 6, 233–243.

Zona, D., Oechel, W., Kochendorfer, J., Paw, U., Salyuk, A., Olivas, P., Oberbauer, S., Lipson, D., et al. (2009), "Methane fluxes during the initiation of a large-scale water table manipulation experiment in the Alaskan Arctic tundra," *Global Biogeochemical Cycles*, 23.

Zscheischler, J., Westra, S., Hurk, B. J., Seneviratne, S. I., Ward, P. J., Pitman, A., AghaKouchak, A., Bresch, D. N., Leonard, M., Wahl, T., et al. (2018), "Future climate risk from compound events," *Nature Climate Change*, p. 1.

Biography

Yanlan Liu earned a B.Eng. degree in Hydraulics Engineering from Tsinghua University in 2014. In the same year, she joined Duke University for a Ph.D. degree in Environmental Science and a M.S. degree in Statistical Science.